Novel use of miniature CPC in photovoltaic/thermal and radiative cooling systems

by

Ya DAN

Student ID: 20406839

Supervisors: Dr. Yuehong Su, Dr. Siddig Omer, Dr. Mingke Hu

Thesis Submitted in Partial Fulfilment of the Requirements for the Degree of

Doctor of Philosophy

in the Department of Architecture and Built Environment

Faculty of Engineering

University of Nottingham

I hereby certify that this is entirely my own work unless otherwise stated, and I have all necessary rights and consents to publicly distribute this dissertation via the University of Nottingham's eTheses archive.

13 December 2024

ABSTRACT

The rapid development of modern society has significantly increased energy consumption, particularly in the building sector. More than 80% of the primary energy supply still relies on non-renewable sources such as fossil fuels, raising concerns about energy shortages and environmental pollution. To promote energy conservation and transition to a sustainable society, research and development of sustainable energy technologies is becoming increasingly imperative. Among various strategies, photovoltaic thermal (PVT) systems, which use solar energy (~5800K) to provide heat and electricity to buildings, and passive radiative sky cooling (RC) technology, which utilizes the cold outer space (~3K) to cool buildings, are seen as attractive approaches. However, RC technology currently faces the challenge of inherent low cooling power, limiting its ability to meet the cooling demands of buildings. Therefore, enhancing the cooling performance of RC technology is urgently needed. Additionally, standalone building-integrated PVT system and RC technology encounter challenges such as seasonal adaptability and single functionality. To effectively integrate PVT and RC systems within a limited building envelope, exploring new configurations is crucial. In this thesis, a concentrated RC system based on a compound parabolic concentrator (named CPC-RC module) is deeply studied and continuously optimizes its structure to enhance cooling performance. Additionally, a hybrid system integrating CPC-RC modules with PVT modules is proposed. This system can simultaneously collect solar energy and cold energy for heating and cooling buildings, aiming to reduce energy consumption and offer an innovative solution for promoting net-zero carbon buildings.

This thesis first proposes a modelling approach to accurately characterize the cooling performance of RC modules, addressing the issue in existing theoretical analyses that often overestimate of cooling power. Additionally, utilizing this approach evaluates the cooling performance of CPC-RC module on different typical days. Numerical analysis demonstrates that CPC-RC module exhibits excellent cooling performance in summer, with an average nighttime cooling power of 130.10 W/m^2, which is 5.7% and 18.1% higher than that of inverted trapezoidal concentrator-based RC module and flat RC module, respectively. Experimental results also show that the temperature reduction capacity of CPC-RC modules is 30% greater than the flat RC modules. However, during the daytime, CPC-RC module

cannot achieve self-cooling due to the solar concentration characteristic by the CPC. To address this issue, the mirror CPC structure in the CPC-RC module has been replaced with a CPC made of dissimilar materials, with one side transparent and the other mirrored. This new module is referred to as the DCPC-RC module, features a unique CPC structure that allows part of the solar radiation to pass through the transparent side, achieving excellent daytime cooling performance. Experiments have shown that the module can achieve a cooling effect of 0.95 °C below ambient temperature during the daytime. This new configuration provides a design concept for integrating RC modules with PVT modules by using a transparent infrared reflective film (TIRF) to direct solar radiation toward the PVT modules while effectively reducing the solar radiation reaching the RC emitter. This thesis further proposes and develops an innovative system that integrates PVT and RC modules based on a transparent CPC covered with TIRF (referred to as TIRF-TCPC-PVTRC system) to achieve simultaneous heating and cooling, thereby meeting the dynamic energy demand of the building throughout the year. The experimental results show that the TIRF-TCPC-PVTRC system achieves an 88% improvement in cooling capacity compared to the PVTRC module without the TCPC structure, demonstrating excellent cooling performance. However, due to the weighted average solar transmittance of the used TIRF only being 0.69, the conversion efficiency of the TIRF-TCPC-PVTRC module decreased by 36% compared to the PVTRC module. This novel system integrates two different energy collections modules into a single unit, maximizing the use of renewable energy from both the sun and outer space. This integrated approach is expected to address the challenges faced by individual RC and PVT modules, such as low efficiency and intermittent operation.

Key words: Compound parabolic concentrator, radiative sky cooling, photovoltaic/thermal, solar energy utilization, energy-saving.

LIST OF PUBLICATIONS

International journal papers

Dan, Ya., Hu, Mingke., Suhendri, Suhendri., Su, Yuehong., Saffa, Riffat. Harnessing the characteristic of compound parabolic concentrators for directional concentration of emitted thermal radiation and so lar shielding in building-integrated radiative cooling. ***Energy and Buildings***, *307 (2024) 113922.*

Dan, Ya., Hu, Mingke., Su, Yuehong., Saffa, Riffat. A generalized modelling approach to performance analysis of radiative sky cooling with complicated configurations and external environments. ***Renewable energy,*** *237 (2024) 121729.*

Dan, Ya., Hu, Mingke., Wang, Qiliang., Su, Yuehong., Saffa, Riffat. Comprehensive evaluation of inte grating radiative sky cooling with compound parabolic concentrator for cooling flux amplifying. ***Ener gy,*** *312 (2024) 133673.*

Dan, Ya., Hu, Mingke., Wang, Qiliang., Su, Yuehong., Saffa, Riffat. Enhancing radiative sky cooling performance by employing crossed compound parabolic concentrating configurations. ***Renewable energy,*** *239 (2024) 121979.*

Suhendri, Suhendri., Hu, Mingke., **Dan, Ya.**, Su, Yuehong., Zhao, Bin., Saffa, Riffat. Building energy-saving potential of a dual-functional solar heating and radiative cooling system. ***Energy and Buildings***, *303 (2024) 113764.*

Wang, Qiliang., **Dan, Ya.**, Saffa, Riffat., Yang, Hongxing., Su, Yuehong., Hu, Mingke. Harvesting energy from the sun and space: A versatile collector for simultaneous production of electricity, heat, and cold energy. ***The Innovation Energy***, *1*(1), 100013-1.

Dan, Ya., Wang, Qiliang., Hu, Mingke., Su, Yuehong., Saffa, Riffat. A novel radiative cooling system with a dissimilar material-based compound parabolic concentrator for mitigating the harassment of daytime solar radiation. ***Renewable energy.*** (Under review)

Conference papers

Dan, Ya., Hu, Mingke., Su, Yuehong., Saffa, Riffat. (2023). A novel modelling approach for performance analysis of a concentrated radiative cooling system using the compound parabolic concentrator. *20th International Conference on Sustainable Energy Technologies* (SET 2023), Nottingham, UK.

Dan, Ya., Hu, Mingke., Wang, Qiliang., Su, Yuehong., Saffa, Riffat. (2024). A comprehensive study on the cooling performance of the radiative cooling module with crossed compound parabolic concentrator. Alternative Energy Sources, Materials & Technologies (AESMT'24). Sophia, Bulgaria.

Dan, Ya., Wang, Qiliang., Hu, Mingke., Zhao, Dongliang., Su, Yuehong., Saffa, Riffat. (2024). A novel radiative cooling system integrated with an asymmetric material-based compound parabolic concentrator. Alternative Energy Sources, Materials & Technologies (AESMT'24). Sophia, Bulgaria.

Dan, Ya., Wang, Qiliang., Hu, Mingke., Li, Xue., Pei, Gang., Su, Yuehong., Saffa, Riffat. (2024). A novel system based on a transparent compound parabolic concentrator covered with transparent infrared reflective films for simultaneous utilization of solar energy and radiative sky cooling. *21st International Conference on Sustainable Energy Technologies* (SET 2024), Shanghai, China.

ACKNOWLEDGEMENT

As I conclude this writing, my more than three-year doctoral journey in the UK is coming to an end. This period has provided me not only with immense knowledge but also a transformation in my mindset. At this moment, in addition to thanking myself for persevering and never giving up, I must extend my deepest gratitude to my supervisors, family, and friends for their constant and unwavering support.

First and foremost, I am deeply grateful to my supervisor, Professor Yuehong Su, for his meticulous guidance and support throughout the research for this thesis. His profound knowledge and quick thinking always provided clarity when I felt lost. Since my undergraduate and master's studies were in fields quite different from my doctoral research, my progress was initially slow. However, he patiently guided me step by step in the right direction, enabling me to complete my research. I would also like to express my sincere thanks to Dr Mingke Hu and Dr Qiliang Wang for their invaluable assistance. Dr Hu began mentoring me from the time I wrote my first journal paper, offering thorough guidance on academic writing from the very beginning. He taught me how to cultivate systematic logical thinking and instilled in me the importance of maintaining a rigorous pursuit of truth. Thanks to his guidance, I made significant progress, for which I am deeply appreciative. Additionally, I owe great thanks to Dr Wang for his patient and insightful guidance in my research. Each time I discussed academic problems with him, he patiently helped me solve challenges and pointed me in the right direction. With the help of these three teachers, I was able to successfully complete my doctoral studies and research. Their support will always remain in my heart.

Apart from my supervisors, I am also thankful for the classmates and senior students I met during my doctoral journey. We shared our frustrations and difficulties during the PhD process and encouraged each other to move forward. In the grey and gloomy weather of the UK, their presence became the motivation for me to keep pushing forward.

Finally, I would like to express my heartfelt gratitude to my parents. They have always supported my academic pursuits, whether it was my master's or PhD studies. Whenever I had an idea, they were the first to support it. With them as my backing, I was able to pursue the life I desired in a foreign country without financial concerns.

I know that graduating with a PhD is not the end of learning, and I will continue to improve myself in the future. However, I firmly believe that everything I have learned over the past three years will give me the courage to conquer one peak after another in the future. Once again, I would like to thank everyone who has helped me, and I am also grateful for all the challenges and difficulties I have encountered. I have always believed that "everything is the best arrangement," and I hope that every day in the future will be our best day.

NOMENCLATURE

A	Width of the CPC front aperture, m	κ	Solar energy conversion efficiency
C	Concentration ratio of concentrator	ω	Radiation beam ratio, %
G	Total incident solar radiation, W/m^2	θ_{max}	Maximum half-acceptance angle of CPC
H	Height of concentrated RC modules, mm	θ	Zenith angle, °
I_b	Blackbody spectral intensity, W·m^{-2}·μm^{-1}·sr^{-1}	θ_h	Solar altitude angle, °
i	Number of reflections	φ	Azimuth angle, °
L	Length of RC modules, mm	σ	Stefan-Boltzmann constant, W·m^{-2}·K^{-4}
P	Power density, W/m^2	**Subscripts**	
T	Temperature, K or °C	amb	Ambient
t	Specific daytime hour	cool	Cooling
W	Bottom width of RC modules, mm	emi	Emitter
Greek symbols		eff	Effective
α	Absorptivity	non-rad	Heat conduction and convection
β	Respective ratios of the radiation beam, %	gro	Ground
ε	Emissivity	gro_day	Ground (daytime)
ρ	Reflectivity	sur	Aboveground obstacles
$\eta_{_sol}$	Solar receiving ratio, %	con	Concentrator
η	Solar shielding ratio, %	sol_dir	Direct solar radiation
λ	Wavelength, μm	sol_dif	Diffuse solar radiation
δ	Radiation beam	col	Solar collector
τ	Transmittance		
ξ	Sky dome coverage ratio		

LIST OF CONTENTS

ABSTRACT ..... **I**

LIST OF PUBLICATIONS ..... **III**

ACKNOWLEDGEMENT ..... **V**

NOMENCLATURE ..... **VI**

LIST OF FIGURES ..... **XI**

LIST OF TABLES ..... **XXI**

1. Introduction **1**

1.1 Background 1

1.2 Statement of the problems 2

1.3 Novelty of thesis 3

1.4 Aim and objectives 4

1.5 Thesis structure 6

2. Literature review **8**

2.1 Introduction 8

2.2 Radiative sky cooling (RC) technology 10

2.2.1 Fundamentals of RC technology *10*

2.2.2 Applications of RC technology in buildings *17*

2.2.3 Applications of RC technology integrated with concentrators *36*

2.2.4 Summary *41*

2.3 Compound parabolic concentrators (CPCs) 42

2.3.1 Different structure of the CPC *43*

2.3.2 Applications of the CPC in solar energy conversion *50*

2.3.3 Applications of the CPC in daylighting..... *62*

2.4 Summary..... 65

3. Innovative use of optical simulation for performance analysis of RC modules with complex configuration..... 66

3.1 Introduction..... 66

3.2 Modelling approach..... 67

3.2.1 Directional radiative heat exchange between the RC module and external environment... *67*

3.2.2 Mathematical framework..... *70*

3.2.3 Model validation..... *73*

3.3 Nighttime maximum net cooling performance analysis of RC modules..... 74

3.3.1 Description of different configurations of RC modules..... *74*

3.3.2 Effect of modules structures..... *76*

3.3.3 Effect of different emitter deployment strategies..... *78*

3.3.4 Effect of diverse external environments..... *82*

3.4 Daytime solar radiation absorption analysis of RC modules..... 84

3.4.1 Solar radiation-related simulation model..... *84*

3.4.2 Performance indicator..... *85*

3.4.3 Effect of tilt angle on RC modules..... *86*

3.4.4 All-day total absorbed solar radiation on RC modules..... *87*

3.5 Summary..... 88

4. Numerical study and experimental evaluation of two-dimensional (trough) compound parabolic concentrator (CPC) - based radiative cooling (CPC-RC) module..... 90

4.1 Introduction..... 90

4.2 Function of the CPC structure in CPC-RC module 91

4.2.1 Solar shield mode *91*

4.2.2 Thermal radiation concentration and shield mode *92*

4.3 Comparative numerical study of CPC-RC module on four typical days 94

4.3.1 Novel modelling approach *95*

4.3.2 Comparative analysis of CPC-RC module and other RC modules *99*

4.3.3 Performance analysis of CPC-RC module with different inclined placements *104*

4.3.4 Performance analysis of CPC-RC module with different RC emitters *110*

4.4 Comparative experiment of CPC-RC module against other RC modules 113

4.4.1 Design and preparation of experimental RC modules *114*

4.4.2 Performance of CPC-RC and flat-RC modules with and without PE film *118*

4.4.3 Performance of CPC-RC, trapezoidal-RC and flat-RC modules *120*

4.4.4 Performance of CPC-RC and flat-RC modules with different inclined placements *121*

4.5 Summary 125

5. Comprehensive analysis of RC module integrated with dissimilar material-based CPC (DCPC-RC module) 126

5.1 Introduction 126

5.2 Description of DCPC-RC module and solar profile angle 126

5.2.1 Introduction of DCPC-RC module *126*

5.2.2 Solar profile angle *129*

5.3 Experiment study of DCPC-RC module 130

5.3.1 Experimental RC module *130*

5.3.2 Experimental results *131*

5.4 Effect of different structural and external environment configurations on DCPC-RC module cooling performance 134

5.4.1 Effect of different CPC wing frameworks *134*

5.4.2 Effect of DCPC wing frameworks with different spectral characteristics *137*

5.4.3 Effect of the geographical location of DCPC-RC modules *141*

5.5 Summary 146

6. Incorporation of transparent infrared-reflective film (TIRF) with CPC-RC for novel simultaneous solar collection and radiative cooling 147

6.1 Introduction 147

6.2 Description and optimization of TIRF-TCPC-PVTRC system 147

6.2.1 Introduction of the TIRF-TCPC-PVTRC system *147*

6.2.2 Cooling performance evaluation of TIRF-TCPC-PVTRC module *148*

6.2.2 Optimization of the TIRF-TCPC-PVTRC module *152*

6.3 Experimental study of optimized TIRF-TCPC-PVTRC system 157

6.3.1 Experimental preparation *158*

6.3.2 Experimental results analysis *160*

6.4 Summary 165

7. Conclusion 166

7.1 Summary of findings and contributions 166

7.2 Limitation and recommendation 168

References 170

Appendix 200

LIST OF FIGURES

Figure 1-1: Final energy consumption and carbon emissions for building cooling by region in the Net Zero Scenario [12]. 2

Figure 1-2: The schematic diagram of the proposed TIRF-TCPC-PVTRC system. 4

Figure 1-3: Flow chart of this thesis structure. 7

Figure 2-1: The normalized AM 1.5 solar spectrum and atmospheric transmission in the zenith direction on a clear day [39]. 10

Figure 2-2: Schematic of the heat balance of an RC emitter. 11

Figure 2-3: The sky emissivity for different zenith angles from 0° to 75° [52]. 15

Figure 2-4: Radiative cooling coatings and SEM images [79]. 18

Figure 2-5: Field test setups from (a) an isometric view. (b) The top view [80]. 19

Figure 2-6: Schematic of passive daytime RC and the measured spectral properties of the MgO paints [81]. 20

Figure 2-7: (a) Spectral reflectivity [$R(\lambda)=1-\varepsilon(\lambda)$] and (b) Infrared emissivity of a 300-μm-thick P(VdF-HFP)HP coating [89]. 21

Figure 2-8: (a) natural wood and (b) cooling wood. SEM image of the (c) cooling wood and (d) partially aligned cellulose nanofibers of the cooling wood. (e) Schematic showing the wood structure strongly scattering solar irradiance. (f) Schematic of infrared emission by molecular vibration of the cellulose functional groups. (g) Setup of the real-time measurement [93]. 22

Figure 2-9: (a) The glass-Al_2O_3 particle shows good fluidity. (b) The radiative cooling glass coating is applied on a ceramic tile. (c) The radiative cooling glass coating can be fabricated on a large scale [95]. 23

Figure 2-10: The experimental platform consisting of two single - space model rooms [99]. 24

Figure 2-11: Exterior of the roof before/after applying the RC film [102]. 25

Figure 2-12: Field experiment setup of green roof, cool roof and conventional roof. (a) Site photo (b) Plan view [104]. 25

Figure 2-13: (a) Cool paint application. (b) roof detail and (c) coatings used for the experiment [110]. 27

Figure 2-14: (a) Photo and (b) schematic of the PRC-CR and concrete-roof room [112]. 27

Figure 2-15: Schematic of a RC system integrated with residential building [27]. 28

Figure 2-16: Building-integrated nighttime RC systems [15]..... 29

Figure 2-17: The photograph of the experimental chambers, (b) Schematic diagram of wall and floor structure, and (c) Schematic diagram of OR (ordinary roof), PCR (phase change roof), and RC-PCR. 30

Figure 2-18: (a) Schematic of modelling building and the whole RC system with an auxiliary AC unit [120]. (b) The RadiCold module and the bilayer RadiCold metafilm [14]. (c) Building-integrated RadiCold system [14]. 31

Figure 2-19: (a) Building façades integrated with PV-RSC system [116]. (b) The schematic of the PCM-embedded wall with RC module [127]. (c) The coupled system of the pipe-encapsulated PCM wall and RC module [128]. (d) The basic structure of the novel all-day cooling RC-PCM-wall [129]..... 34

Figure 2-20: (a) Schematic of the semi-transparent RC glass and its energy transfer diagram [133]. (b) Schematic diagram of the dynamic glass and its two modes [134]. 35

Figure 2-21: (a) Schematic structure of the radiative cooling regulating thermochromic window. (b) Working principle of radiative cooling regulating thermochromic window in summer and winter [136]. 36

Figure 2-22: (a) Schematic diagram and photograph of the cooling system with tapered waveguide structure [36]. (b) Working principle with separated radiation and condensation side and structure of selective emitter [142]. (c) Schematic diagram and In situ experimental set-up [46]. (d) Photos of the experimental apparatus with a top view and cross-section view of the radiative cooling device [45]. 38

Figure 2-23: Schematic of the RC with different reflectors [143]. 39

Figure 2-24: Schematic of the "concentrated radiative cooling" device [37]. 39

Figure 2-25: Radiative cooling performance of the double-sided thermal emitter system [144]. 40

Figure 2-26: Experimental demonstration of the theoretical optimization of conical concentrators [145]. 41

Figure 2-27: The structure of the aCPC. 44

Figure 2-28: The surface structure of the FE-CPC[166]. (a) Kunming ϕ = 24.85°. (b) Chengdu ϕ = 30.67°. (c) Xi'an ϕ = 34.26°. (d) Beijing ϕ = 39.93°. 44

Figure 2-29: (a) the angular rotation of the 2-D cross-sections to produce the rotationally asymmetrical CPC. (b) An example of a rotationally asymmetrical CPC. 45

Figure 2-30: Prototype of crossed CPC+si PV cell [178]. 46

Figure 2-31: (a)Geometrical structure of the designed 3-D concentrator by Sellami. 47

Figure 2-32: The structure of the IAR-CPC [183]. 48

Figure 2-33: Schematic diagram of M-CPC [186]. 49

Figure 2-34: A design of miniature CPC [192]. 50

Figure 2-35:Different materials of crossed CPC in LCPV system 51

Figure 2-36: Diagram illustrating the BFI-ACP-PV system [169]. 53

Figure 2-37: Cross-section of the PVT System (mm) [206]. 54

Figure 2-38: The Schematic of (a) CPC and (b) ECPC [163]. 54

Figure 2-39: Optical and thermal losses in a CPVT system: (a) Unglazed and (b) Glazed [159]. 55

Figure 2-40: Schematic diagram of the perspective and sectional view of PVT/D system [207]. 56

Figure 2-41: The schematic diagram of the EBIETC system [209]. 57

Figure 2-42: The schematic of the mini-CSC with a solar evacuated tube [210]. 57

Figure 2-43: The Schematic of the ACPC-coupled evacuated tube absorber [211]..... 58

Figure 2-44: The schematic of the CPC-CSC [160]. 59

Figure 2-45: Schematic diagram of the LFRC system [216]. 60

Figure 2-46: The schematic of LFRC with CPC [218]. 60

Figure 2-47: Schematic of square parabolic dish with CPV receiver, electrical and thermal load connected [219]..... 61

Figure 2-48: The schematic of the dense array CPV system [220]..... 61

Figure 2-49: The overall schematic diagram of the CPV/D system: (a) CPV/D array; (b) design sketch of the building integration; (c) inner view of the CPV/D system when integrating with building roof or replacing the skylight [223]. 63

Figure 2-50: The schematic diagram of the SSF-covered CPC array in the greenhouse roof [226].... 64

Figure 3-1: Schematic of heat exchange between the building-integrated RC modules and external environment. 66

Figure 3-2: Schematic of the heat exchange between flat-RC and concentrated-RC modules with the sky. 67

Figure 3-3: Schematic of the reciprocity principle in (a) concentrated- and (b) non-concentrated-RC systems. In the figure, the blue and orange lines, which overlap in reality, are depicted as two parallel lines to facilitate clearer representation. 68

Figure 3-4: (a) & (b) Effect of the absence or presence of a concentrator on the directional radiation beam emitted by the RC emitter. (c) & (d) Radiative heat transfer of the flat-RC and inverted trapezoidal-RC modules in different azimuth and zenith angle directions when obstacles are present. 70

Figure 3-5: Spectral sky emissivity at different zenith angles. The zenith direction exhibits the lowest emissivity among different zenith angles, equivalent to the highest sky transmittance, which is more conducive to radiative cooling. 73

Figure 3-6: Simulated and experimental net cooling power densities of an RC module. The data computed using the proposed approach (green points) is very close to the experimental data (red points), with the *RMSD* being 34.45% lower than that in Ref. [14]. 74

Figure 3-7: Schematic of a flat-RC module and three concentrated-RC modules with different concentrators. 75

Figure 3-8:Schematic of 2D inverted trapezoidal-RC modules with different emitter deployment strategies. 76

Figure 3-9:Directional radiation angular ratio curves of the flat-RC module and three concentrated-RC modules with different concentrating structures. 77

Figure 3-10: Absorbed external environmental thermal radiation and net cooling power density of four RC modules..... 78

Figure 3-11: Ratio of directional radiation beam reaching different zenith angles to total hemispheric radiation beam from the RC emitter..... 79

Figure 3-12: Radiative heat transfer of 2D inverted trapezoidal-RC modules with (a) flat emitter and (b) inverted V-shaped emitter. 79

Figure 3-13: (a) Thermal radiation power that cannot escape from the 2D inverted trapezoidal-RC modules with different emitter deployment strategies. (b) External environmental thermal radiation and net cooling power density for five RC modules. 81

Figure 3-14: Cooling power of six 2D inverted trapezoidal-RC modules with different emitter deployment strategies. At the maximum allowable tilt angle, it is shown in the blue square that the cooling power of the module can reach 79.23 W. 82

Figure 3-15:Radiative heat exchange between the flat-RC module and sky and local surroundings. To more clearly and simplified express the radiative heat exchange, the external environment is represented in the form of a cross-section diagram (actually the entire external environment is a hemisphere.).... 83

Figure 3-16: (a) Absorbed external environmental thermal radiation and net cooling power density of the flat-RC module at night under different sky dome coverage ratios. (b) A comparative case with the local surrounding temperature and sky dome coverage ratio set at 50 °C and 0.5, respectively. 84

Figure 3-17: Different spectral properties of RC emitters under solar spectrum. 85

Figure 3-18: Solar radiation absorbed by (a) black-painted emitter and (b)ideal emitter different tilt angles on typical days. 87

Figure 3-19： Total solar radiation absorbed by the inverted trapezoidal-RC and flat-RC modules at three placements on four typical days. (a) Black-painted RC emitter (b) Ideal RC emitter 88

Figure 4-1: Schematic of the radiative heat exchange for the CPC-RC module..... 91

Figure 4-2: Schematic of the CPC-RC module shield against part of unfavourable radiation during the daytime..... 92

Figure 4-3: (a) Spectral atmospheric emissivity of four different zenith angles in the 0.3-25 μm wavelength range; (b) the weighted average atmospheric emissivity between the 8 and 13 μm. 93

Figure 4-4: Schematic diagram of (a) the radiation path through the atmosphere; and (b) the radius of the earth, thickness of the atmospheric layer, and size of the CPC are indicative. 94

Figure 4-5: Schematic of the CPC-RC module shield angular thermal radiation at night. 94

Figure 4-6: Different incoming thermal radiation beam paths reach the CPC-RC module's emitter.... 96

Figure 4-7: Ratio of the radiation beam from zenith angles (θ) that reaches the RC emitter after i-reflections to the total radiation beam at that zenith angle. (a) CPC-RC module. (b) Inverted trapezoidal-RC module. 97

Figure 4-8: Ambient temperature and solar irradiance for four typical days in Guangzhou, China from the EnergyPlus database..... 99

Figure 4-9: Schematic diagram of the three RC modules. 100

Figure 4-10: Direct solar receiving ratio for two RC modules on four typical days..... 101

Figure 4-11: (a) Difference in hourly cooling power density for different RC modules on four typical days. (b) Average cooling power density for different RC modules during daytime and nighttime. (c) All-day average cooling power density for different RC modules. 104

Figure 4-12: Direct solar receiving ratio for CPC-RC modules on four typical days. 105

Figure 4-13: Absorbed solar radiation for CPC-RC modules on four typical days. 107

Figure 4-14: Difference in hourly cooling power density for CPC-RC modules on four typical days. 109

Figure 4-15: (a) Average cooling power density of CPC-RC modules with different tilt angles during the daytime and nighttime in Guangzhou, China. (b) Optimal tilt angle to obtain best all-day cooling performance on 21st June in Guangzhou, China. 110

Figure 4-16: Spectral properties of the different RC emitters. 111

Figure 4-17: (a) Difference in hourly cooling power density and (b) daytime and nighttime average cooling power density for the CPC-RC modules tilted at the optimal tilt angle with different RC emitter on four typical days. (c) All-day average cooling power density for different RC modules on four typical days. 113

Figure 4-18: Schematic cross-section view of the experimental CPC-RC module. 114

Figure 4-19: Spectral characteristics of the metamaterial-covered emitter, black-painted emitter, and CPC surface. The reason for the CPC reflectivity exceeding 1 after 3 μm in the graph is that the measured reflectivity of the CPC surface by the Fourier Transform Infrared Spectrometer surpassed that of the reference material. 115

Figure 4-20: (a) Schematic of the RC experimental system. (b) In-situ experimental setup of the RC system. The experimental system is located in the open field at the University of Nottingham (52.94°N, 1.09°W), UK with the site altitude being 60 m. 116

Figure 4-21: Experimental setup schematic of the CPC-RC and flat-RC modules with and without PE film. 117

Figure 4-22: Experimental setup schematic of three different RC modules. 117

Figure 4-23: Experimental setup schematic of three different RC groups under different placements. 118

Figure 4-24: (a) Weather data in Nottingham, UK on 16th of May 2023. (b) Measured emitter temperatures of the CPC-RC and flat-RC modules with or without PE film. (c) Average temperature differences (ΔT) between the ambient air and emitters. 120

Figure 4-25: (a) Measured emitter temperatures of the CPC-RC, trapezoidal-RC and flat-RC modules. (b) Average temperature difference (ΔT) between the ambient air and emitters. 121

Figure 4-26: (a) Weather data in Nottingham, UK on 2nd of May 2023. (b) Measured emitter temperatures of the three placements. (c) Average temperature differences (ΔT) between the ambient air and emitters. 123

Figure 4-27: (a) Weather data in Nottingham, UK on 24th of May 2023, and solar irradiance received by pyranometers in different orientations. (b) The temperature of the 3 groups of modules during the day. (c) Average temperature differences ((ΔT) between the ambient air and emitters 125

Figure 5-1: Schematic diagram of DCPC-RC multi-module system. 128

Figure 5-2: Radiative heat exchange between (a) mirror CPC-RC and (b) DCPC-RC system and external environment. 129

Figure 5-3: Definition of solar profile angle (ϕ). 130

Figure 5-4: In-situ experimental setup of the RC systems. 131

Figure 5-5:(a) Measured emitter temperatures of three RC modules alongside ambient temperature and solar irradiance. (b) Weather data in Nottingham, UK on 25th June 2024. (c) Temperature differences (ΔT) between the ambient air and RC emitters. 132

Figure 5-6: (a) Measured emitter temperatures of three RC modules alongside ambient temperature and solar irradiance. (b) Weather data in Nottingham, UK on 26th June 2024. (c) Temperature differences (ΔT) between the ambient air and RC emitters. 134

Figure 5-7: Solar shielding ratio of different CPC-RC modules under different solar profile angles (ϕ). 136

Figure 5-8: Traced incoming solar radiation on DCPC-RC multi-module system under different solar profile angles (ϕ). 136

Figure 5-9: Absorbed solar radiation and net cooling power density for three RC modules under different solar profile angles. 137

Figure 5-10: Weighted average transmittance of DCPC acrylic wing framework with and without TIRF. 138

Figure 5-11: Solar shielding ratio for the DCPC-RC modules with and without TIRFs under different solar profile angles. 139

Figure 5-12: Schematic diagram of thermal radiation from the solar collector and thermal radiation that cannot escape from the DCPC-RC multi-module system. 140

Figure 5-13: Absorbed solar radiation and radiative cooling power density for DCPC-RC modules with and without TIRF. 141

Figure 5-14: Hours percentage of different solar profile angle intervals in different cities. 142

Figure 5-15: Cooling performance for the DCPC-RC module under different ambient temperatures and solar profile angles (ϕ). .....错误!未定义书签。

Figure 5-16: Solar shielding ratio for the DCPC-RC modules tilted at different angles to the anti-sunward side under different solar profile angles. 144

Figure 5-17: Cooling performance for DCPC-RC modules tilted at different angles to the anti-sunward side in different cities and the corresponding hours percentage ratio throughout the year. 145

Figure 6-1: The schematic diagram of the TIRF-TCPC-PVTRC system. 148

Figure 6-2: Simulated and experimental temperatures of the TIRF-TCPC-PVTRC module. 149

Figure 6-3: Solar receiving ratio and absorbed solar radiation for the PVT collector and flat RC emitter of the TIRF-TCPC-PVTRC module. 151

Figure 6-4: Net cooling power density for (a) TIRF-TCPC-PVTRC module and (b) flat-RC module under different ambient temperatures and solar incident angles. 152

Figure 6-5: Different TIRF-TCPC structures in TIRF-TCPC-PVTRC modules. (a) Standard structure. (b) Lens-walled structure. (c) Solid structure. (d) Cross-sections of three TIRF-TCPC structures. ... 154

Figure 6-6: Solar receiving ratio for PVT module under (a) standard TIRF-TCPC. (b) Lens-walled TIRF-TCPC. (c)Solid TIRF-TCPC structures. 155

Figure 6-7: (a) 5° lens-walled TIRF-TCPC-PVTRC and (b) Solid TIRF-TCPC-PVTRC modules with different RC emitters..... 156

Figure 6-8: Solar receiving ratio for the PVT module in different TIIRF-TCPC-PVTRC module with different RC emitters..... 157

Figure 6-9: Spectral properties of the TIRF. (a) Transmittance in solar spectrum. (b) Reflectivity under mid- and far-infrared spectrum. 158

Figure 6-10: (a) Photograph of in-site experimental devices. (b) Cross-section view of the two PVTRC systems. 159

Figure 6-11: Schematic diagram of solar cells in (a) PVTRC system and (b) optimized TIRF-TCPC-RC system. (c) Photo of PV Analyzer field test. 161

Figure 6-12: Meteorological data during the experiment 162

Figure 6-13:Ambient temperature and the temperature of different modules in the (a) PVTRC system and (b) optimized system. 163

LIST OF TABLES

Table 2-1: Correlations of the total heat transfer coefficient. 16

Table 3-1: Key parameter settings for case study. 75

Table 3-2: Total, hemispherical emissivity of the external environment for four RC modules. 77

Table 3-3: Key parameters of the 2D inverted trapezoidal-RC modules with five different emitters. . 80

Table 3-4: Total, hemispherical emissivity of the external environment for the flat-RC module under different sky dome coverage ratios (ξ) 83

Table 4-1: Key parameter settings for case study. 99

Table 4-2: Effective direct sunlight reflectivity for the RC modules. (CPC in the table refers to CPC-RC module, and trapezoidal refers to inverted trapezoidal-RC module) 102

Table 4-3: Equivalent external environmental emissivity for the CPC-RC modules tilted at different angles to the anti-sunward side. 106

Table 4-4: Effective direct sunlight reflectivity for the CPC-RC modules tilted to the anti-sunward side (module tilted 0° represents the module is placed horizontally). 106

Table 4-5: List of testing and monitoring devices in the experimental system. 116

Table 5-1: List of testing and monitoring devices in the experimental system. 131

Table 5-2: Key parameters setting for case studies 135

Table 5-3: Equivalent sky emissivity for three DCPC-RC modules. 139

Table 5-4: Equivalent sky emissivity for DCPC-RC modules tilted at three different angles. 144

Table 6-1: Key parameters setting for case studies. 150

Table 6-2: List of testing and monitoring devices in the experimental system. 159

Table 6-3:Maximum power output of the two systems on 7th August,2024 (1 is PVTRC system and 2 is optimized system) 160

Table 6-4: Solar energy conversion efficiency of the two systems on 7th August,2024 (1 is PVTRC system and 2 is optimized system)..... 161

Table 6-5: Average daytime and nighttime temperatures of various components of the two systems. 164

1. Introduction

1.1 Background

Global warming, caused by the anthropogenic greenhouse effect is a critical issue for society is well known. Since 1990, global temperature rise has nearly tripled, contributing to more heat waves and extreme weather events [1]. Over the past 20 years, hot weather has become more frequent, exposing a significant portion of the global population to a heightened risk of heat stress, negatively impacting thermal comfort and human health [2]. Moreover, as people spend most of their time indoors, high ambient temperatures increase the risk of overheating for building occupants. Consequently, the demand for cooling has risen in modern society, making cooling systems one of the most energy-intensive components of contemporary infrastructure [3]. Approximately buildings account for 40% of primary energy consumption in Europe, with around 80% of that energy derived from fossil fuels to operate heating, ventilation, and air conditioning (HVAC) systems [4,5]. Without improvements to building envelopes and systems, global electricity demand for building cooling could increase by 45% by 2050 compared to 2016 levels [6].

Furthermore, energy consumption is the primary source of global greenhouse gas (GHG) emissions, accounting for more than three-quarters of total emissions. In 2022, global CO_2 emissions from fuel combustion rose by 1.3% compared to pre-COVID-19 levels. This increase is largely due to the continued reliance on non-renewable fuels for energy supply, with coal accounting for 45%, oil for 33%, and natural gas for 22% [7]. This dependence on fossil fuels presents a significant challenge to achieving the goal of reducing global energy-related CO_2 emissions to net zero by 2050.

Figure 1-1 illustrates the final energy consumption and carbon emissions from building cooling in each region from 2000 to 2030 [8]. It can be observed that the Asia Pacific and North America regions consumed the most energy in 2022, with 3.2 and 2.3 EJ, respectively. In the same year, total CO_2 emissions reached 1.02 Gt, representing a 10.9% increase compared to 2020. This rise is attributed to high natural gas prices and extreme weather events, which forced many regions to rely on coal to ensure electricity supply, leading to higher emissions. However, under the Net Zero Emissions by 2050 Scenario (NZE), total CO_2 emissions could be reduced to 0.38 Gt by 2030 [9]. To achieve this target,

all available clean energy technologies, including renewable energy, electric vehicles, and energy-efficient building renovations, must be deployed on a large scale between now and 2030.

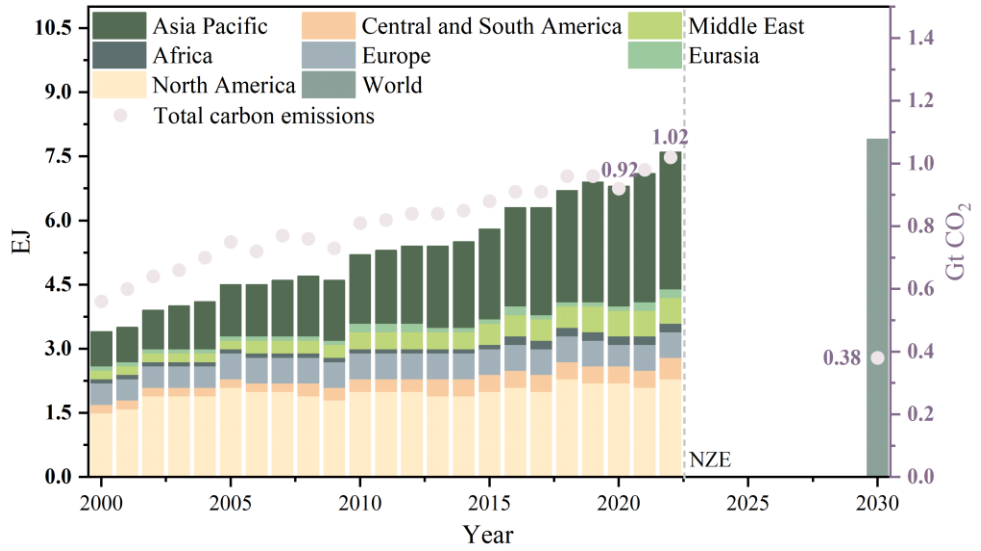

Figure 1-1: Final energy consumption and carbon emissions for building cooling by region in the Net Zero Scenario [9].

1.2 Statement of the problems

In this context, reducing energy consumption for cooling buildings is a crucial global strategic concern. To tackle this challenge, pursuing passive cooling technologies is an urgent and environmentally friendly solution. Among these, radiative sky cooling (RC) is a promising carbon-free strategy that can effectively mitigate the urban heat island effect and reduce energy consumption driven by increasing cooling demands [10]. However, the inherently low power density of RC technology, typically characterized by a cooling flux of approximately 100 W/m^2 [11] at ambient temperature, is easily offset by the intense power density of daytime solar radiation, approximately 1000 W/m^2 [12]. This disparity makes RC technology inadequate for meeting the all-day cooling needs of buildings, particularly during the daytime when cooling demands are highest [13]. Therefore, it is crucial to enhance the cooling power density and reduce the harassment of solar radiation on the RC system.

The mainstream focus of current research is to improve the cooling performance of RC systems by developing RC emitter materials with near-ideal spectral selectivity. These materials are characterized by extremely low absorptivity in the solar spectrum and high emissivity close to 1 within the 'atmospheric window' [15,16]. As research progresses, many near-ideal spectrally selective materials have been developed, verifying the feasibility of achieving RC throughout the day [16–18]. However,

producing these materials with superior properties necessitates complex and rigorous processing methods [19–21], making them costly and hindering their large-scale application in actual building scenarios. Fortunately, beyond utilizing spectrally selective materials to obtain high cooling power density, RC modules can also improve cooling power by integrating with a concentrator (referred to as a concentrated RC module) to improve cooling performance. Furthermore, integrating RC systems into buildings presents another challenge: deploying RC modules alone may limit the applicability and flexibility of the energy provided, making it difficult to meet varying needs across different times and seasons. To address the issue of poor seasonal adaptability in RC technology, combining RC systems with solar energy utilization systems is considered an effective solution for meeting the dynamic energy demands of buildings throughout the year [14].

1.3 Novelty of thesis

1. **Design a novel dissimilar concentrated RC module:** A novel RC system integrated with a dissimilar material-based compound parabolic concentrator (DCPC) is developed. The CPC functions as a thermal radiation shield during the daytime and as a concentrator of thermal radiation during the nighttime. The feasibility of enhancing RC performance is validated through experiments, and the impacts of environmental parameters and different configurations on the module's performance are examined using the proposed modelling approach.

2. **Propose an innovative system integrated PVT with RC modules:** A hybrid system integrating CPC-RC modules with PVT modules is developed and tested. The system features an innovative transparent CPC structure, covered with a transparent infrared reflective film (TIRF), with RC and PVT modules alternately installed at the bottom of the CPC and in the gap between two CPCs. This configuration allows for the simultaneous collection of solar and cold energy, as shown in Figure 1-2. After optimizing the component configurations, tests demonstrate that the system efficiently harnesses renewable energy from both the sun and outer space. This system addresses the inefficiencies and intermittent operation of standalone RC and PVT modules, providing a more effective solution to meet building energy demands across different seasons.

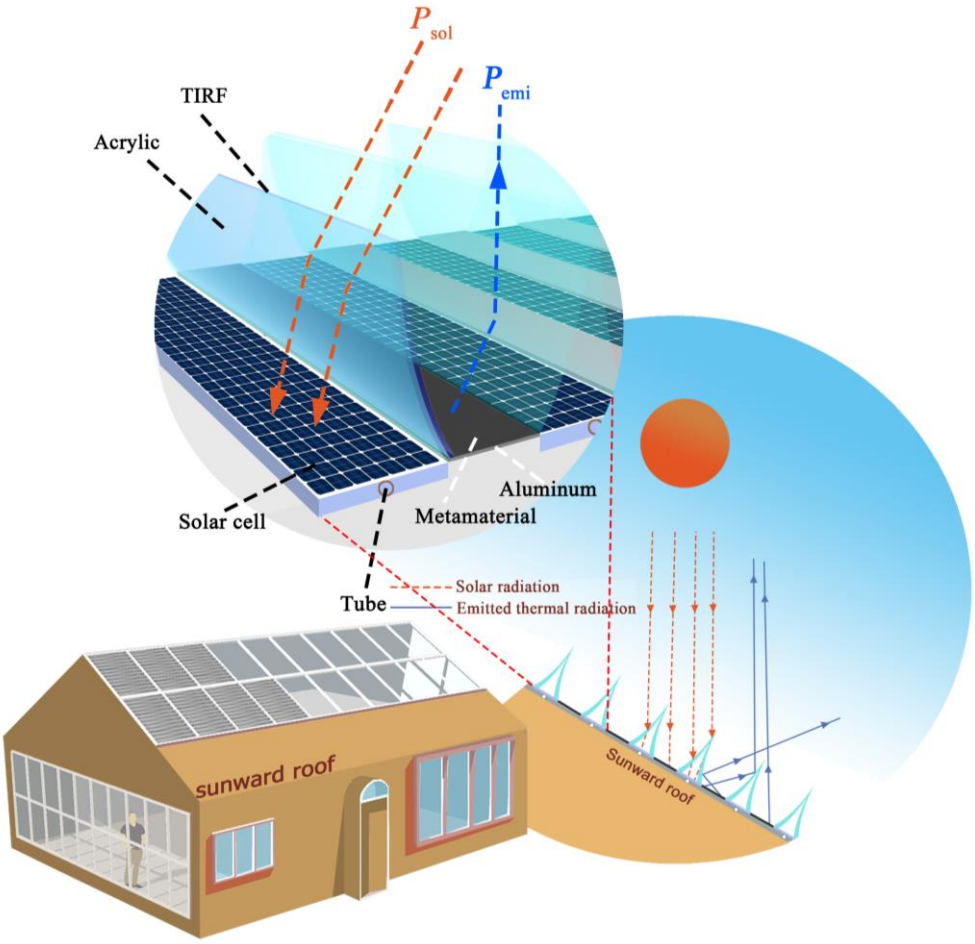

Figure 1-2: The schematic diagram of the proposed TIRF-TCPC-PVTRC system.

3. **Propose a novel modelling approach:** A novel modelling approach is proposed to accurately characterize the cooling power of the RC module and evaluate the heat exchange between the RC emitter and the surrounding environment. This approach is particularly suited for analysing cooling performance in complex configurations, such as concentrated RC systems.

1.4 Aim and objectives

This study aims to develop a hybrid system that integrates RC technology with PVT modules to achieve simultaneous heating and cooling, addressing the limitations of single-function energy harvesting modules and enhancing seasonal adaptability. The system uses PVT modules to provide electricity and hot water to the building during the daytime, while RC emitters provide building cooling. At night, the cold energy generated by the PVT and RC modules can be used to cool the building. The system utilizes collected sustainable energy to meet the building's energy demands, achieving a self-sufficient model. This offers a new solution for advancing the development of net-zero carbon buildings.

The specific objectives of this thesis include:

1. **Propose a novel modelling approach:** Based on the existing relevant literature, an approach using optical modelling software and mathematical model will be proposed to accurately characterize the cooling performance of RC modules under complex configurations.
2. **In-depth study of compound parabolic concentrator-based RC modules:** The cooling performance of the CPC-RC module will be evaluated and tested through the proposed modelling approach and field experiments. The CPC's potential as an unwanted thermal radiation shield during the day and as a thermal radiation concentrator at night will be explored, demonstrating its effectiveness in enhancing cooling capacity.
3. **Further improve the proposed CPC-RC module:** A new CPC configuration will be proposed and optimized to allow solar radiation to pass through while reflecting infrared thermal radiation, forming the basis for a hybrid system that enhances RC performance and simultaneously collects solar energy. Additionally, the feasibility of the new module in maintaining sub-ambient temperatures throughout the day will be tested by the experiments.
4. **Design, build and test an innovative system integrating PVT and RC module:** A hybrid system that integrating PVT and RC modules will be designed and developed. Its structural configuration will be optimized through software simulation to obtain excellent performance. Subsequently, the solar energy conversion efficiency and component temperature of the optimized system need to be tested by experiments to verify whether it can collect solar energy and cooling energy at the same time.

The core objective of this thesis is to enhance the cooling performance of RC modules and achieve all-day cooling effect. Additionally, this thesis aims to address the challenge of integrating standalone RC or PVT modules, such as limited seasonal adaptability and single functionality. To overcome these issues, we propose a novel energy system with an innovative configuration that provides a solution capable of meeting the dynamic energy demands of buildings, thereby contributing to the achievement of net-zero carbon buildings.

1.5 Thesis structure

This thesis is divided into seven chapters. Chapter 1 provides the introduction, and Chapter 7 is conclusion. Other five chapters form the main body of the thesis. The flowchart of the thesis is shown in Figure 1-3. An overview of each chapter is as follows:

- **Chapter 1**: This chapter introduces the research background and identifies existing research gaps, leading to the research objectives and the novelty.
- **Chapter 2**: This chapter provides a review of the development of radiative cooling (RC) technology and compound parabolic concentrators (CPCs), with a detailed discussion of the application of RC technology in buildings and the RC systems integrated with concentrators.
- **Chapter 3**: This chapter proposes an accurate modelling approach, based on optical modelling software and theoretical analysis. This approach is utilized to evaluate the nighttime cooling power density of RC modules with different RC structures and with different configurations. Additionally, the solar radiation absorbed by the RC modules during the daytime is analyzed through software simulation.
- **Chapter 4**: This chapter introduces a concentrated RC module based on a mirror CPC (named as a CPC-RC module) and compares the cooling performance of various RC modules using the modelling approach from Chapter 3. Additionally, experimental measurements of the temperature reduction in different RC modules are conducted.
- **Chapter 5**: This chapter optimizes the CPC-RC module by replacing the mirror CPC with a dissimilar material CPC structure, forming a novel DCPC-RC module. The improvement in cooling capacity is validated through modelling and experimental methods.
- **Chapter 6**: Inspired by the DCPC-RC module, this chapter proposes a transparent CPC-RC module covered with a transparent infrared reflective film, integrating it with a PVT module into a hybrid system (TIRF-TCPC-PVTRC system) to enable the simultaneous collection of thermal and cold energy. The cooling performance of the RC module in the system is preliminarily

evaluated using the modelling approach, while the performance of the PVT and RC modules is tested experimentally.

- **Chapter 7**: This chapter summarizes the research results of the thesis, highlights existing limitations, and offers suggestions and directions for future research.

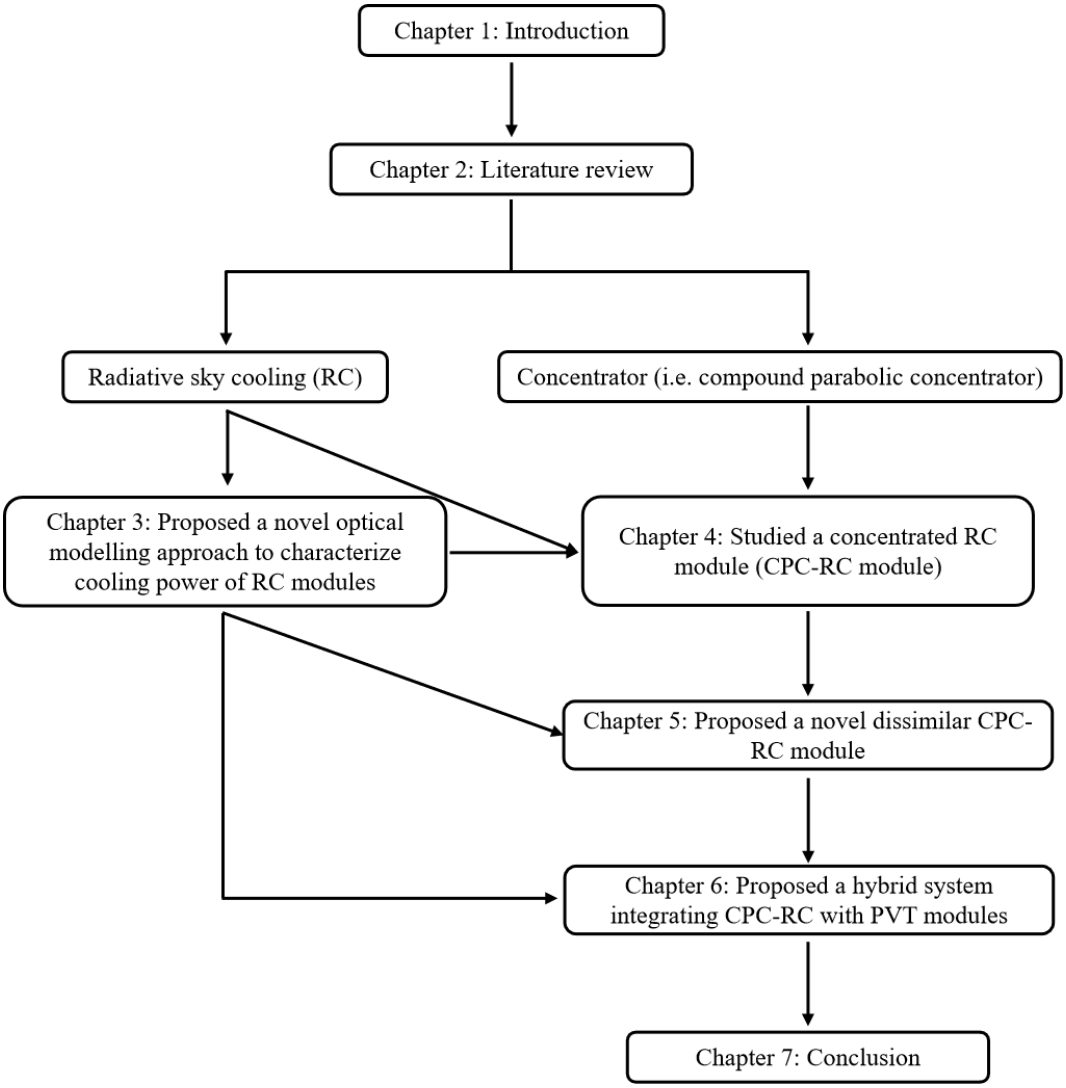

Figure 1-3: Flow chart of this thesis structure.

2. Literature review

2.1 Introduction

In modern society, as living standards improve, the pursuit of higher thermal comfort levels has become more prominent. This has led to a significant increase in the building sector's heating and cooling demand, resulting in substantial energy consumption [15,16]. However, 81% of the world's primary energy supply still comes from non-renewable and environmentally harmful sources, such as fossil fuels [17]. Concerns about energy shortages and environmental degradation have steadily increased. As a result, promoting renewable and sustainable energy technologies is becoming increasingly necessary. The sun (~5800K) and the deep universe (~3K) serve as natural sources of heat and cold, continuously providing energy for life on Earth, making the planet's temperature suitable for biological survival [18]. Further developing technologies to harness solar energy and cold energy from the deep universe could provide buildings with the necessary energy to meet seasonal demands. First, solar energy utilization technologies, such as photovoltaic (PV), photothermal (PT), and their combined form, solar photovoltaic/thermal (PVT) technologies, are relatively mature, converting solar radiation into electrical and thermal energy, respectively [19]. Additionally, although utilising the universe's coldness, i.e., radiative cooling technology, has a long history, it has only recently gained more new development [12].

In solar energy utilization technologies, concentrators are considered essential for enhancing the conversion efficiency of solar energy systems [20]. Among these, compound parabolic concentrators (CPCs) are extensively employed in building-integrated systems, as they eliminate the need for additional solar tracking mechanisms [21]. However, these systems can present challenges, such as uneven light distribution and excessive temperatures on photovoltaic cells, which can reduce the performance of concentrated photovoltaic (CPV) systems. To mitigate this issue, concentrated PVT technology, which integrates CPV systems with concentrated thermal (CPT) systems, has been developed to partially dissipate and utilize waste heat using a cooling fluid. In addition, various innovative cooling technologies, such as radiative cooling, have been introduced to improve both the

efficiency and lifespan of photovoltaic modules. Researchers have demonstrated that incorporating radiative cooling mechanisms into solar devices provides additional advantages, including multifunctionality, enhanced efficiency, continuous operation, and adaptability across seasons.

Radiative sky cooling (RC) is ubiquitous in daily life and has obtained widespread attention as a promising passive building cooling strategy [22,23]. In the building sector, it can be used to cool the air [24] and envelopes [25] or provide cooling for air conditioning or refrigeration systems [26,27]. Unlike conventional vapor compression cooling, which provides localized cooling at the cost of releasing more heat into the environment through a fossil energy-driven thermodynamic cycle, RC technology emits heat to the cold outer space via the "atmospheric window" (8–13 μm) in an energy- and carbon-free manner, enabling significant energy savings and environmental benefits [12]. However, the cooling efficiency of RC systems is often affected by the spectral properties of the RC emitter surface [28–30] as well as various external factors, including solar intensity [31], relative humidity [32], sky view factor [33], etc. In recent years, extensive research on RC technology has led to the development and validation of numerous methods to enhance RC cooling power, making it an increasingly attractive option for building cooling.

Among various RC systems, the concentrated RC system has attracted considerable attention [34]. Inspired by concentrated solar energy utilization system, this system integrates a concentrator with an RC emitter, using the concentrator to direct emitted thermal radiation toward the most transparent zenith direction while blocking thermal radiation from wider zenith angles. This approach enhances the cooling performance of the module.

This chapter provides a comprehensive review of the RC technology, along with the development of CPCs in solar energy utilization, offering new insights into their integration. Given the current focus on reducing energy consumption and carbon emissions in the building sector, the review primarily analysed the application of RC technology in building. Section 2.2 reviews the principles and application of RC technology. Specifically, Section 2.2.1 outlines the fundamentals of RC technology, while Section 2.2.2 introduces the application of RC systems in the building sector. Finally, Section 2.2.3 specifically addresses the novel concentrated RC system, including its design principles and

advantages. Section 2.3 provides a review of CPCs, discussing various structural designs and summarizing their applications in solar energy utilization and building daylighting control. Finally, Section 2.4 examines the challenges and prospects of integrating concentrated RC systems with solar energy collection systems.

2.2 Radiative sky cooling (RC) technology

2.2.1 Fundamentals of RC technology

Solar radiation and infrared radiation emitted by the Earth's surface together constitute environmental radiation [35]. This environmental radiation interacts with the Earth's atmosphere to maintain the planet's energy balance and regulate surface temperature. Incoming short-wavelength solar radiation (0.3–2.5 μm) can be reflected, absorbed, or scattered by atmospheric air molecules and clouds [12]. Similarly, terrestrial radiation, which is emitted from the Earth's surface and primarily falls within the 2.5–50 μm wavelength range, undergoes absorption and scattering as it passes through the atmosphere. When water vapor content is low and the air is relatively dry, the absorptivity of atmospheric radiation in the 8-13 μm wavelength range is very low, with spectral transmittance approaching 1, as shown in Figure 2-1 [36].

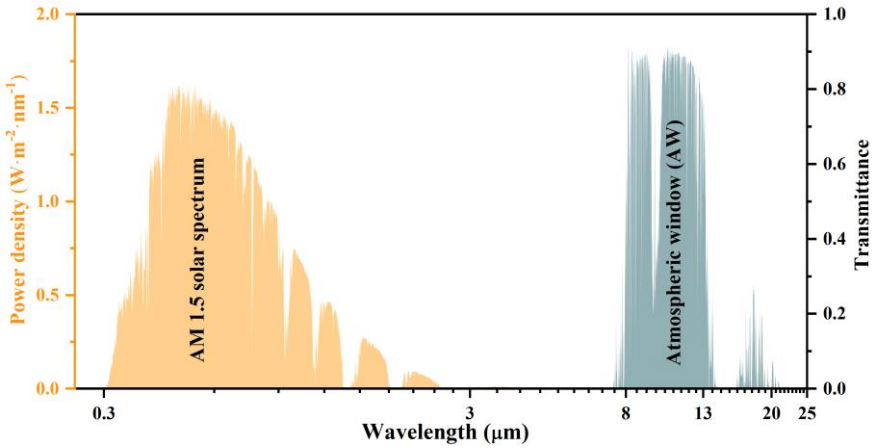

Figure 2-1: The normalized AM 1.5 solar spectrum and atmospheric transmission in the zenith direction on a clear day [36].

Figure 2-2 simplifies and depicts the heat exchange of a flat RC emitter. When the RC emitter is directly exposed to the atmosphere, and the effects of surrounding buildings, trees, and the ground are neglected, the RC effect is influenced by solar radiation, terrestrial thermal radiation, and non-radiative heat transfer. Cooling effect occurs when the thermal radiation emitted by the emitter (P_{emi}) exceeds the sum of the absorbed solar energy (P_{sol}), sky thermal radiation (P_{sky}), and incoming non-radiative

heat ($P_{non\text{-}rad}$, via heat conduction and convection). Consequently, by decreasing P_{sol}, P_{sky} and $P_{non\text{-}rad}$ while increasing P_{emi}, the cooling power of the RC system can be improved. Based on the principle of energy conservation, the daytime and nighttime cooling power of an RC emitter can be calculated by considering the balance of multiple heat inputs and outputs, which can be expressed as [37]:

$$P_{cool_day} = P_{emi} - P_{sol} - P_{sky} - P_{non\text{-}rad} \tag{2.1}$$

$$P_{cool_night} = P_{emi} - P_{sky} - P_{non\text{-}rad} \tag{2.2}$$

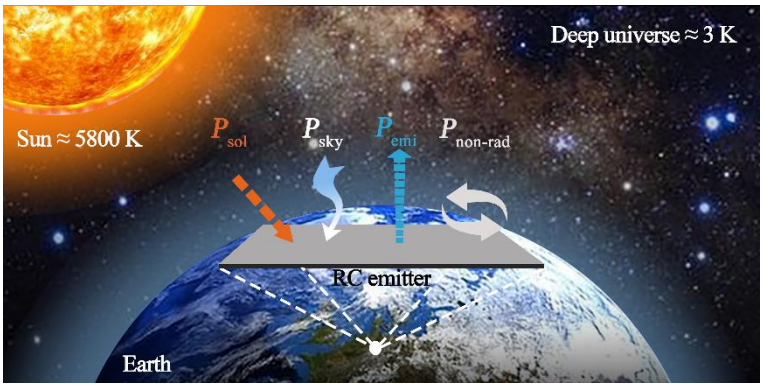

Figure 2-2: Schematic of the heat balance of an RC emitter.

The first three parameters will be discussed in detail in Subsection 2.2.1.1 to Subsection 2.2.1.3, while the impact of non-radiative heat transfer on RC performance will be examined in Section 2.2.1.4.

2.2.1.1 Radiation power emitted by the RC emitter

The thermal radiation power of an RC emitter is determined solely by its spectral characteristics and is not influenced by external environmental factors. The total radiation power per unit area of the emitter (P_{emi}) represents the rate at which radiation is emitted across all wavelengths and in all directions, as described by the following equation [35]:

$$P_{emi}(T_{emi}) = \int \cos\theta d\Omega \int_0^\infty I_{bb}(\lambda, T_{emi}) \varepsilon_{emi}(\Omega, \lambda) d\lambda \tag{2.3}$$

where T_{emi} is the absolute temperature of the emitter; $\varepsilon_{emi}(\Omega, \lambda)$ is the emissivity of the emitter as a function of wavelength and direction. Since the emissivity of an emitter remains nearly constant at the temperature of interest, it is typically assumed to be independent of temperature [12]; Ω represents the solid angle between the radiation direction and the normal to the emitter, which can be expressed in terms of the zenith angle θ and the azimuth angle φ. Thus, Eq.2.3 can be rewritten as follows:

$$P_{\text{emi}}(T_{\text{emi}}) = \int_0^{\infty}\int_0^{2\pi}\int_0^{\pi/2} \varepsilon_{\text{emi}}(\theta,\varphi,\lambda) I_{bb}(\lambda, T_{\text{emi}}) \cos\theta \sin\theta d\theta d\varphi d\lambda \tag{2.4}$$

where $\varepsilon_{\text{emi}}(\theta, \varphi, \lambda)$ refers to the spectral, directional emissivity of the emitter; and $I_{bb}(\lambda, T_{\text{emi}})$ is the blackbody spectral intensity at the emitter temperature T_{emi}, which can be further expressed as

$$I_{bb}(\lambda, T_{\text{emi}}) = \frac{2hc^2}{\lambda^5[\exp(hc / \lambda k T_{\text{emi}}) - 1]} \tag{2.5}$$

According to Planck's law, where h is $6.626 \cdot 10^{-34}$ J·s and k=$1.381 \cdot 10^{-23}$ J/K are the universal Planck and Boltzmann constants, respectively; c is $2.998 \cdot 10^{8}$ m/s is the speed of light in vacuum; λ is the wavelength.

The emissivity of different materials can vary depending on the wavelength (λ) and direction (θ, φ), as shown in Eq 2.4 or it may differ when averaged over a specific wavelength band and direction. In RC applications, the integrated weighted average emissivity of the 8-13 μm range in the zenith direction is particularly important due to the significance of the "atmospheric window".

For simplicity in studies, the $\varepsilon_{\text{emi}}(\theta, \varphi, \lambda)$ for the RC emitter can be approximately characterized by the total hemispherical emissivity (ε_{emi}), which represents the total radiation energy emitted across all wavelengths and in all directions from the emitter.

$$\varepsilon_{\text{emi}} = \frac{\int_0^{\infty} \varepsilon_{\lambda}(\lambda) E_{\lambda,\text{b}}(\lambda, T) d\lambda}{E_{\text{b}}(T)} \tag{2.6}$$

If the total, hemispherical emissivity of the emitter is known, according to the Stefan-Boltzmann law, the P_{emi} can be described as [38]:

$$P_{\text{emi}} = \varepsilon_{\text{emi}} \sigma T_{\text{emi}}^4 \tag{2.7}$$

where σ is the Stefan-Boltzmann constant, $5.67 \cdot 10^{-8}$ W/m^2·K^4.

2.2.1.2 Solar radiation absorbed by the RC emitter

Approximately 1354 W/m^2 of solar radiation reaches the top of the Earth's atmosphere [39]. After passing through the Earth's atmosphere, some of solar radiation is absorbed or reflected by atmospheric components, aerosols, and clouds, leaving around 1000 W/m^2 of solar irradiance to reach the Earth's

surface, which is an order of magnitude greater than the RC capacity [37]. Consequently, even if the solar absorptivity of the RC emitter is lower, it still significantly affects daytime RC performance. It is evident that solar radiation is predominantly shortwave (0.3- 2.5 μm), with a peak around 0.5 μm in the visible light range [40].

The absorbed solar power is given by

$$P_{sol} = \int \alpha_{emi}(\theta, \lambda) I_{sol}(\lambda) \cos\theta d\lambda \tag{2.8}$$

where $\alpha_{emi}(\theta, \lambda)$ is the absorptivity of the emitter as a function of direction and wavelength; I_{sol} is the direct spectral solar irradiance; θ is the angle between the incident direction of solar radiation and the normal direction of the RC emitter.

Early research on RC technology focused on its nighttime cooling performance, as achieving cooling under intense daytime sunlight presented significant challenges [41]. Fortunately, extensive studies on reducing solar radiation interference in RC systems, such as using materials with near-ideal spectral properties [31,42] or incorporating additional solar shielding devices [43,44], have made it possible to achieve daytime RC with sub-ambient temperatures.

2.2.1.3 Sky thermal radiation absorbed by the RC emitter

Sky radiation, also referred to as atmospheric radiation, has been extensively studied due to its significant role in various fields such as meteorology [45,46] and climate research [47].

In the field of RC technology, atmospheric radiation holds important research significance as it directly affects the cooling power of RC systems. Atmospheric radiation received at the Earth's surface is primarily concentrated in the 5 to 8 μm and above 13 μm wavelength ranges [38]. However, in the 8 to 13 μm range, atmospheric absorption is minimal, a region known as the "atmospheric window" (AW). Within this AW range, the atmosphere absorbs and scatters very little thermal radiation, allowing surface radiation to pass through into space, thereby enabling effective cooling [22]. Most of the terrestrial thermal radiation that can pass through the atmosphere falls within this range, which helps explain how the Earth maintains a stable surface temperature. The sky (atmospheric) thermal radiation absorbed by the RC emitter can be expressed as:

$$P_{\text{sky}}(T_{\text{amb}}) = \int \cos\theta d\Omega \int_0^{\infty} I_{bb}(\lambda, T_{\text{amb}}) \varepsilon_{\text{emi}}(\Omega, \lambda) \varepsilon_{\text{sky}}(\Omega, \lambda) d\lambda \tag{2.9}$$

According to the E.q 2.4, E.q 2.9 can be rewritten as:

$$P_{\text{sky}}(T_{\text{amb}}) = \int_0^{\infty} \int_0^{2\pi} \int_0^{\pi/2} \varepsilon_{\text{emi}}(\theta, \varphi, \lambda) I_{bb}(\lambda, T_{\text{amb}}) \varepsilon_{\text{sky}}(\theta, \varphi, \lambda) \cos\theta \sin\theta d\theta d\varphi d\lambda \tag{2.10}$$

where $I_{bb}(\lambda, T_{\text{amb}})$ is the is the blackbody spectral radiance for a temperature T_{amb}, $\text{W}\cdot\text{m}^{-2}\cdot\mu\text{m}^{-1}\cdot\text{sr}^{-1}$; T_{amb} is the absolute air temperature near the ground; $\varepsilon_{\text{sky}}(\theta,\varphi,\lambda)$ is the emissivity of sky as a function of direction and wavelength, which is the ratio of the actual atmospheric radiation to the corresponding blackbody radiance at a certain angle and wavelength.

Considering that the sky emissivity is azimuth-independent, and most of RC emitters can be approximated as diffuse surfaces with the intensity of the emitted radiation being independent of direction. Additionally, according to Kirchhoff's law, the emissivity at a given wavelength and direction is equal to the absorptivity at the same wavelength and direction under thermal equilibrium. Eq. 2.10 can be simplified as:

$$P_{\text{sky}} = 2\pi \int_0^{\infty} \int_0^{\pi/2} \alpha_{\text{emi}}(\lambda) I_{bb}(\lambda, T_{\text{amb}}) \varepsilon_{\text{sky}}(\theta, \lambda) \cos\theta \sin\theta d\theta d\lambda \tag{2.11}$$

The equation shows that sky emissivity depends on both the spectrum and zenith angle. Additionally, factors such as air humidity [32], cloud cover [48], and latitude [49] also influence sky emissivity. In this section, we focus on the relationship between sky emissivity and zenith angle.

Under clear-sky conditions, the spectral, directional sky transmittance $\tau_{\text{sky}}(\lambda, \theta)$ can be approximately considered equal to $[1-\varepsilon_{\text{sky}}(\theta, \lambda)]$, in which $\varepsilon_{\text{sky}}(\theta, \lambda)$ represents the spectral, directional sky emissivity. The spectral emissivity of the atmosphere at 0° zenith angle can be obtained from C. G. Granqvist and A. Hjortsberg [50], while that of other zenith angles is calculated using the following "box model" equation [50]:

$$\varepsilon_{\text{sky}}(\theta, \lambda) = 1 - \left[1 - \varepsilon_{\text{sky}}(0, \lambda)\right]^{1/\cos\theta} \tag{2.12}$$

Figure 2-3 illustrates the atmospheric emissivity at three different zenith angles within the 5-25 μm range [50]. A larger zenith angle results in higher emissivity, indicating that the sky thermal radiation emitted from this angle is also greater. Therefore, minimizing the absorption of sky thermal radiation

by the emitter surface requires blocking the sky thermal radiation from large zenith angles as much as possible to reduce their impact on the emitter.

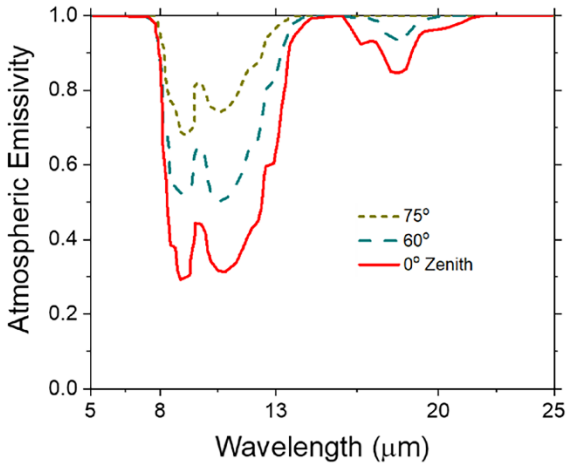

Figure 2-3: The sky emissivity for different zenith angles from 0° to 75° [50].

However, the spectral sky emissivity $\varepsilon_{sky}(\theta, \lambda)$ is highly complex and difficult to determine due to variations in atmospheric composition and regional environments. Fortunately, with advancements in the research of sky radiation, sky emissivity at a specific location can be directly measured using a spectroradiometer. In addition to direct measurements, it can also be calculated using sky transmittance obtained using specialized software. Common atmospheric transmission models and code databases such as LOWTRAN [51], MODTRAN [52] or HITRAN [53] can calculate sky transmittance using ground meteorological data, further can characterize the sky emissivity.

In practical applications, to more easily characterize the heat exchange between the RC emitter and the sky, an effective parameter known as effective sky emissivity (also referred to as total, hemispherical sky emissivity, ε_{sky}) is often used to represent the overall radiative effect of the entire atmosphere [54] This approach assumes a continuous spectrum and does not consider the actual spectral distribution of outgoing and incident radiation, using the sky temperature near the ground (referred to as equivalent sky temperature, T_{sky}) [12]. Since the 20th century, an increasing number of researchers have proposed empirical formulas relating sky emissivity to meteorological parameters, such as water vapor pressure [55,56], dewpoint temperature [57,58] and cloud correction factor [59]. However, when using these statistical correlations as substitutes for sky emissivity, it is essential to carefully consider their validity conditions, such as spectral wavelength ranges, regional differences and cloud cover.

Generally, in most cases, the effective sky emissivity is sufficient for calculating RC power. According to the Stefan-Boltzmann law, the P_{sky} can be simplified as [38]:

$$P_{sky} = \alpha_{emi}\sigma T_{sky}^4 \tag{2.13}$$

$$P_{sky} = \alpha_{emi}\varepsilon_{sky}\sigma T_{amb}^4 \tag{2.14}$$

where α_{emi} and ε_{sky} are respectively the total, hemispherical absorptivity of the RC emitter and total, hemispherical sky emissivity; and T_{sky} and T_{amb} are respectively the equivalent sky temperature and ambient temperature, K; Combining Eqs. 2.13 and 2.14, the ε_{sky}, also named as the equivalent sky emissivity, can be expressed as:

$$\varepsilon_{sky} = \frac{T_{sky}^4}{T_{amb}^4} \tag{2.15}$$

2.2.1.4 Non radiative heat transfer

In addition to being affected by environmental thermal radiation and solar radiation, the RC emitter is directly exposed to the atmosphere, where other non-radiative heat exchange between the emitter surface and the surrounding environment also occurs, impacting its cooling power. The non-radiative heat loss can be described by the following:

$$P_{non\text{-}rad} = hA(T_{amb} - T_{emi}) \tag{2.16}$$

where h is an overall heat transfer coefficient, represents the combined effects of convection and conduction between the environment and the emitter surface; A is the emitter surface area, m^2; T_{amb} and T_{emi} is the temperature of the ambient and emitter, K.

To accurately characterize $P_{non\text{-}rad}$, it is essential to precisely evaluate the total heat transfer coefficient (h). Numerous studies have developed various empirical formulas to describe this parameter, based on extensive experiments and simulations, as summarized in Table 2-1.

Table 2-1: Correlations of the total heat transfer coefficient.

Authors, year	Total heat transfer coefficient ($W/m^2 \cdot K$)	Wind speed range	With windshield or not
Clark and Berdahl [60], 1980	h=2.8+0.76v	1.5<v<5 m/s	No
	h=3.5	v<0.5 m/s	No
Nilsson and Niklasson [61],1995	h=2.8+3v	Not mention	No
Erell and Etzion [62], 2000	h=1.8+3.8v	1.35<v<4.5 m/s	No

Hanif et al. [63], 2014	h=3.1+4.1v	0.1<v<2 m/s	No
Raman et al. [31], 2014	h=6.9	Not mention	Yes
Liu et al. [64], 2017	h=3.5	0<v≤1.5 m/s	No
Zhao et al. [11],2019	h=8.3+2.5v	0<v<8 m/s	No
	h=2.5+2.0v	0<v<8 m/s	Yes

As shown in Table 2-1, the values of h used in different studies vary significantly. However, most empirical formulas indicate that h increases with rising ambient wind speed, leading to an increase in $P_{\text{non-rad}}$. Whether non-radiative heat transfer losses are beneficial or detrimental to RC performance depends on the difference between T_{amb} and T_{emi}. For example, for above-ambient applications, such as RC systems in cooling solar cells or power plant's condensers, non-radiative heat transfer aids in cooling process. Conversely, when aiming for achieve sub-ambient temperatures, minimizing non-radiative heat losses is crucial. Therefore, reducing the h value is essential. The primary method to suppress non-radiative heat transfer involves using infrared-transparent windshields or polyethylene (PE) films as convection shield above the RC surface.

2.2.2 Applications of RC technology in buildings

With the advancement of RC technology and materials science, many RC materials with near-ideal spectral properties have been developed [65–68], offering new ideas for high-performance cooling throughout the day. However, research on reliable systems that integrate RC technology with buildings to reduce cooling energy consumption remains limited. In this section, we will provide a comprehensive review of the applications of RC in the building sector, analysing its energy-saving potential in detail. The analysis will cover the cooling performance of RC systems during both day and night, as well as the use of RC technology alone or in combination with active cooling technologies.

2.2.2.1 Material in passive RC roofs

The roof of a building is directly exposed to solar radiation, which is the component most likely to absorb the unwanted heat [69]. It significantly influences the building's total cooling load, accounting for 5%–10% of its overall energy consumption [70]. However, due to its direct exposure to the atmosphere and large surface area, the roof is well-suited for integration with RC technology, which can effectively reduce heat gain and lower the building's cooling energy consumption.

For passive RC roofs, a common approach is to apply a selective coating or paint with low solar absorptivity and high atmospheric emissivity to the roof surface, helping to reduce indoor temperatures [31,71]. This type of roof is known as a "cool roof", one of the most popular passive cooling technologies in building applications [12]. Nahar et al. tested eight passive roof cooling technologies, such as roof insulation and roof with white-glazed tiles, for their effectiveness in reducing indoor temperatures [72]. They found that white-coloured roofs provided the best cooling performance and improved comfort in arid regions.

While existing commercial white paints, such as TiO_2 particle paint or double-layer paint can effectively reduce roof temperatures at night [73,74], they are insufficient for achieving passive sub-ambient cooling during the day due to their high absorptivity in the ultraviolet (UV) band [75]. To address this issue, Li et al. introduced a new white paint using $CaCO_3$, which achieved a high solar reflectance of 95.5% and was able to lower temperatures by 1.7 °C below ambient at noon [76]. A year later, they further developed ultra-white $BaSO_4$ paint and film with a solar reflectivity of 98.1% and high infrared emissivity of 95% [77]. The schematic of the $BaSO_4$ paint and film and SEM images are shown in Figure 2-4. Field test results demonstrated that, even under 907 W/m^2 of solar radiation, the $BaSO_4$ paints were able to maintain temperatures 4.5-10 °C below ambient, highlighting their ability to provide consistent cooling power regardless of solar intensity.

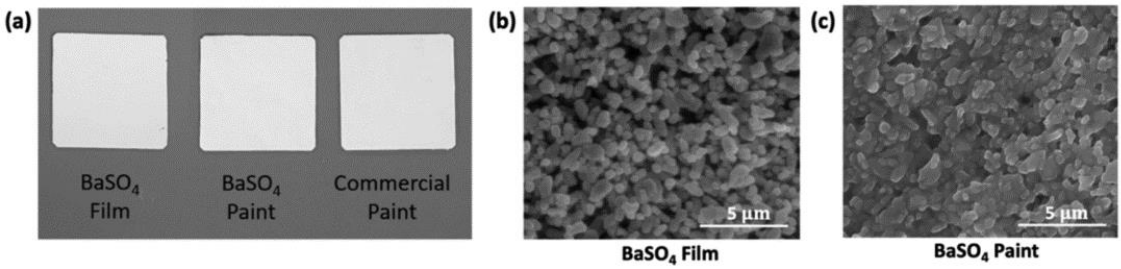

Figure 2-4: Radiative cooling coatings and SEM images [77].

Joseph et al. conducted field experiments in the tropical climate of Malaysia to test the indoor temperatures under four different roof types: a control corrugated zinc, a commercial white paint (Dulux Aura High Gloss), and two cooling paints, $BaSO_4$ and $CaCO_3$ [78]. The experimental setup is shown in Figure 2-5. The results demonstrated that both the $BaSO_4$ and $CaCO_3$ acrylic paints achieved significantly sub-ambient temperatures throughout the day, with $BaSO_4$ acrylic paint consistently

outperforming $CaCO_3$ acrylic paint. Additionally, during peak solar radiation, the maximum sub-ambient temperature reductions were 6.1 °C for the $BaSO_4$ acrylic paint and 6.0 °C for the $CaCO_3$ acrylic paint and the average daytime cooling powers were 47.5 and 48.8 W/m^2, respectively, indicating excellent cooling performance.

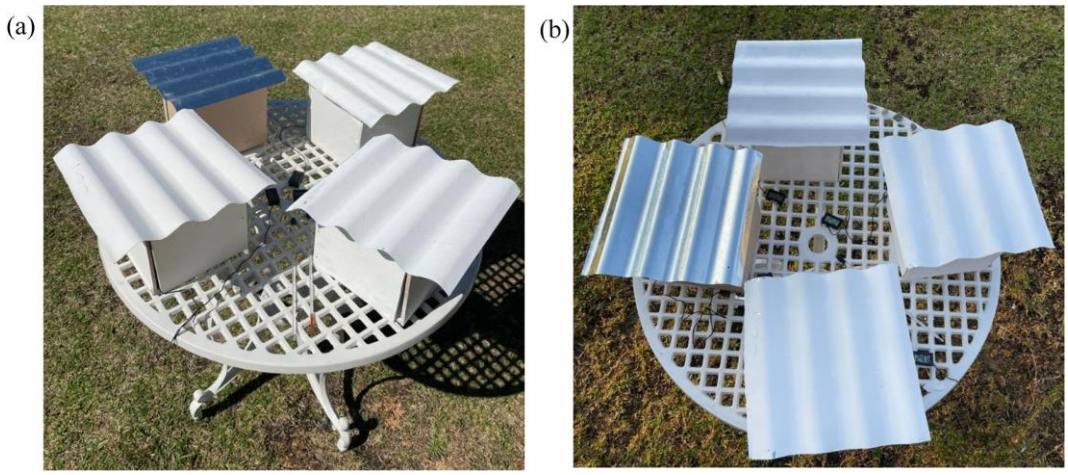

Figure 2-5: Field test setups from (a) an isometric view. (b) The top view [78].

In addition to $BaSO_4$ and $CaCO_3$ particles, Tang et al. developed a simple, scalable, and high-performance MgO coating and investigated its cooling potential in building applications [79]. The coating exhibited a high solar reflectivity of 0.95 and a broadband infrared emissivity of 0.93, which shown in Figure 2-6. When applied to the roof of a building, experiments showed that the wall's inner surface could be reduced by up to 9.2 °C below ambient even at noon, with a maximum cooling energy savings of approximately 10 kWh/(m^2 · yr).

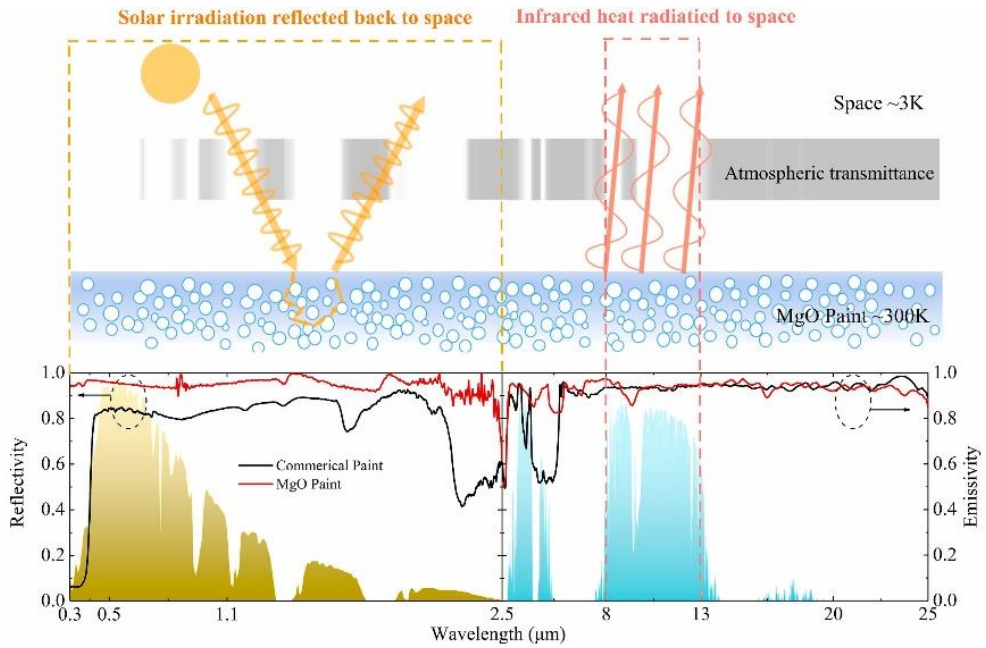

Figure 2-6: Schematic of passive daytime RC and the measured spectral properties of the MgO paints [79].

Furthermore, Felicelli et al. designed and fabricated a thin, lightweight nanoporous hexagonal boron nitride (hBN)-acrylic paint for daytime cooling [80]. Field tests demonstrated that this paint could achieve all-day cooling under direct sunlight, with daytime temperatures averaging 5-6 °C below ambient temperatures. Although the cost of this novel paint is higher than that of $BaSO_4$ particles, its lightweight nature makes it especially appealing for weight-sensitive applications, such as building roofs, aircraft, and wearable technology.

In addition, hollow spheres made of other relatively low refractive index materials are also commonly used in cool roof applications. However, their low refractive index can reduce scattering efficiency. To address this, Atiganyanun et al. proposed a new photonic random medium based on paint-format microspheres [81]. Experimental results demonstrated that, even during periods of strong solar radiation (11:00 to 16:00), this new coating reduced substrate temperatures by 4.7 °C compared to commercial white paint. Additionally, Syurik et al. developed a bio-inspired film by optimizing the morphology of low-refractive-index media, drawing inspiration from the scales of Cyphochilus beetles [82]. This film can transition between white and transparent when exposed to conventional liquids, offering high reflectivity at short wavelengths. It has potential applications on building roofs to meet varying energy demands across different seasons. Similarly inspired by the white Cyphochilus beetles, Zou et al. developed biomimetic bright-white polystyrene using a one-step spin-coating-assisted vapor-induced phase separation (VIPS) method [83].

In addition to conventional RC paint materials, several advanced polymer-based RC materials have been developed to facilitate large-scale RC applications were developed [84,85]. Gentle and Smith proposed a novel super-cool roof with the polymer multilayer on silver [86]. Field experiments compared the outdoor temperature of roofs using this material and using corrugated metal. The results showed that, even without convective shielding and under high-intensity solar radiation, the temperature of the silver-based material also could 11 °C lower than that of high-quality commercial corrugated metal roofs. Additionally, Mandal et al. developed a porous poly (vinylidene fluoride-co-) [P(VdF-HFP)HP] material with effective RC performance [87]. This material exhibits a solar reflectivity greater

than 0.96 and an infrared emissivity of 0.97, and it can be easily applied to building roof by spraying. Its impressive spectral properties are illustrated in Figure 2-7. Experimental results show that, with solar radiation of 750 W/m^2, the P(VdF-HFP)$_{HP}$ coating, without any convection shielding, can achieve a cooling power of 96 W/m^2, demonstrating its potential to reduce air conditioning costs in buildings.

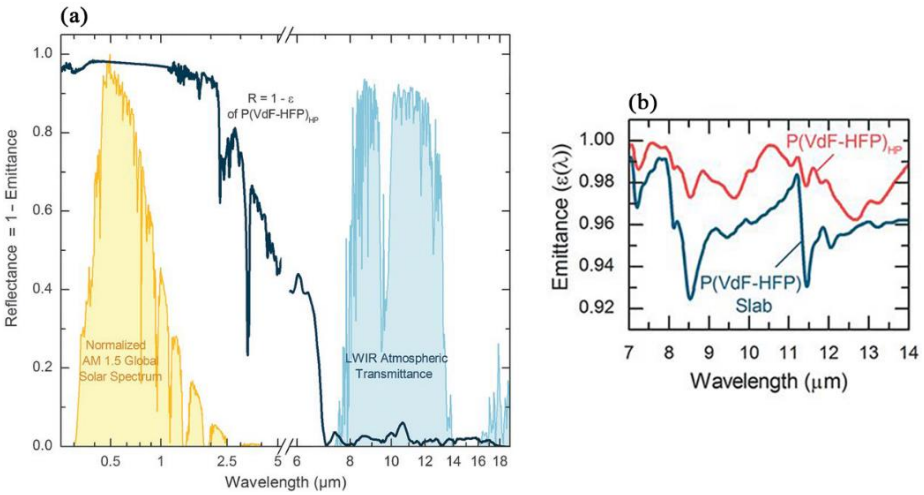

Figure 2-7: A novel radiative cooling material. (a) Spectral reflectivity [$R(\lambda)=1-\varepsilon(\lambda)$] and (b) Infrared emissivity of a 300-μm-thick P(VdF-HFP)HP coating [87].

Zhai et al. manufactured a randomized glass-polymer hybrid metamaterial, called RadiCold, by randomly embedding resonant polar dielectric microspheres into a polymer matrix [42]. The RadiCold film shows a high solar reflectivity of over 96% and an emissivity of more than 0.93 in the atmospheric window. Field experiments demonstrated that it could achieve a cooling power of 93 W/m^2 at noon.

However, most polymer-based RC materials rely on phase-inversion chemistry methods for large-scale development, while this approach significantly improves the manufacturability of new materials, it often results in high volatile organic compounds (VOCs) emissions, contributing to environmental pollution. To address this issue, researchers have developed aqueous processing-based coating [88–90]。Specifically, Gong et al. developed a scalable aqueous with zero-VOC emission RC paint with an average infrared emissivity of 0.92 and a solar reflectivity of 0.94 [89]. Field experiments in Hong Kong showed that it could achieve sub-ambient temperatures within 72 hours, with a maximum temperature reduction of 6 °C. Additionally, Xue et al. incorporated TiO_2 powder and glass microspheres into a polystyrene-acrylate emulsion as the matrix material to create a fluorescent RC material suitable for building coatings. This material enhances daytime cooling while preventing excessive cooling at night

[90]. Field daytime experiments conducted in Beijing demonstrated that the coated roof consistently maintained a sub-ambient temperature, with a maximum reduction of 7 °C.

In addition to coatings and films, researchers have developed various passive RC building materials with high solar reflectivity, including wood [91], ceramics [92] and glass [93]. Li et al. developed a cooling wood by completely delignifying and densifying the wood, achieving an average solar reflectivity of 96% and an infrared emissivity close to 1, as shown in Figure 2-8 [91]. Simulations of energy savings in apartments across the United States indicated that cities with hot, dry climates offer the greatest potential for cooling energy savings, with cooling wood potentially reducing energy usage by 20–60%, significantly lowering the energy load for indoor climate control.

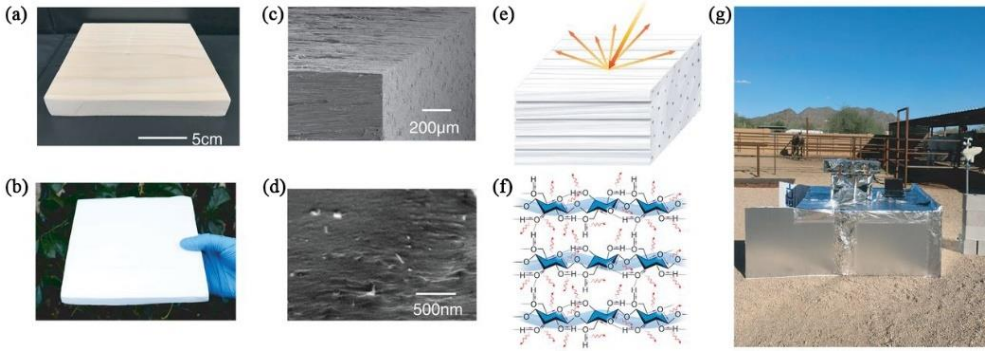

Figure 2-8: Cooling wood demonstrates passive daytime radiative cooling. (a) natural wood and (b) cooling wood. SEM image of the (c) cooling wood and (d) partially aligned cellulose nanofibers of the cooling wood. (e) Schematic showing the wood structure strongly scattering solar irradiance. (f) Schematic of infrared emission by molecular vibration of the cellulose functional groups. (g) Setup of the real-time measurement [91].

Lin et al. created a honeycomb ceramic with a layered porous structure designed to achieve efficient light scattering and near-perfect solar reflectivity of 99.6% [92]. Experimental results showed that the cooling ceramic could be 4.3 °C lower than the ambient temperature and 8 °C lower than common commercial tiles, even under solar intensity as high as 800 W/m^2. Furthermore, the cooling ceramic demonstrated excellent cooling performance, with a cooling power of 134.5 W/m^2. Zhao et al. designed and demonstrated a solution-processed photonic "cool glass" coating, as illustrated in Figure 2-9 [93]. Outdoor experiments showed that, even with relative humidity at 80% and solar radiation at 800 W/m^2, the glass substrate's temperature was 3.5 °C lower than the ambient temperature. Additionally, simulations indicated that applying the "cool glass" coating to the roof of a mid-rise apartment could reduce annual carbon dioxide emissions by approximately 10%.

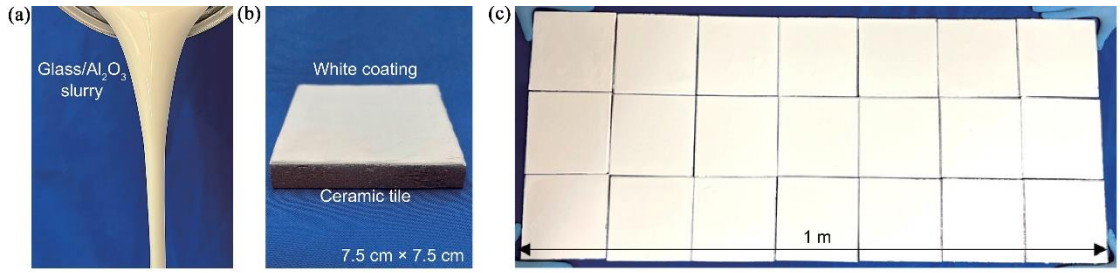

Figure 2-9: Fabrication and morphology of the radiative cooling glass coating. (a) The glass-Al_2O_3 particle shows good fluidity. (b) The radiative cooling glass coating is applied on a ceramic tile. (c) The radiative cooling glass coating can be fabricated on a large scale [93].

2.2.2.2 Application of passive RC roofs

RC roofs have significant potential for mitigating the urban heat island effect [94]. Researchers proposed various modelling methods and conducted field experiments to evaluate the impact of applying RC materials on roofs on energy savings in air-conditioned buildings.

Baniassadi et al. utilized software to simulate the impact of high-reflectivity roofs on energy conservation in residential buildings in Los Angeles [95]. The results showed that when high-reflectivity roofs are implemented on a large scale, they can reduce cooling energy costs by 24–41% for low-performance buildings. They further evaluated the potential energy and climate benefits of buildings with super-cool materials on their roofs [96]. The findings revealed that super-cool roofs could maintain indoor temperatures below ambient temperatures, providing significant cooling benefits and reducing the overall energy consumption of residential buildings by 28%. Similarly, in Los Angeles, Fang et al. compared the cooling performance of a RadiCold cool roof, a polypropylene and ethylene–propylene rubber polymerized together (TPO) cool roof and a traditional tile roof through experiments, with the experimental platform shown in Figure 2-10 [97]. Results indicated that, even without roof insulation, the indoor air temperature of the RadiCold room remained below or close to ambient levels when solar radiation peaked at 840 W/m^2 during the day. Additionally, they developed a novel Roof Thermal Transfer Value (RTTV) model to assess the performance of different roof materials in absorbing or dissipating heat throughout the year. The study revealed that during Los Angeles' hottest months, RadiCold cool roofs could save 23.1 kWh/m^2 of cooling electricity per square meter of roof area compared to shingled roofs. Ma et al. also studied the impact of RadiCold cool roofs on the cooling performance of buildings in China. Unlike Fang et.al., they explored the energy-saving potential and

economic feasibility of using the RadiCold film on the roofs of prefabricated buildings [98]. The study compared the annual cooling electricity consumption of RadiCold, traditional tile, and white-painted roofs. The results showed that in hot regions like Guangzhou, RadiCold cool roof saved approximately 646.1 kWh of cooling electricity compared to those with tile roofs, and 132.2 kWh compared to buildings with white-painted roofs.



Figure 2-10: The experimental platform consisting of two single - space model rooms [97].

In addition, Chen et al. evaluated the potential for electricity savings in building cooling using super-cool coatings in China and examined their environmental impact [99]. They first conducted field experiments comparing the temperature changes of five different RC coatings applied to aluminium roofs with a common aluminium roof. The results showed that roofs with RC coatings could reduce temperatures by an average of 3.1-7.5 °C compared to aluminium-based roofs. They then used a novel developed model to numerically analyse the application of super-cool roofs in China and found that, in hot and humid regions, even with solar radiation exceeding 900 W/m^2, super-cool roofs could still achieve temperatures 2.6 °C below ambient. Additionally, compared to traditional white roofs, the application of super-cool roofs could reduce carbon emissions by an average of 8.6-19.7 kg/(m^2·yr).

Wang et al. evaluated the cooling performance of RC film on commercial-scale warehouse roofs [100]. They conducted a field experiment by applying a double-layer RC film with solar reflectivity of 0.92 and atmospheric window emissivity of 0.91 to the warehouse roof, as shown in Figure 2-11. The experimental results revealed that after applying RC film, the roof temperature remained sub-ambient

levels even under direct sunlight during the day. Furthermore, the average daily cooling power consumption of the RC film-roof was 249.6 kWh, a significant reduction from the 448.6 kWh consumed by the uncoated roof. They also simulated the energy-saving performance of RC roofs in different cities and found that applying RC films to traditional steel roofs could reduce cooling energy consumption by 21.2%-65.2%.



Figure 2-11: Exterior of the roof before/after applying the RC film [100].

Yang et al. found that compared to green roofs, cool roofs reduced heat gain by approximately 0.14 kWh/m^2 (8%) than the conventional roof during peak hours in Singapore (9:00 to 17:00), whereas green roofs showed a much smaller reduction of about 0.008 kWh/m^2 [101]. Additionally, He et al. conducted a field experiment in Shanghai to compare the thermal performance of green roofs and cool roofs, as shown in Figure 2-12 [102]. In this paper, RC coating on cool roof is made by polyethylene film, woven fabric and metal coating. Results indicated that in summer, cool roofs provided an average cooling effect of 3.3 °C on the roof surface, while green roofs achieved a cooling effect of only 2.9 °C. However, simulation results also showed that cool roofs increased heating loads by 10.4% in winter, which is not conducive to building energy efficiency. In contrast, green roofs help reduce heating loads.

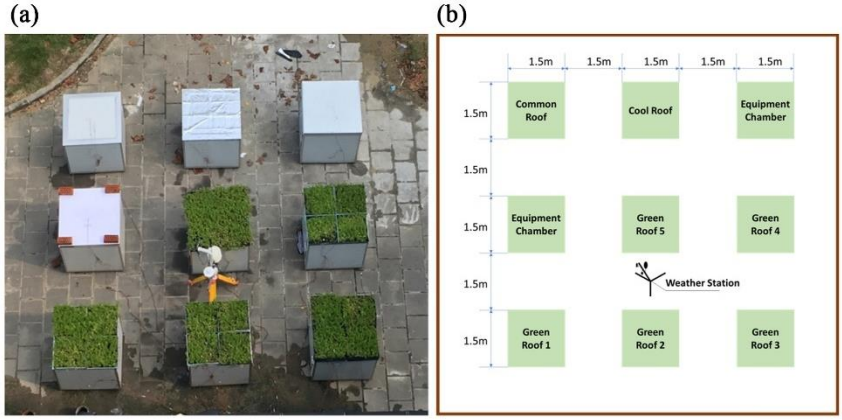

Figure 2-12: Field experiment setup of green roof, cool roof and conventional roof. (a) Site photo (b) Plan view [102].

To address the issue of increased winter heating loads caused by static cool roofs, dynamic cool roofs (DCR) have been introduced as an ideal solution [103]. DCR technology utilizes advanced coatings that can adjust solar reflectivity, reflecting sunlight during the cooling season and absorbing heat during the heating season. Examples include thermochromic (TC) or directional reflective materials [104] . Zhang et al. evaluated the energy-saving performance of five different colours of TC coatings on office buildings in Shanghai, China, using simulation software [105]. The results showed that TC materials reduced the annual energy consumption of office buildings by 0.73 to 1.47 kWh/m^2 compared to traditional cooling coatings, highlighting their excellent energy-saving potential. Additionally, Zinzi et al. assessed the transition temperature and switching amplitude (the difference between low and high reflectivity) of DCR through energy-saving simulations of TC roofs in residential buildings in the Mediterranean basin [106].

2.2.2.3 Passive building-integrated RC systems

As RC technology advances, it has become increasingly evident that integrating RC systems with building envelope structures, such as roofs and walls, can offer users a more comfortable indoor environment. Recently, numerous optimized building-integrated RC systems have been proposed, demonstrating excellent energy-saving performance and significant potential to mitigate the UHI effect.

Yue et al. proposed a superhydrophobic cellulose aerogel cooler (SHB-CAC), which is self-cleaning and suitable for building envelope structures [107]. The outdoor experimental setup used a foam shell covered with aluminium foil as the frame and SHB-CAC as the roof. Results demonstrated that at high solar intensities of approximately 800 W/m^2, significant sub-ambient cooling was achieved, with an average temperature reduction of 9 °C below ambient. Additionally, simulations indicated that using this aerogel cooler in Chinese buildings could reduce energy consumption by 43.4% compared to the building baseline consumption. Based on research on RC aerogel materials, De Masi et al. proposed a new aerogel-based cool roof with a solar reflectance of 84% and thermal emissivity of 90% [108]. They also examined the thermal performance of a full-scale building with an aerogel-cooled roof under real climate conditions, as shown in Figure 2-13.

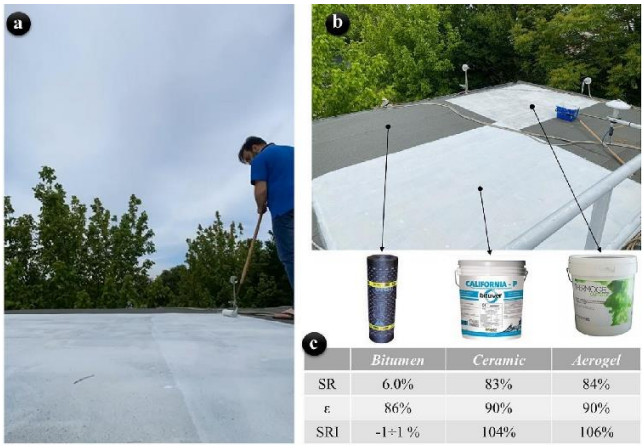

	Bitumen	Ceramic	Aerogel
SR	6.0%	83%	84%
ε	86%	90%	90%
SRI	-1÷1 %	104%	106%

Figure 2-13: A new aerogel-based cool roof. (a) Cool paint application. (b) roof detail and (c) coatings used for the experiment [108].

Their findings revealed that the aerogel coating could reduce the average daytime surface temperature by 9.7 °C in summer, demonstrating optimal performance during the hottest months.

Chen and Lu established a model to assess the cooling performance of RC roofs and applied it to evaluate the energy-saving potential of RC roofs in cities with different climates across China [109]. The simulation results indicated that RC roofs offer substantial energy-saving potential, with annual energy savings of 9 .3% in Kunming and 7.1% in Hong Kong. In addition, Zhang et al. investigated the thermal performance of passive RC-based cool roof (PRC-CR) through experiments and numerical analysis [110]. The experimental setup is shown in Figure 2-14. Test results in Hefei, China, revealed that when the temperature control system was turned off, the maximum summer temperature in the PRC-CR room was 5.5 °C lower than that of a room with a standard concrete roof. Numerical analysis showed that PRC-CR can reduce the total building load in regions where cooling dominates. However, they also found that PRC-CR increases the building's heating load during winter.

(a) (b)

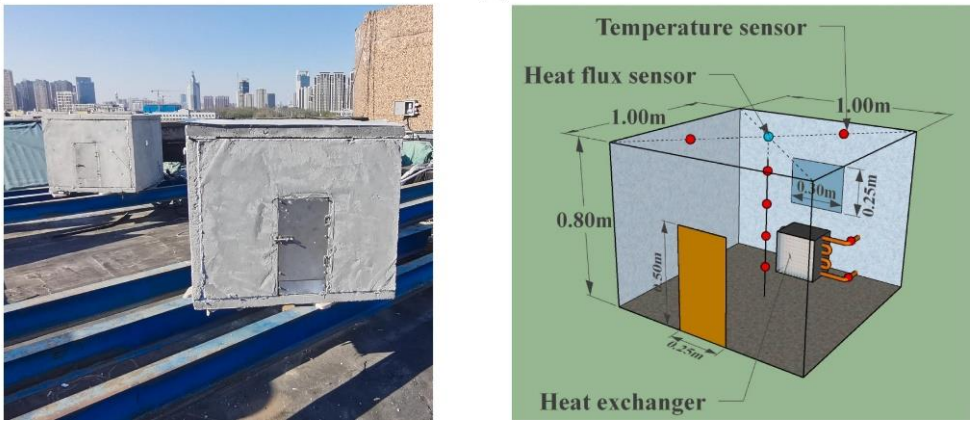

Figure 2-14: PRC-CR and concrete-roof room. (a) Photo and (b) schematic [110].

The above literature highlights the demand to consider the applicability of RC roofs in different regions in both cooling and heating periods. Liu et al. introduced a roof transient heat transfer model that combines one-dimensional transient heat transfer and spectral-dependent methods [111]. After validating the cooling performance of RC coatings with a solar reflectivity of 0.85 and an emissivity of 0.95 through field experiments, the model was used to further assess the building energy-saving performance of this RC roof in various climates. Simulation results showed that, during summer, the annual energy-saving effect of RC roofs in Guangzhou, Shanghai, and Beijing was 84.9%, 30.3%, and 2.4% lower, respectively, compared to traditional roofs.

Zhao et al. proposed a new roof-integrated RC system that combines RC technology with attic ventilation to reduce attic temperatures [24]. The schematic diagram of the roof-integrated RC system is shown Figure 2-15. The RC material used in this system is RadiCold, which can easily achieve sub-ambient temperatures to cool the indoor environment. Experimental results demonstrated that the novel system could obtain 3-5 °C reduction below the ambient during the day. Simulation studies further showed that, compared to ordinary shingle roofs with R-10 attic insulation, the roof-integrated RC system can save 1.2-3.6 kWh/m^2 annually.

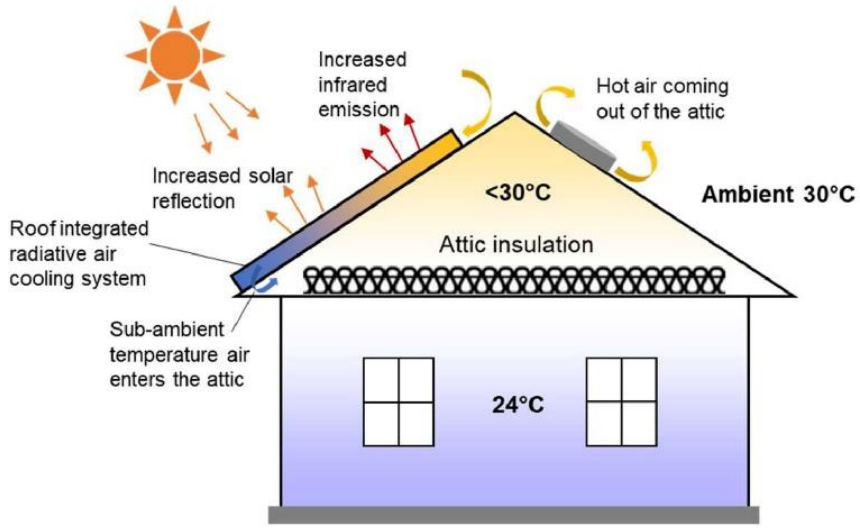

Figure 2-15: Schematic of a RC system integrated with residential building [24].

2.2.2.4 Active building-integrated RC systems

The previous section primarily summarized the application of passive RC strategies in buildings. To further enhance energy efficiency, external energy sources (such as fans and pumps) are often required to transfer and utilize the generated cooling energy. As a result, an increasing number of active building-

integrated RC systems have been proposed. These systems include air-cooling systems [64], open-loop or closed-loop water systems [112] and hybrid systems that combine RC with phase change materials (PCM) [113] or other energy systems, such as photovoltaic/thermal systems [114]. Figure 2-16 presents schematic representations of several exemplary building-integrated RC systems. Among these, Figure 2-16 (a-c) utilizes air as the heat transfer medium [12], whereas segments Figure 2-16 (d-f) employ water [115].

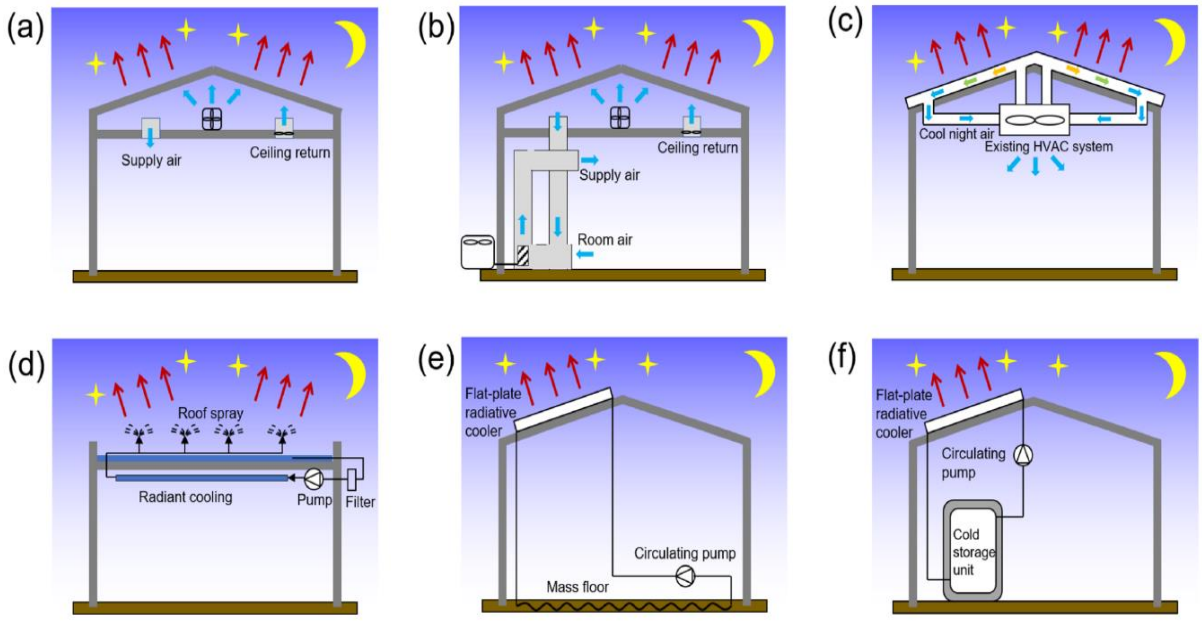

Figure 2-16: Building-integrated nighttime RC systems [12].

A typical air-cooling system comprises an RC surface (such as a roof-mounted radiator or cool roof), an air circulation loop, or a fan to drive airflow [12]. Yew et al. evaluated the effect of different air cooling systems on attic temperature in Malaysia [116]. They experimentally compared the attic temperatures under RC roofs integrated with a modified moving air cavity (MAC) using solar-powered fans and those with a conventional MAC. The experimental results showed that the three roofs coated with RC material exhibited the best cooling performance. However, the integrated MAC-solar fans can reduce the temperature by about 1.5 °C compared to the conventional MAC system. Furthermore, Liu et al. proposed a novel roof design (RC-PCR) that combines RC coating with a PCM to significantly reduce the heat entering buildings through the roof during the day [113]. They experimentally measured the indoor surface temperature and air temperature of three buildings with different roofs, the experimental setup shown in Figure 2-17. The results indicated that, compared to ordinary roof and

phase change roof, the RC-PCR roof achieved the best cooling performance, lowering the average indoor surface temperature by 1.5-1.8 °C and the average air temperature by 0.7-2 °C. While the RC-PCR roof had a slight negative impact in winter, the reduction in cooling load during summer was far greater than the increase in heat load during winter, demonstrating its significant potential for reducing building energy consumption.

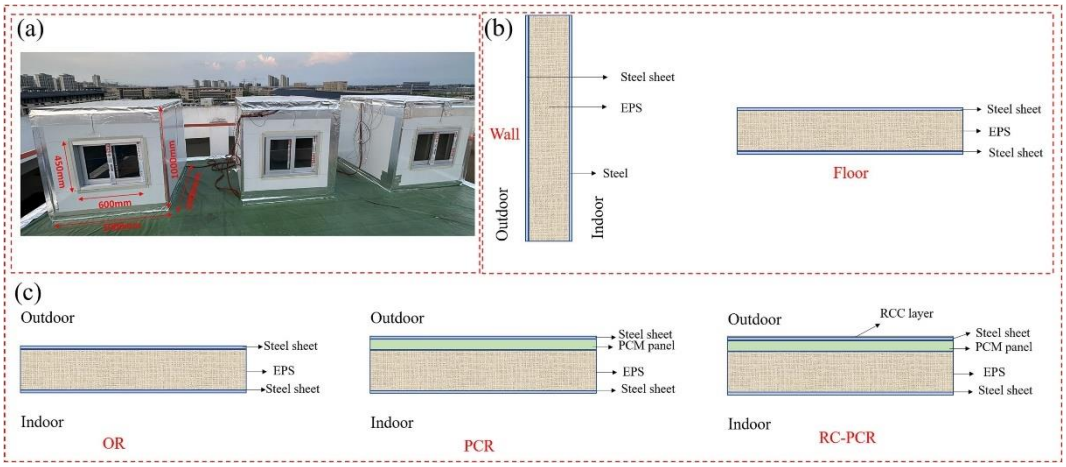

Figure 2-17: A novel roof design (RC-PCR). (a)The photograph of the experimental chambers. (b) Schematic diagram of wall and floor structure, and (c) Schematic diagram of OR (ordinary roof), PCR (phase change roof), and RC-PCR [113].

In addition to air-cooling systems, water can also be used as a heat transfer fluid to form a water-based active RC system, whose average net cooling power is usually around 40 to 80 W/m^2 [117]. Water-based RC systems can be divided into two types according to whether there is cold storage equipment, one is directly used as an in-site cooling source, like Figure 2-16 (d), and the other is a cooling storage system, like Figure 2-16 (f). When water-based RC systems are used as an in-site cooling source, the water temperature after cooling may not meet the chilled water requirements of traditional building air conditioning systems. Therefore, most water-based RC systems supply cooled water to radiant floor or ceiling systems, which do not require extremely low water temperatures.

Yuan et al. developed a new water-based RC system to achieve effective daytime RC by applying the RadiCold material to the top of an aluminium box containing an enclosed water body [118]. The experimental results demonstrated that the watered-based RC module effectively achieved a cooling effect, maintaining the water temperature at 2-14 °C below ambient temperature. Additionally, they simulated the module integrated into a building's roof, with the cooled water serving as a potential "free" cooling source for a radiant cooling floor system, as shown in Figure 2-18 (a). The results indicated that

the cooling load provided by the RC system could meet more than 70% of the building's cooling energy needs. Also utilizing the RadiCold material, Zhao et al. developed an RC collection module capable of cooling water to 10.6 °C below ambient temperature at noon [11]. The schematic cross-section of the module is shown in Figure 2-18 (b). Additionally, they used simulation software to model the RadiCold system combined with scheduled operations and a cold storage unit, designed to store the cold energy generated at night for retrieval during the day, thereby reducing the air conditioning cooling load. The system schematic is shown in Figure 2-18 (c). The results indicated that in different locations, the RadiCold system could save 64%-82% of cooling electricity in winter and 32%-45% in summer.

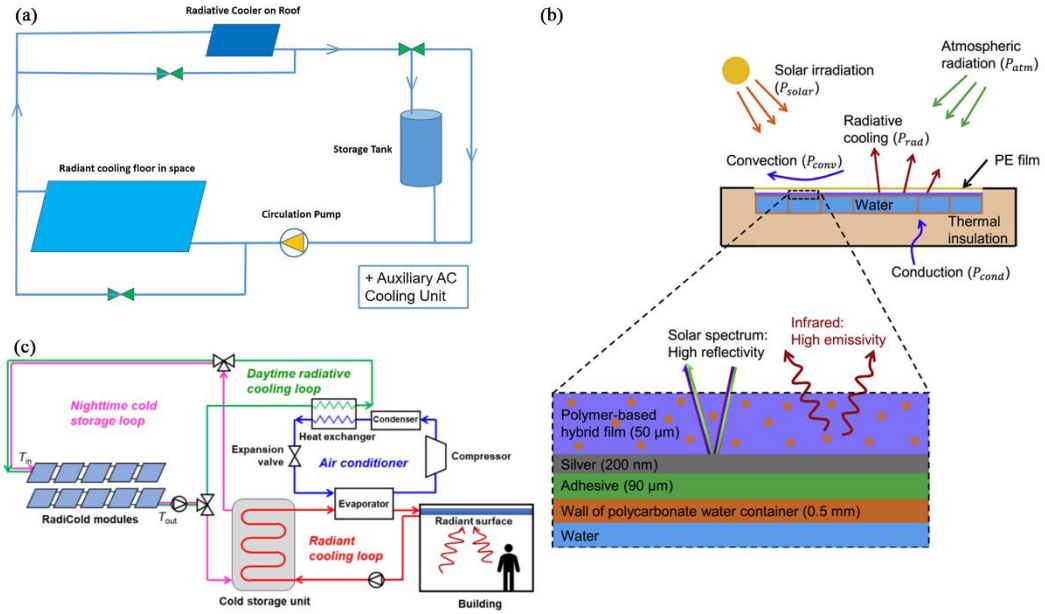

Figure 2-18: Different water-based active RC systems. (a) Schematic of modelling building and the whole RC system with an auxiliary AC unit [118]. (b) The RadiCold module and the bilayer RadiCold metafilm [11]. (c) Building-integrated RadiCold system [11].

In addition, Yang et al. conducted a theoretical study on a water-based RC module using ideal selective RC materials [119]. The study found that during a 10-hour cooling process, the temperature difference between the environment and the water gradually increased from 1.0 to 3.76 °C. However, because the module lacked a non-radiative shielding device, heat transfer from the surrounding air to the RC emitter increased, leading to a gradual decline in RC power from 53.5 to 38.5 W/m^2. Zhou et al. proposed a RC system that combines water-based RC panels with heat exchangers and cold storage units to cool residential buildings [120]. They developed a numerical model to evaluate indoor air temperature performance. Simulations of a typical U.S. residential building revealed that, with a water flow rate of 0.001 kg/(s·m^2), the indoor air temperature could drop by up to 5.1 °C. Additionally,

utilizing the energy stored in the cold storage unit to meet peak cooling demand could further reduce the air temperature by 6.6-12.7 °C. This study demonstrates that the combination of daytime RC panel and cold storage unit is a promising strategy for building cooling.

Water-based RC systems can also be combined with other energy systems to enhance energy conservation and efficiency. For instance, Fakouriyan et al. proposed a renewable hybrid system that integrates RC and PVT systems to provide heating, cooling, and electricity for buildings [121]. They developed a simulation model to compare the performance of water-cooled PVT system and RC-cooled PVT system. The results showed that using aluminium pipes to circulate water and dissipate heat from the PVT system increased electrical efficiency by 9.1%. Additionally, applying an RC coating to the PVT system further improved electrical efficiency by 3.7%.

Compared to passive building-integrated RC systems, active building-integrated RC systems that incorporate external energy sources, such as fans or pumps, are more practical and better suited to the needs of users. These systems also address the challenge of passive systems generating additional heating loads in winter, while ensuring sufficient cooling for building requirements.

2.2.2.5 Application of RC technology with other building components

When RC technology is integrated into buildings, it is typically placed on the roof to maximize cooling power and reduce indoor temperatures. However, in high-rise buildings, the roof area alone is insufficient to meet the cooling demands of the entire structure, and heat gains from exterior walls and windows cannot be ignored. As a result, many researchers have explored the application of RC technology to building walls and windows [122–124]. This new enclosure design has been shown to reduce the building's cooling load, contributing to energy conservation.

Systems integrated RC modules with building walls can be broadly divided into two categories. one involves installing the RC module directly on the wall, while the other places the RC module on the roof, forming a hybrid system with the wall. Zhang et al. proposed a novel system integrating PV and RC modules on building facades (PV-RSC), as shown in Figure 2-19 (a) [114]. In this system, PV modules are installed on the south wall of the building, while RC modules are placed on the north wall. They developed a numerical model to analyse the cooling performance of the system in Beijing, China.

The results indicated that increasing the water flow rate improved the cooling performance of the PV-RSC system. The average cooling power of the RSC system, with a heat dissipation area of 0.61 m^2, ranged between 130-220 W, contributing positively to building cooling in summer. Additionally, RC systems can be integrated with PCM walls to enhance energy efficiency. Yan et al. proposed a novel PCM-embedded wall system coupled with an RC module [125]. Figure 2-19 (b) shows the schematic diagram of the novel systems. During the day, the PCM absorbs the heat from the outdoor thermal environment, reducing heat entering the room. At night, the heat inside the PCM is transferred by water in the circulation system to the RC module and emitted to outer space. Simulation results showed that the system could reduce the cooling load by 54.2% during the cooling season, lowering the inner wall surface temperature by 1.6 °C compared to conventional walls, demonstrating excellent energy-saving performance. Subsequently, they developed a coupled system of a pipe-encapsulated PCM wall and RC module with self-activation capability and conducted experimental research, which can be seen in Figure 2-19 (c) [126]. The experimental results demonstrated that when the indoor temperature was not controlled, the inner surface temperature of the coupled wall was reduced by 1.1 °C compared to the PCM wall without the RC module. Additionally, the average heat gain through the wall was reduced by 10.6 W/m^2. Furthermore, He et al. proposed a novel all-day cooling wall that integrates PCM, micro-channel heat pipes (MCHPs), and RC panels, as shown in Figure 2-19 (d) [127].

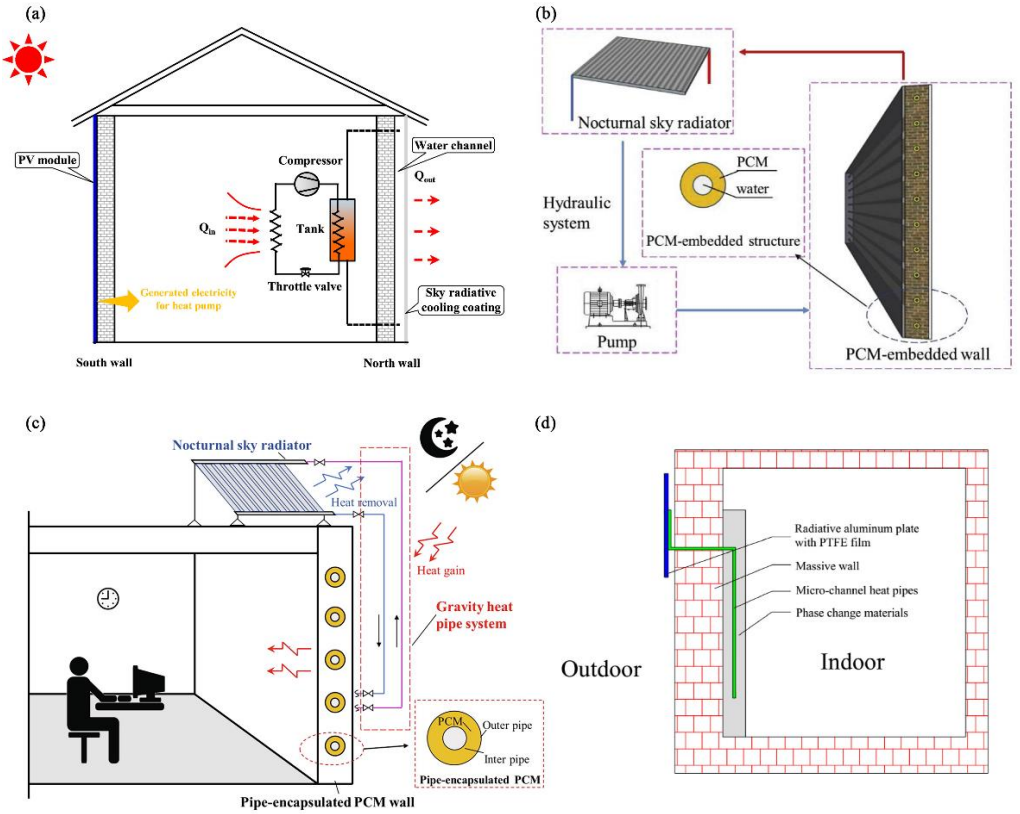

Figure 2-19: Different RC systems integrated with building facades. (a) Building façades integrated with PV-RSC system [114]. (b) The schematic of the PCM-embedded wall with RC module [125]. (c) The coupled system of the pipe-encapsulated PCM wall and RC module [126]. (d) The basic structure of the novel all-day cooling RC-PCM-wall [127].

They constructed three laboratories to test the cooling effect: one with the proposed wall applied to the south side, and the other two featuring ordinary PCM walls and brick walls, respectively. The experimental results indicated that the average temperature in the laboratory with the proposed wall was 0.3 °C and 0.8 °C lower than in the other two laboratories, improving indoor thermal comfort. Additionally, its cooling load was 47.9% lower than that of the brick wall.

RC technology can also be applied to building windows. As a key component of natural ventilation and daylighting, windows often exhibit low energy efficiency, accounting for 60% of total energy loss in buildings [128]. Therefore, there is an urgent need for technologies that can enhance their energy performance. One of the most common energy-saving solutions is the smart window, which dynamically adjusts solar transmittance in the visible and near-infrared ranges [129]. When combined with RC technology, smart windows can further reduce energy consumption and improve overall building efficiency.

Yi et al. applied a transparent RC film with selective solar transmittance and high AW emissivity on roof glass to improve building energy efficiency [130]. Simulation results showed that in regions with hot summers and cold winters, applying the transparent RC film could result in annual air conditioning energy savings between 40.9% and 51.8%, demonstrating both its energy-saving potential and economic feasibility. However, during the day, the glass temperature can still easily exceed ambient temperatures, indicating that high AW emissivity alone is insufficient to meet cooling demands. In response, Zhao et al. developed a semi-transparent RC glass with high infrared emissivity [131]. This glass integrates a semi-transparent solar film with high transmittance in the visible light range and a transparent RC film with high emissivity in the infrared region, effectively reducing heat gain. The schematic of ST/RC glass and its energy balance diagram are shown in Figure 2-20 (a). Experimental results showed that this new glass lowered indoor air temperatures by up to 16.4 °C compared to standard glass, proving its ability to regulate the building's thermal environment. Zhao et al. introduced a dynamic glass that can switch between solar heating and radiative cooling modes using a reversible silver electrodeposition method [132]. The schematic diagram is shown in Figure 2-20 (b). Outdoor tests demonstrated that in radiative cooling mode, when solar radiation was around 600 W/m^2, the glass maintained indoor temperatures about 2 °C lower than the ambient temperature. In solar heating mode, simulation results indicated that it could provide a net heating power of approximately 400 W/m^2.

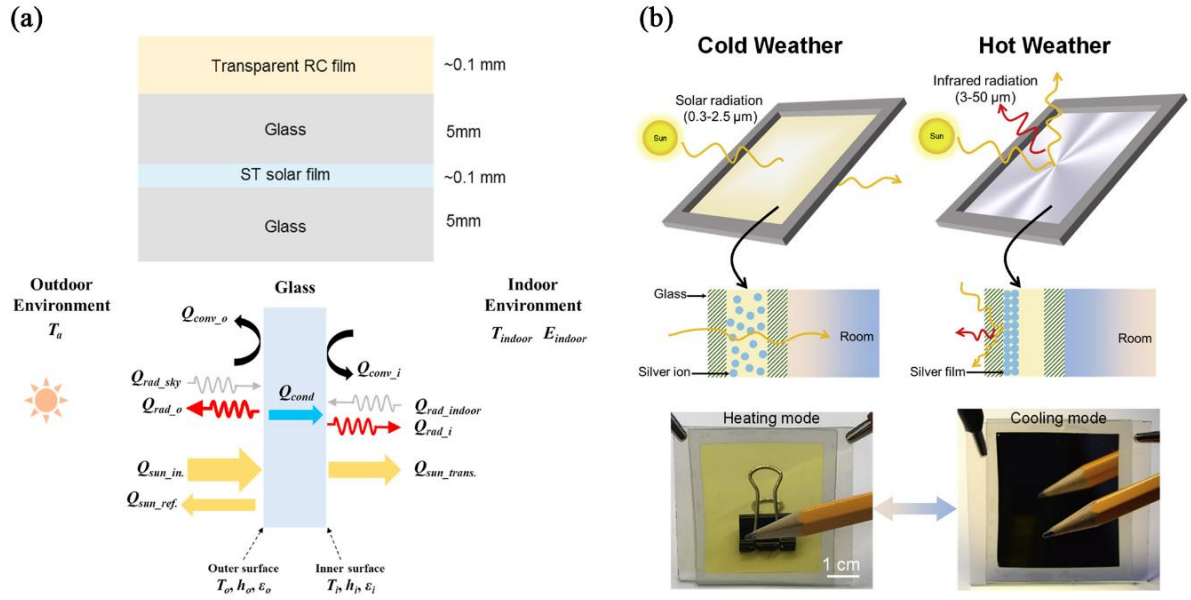

Figure 2-20: Different transparent RC films. (a) Schematic of the semi-transparent RC glass and its energy transfer diagram [131]. (b) Schematic diagram of the dynamic glass and its two modes [132].

In addition, Wang et al. developed a tuneable emissivity thermochromic (TET) smart window that simultaneously adjusts solar transmittance and thermal radiation [133]. In outdoor experiment, the TET smart window reduced the maximum air temperature by 5.4 °C compared to ordinary glass. Simulation results indicated that it could achieve energy savings of 18.8% in cold climates like Beijing, China. To further enhance energy efficiency, they also proposed a new transparent RC regulating thermochromic (RCRT) smart window [134]. Figure 2-21 depicts the schematic diagram and working principle of the new smart window. This window can automatically adjust its near-infrared transmittance and emissivity, promoting RC in warm weather and inhibiting RC in cold weather to reduce additional heating loads. Energy consumption for a full-scale building was simulated using software. The results showed that compared to commercial Low-E windows, the new RCRT window demonstrated superior energy-saving performance across various climate zones, achieving energy savings of 324.6 MJ/m^2.

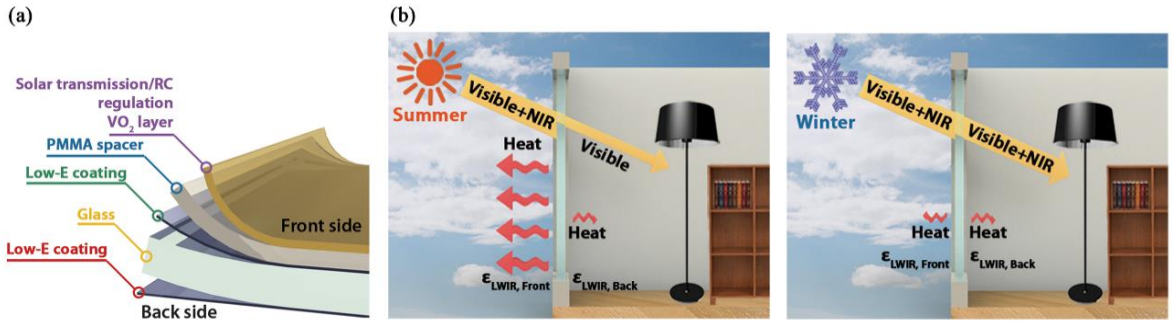

Figure 2-21: Structure and concept of an RCRT window. (a) Schematic structure of the radiative cooling regulating thermochromic window. (b) Working principle of radiative cooling regulating thermochromic window in summer and winter [134].

2.2.3 Applications of RC technology integrated with concentrators

2.2.3.1 Development of concentrated RC scheme

In recent decades, there has been a profound exploration of RC driven by significant advancements in materials science and technology. This progress has led to the development of novel RC materials, including metamaterials and polymer-based materials, which exhibit nearly ideal spectral characteristics [42,67,91,135–137]. However, while these innovations have advanced RC technology, further enhancements in the material's spectral selectivity require ongoing optimization experiments and complex manufacturing processes, which hinder the large-scale application of RC technology [138,139]. Therefore, in terms of enhancing RC power, further research prospects perhaps should lie not so much in material advancements but in exploring structural optimization at system levels.

In this context, the development of external shielding structures for RC systems is being explored [40,43]. These structures are designed to minimize the absorption of unfavourable thermal radiation and solar radiation by the RC emitter, enabling improved cooling even with RC emitters which have relatively poor spectral selectivity. Currently, shielding strategies can be broadly categorized into two types. The first involves assembling a shading device around the RC emitter, such as enclosed envelopes made from spectral-selective films forming tapered waveguides [33] or truncated cone-shaped shields [140]. The second category employs independent unenclosed structures, such as flat plate shields [44] and ring shields [43] to maximally block solar radiation, as shown in Figure 2-22. However, in practical applications, the large footprint of enclosed shielding structures is not suitable for areas with limited space, such as building roofs, while standalone shielding devices may introduce new issues related to installation and aesthetic requirements.

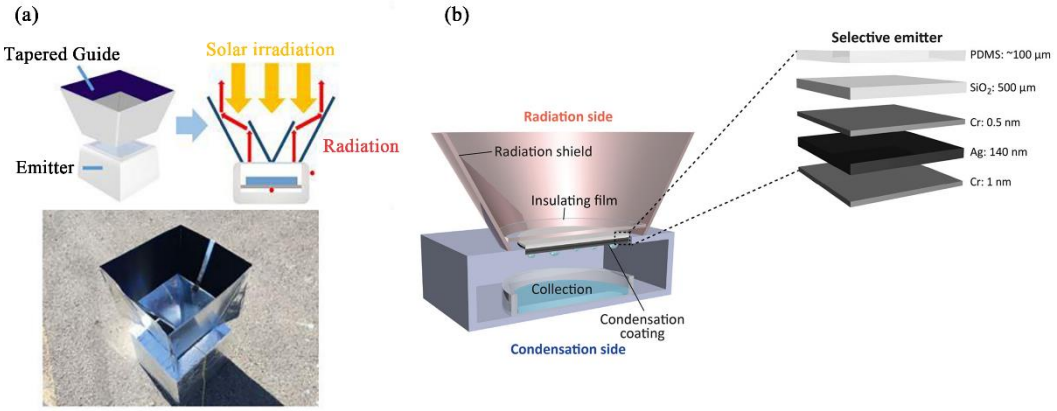

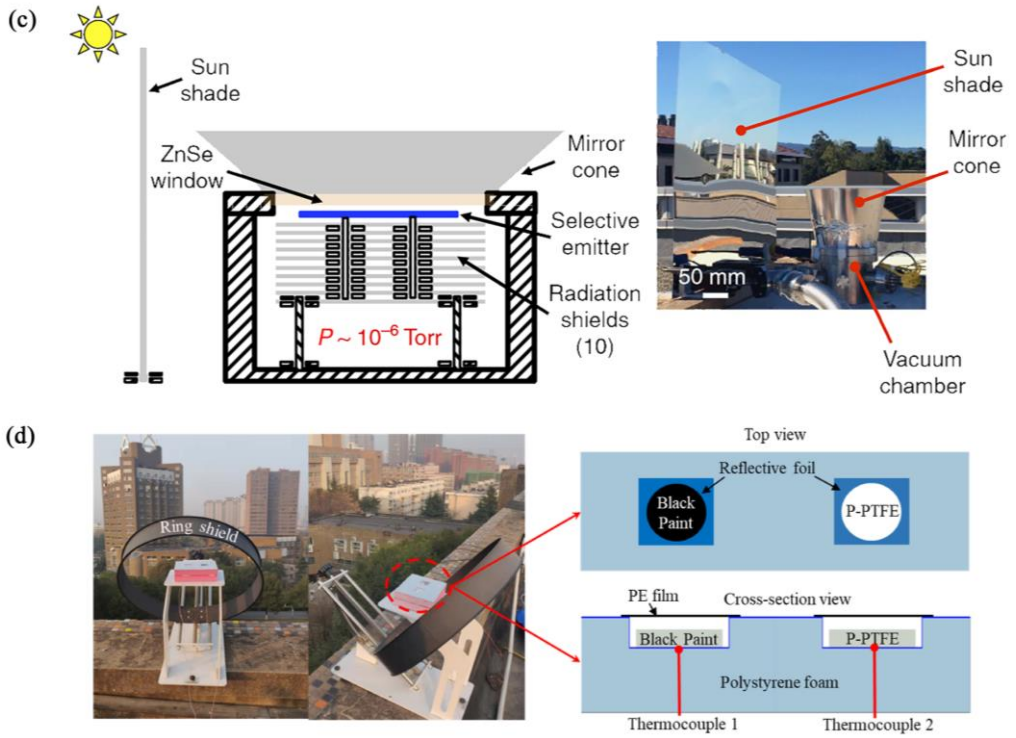

Figure 2-22: RC systems with different shading devices. (a) Schematic diagram and photograph of the cooling system with tapered waveguide structure [33]. (b) Working principle with separated radiation and condensation side and structure of selective emitter [140]. (c) Schematic diagram and In situ experimental set-up [44]. (d) Photos of the experimental apparatus with a top view and cross-section view of the radiative cooling device [43].

In addition to installing independent shielding devices around the RC modules, the novel concentrated RC modules recently proposed, inspired by the design of concentrated solar energy collection systems. Its objective is to further enhance RC power [34]. Concentrated RC systems utilize concentrators (reflectors) to direct and concentrate the hemispherical thermal radiation emitted by RC emitters towards the most transparent region of the sky, typically around the zenith (0° direction), facilitating efficient radiative heat dissipation into deep space [34]. Simultaneously, the concentrators utilize the height discrepancy between them and the RC emitters as a shielding mechanism, preventing a portion of the unfavourable radiation from large zenith angles from entering the concentrators [141–143], effectively reducing the absorption of P_{sol}, P_{atm}, and P_{sur} by the emitter surfaces. Consequently, the cooling effect of the system can be enhanced.

2.2.3.2 Various Concentrated RC Systems

Concentrated RC systems commonly employ concentrators with various structural designs such as parabolic troughs [34,144], inverted pyramids [145], truncated or non-truncated inverted cones [44], and V-grooves [142]. Voorthuysen and Roes proposed a scheme that combines RC technology with

wind cooling to cool large parabolic trough solar power plants [144]. Recently, Pirvaram et al. conducted a comprehensive study on the cooling performance of novel systems with RC emitters placed on different 3D parabolic reflectors [141]. The schematic of the RC with different reflectors are shown in Figure 2-23. Simulation results revealed that using a smaller diameter parabolic reflector, in conjunction with a reduced focal length, can lower the temperature of the RC system. This approach helps minimize the area required to achieve effective sub-ambient cooling performance.

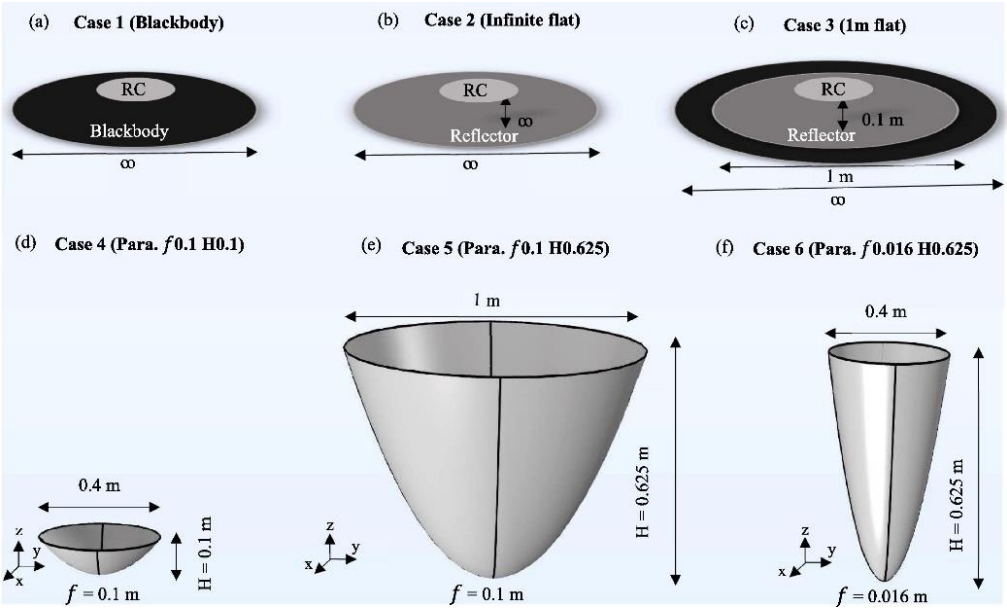

Figure 2-23: Schematic of the RC with different reflectors [141].

Similarly, Peoples et al. integrated the RC system into a mid-infrared reflective trough, as illustrated in Figure 2-24 [34]. In this novel system, thermal radiation emitted by the lower surface of the tube (which previously had no RC effect) can be reflected to outer space by reflectors. Field experiments demonstrated that the temperature drop of the RC tube with the reflective trough is more than double that of a standalone RC tube.

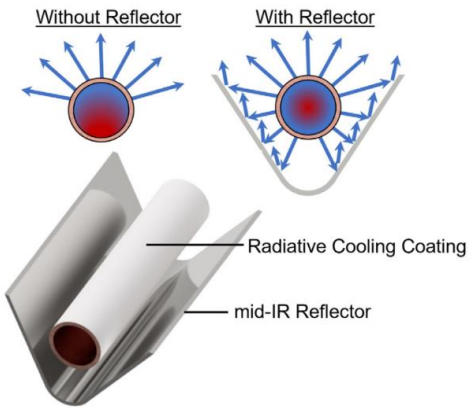

Figure 2-24: Schematic of the "concentrated radiative cooling" device [34].

Chen et al. proposed a novel device capable of achieving continuous passive cooling both day and night [44]. The device features a vertical flat sunshade combined with a mirror cone concentrator mounted on the emitter, designed to minimize the impact of direct and diffuse solar radiation. Experimental results demonstrate that this innovative system can lower ambient air temperatures by an average of 37 °C over a 24-hour day-night cycle. Additionally, Zhou et al. developed a single system capable of simultaneously collecting solar heat and reflecting thermal radiation emitted by the RC emitter [142]. This is achieved by installing two solar spectrally selective mirrors at both ends of the vertical RC emitter, as illustrated in Figure 2-25. Outdoor experimental results show that the system can achieve a temperature more than 12 °C lower than the ambient temperature. Furthermore, the spectrum-selective mirror functions as a solar absorption plate, capturing energy that would otherwise be detrimental to the RC system. This hybrid system has the potential to simultaneously reduce both cooling and heating costs for existing heating and air-conditioning systems.

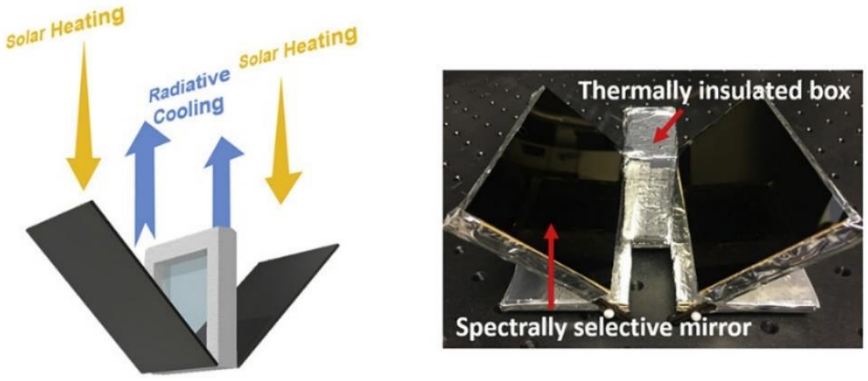

Figure 2-25: Radiative cooling performance of the double-sided thermal emitter system [142].

In the selection of concentrator materials, aluminium is frequently favoured due to its high reflectivity (or low absorption) across both the solar spectrum and infrared region [34,146]. Dong et al. suggested that the existing theoretical methods for characterizing the cooling power of concentrated RC systems overlook the constraints of reciprocity, leading to a potential overestimation of system cooling capacity [143]. They proposed a new theoretical framework and tested the optimized performance of RC systems using aluminium conical concentrators, as shown in Figure 2-26. The results indicate that employing electroplated Al_2O_3 RC emitter with optimized conical concentrators can enhance nighttime RC performance by 26%. Moreover, alternative cost-effective and highly reflective materials, including stainless steel, cermet mirrors [142], and Mylar [140], have exhibited promising potential for

concentrator fabrication. Recent physical and mathematical models have substantiated significant enhancements in the cooling efficiency of concentrated RC systems, resulting in a temperature reduction exceeding twofold compared to conventional RC devices lacking concentrators [34].

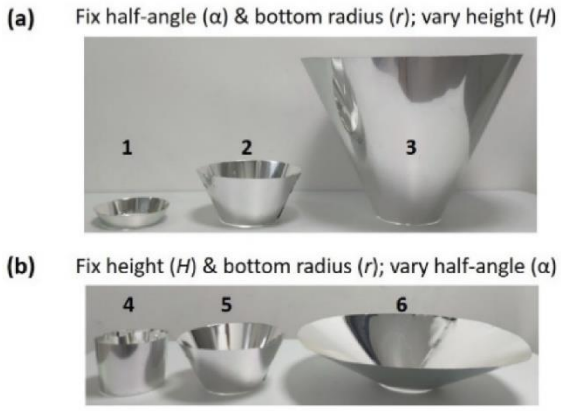

Figure 2-26: Experimental demonstration of the theoretical optimization of conical concentrators [143].

However, most current research on concentrated RC modules focuses on nighttime experiments and analysis, highlighting the thermal radiation shielding advantages and thermal concentration effects of the concentrator. This focus often overlooks the potential solar concentration effects during the day, which may lead to an overestimation of the cooling performance of concentrated RC systems. Therefore, more in-depth studies on concentrators are needed to determine if solutions can mitigate this issue. Additionally, few studies have compared the cooling performance of concentrated RC systems with different concentrator designs to identify the optimal configuration for achieving all-day RC effectiveness.

2.2.4 Summary

Before the concentrated RC system was proposed, concentrating technology is widely used in another renewable energy field, concentrated solar energy utilization. This technology employs concentrators to focus a large area of solar irradiance onto a smaller receiver. Among various concentrators, low-concentrators such as the compound parabolic concentrator (CPC) introduced by Winston [147] in 1974, has gained wide practical applications due to their cost-effectiveness and the exemption from requiring additional auxiliary tracking systems. It has been demonstrated that the CPC effectively captures direct solar radiation as well as a portion of scattered radiation when the incident angle is smaller than the half-acceptance angle of the concentrator, consequently improving the

concentration efficiency [21,148,149]. Although previous studies have integrated RC emitters with various concentrators, demonstrating their advantages in enhancing RC performance, research on integrating CPCs with RC emitters to create a novel type of concentrated RC systems remains limited [150]. The integration of a CPC structure with an RC emitter offers significant research potential and broader application opportunities. The following section will present a detailed review of the development and latest applications of CPC structure.

2.3 Compound parabolic concentrators (CPCs)

Using a concentrator to focus a large area of solar radiation onto a smaller absorber, the overall power generation of traditional solar collectors can be significantly enhanced [151]. Therefore, the choice of concentrator is crucial for increasing system power output. Among various concentrators, low-concentration concentrators play a vital role in solar concentration applications, typically used for concentrated PVT (CPVT) [152], concentrated PV (CPV) [153], and concentrated PT (CPT) systems [154]. Currently, the cost of PV has lowered significantly. However, the cost can be reduced further by substituting affordable low-concentration concentrators for solar cells. In addition, low concentrators can obtain a higher temperature than solar collectors lacking a concentrator [155].

In 1974, Winston first described the principle and geometry of two-dimensional (2D) compound parabolic concentrator (CPC) [147]. He proposed that from an optical point of view, CPCs based on the principle of non-imaging optical edge rays are considered more potential reflectors. With more and more related research, CPCs are recognized as a promising solution for solar energy concentration and daylighting [21]. It can capture more sunlight when the solar incident angles smaller than its maximum half-acceptance angle [149]. Since then, the optical properties of CPCs have been widely studied and applied in various aspects of solar energy research, and researchers' attempts have been made to introduce them into more disciplines. Tian et al. published a review in 2018 summarizing CPC research focused on solar energy applications since 2000 [21]. However, in the past five years (2017~present), many new technologies and applications of CPCs have emerged. This section aims to comprehensively summarize CPC research related to solar energy applications since 2017 and to review the latest development trends in CPCs over the past few years. Subsection 2.3.1 begins by discussing existing

CPC types and classifies CPC based on different structures. Subsection 2.3.2 provides an overview of CPC applications in solar energy conversion, including in photovoltaic and photothermal areas. Subsection 2.3.3 explores various applications of CPCs in daylighting.

2.3.1 Different structure of the CPC

2.3.1.1 Two-dimensional (trough) CPC

Previous researchers have investigated the formation and many applications of 2D CPCs. In recent studies, it has been applied to building integrated CPV systems [156], integrated PV cells [157] combined with evacuated tubes as solar absorbers [158]. Masood et al. designed a novel two-dimension (2D) symmetric CPC for building integration and rooftop photovoltaic applications. In their study, they used MATLAB code to determine the optimal truncation position for the CPC [159]. A detailed statistical analysis of the synergistic effects of the independent design parameters on the response was conducted using the response surface modelling method. They concluded that a 50% truncated CPC with a 21.58° half-acceptance angle and an aperture width of 193.98 mm represents the optimal CPC geometry. Furthermore, in their dataset, they built an empirical model to establish relationships between the control factors and response variables of the proposed concentrator, which were developed and solved analytically using MATLAB. The presented data can be used for statistical modelling and design optimization of the 2D SCPC [160]. Chandan et al. integrated a homogenizer into a 2D CPC and studied the performance of standard CPC and elongated compound parabolic concentrators (ECPC) integrated into LCPVT system [161]. The experimental results showed that the integration of the homogenizer improved electrical efficiency by 23% compared to the CPC with the same geometric concentration ratio (C). When integrating the homogenizers, often linear extensions to the CPC profile (also known as extended CPCs), can reduce non-uniform illumination. In further research, they investigated a 2.5x elongated CPC truncated to 1.7x, which was coupled to a desiccant-based cooling system [162].

2.3.1.2 Two-dimensional asymmetrical CPC

Based on the lens-wall structure, Li et al. proposed a novel asymmetric lens-walled CPC (aCPC), which consists of asymmetric compound parabolic curves and can be combined with the building south wall [163]. The geometry of the aCPC is shown in Figure 2-27, where the outer profile consists of two

asymmetric compound parabolic curves that collect escaping sunlight through specular reflection. Further optimizations were made to adapt the aCPC to the solar incidence angles at different latitudes. Experimental results show that the aCPC has an acceptance angle of up to 60° with an average optical efficiency of 74%.

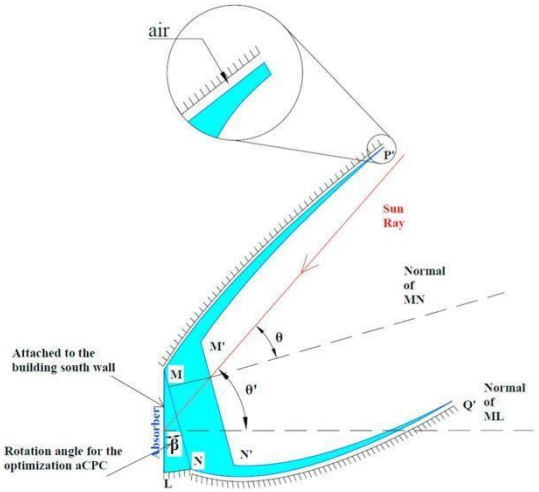

Figure 2-27: The structure of the aCPC.

Also aiming to integrate CPC with the south-facing building wall, Deng et al. building on a preliminary investigation [154], studied a 2D asymmetric truncated CPC [164]. The half-acceptance angle was designed based on the solar altitude angles at the summer and winter solstices, and the average optical efficiency within the optimized acceptance angle range was 64.51%. Figure 2-28 shows the CPC designs for four Chinese cities, adapted to different solar altitude angles.

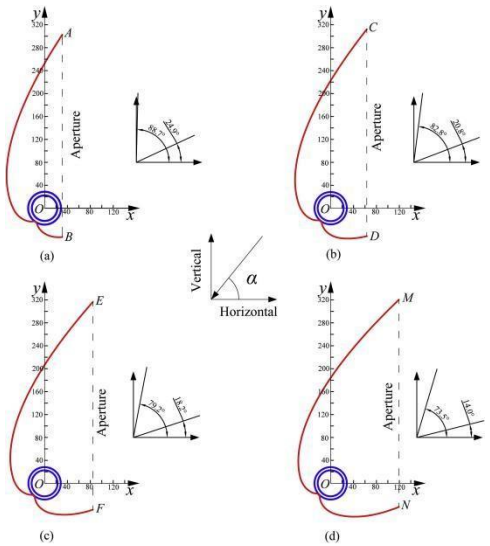

Figure 2-28: The surface structure of the FE-CPC[164]. (a) Kunming ϕ = 24.85°. (b) Chengdu ϕ = 30.67°. (c) Xi'an ϕ = 34.26°. (d) Beijing ϕ = 39.93°.

Xuan et al. proposed two narrow-lens asymmetric CPCs: the asymmetric lens-mirror concentrator and the asymmetric air-gap-lens-mirror concentrator, both of which can be coupled with photovoltaics [165]. In addition, they optimized the simulation to reduce shadows created by the systems using a simple array of concentrators. Through the simulated and experimental validation, they found that the current asymmetric concentrators can achieve a wide acceptance angle range of 10° to 85° while maintaining high optical efficiency. In further research, they developed a system and formation process for an aCPC, with the angular receiving range as the objective function. As a result, a dielectric aCPC with nearly perfect angular acceptance optical efficiency was achieved [166]. Furthermore, Lu et al. designed and tested an air-filled, truncated non-tracking aCPC with a geometric concentration ratio of 2.0x and half-acceptance angles of 0° to 55°, which can be integrated with building's envelop [167].

2.3.1.3 Three-dimensional CPC

Abu-Bakar et al. proposed and designed a novel rotationally asymmetrical CPC for use in building integrated CPC (BICPV) systems, based on the dielectric total internal reflection concentrator, as shown in Figure 2-29 [168,169]. A rotationally asymmetrical CPC can achieve an optical concentration gain of up to 6.18, depending on the half-acceptance angle, compared to a non-concentrating cell. Compared to a bare solar cell, the rotationally asymmetrical CPC prototype, with a geometric concentration ratio of 3.66x, increases the short-circuit current by a factor of 3.01. In summary of its practical advantages, Foster et al. studied the performance of the rotationally asymmetrical CPC under diffuse radiation. Simulation experiments showed that the incident angle of the ray did not affect the results, as diffuse rays originate from multiple directions. The optical concentration gain under diffuse radiation was found to be 2.12 [170].

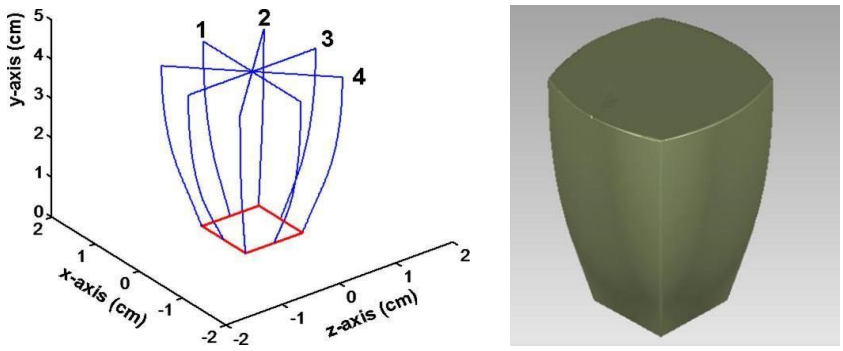

Figure 2-29: (a) the angular rotation of the 2-D cross-sections to produce the rotationally asymmetrical CPC. (b) An example of a rotationally asymmetrical CPC.

Then, Zawadzki et al. conducted a life cycle assessment of rotationally asymmetrical CPV modules. They concluded that these modules can reduce costs by 29.09% compared to traditional PV modules, with a payback period of 6.63 years, significantly shorter than the 8.01 years required for traditional PV modules [171].

Additionally, a crossed CPC is a three-dimensional circular CPC with square inlet and outlet aperture areas. This is accomplished by intersecting two 2D CPC slots perpendicularly with optical efficiency comparable to 3D CPC. Tian's review summarizes the previous studies on crossed CPCs in 2018, and found that most crossed CPCs performed well in optical efficiency, however, the optical flux distribution was not uniform at the exit aperture, resulting in hot spots affecting the conversion efficiency of PV cells [172]. In this context, Aykapadathu et al. proposed and fabricated a novel solar hybrid photovoltaic/heat absorption/reflection crossed CPC module [173]. The module has a 4x crossed CPC structure with a truncated concentration of 3.6x and a half-acceptance angle of 30°. In addition, the feasibility of this module for BICPV system was also tested. After this, Shanks et al. proposed a novel CPV system using the crossed CPC prototype previously optimized by other researchers [174,175]. The study combines crossed CPC with crystalline silicon solar cells integrated into double-glazed windows to create PV windows [176]. Through simulations and experiments, these PV windows were compared with ordinary double-glazed windows and crystalline silicon photovoltaic windows without crossed CPC. The results show that the windows integrated with crossed CPC and crystalline silicon cells have the best daylight availability. The prototype of the crossed CPC+Si PV cell is shown in Figure 2-30.

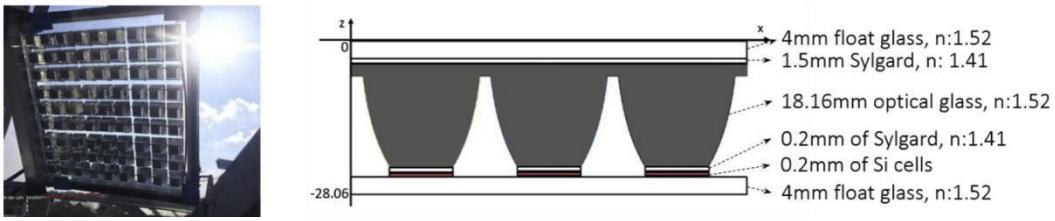

Figure 2-30: Prototype of crossed CPC+si PV cell [176].

2.3.1.4 Irregular CPCs

In practical engineering applications, standard CPCs have high manufacturing, maintenance, and transportation requirements. Additionally, a major issue with CPCs is that their concentrated light can

produce uneven illumination on photovoltaic cells, leading to hot spots and significantly reducing system reliability and power generation [177]. Consequently, in recent years, many irregular CPCs with specialized structures and improved optical properties have been proposed.

Square elliptical hyperboloid (SEH) is a novel type of static non-imaging transparent 3D concentrator manufactured for translucent integrated CPV (TICPV) based on the structure of crossed CPC [178]. The geometrical structure of the SEH and the final views created in SolidWorks are shown in Figure 2-31. The SEH features an elliptical entry and a square exit. This system achieved a 6x concentration ratio, 55% of optical efficiency, and a 50° of half-acceptance angle. However, the incident solar concentration on the solar cell was non-uniform.

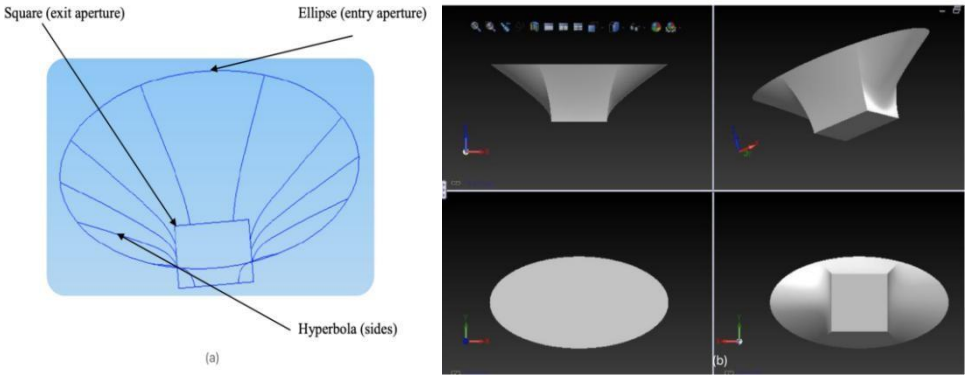

Figure 2-31: (a)Geometrical structure of the designed 3-D concentrator by Sellami.
(b) The final view of SEH built by SolidWorks [178].

Building on the preliminary research of SEH, Khalid et al. designed a low concentrating CPV module coupled to PV cells and filled it with argon gas [179]. They proposed that the SEH is small and practical enough for BIPV applications, and can be precisely integrated into transparent facades, windows, or roofs. Due to the transparency and extremely low solar thermal gain of the SEH, Sharma et al. [180] assembled it into 10 mm by 10 mm square silicon solar cells and integrated it into a window-integrated CPV system.

Additionally, to improve the original half-acceptance angle and concentration ratio of the CPC, Gao and Chen designed a novel CPC with synchronous improvement in original acceptance angle and concentration ratio (IAR-CPC) using the Monte Carlo ray-tracing method, edge ray principle, and ray reflection law, as shown in Figure 2-32 [181]. Initial testing revealed that as the optical aperture width angle increases, the geometric concentration ratio of the novel CPC decreases, while the acceptance

angle and average optical efficiency increase. When the optical aperture width angle is 60°, the geometric concentration ratio is 1.16x, the acceptance angle is 74.39°, and the average optical efficiency is 86.77%. Furthermore, they researched and found that under the same aperture width as standard CPC, its average optical efficiency is 96.66%, which is 4.32% higher than that of standard CPC. Additionally, the original acceptance angle increased by 17.56% [182].

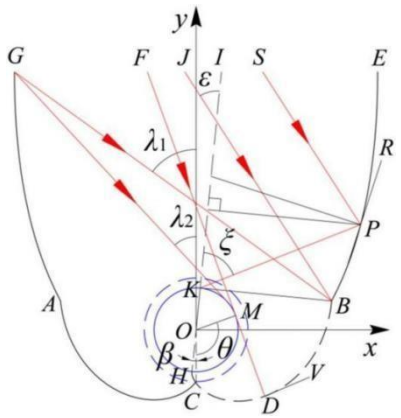

Figure 2-32: The structure of the IAR-CPC [181].

Moreover, a multi-section CPC (M-CPC) has been designed to solve the problems of non-uniformity CPC luminous flux distribution and the slight acceptance angle. Its design principle is to use multi-segment reflective surfaces to replace the parabolic reflective surfaces of standard CPC (S-CPC) [183]. Seven M-CPCs with varying numbers of cross-sections were designed, and their optical performance was analysed through simulations and experiments. It was ultimately found that M-CPCs with seven plane cross-sections demonstrated high optical efficiency over a wide range of incident angles (approximately 95% efficiency) and excellent angle acceptance (100%). In addition, it is found that the M-CPC not only improves the uniformity of energy flux distribution on the connected absorber but also enlarges the half-acceptance angle and extends working time for the system. Similar to this conclusion, Xu et al. proposed a novel M-CPC module, which the schematic diagram is shown in Figure 2-33 [184]. To optimize the design and address the issues of non-uniform energy distribution on the cylindrical absorber and the complexities of using the S-CPC parabolic structure, simulations and experiments were conducted. The results concluded that the M-CPC$_5$, with five single-sided reflective planes, is the best structure, offering an acceptance angle range of ±47° and superior uniformity of energy flux distribution on its cylindrical absorber compared to the S-CPC.

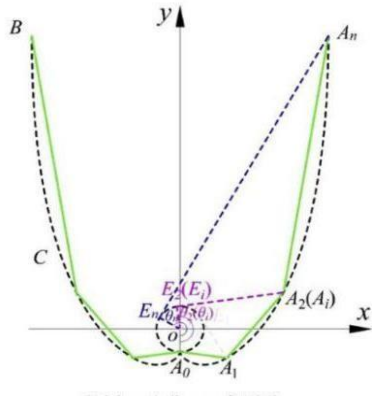

Figure 2-33: Schematic diagram of M-CPC [184].

However, previous design strategies for M-CPCs have often focused on single-ray reflections, overlooking the overall optical efficiency after multiple reflections. To address this issue, Hu et al. optimized the M-CPC using a particle swarm optimization (PSO) algorithm and explored the optical performance of M-CPC models with varying numbers of planar reflectors [185]. They concluded that as the number of planar reflectors increases, the optical properties of the M-CPC approach those of the S-CPC.

In addition, many complex CPC structures have been proposed. For example, Indira et al. used Monte Carlo ray tracing simulations to study a new CPC and PTC hybrid system [186], while Ortega et al. proposed a novel annular compound parabolic concentrator (TCPC) [187,188]. Both research teams demonstrated the excellent optical efficiency and performance of their systems through experimental or simulation methods.

As the application of CPC devices becomes increasingly widespread, the high fabrication costs and large size of traditional CPCs limit their use in applications requiring portability. Reducing the size of CPCs is, therefore, a key consideration. In some cases, novel fabrication processes for miniature CPCs have been proposed to develop more compact designs efficiently. Hajjar et al. designed a compact compound parabolic concentrator using MATLAB to meet the optical receiver size requirements for optical wireless communication [189]. They fabricated two prototype concentrators with an entrance diameter of 7 mm and an output diameter of 500 μm using micro-milling equipment from the microwave division of Telecom Bretagne. After that, Choi et al. [190] and Hsiang et al. [191] designed CPCs in micrometres and applied them to different fields. Specifically, Choi et al. designed and

fabricated a small CPC device with a total width of 30 mm using ultra-fine planning and injection moulding with diamond tools. The CPC unit consists of 60 micro-CPCs, where the incident area width is 500 μm, the concentrating area width is 218 μm, and the height is 314 μm. The diagram of the CPC unit is shown in Figure 2-34. Additionally, Hsiang et al. designed a microlens-topped CPC with a height of only 20 μm and integrated it with a tailored LED to confine the emitted light to a narrow angle.

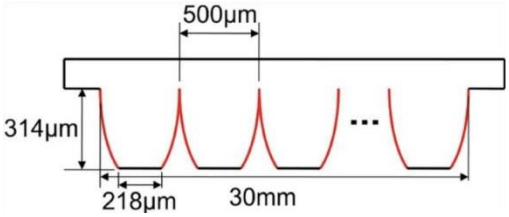

Figure 2-34: A design of miniature CPC [190].

This subsection primarily summarizes standard and irregular CPC structures, highlighting their unique optical or other advantages. The following subsection will explore the application of CPC structures in the field of solar energy utilization.

2.3.2 Applications of the CPC in solar energy conversion

Currently, CPCs are widely used in various solar energy utilization systems, with their primary goal being to collect as much sunlight as possible and reflect it to heat collectors or transmit it directly to PV cell to generate electricity. This section primarily introduces a series of applied research studies on solar energy conversion using CPCs.

2.3.1.1 CPCs in photovoltaic/thermal systems

For the past five decades, PV applications have been widely used due to various advantages, such as higher optical efficiency and the ability to collect both diffuse and direct radiation. Thanks to the advancement of PV technology, concentrators, especially CPCs, have been integrated with PV and PVT systems to enhance performance and utilization efficiency. CPV or CPVT systems offer several advantages over traditional flat-panel devices for building integration, including higher electrical conversion efficiency in PV cells, improved heat collection by thermal collectors, better space utilization and easier recycling of constituent materials [192].

In terms of improving the conversion efficiency of PV cells, Lu et al. established two new CPV cells based on known CPV cells by changing the position and number of busbars in crystalline silicon solar

cells [193]. The results show that, compared with the traditional PV cell located on the right side of the busbar of the crystalline silicon solar cell, the electrical efficiency of the CPV cell which the busbar is placed in the middle region of the crystalline silicon solar cell is relatively improved by 14.76%. Finally, it is concluded that the busbar optimization based on the non-uniform illumination intensity distribution formed by the concentrator will help to improve the electrical performance of CPV cells. Furthermore, Li et al. assembled a new type of asymmetric CPC and PV cell to fabricate an asymmetric CPV integrated module [163]. The experimental results show that the concentration ratio of the maximum power obtained from asymmetric CPV system is 1.74 times that of the energy received from PV without a concentrator. Xuan et al. explored the integration of a dielectric asymmetric CPC with PV system [166]. Through ray-tracing simulations and experiments, they demonstrated the optical performance of this design. The results showed that, compared to a non-concentrating photovoltaic cell, the dielectric asymmetric CPC, with a geometric concentration ratio of 2.4x, increased the short-circuit current by 87.0% and the maximum power by 96.6% within incidence angles ranging from 0° to 85°. Additionally, the electrical performance of the asymmetric CPV module was evaluated using an indoor solar simulator from Newport Corporation in a controlled dark environment at a temperature of 25 °C. With a geometric concentration ratio of 2.4x, the asymmetric CPC demonstrated an acceptance angle range of up to 65° with high optical efficiency [194]. Shanks et al. compared the optical performance and power output of low-concentration CPV systems based on crossed CPCs made from different materials, as shown in Figure 2-35[176]. They found that although glass has higher transmittance, devices made from the plastic Topas material achieved nearly double the power-to-weight ratio of glass devices, with only slightly lower maximum power output.

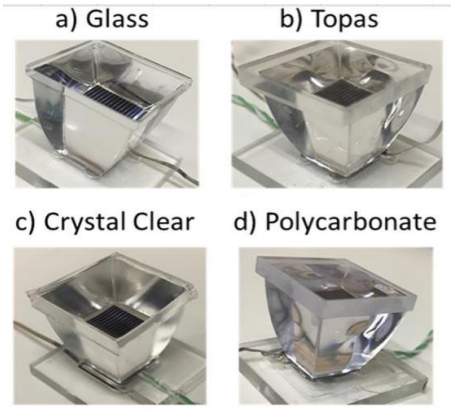

Figure 2-35:Different materials of crossed CPC in LCPV system

Additionally, due to the poor thermal conductivity of the plastic Topas material, the temperature of the PV cells increased by only 5 °C. However, for CPV or CPVT systems, the decision to use glazed or unglazed configurations depends on the surrounding dust environment and the desired energy output level.

Parupudi et al. designed a novel CPV system's geometries and simulated their optical efficiency at various truncation levels and incidence angles using the ray tracing module in COMSOL [20]. They also developed an analytical model to predict the annual energy output and payback period for the CPV system compared to an equivalent area of a conventional flat module. Their findings concluded that a system combining a CPC with an m-Si cell generates more power than an m-Si cell without a concentrator. In a 10-month outdoor experiment conducted in Brunel, UK, they tested the actual performance of three geometrically equivalent CPV modules with m-Si cells. The experimental results showed that the asymmetric CPC, with a geometric concentration ratio of 1.53x, had the shortest payback period of 6.5 years, with power generation per unit area 32.5% higher than a flat PV module. Meanwhile, the power generation of the CPC and V-Trough systems was 21.0% and 5.3% higher, respectively [195].

In addition to enhancing the conversion efficiency of PV cells, the CPV structure can also help reduce the system's temperature. Lowering the system temperature significantly improves cell conversion efficiency, with power losses ranging from 0.4% to 0.65% for every 1K increase in temperature [196]. As the PV cell's conversion efficiency decreases, the unconverted solar flux absorbed by the heat sink causes the CPV module's temperature to rise further, leading to adverse effects. Therefore, cooling of the modules is crucial. The techniques for cooling PV cells include forced and natural air [197,198], water [199], phase change material (PCM) [180,200] and other thermoelectric assisted methods. Nižetić et al. found that based on the results of the analysis of PV system active cooling strategies, as well as case studies (particularly Mediterranean climate conditions), water-based cooling should first be considered as a viable cooling option [199]. Contrary to their research, Asefi et al. proposed that water cooling technology has the apparent disadvantage that evaporation reduces efficiency, and it also requires additional cost of pumps or fans to maintain the output of the system, so

this cooling technology is gradually phased out [201]. To solve these challenges, the building-integrated PV with PCM (BIPV-PCM) module has been developed, which shows better performance than air-based and water-based thermal regulation [202]. For instance, Lu et al. developed an asymmetric CPV system in building façade (BFI-ACP-PV system), as illustrated by the 3D model in Figure 2-36 [167]. They found that the electrical conversion efficiency of the BFI-ACP-PV coupled with PCM can increase by over 5% compared to a similar system without PCM integration at the rear when the incident solar radiation intensity was 280 W/m^2. This efficiency improvement increased to over 10% when the incident solar radiation intensity reached 670 W/m^2.

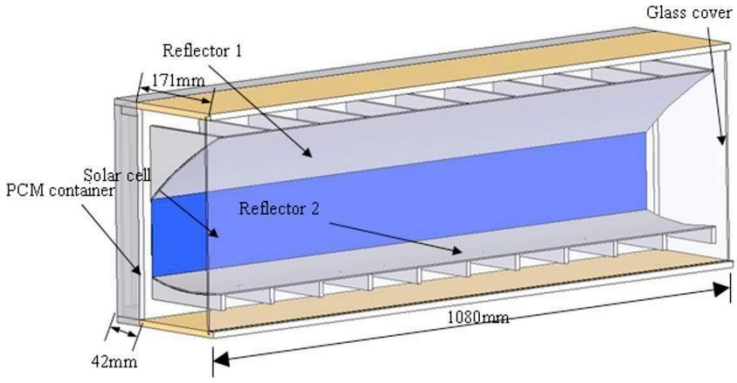

Figure 2-36: Diagram illustrating the BFI-ACP-PV system [167].

In addition to being combined with PV systems, CPC can also be integrated into PVT systems. Chen et al. studied the performance of CPC in building energy efficiency and designed a novel space heating system that integrates a CPVT system with absorption and ground source heat pumps for hotels and office buildings [203]. Multiple variables were modelled and validated. The results indicate that integrating solar and geothermal energy can effectively supplement space heating needs. Compared to a pure ground source heat pump system, the integrated system showed the best performance in office buildings, with a 32% increase in energy-saving rate and a 9% reduction in annual costs. In addition, Chou et al. designed novel BIPV panels that integrate mono-crystalline silicon panels with vacuum tube collectors and CPC mirrors [204]. The cross-section of the BICPVT system is shown in Figure 2-37. This innovative system achieved a daily solar thermal collection efficiency of 88%, significantly higher than traditional solar collectors. The system was installed on building roofs, and field tests demonstrated a notable improvement in performance compared to systems using only solar thermal collectors or standalone systems for solar power and heat collection.

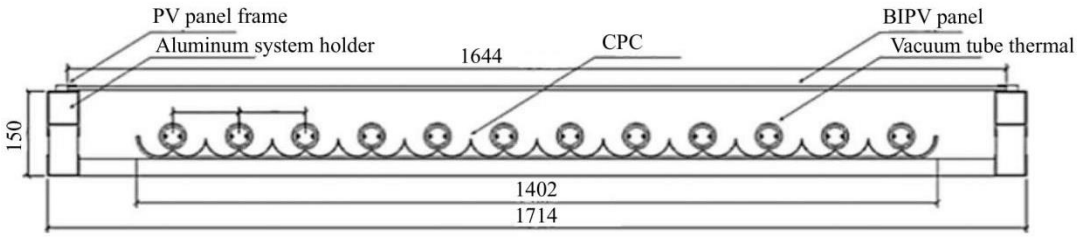

Figure 2-37: Cross-section of the PVT System (mm) [204].

Chandan et al. developed an optically coupled electrical model for a CPC and an elongated CPC, as illustrated in Figure 2-38, to simulate the electrical efficiency of a PVT module [161]. The experimental results showed that for the CPC, the peak electrical efficiency at a concentration ratio of 2x reached 14%, while at 2.5x, it reached 13.6%. In comparison, the electrical efficiency of the elongated CPC with a 2.5x configuration improved by approximately 37%, and the 2x elongated CPC improved by around 23%. Furthermore, they created a coupled optical, electrical, and thermal model to predict system performance [162]. Optical simulations revealed that the CPC had higher optical efficiency than the elongated CPC and exhibited 1-2% better thermal performance. However, at normal incidence angles, the electrical performance of the elongated CPC was 12% higher than that of the CPC. Additionally, they explored the coupling of a low CPVT system with a desiccant-based cooling system, finding that the coefficient of performance improved by 50%.

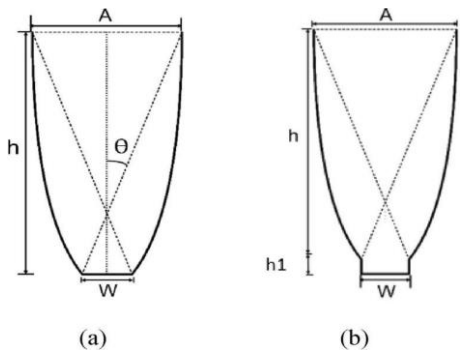

Figure 2-38: The Schematic of (a) CPC and (b) ECPC [161].

Parthiban et al. found that few numerical studies have used integrated optical, thermal, and electrical models to evaluate the overall performance of CPVT systems [157]. To address this gap, they developed a three-dimensional steady state photothermal and electrical integrated model. Glazed and unglazed 2D CPCs were optically analysed at various angles of incidence. The non-uniform heat fluxes were mapped onto solar cells to simulate thermal performance. Figure 2-39 illustrates the optical and thermal losses of both glazed and unglazed CPVT systems. The results showed that the optical efficiency of the

unglazed CPC was higher than that of the glazed CPC, and the unglazed CPVT system produced more power and had a higher overall system output than the glazed CPVT system.

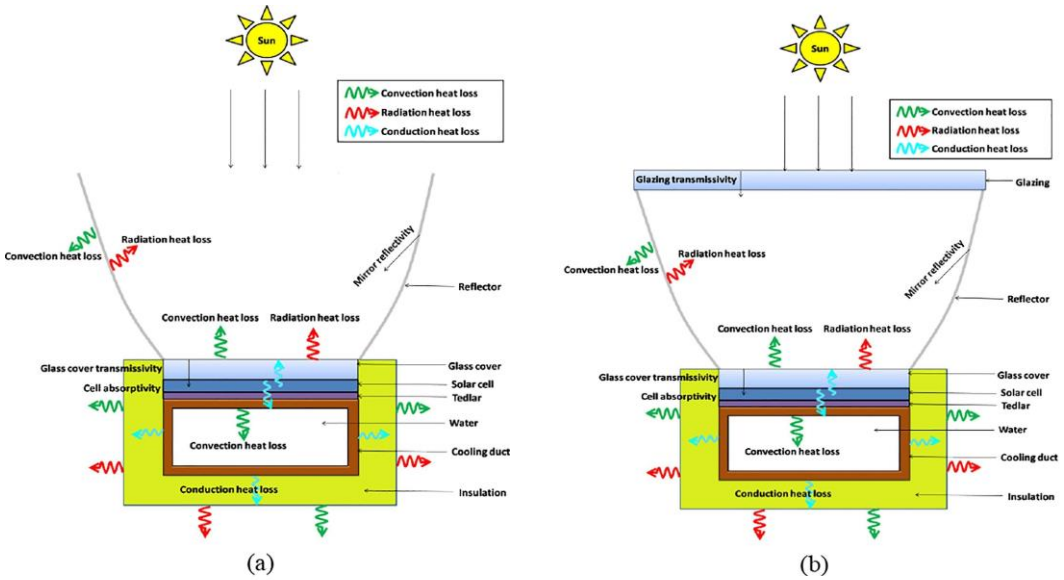

Figure 2-39: Optical and thermal losses in a CPVT system: (a) Unglazed and (b) Glazed [157].

Tian et al. designed a novel multi-functional photovoltaic/thermal/daylighting (PVT/D) system by incorporating a transpired solar collector with the dielectric CPC panel [197]. The Schematic diagram of the perspective and sectional view of PVT/D system is shown in Figure 2-40. Results show that the designed PVT/D system could largely remove the heat generated on the PV cells to achieve higher PV operation efficiency. Additionally, the design incorporating a transparent perforated plate beneath the dielectric CPC panels minimizes heat flux to the atrium, thereby reducing cooling loads. Tian et al. used Grasshopper software to design a multiple non-linear regression model for dielectric crossed CPCs, defining equivalent heights and azimuths of inclined surfaces to investigate their performance in building energy efficiency [205]. To evaluate the suitability of dielectric crossed CPC panels in different locations, they selected 14 cities in the northern hemisphere with latitudes between 13° and 67° for simulation studies. They compared the energy performance of three types of windows: standard double glazing (DB), double glazing with a dielectric crossed CPC layer (dielectric crossed CPC-DB), and double glazing with a dielectric crossed CPC layer and a Low-E coating (dielectric crossed CPC-LowE). The results indicated that dielectric crossed CPC panels are more suitable for cities with long summers or prevalent clear skies, such as Los Angeles, where total energy savings of up to 13% can be achieved.

In contrast, in places with long cold seasons, they are less suitable due to reduced solar gain and increased consumption of heating and artificial lighting, which can raise the total load by 1-5%.

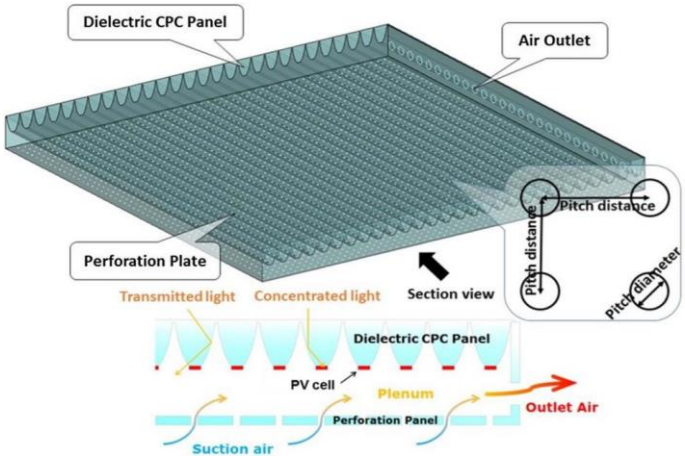

Figure 2-40: Schematic diagram of the perspective and sectional view of PVT/D system [205].

2.3.1.2 CPCs in solar thermal systems

The most common application of CPCs in solar thermal systems for industry and public buildings is to enhance the performance of systems that produce hot water, steam, and hot air to meet technical needs. CPCs are generally used in low-temperature (up to 100 °C) solar thermal technology. In recent years, studies combining CPCs with evacuated tube receivers have shown that this combination represents the optimal solution for high-performance stationary collectors, leveraging both thermal and optical methodologies [206].

By combining an M-CPC with a cylindrical absorber, Xu et al. achieved a significant improvement in the uniformity of energy distribution on the cylindrical absorber through both simulation and experimentation, compared to a standard CPC [184]. Deng et al. focused on integrating CPC with an evacuated tube collector (CPC-ETC) with building facades and proposed an embedded building-integrated solar evacuated tube collector with a CPC [207]. The schematic diagram of the system is shown in Figure 2-41. They simulated and tested the system's thermal performance by establishing a heat transfer model. The results indicated that the maximum instantaneous thermal efficiency and average thermal efficiency of the system was 55.4% and 51.4%, respectively. In a subsequent study, they verified the photo-thermal performance of the system through simulations and experiments. Using the validated numerical model, they evaluated and predicted annual heat gains for cities at different

latitudes, including Kunming, Chengdu, Xi'an, and Beijing, with final values of 825.17, 447.84, 655.77, and 441.38 MJ/m², respectively [164].

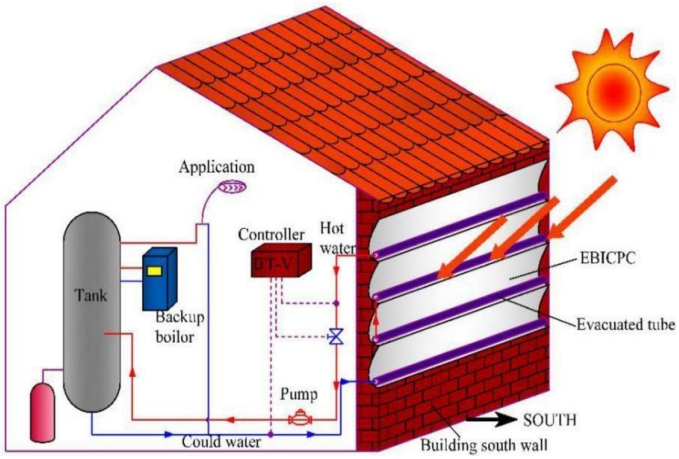

Figure 2-41: The schematic diagram of the EBIETC system [207].

Gao and Chen proposed a novel CPC with fully glass-evacuated tubes, called the IAR-CPC [182]. Experimental results showed that the IAR-CPC system collected 66.1485 MJ of annual solar radiation, an increase of 1.025 MJ compared to the S-CPC system. In the same year, Xia et al. coupled a truncated CPC with a geometric concentration ratio of 1x with a solar evacuated tube to enhance its thermal performance [208]. The schematic of the mini-CPC is shown in Figure 2-42. Compared to the evacuated tube without a CPC, the temperature increases of the mini-CPC evacuated tube was 27.3% higher, as demonstrated through simulations and experiments. The study concluded that the mini-CPC evacuated tube exhibited better performance, achieving higher temperatures and thermal efficiency under the same conditions.

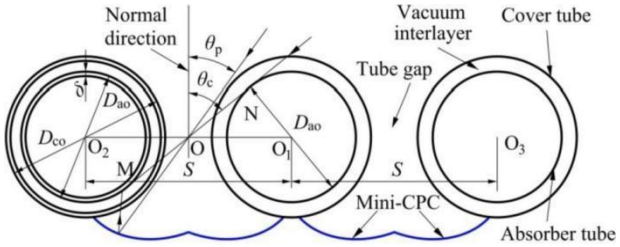

Figure 2-42: The schematic of the mini-CSC with a solar evacuated tube [208].

Chen and Yang also opted to truncate the CPC into a mini-CPC and designed an asymmetric CPC coupled with an east-west horizontally aligned evacuated tube absorber [209]. The schematic of this asymmetric CPC-coupled ETC is shown in Figure 2-43. This design was intended to achieve a seasonal dual function: acting as a concentrator in winter and as a shading device to prevent overheating in summer. By establishing a photothermal model and conducting field tests, the system was compared

with an ETC without an asymmetric CPC. The experimental results showed that the average optical efficiency of the asymmetric CPC was 39% in August and 70% in December, which are significantly different. In contrast, the optical efficiency of the ETC remained around 46% throughout. This solar system demonstrated excellent performance in winter while also reducing the risk of overheating in summer.

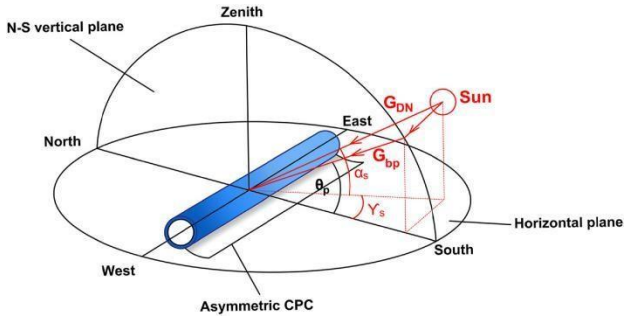

Figure 2-43: The Schematic of the ACPC-coupled evacuated tube absorber [209].

Ma et al. developed a novel CPC with ETC using a medium-temperature selective coating by co-sputtering titanium and aluminium targets [210]. A copper U-tube manifold with anti-oxidation treatment and an aluminium fin was incorporated to enhance the collector's performance. The cover glass tube was treated with an anti-reflection coating, and non-flash getters were used to maintain the vacuum in the collecting tubes. According to thermal test results, the instantaneous efficiency based on gross area reached 46% at 150 °C.

A review by Vijayakumar et al. showed that nanofluids enhance the performance of a CPC when combined with an evacuated tube and a heat pipe [211]. The review also highlighted several prospects for expanding the use of CPCs with nanofluids in other industries in the future. Based on the review, Bhalla et al. proposed a volumetrically absorbing receiver based on nanofluids, housed in a novel asymmetric CPC [212]. They developed a comprehensive single-phase theoretical model to assess its thermal performance, demonstrating that volume fraction has a significant impact. The findings revealed that silver nanoparticles reduced heat loss by 12% compared to carbon nanoparticles, and the thermal efficiency of the nanofluidic collectors with novel asymmetric CPC was 8% higher than nanofluidic collectors without CPC.

Xu et al. developed a novel 2D CPC-based capillary solar collector (CPC-CSC) with a concentration ratio of 4.22x [158]. The schematic of the CPC-CSC system is shown in Figure 2-44. The CPC

concentrates solar radiation on the capillary tubes, heating the working fluid flowing through them. From the simulation and field experiments, it was observed that heat loss from the side surface was neglected in the simulation. When the solar radiation intensity was 1000 W/m^2 and the inlet water temperature was 290 K, the measured instantaneous efficiency of the new CPC-CSC system was 66.0%. In comparison, the numerical simulation predicted an efficiency of 74.7%.

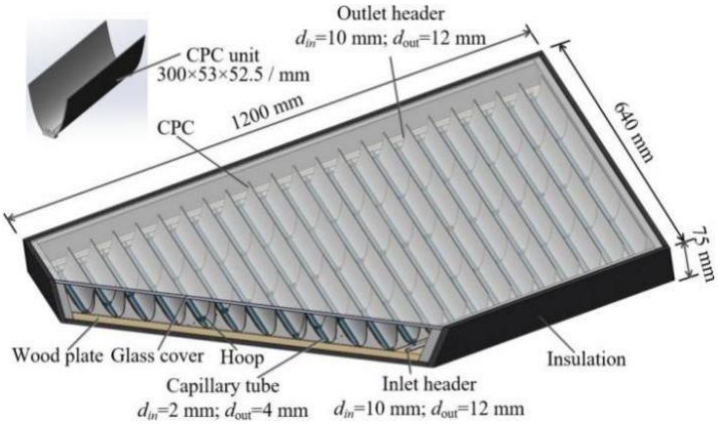

Figure 2-44: The schematic of the CPC-CSC [158].

In recent years, a comprehensive system integrating trough concentrators and linear Fresnel concentrators has been proposed and widely studied. In addition to directly reflecting sunlight onto the collector tube, CPCs can also serve as secondary concentrators in the comprehensive system, further enhancing its overall performance.

Linear Fresnel reflector concentrators (LFRC) typically consist of a single-axis primary reflector array and a fixed receiver assembly. In the comprehensive system, the primary reflector tracks the sun and directs sunlight onto the receiver assembly, which includes one or more absorber tubes and an optional secondary reflector [213].

Cheng et al. developed a novel LFRC optical optimization model using the particle swarm optimization algorithm combined with the Monte Carlo ray-tracing method, utilizing a CPC as the secondary reflector in the system to simulate the optimal optical performance of the LFRC [214]. The schematic diagram of the system is shown in Figure 2-45. Furthermore, Men et al. developed a more general optimization model to optimize the combined optical performance of the LFRC on an annual timescale [215]. In this system, the primary mirror field first reflects sunlight into the CPC, which then collects and directs the light into the receiver.

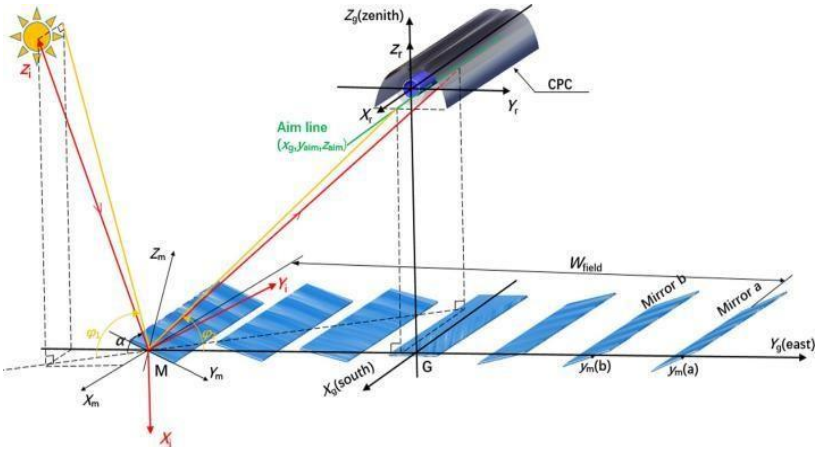

Figure 2-45: Schematic diagram of the LFRC system [214].

Ma et al. designed a LFRC system with a CPC as secondary reflector. The schematic of the LFRC system is shown in Figure 2-46 [216]. To optimize the optical efficiency of the LFRC, they developed a mathematical model of the system using geometric optics in MATLAB and employed the ray-tracing method for simulation and optimization. They then proposed a non-shading mirror field design method, using the half-acceptance angle of the CPC to limit its aspect ratio and designed a corresponding mirror field scheme. The results showed that the optimized CPC for the LFRC system, with a half-acceptance angle of 50° and a truncation ratio of 0.4, achieved a geometric optical efficiency of 84.52%.

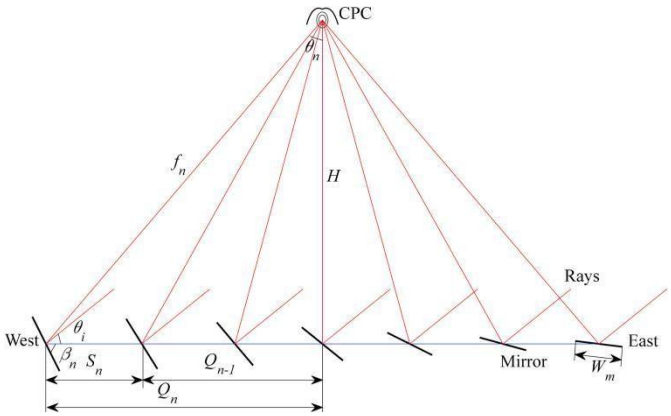

Figure 2-46: The schematic of LFRC with CPC [216].

In addition to the LFRC system, CPCs also can act as a secondary concentrator in parabolic dish concentrator systems. For instance, Lokeswaran et al. designed a novel square parabolic dish system with a CPC array serving as secondary concentrators, achieving an overall geometric concentration ratio of 500x [217]. The system consists of a square parabolic dish with an aperture area of 9 m² as the primary concentrator and a 0.27 m × 0.27 m CPC-integrated optical homogenizer array. The schematic of the square parabolic dish with the CPV receiver, along with the connected electrical and thermal load,

is shown in Figure 2-47. By analysing the optical and electrical performance parameters of the designed 2S-CPV system, the annual cumulative power output is estimated to be 2.19 MWh. Compared to the conventional 1S-CPV system, the electrical performance of the 2S-CPV system is improved by 33.54%.

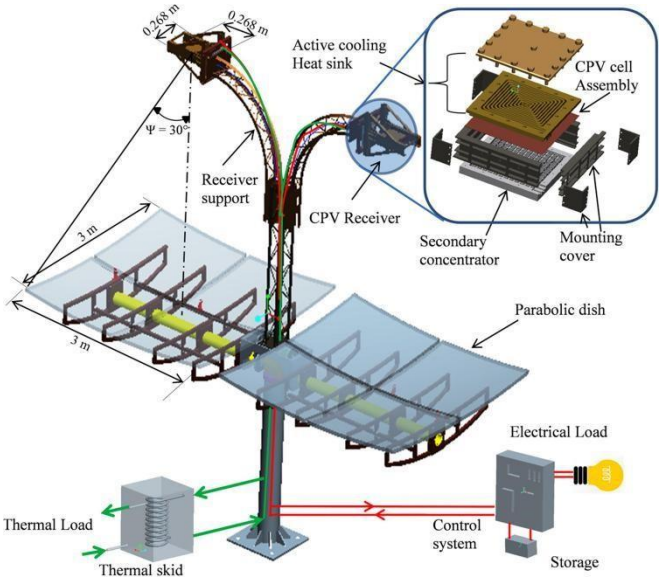

Figure 2-47: Schematic of square parabolic dish with CPV receiver, electrical and thermal load connected [217].

Chong et al. proposed a novel non-imaging dish concentrator coupled with an array of 8 rows × 8 columns CPV system, where a crossed CPC as a secondary concentrator with a large acceptance angle to accommodate higher sun-tracking accuracy tolerances was chosen for the system [218]. The schematic of the system can be seen in Figure 2-48. Optical and electrical characterization of a dense array CPV system was performed to analyse the overall performance of the prototype.

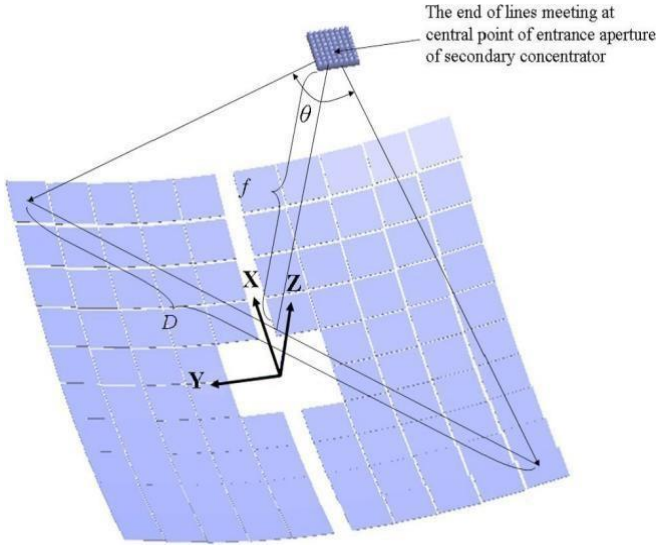

Figure 2-48: The schematic of the dense array CPV system [218].

2.3.3 Applications of the CPC in daylighting.

2.3.3.1 CPC for daylighting control in buildings

Existing literature shows that CPC is a practical choice for BICPV systems because it does not require a tracking system, uses less material, and achieves higher electric-to-heat conversion efficiency. In addition to solar energy collection, certain CPV structures, such as dielectric CPV systems, can also provide illumination for buildings. Over the past few decades, many researchers have focused on developing and promoting innovative technologies for evolving CPV windows that offer light transmittance, flexibility, lightweight design, durability, and ease of implementation [219]. These technologies include applications such as skylights [205], double-glazing windows [175], and solar louvers [220].

Xuan et al. proposed a novel CPV window (CPVW) for building applications, integrating a traditional lens-walled CPC [156]. The lens-walled CPC is coated except for the surface near the PV cells. The uncoated portion allows sunlight to pass through, providing a uniform daylighting environment indoors. They developed a ray-traced simulation model of the integrated window system and verified it with outdoor experimental results. The results demonstrated that, compared to a traditional semi-transparent PV window (PVW), the new lens-walled CPVW not only significantly improves solar energy utilization but also enhances daylighting uniformity and expands the active natural daylighting area. Sun et al. used software to simulate conventional double glazing and three other PVW models [175]. They evaluated their performance using three metrics. The study concluded that the best daylight performance was achieved with windows made of crystalline silicon solar cells combined with crossed CPC. Furthermore, Li et al. proposed a novel lens-walled CPV/D system to achieve the goals of photovoltaic and sunlight control [221]. The schematic diagrams of the novel system are shown in Figure 2-49. They built an optical model to address the optical performance and transmittance of the CPV/D system and conducted experiments to validate the optical model. The simulation results show that the maximum photovoltaic illuminance and total solar radiation of the CPV/D system exceed 8500 lm/m^2 and 700 W/m^2, respectively. CPV/D systems have proven to be compatible with different building roof designs.



Figure 2-49: The overall schematic diagram of the CPV/D system: (a) CPV/D array; (b) design sketch of the building integration; (c) inner view of the CPV/D system when integrating with building roof or replacing the skylight [221].

In addition to being integrated into windows, CPCs can also be applied to louvers. Liang et al. designed a new type of louver solar concentrator and photovoltaic module to address issues in previous BIPV systems [220]. This design reflects most incident sunlight onto the PV system to generate electricity and heat, while the remaining sunlight enters the room for supplementary lighting.

2.3.3.2 CPC for daylighting control with other technologies

Research in recent years has found that the power generated by the sunlight collected by the CPC increases the temperature of the photovoltaic cells, reduces their efficiency, and may also create the risk of overheating in the building. To address this problem, apart from investigating ways to reduce the temperature of the PV cells, use spectral splitting technology on the sidewall of the CPC to reduce the transmittance of direct light, thereby reducing the room temperature and regulating the greenhouse lighting at the same time. For instance, Feng et al. studied the effect of greenhouse transparent covering films on CPC performance and conducted simulations and field tests to evaluate the output power and transmittance of the new CPC [222]. The results showed that the transmittance of the new CPC is about 32% at noon and remains stable at 60% during other times of the day. However, without considering full-spectrum utilization, solar radiation is reflected by the film, leading to energy waste. As a result, researchers have increasingly focused on developing technology to split visible and near-infrared light for indoor lighting and energy conversion. Ulavi et al. proposed a novel "solar window" that combines CPC with wavelength-selective thin film based on the principle of spectral band splitting [223]. These films divide the incident solar spectrum into visible light, which is transmitted to provide natural lighting, and near-infrared light, which is reflected to generate heat for buildings. Additionally, Ma et

al. designed a novel greenhouse covering structure called the spectral splitting film (SSF), which was applied to the surface of the CPC [224]. The PV cells were attached to the bottom of the trough, which serves as the light outlet of the CPC. The schematic diagram of the CPC coupled with the SSF is shown in Figure 2-50. Simulations and experiments revealed that the CPC covered with the SSF achieves a visible light transmittance of over 40% throughout the day, with a maximum transmittance of 57.7%.

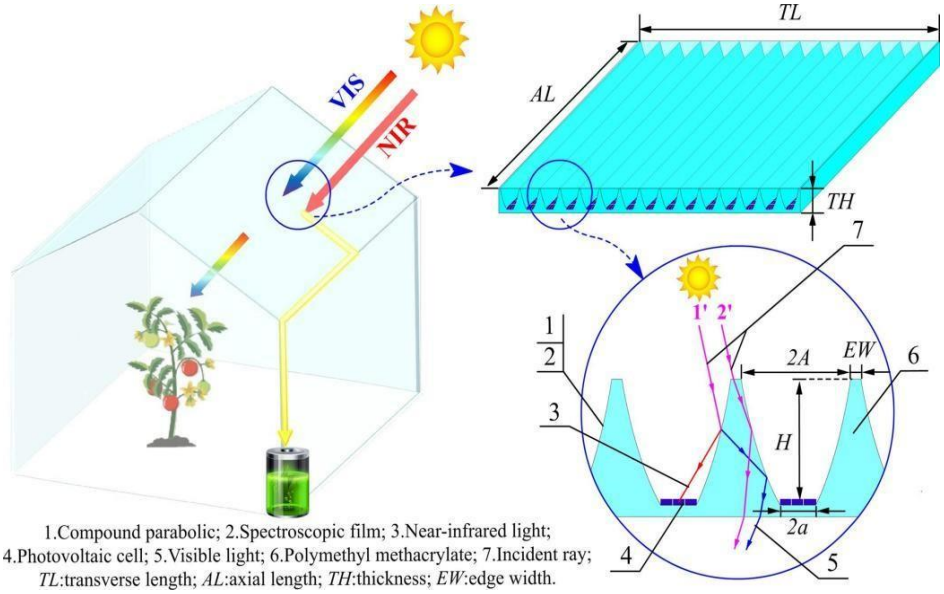

Figure 2-50: The schematic diagram of the SSF-covered CPC array in the greenhouse roof [224]

In addition, Zhang et al. designed a thin film made of metal nanoparticles that compensates for the deficiency of Low-E coatings, which reflect longwave infrared energy [225]. This thin film exhibits significant photothermal effects under near-infrared light radiation. Through a series of parametric energy simulations, the results showed that the photothermal coating can be used as a new energy-saving renovation technology for single-pane windows, achieving heating energy savings of 16.2% to 20.8%.

CPCs can also be applied to light-emitting diodes (LED), which are considered the fourth-generation light source, offering advantages such as long lifetimes, small size, and a large colour gamut. Zhao et al. designed and optimized a rectangular dielectric CPC coupled with an optical microlens array for the light collection engine of an LED micro-projection system [226]. Simulations and experiments demonstrated that the CPC connected to the optical microlens array can gather more than 90% of the light emitted by the monolithic LED array and direct it within the required angle. Similarly, Hsiang et al. invented a 20 μm height micro CPC integrated with a high-performance LED array featuring a

tailored LED structure [191]. They first customized the LED radiation pattern by controlling the interference within the LED chip and then integrated the customized LED into the microlens CPC. By carefully designing the LED device structure, they achieved the ideal LED radiation pattern. Using a hybrid-level optical simulation model, the LED display system enhances driver recognition speed, significantly improving driving safety.

2.4 Summary

This chapter examines the fundamental principles of RC technology and its applications in buildings. While numerous studies have researched the cooling performance of various RC systems, few have investigated the heat exchange between these systems and the surrounding environment under complex conditions, often leading to an overestimation of their cooling capacity. Furthermore, despite advancements in materials science that have led to the development of RC materials with near-ideal spectral properties, thereby improving cooling power, integrating RC systems into building applications continues to face several challenges. These challenges include unsuitable installation locations, insufficient cooling area to meet demand, and a mismatch between cooling times and building cooling demand. To address these issues, researchers have developed concentrated RC systems inspired by concentrated solar energy utilization. However, there is relatively little research on concentrated RC systems, particularly regarding the selection of concentrators. Therefore, it is essential to further explore concentrators compatible with RC technology, such as compound parabolic concentrator (CPC) and verify their cooling capabilities. Future research should also address the limitations of building-integrated RC systems, such as their ability to provide only a single energy source and poor seasonal adaptability. Integrating RC technology with solar energy collection systems may help meet the dynamic energy needs of buildings.

3. Innovative use of optical simulation for performance analysis of RC modules with complex configuration

3.1 Introduction

To enhance RC power density, the integrated application of RC modules with other new technologies has been extensively studied. This includes the integration of concentrators into RC modules (concentrated-RC modules), and their excellent cooling performance has been substantiated [34,142,143]. Synchronously, the theoretical methods and mathematical models characterizing the cooling power density of RC modules are also gradually being developed.

Assuming the view factor between the RC module and the sky to be 1 implies an idealized scenario where the RC module is placed horizontally with an unobstructed view of the cold sky. Under clear nighttime conditions, an average net cooling power density ranging from about 40 [227] to 120 W/m^2 [228] is typically provided by RC modules. However, real-world situations often involve the RC emitter being inclined or vertically (as is often the case when placed on a building's inclined roof or facade), and the emitter's radiative heat exchange with the sky is partially impeded by nearby warm objects like ground, trees, and neighbouring buildings, as depicted in Figure 3-1. Consequently, in traditional performance prediction models, neglecting incoming thermal radiation from the ground (P_{gro}) and aboveground surroundings (P_{sur}) generally tends to result in an overestimation of the RC cooling capacity.

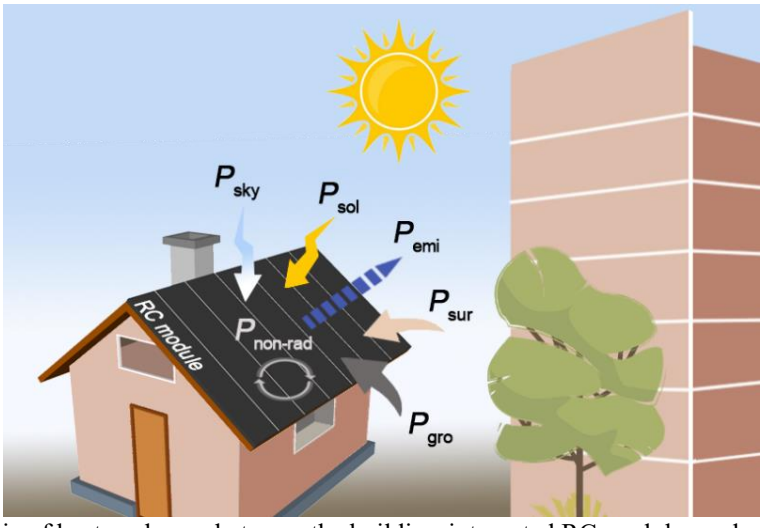

Figure 3-1: Schematic of heat exchange between the building-integrated RC modules and external environment.

Additionally, the integration of RC emitters with concentrators brings about a transformation in its heat exchange dynamics. Specifically, it interacts with only a limited portion of the sky zone instead of the entire sky dome, as illustrated in Figure 3-2. In such scenarios, conventional modelling approaches that characterize sky thermal radiation with a hemispherical-based equivalent sky emissivity become inappropriate due to the failure to account for the divergence in sky emissivity across the sky dome at different zenith angles. Therefore, developing a universal modelling approach capable of accurately evaluating the cooling performance of RC modules across various configurations and real-world environmental settings is critically necessary.

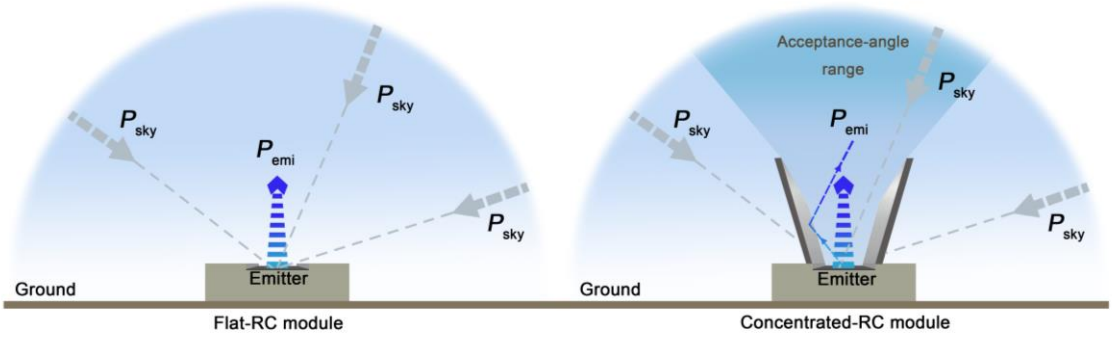

Figure 3-2: Schematic of the heat exchange between flat-RC and concentrated-RC modules with the sky.

In this chapter, an advanced modelling approach is developed, capable of rigorously assessing the radiative heat exchange between the entire external environment and the RC module, providing a more precise characterization of the cooling capabilities of the RC module. In the following sections, comprehensive illustrations are provided regarding the basic principles and mechanisms of this new approach. Subsequently, proofing is achieved that discrepancies in performance among RC modules with various structures in different scenarios (local surroundings and module's placement conditions) can be accurately captured by the proposed approach. This demonstrates the effectiveness and universality of the approach in evaluating RC modules with complicated configurations and surroundings.

3.2 Modelling approach

3.2.1 Directional radiative heat exchange between the RC module and external environment

In this section, Rhino software is employed to precisely construct models of RC modules with various structures. These models are subsequently assigned specific material properties using the Rhino

plug-in Photopia [229], an advanced ray-traced optical software widely utilized for assessing complex non-imaging optical systems [230,231]. After the module material properties are defined, the representative structure of the external environment also needs to be considered. In this simulation, a hemisphere is used to represent the entire external environment, segmented into 90 concentric rings corresponding to zenith angles ranging from 0° (zenith direction) to 90° (parallel to the horizon direction). This division allows for the observation of radiation beam distribution across different concentric rings, facilitating the distinction of radiation beams under different zenith angles. Subsequently, the radiation beams at various zenith angles are normalized by the total hemispherical radiation beam, yielding the directional radiation angular ratio. The total, hemispherical emissivity of the external environment including the sky, ground, and aboveground surroundings, can be determined by multiplying this directional radiation angular ratio with the directional, equivalent emissivity and integrating the results. Then the heat exchange between the RC module and the entire external environment can be calculated (detailed calculations refer to Section 3.2.2). The feasibility of the approach is based on the thermal radiation process following the principle of reciprocity, as shown in Figure 3-3. Reciprocity dictates that wherever a radiation beam emitted by the surrounding environment reaches the emitter (depicted as the orange line in Figure 3-3), there will necessarily be a radiation beam emitted by the emitter following the same path outward (illustrated as the blue line in Figure 3-3).

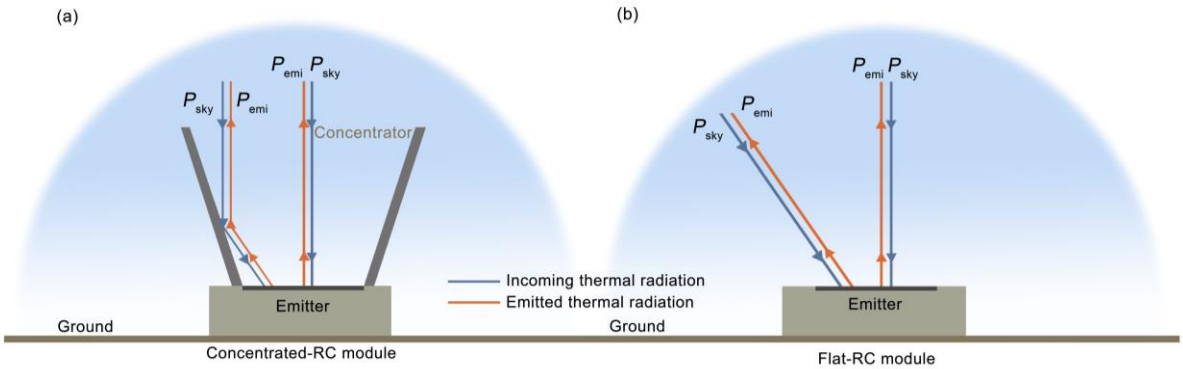

Figure 3-3: Schematic of the reciprocity principle in (a) concentrated- and (b) non-concentrated-RC systems. In the figure, the blue and orange lines, which overlap in reality, are depicted as two parallel lines to facilitate clearer representation.

In the model settings, all concentrated-RC modules utilized the ideal specular aluminium as the concentrator material, and a total of 500,000 radiation beams are hemi-spherically and evenly emitted by the emitter and ultimately exhibit non-uniform distribution on the 90 concentric rings. The sensitivity

of the novel modelling approach to the number of radiation beams has been evaluated. The results demonstrate that when the external environment emissivity for the flat RC module is evaluated using 100,000, 500,000, and 1,000,000 radiation beams, the differences among the module are minimal, with values of 0.663, 0.665, and 0.668, respectively. In Figure 3-4, the schematic of the radiative beams emitted by the two-dimensional (2D) inverted trapezoidal-RC and flat-RC modules and the radiative heat exchange with the external environment is presented. Figure 3-4 (a) indicates the flat-RC module emits radiation beams uniformly across all directions, resulting in a more even distribution across each zenith angle (θ), as depicted by the red line in Figure 3-9. Conversely, from Figure 3-4 (b), due to the concentrator effect, the majority of radiation beams (δ) emitted by the 2D inverted trapezoidal-RC are directed toward concentric rings near the zenith direction, leading to a higher corresponding directional radiation angular ratio (as shown in the light blue line in Figure 3-9). However, regardless of the structural variation of the RC module, it is observed that the presence of nearby obstacles in specific directions obstructs the radiation beams emitted by the emitter from entering the sky. Consequently, the radiation beams received by the external environment at different azimuth angles (φ) also need to be considered.

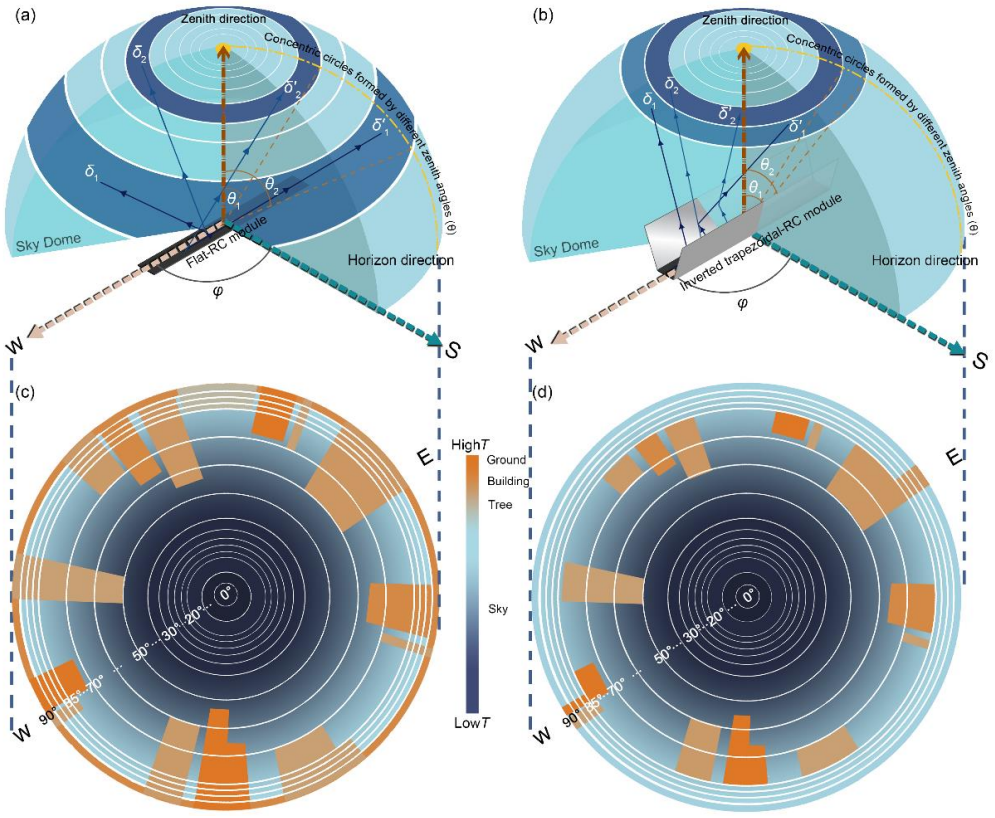

Figure 3-4: (a) & (b) Effect of the absence or presence of a concentrator on the directional radiation beam emitted by the RC emitter. (c) & (d) Radiative heat transfer of the flat-RC and inverted trapezoidal-RC modules in different azimuth and zenith angle directions when obstacles are present.

It is noteworthy that accounting for azimuth angle alters the area of these concentric rings. Consequently, even within a flat-RC module, the directional radiation angular ratio in each concentric ring is not uniform. As shown in Figure 3-4 (c), the flat-RC module, lacking a shielding device in the presence of aboveground surrounding obstacles, undergoes heat exchange with these obstacles. However, in the 2D inverted trapezoidal-RC module, most thermal radiations from obstacles with low zenith angles can be blocked by the concentrator, except for the side openings. Nonetheless, heat exchange between the RC emitter and obstacles may still occur when a portion of the obstacle's thermal radiations falls within the acceptance angle range of the concentrator, as those orange-tinted sections illustrated in Figure 3-4 (d).

3.2.2 Mathematical framework

Different from traditional models, this chapter carefully takes into account the radiative heat exchange between the RC emitter and the whole external environment. In this case, different from Eq 2.1, the P_{cool} is expressed as:

$$P_{cool} = P_{emi} - \overbrace{P_{sky} - P_{gro} - P_{sur}}^{P_{env}} - P_{sol} - P_{non\text{-}rad} \tag{3.1}$$

The absorbed external environmental radiation (P_{env}), a new parameter defined in this chapter, encompasses sky thermal radiation (P_{sky}) and thermal radiation emitted by local surroundings (P_{gro} and P_{sur}), with a wavelength primarily falling in the range of 2.5 to 50 μm [12]. In contrast, solar radiation (P_{sol}) is concentrated mainly in the short wavelength region (0.3-2.5 μm). Notably, in this chapter, the RC emitter temperature is set equal to the ambient temperature to characterize the net radiative cooling power density. Under this condition, the non-radiative heat transfer ($P_{non\text{-}rad}$) between the RC emitter and its surroundings eliminates the need for a wind cover atop the emitter.

Except for P_{env}, all other parameters have been thoroughly explained in the Section 2.2.1. Therefore, only the equation representing P_{env} is discussed in this part.

The external environmental radiation power absorbed by the RC emitter can be expressed as:

$$P_{\text{env}} = \int_0^{\infty} \int_0^{2\pi} \int_0^{\pi/2} \varepsilon_{\text{env}}(\theta, \varphi, \lambda) I_{\text{b}}(\lambda, T_{\text{amb}}) \alpha_{\text{emi}}(\theta, \varphi, \lambda) \cos\theta \sin\theta d\theta d\varphi d\lambda \tag{3.2}$$

where $\varepsilon_{\text{env}}(\theta, \varphi, \lambda)$ is the spectral, directional emissivity of the external environment. A thorough assessment of thermal radiation from the external environment necessitates consideration not only of sky radiation but also radiation from the ground and aboveground surroundings. Consequently, the subscription "env" in Eq.3.2 is assigned as either "sky", "gro", or "sur", depending on whether the RC emitter is radiatively exchanging heat with the sky, ground, or aboveground surroundings at any specific directions (θ, φ). It is important to note that, similar to the equivalent sky emissivity, the terms $\varepsilon_{\text{gro}}(\theta, \varphi, \lambda)$ and $\varepsilon_{\text{sur}}(\theta, \varphi, \lambda)$ in Eqs.3.3 and 3.4 do not represent the real emissivity but instead denote the equivalent emissivity of the ground and aboveground surroundings at ambient temperature T_{amb}. The relationship between the real and equivalent emissivity is written as:

$$\varepsilon_{\text{gro}}(\theta, \varphi, \lambda) = \frac{\varepsilon'_{\text{gro}}(\theta, \varphi, \lambda) T^4_{\text{gro}}(\theta, \varphi)}{T^4_{\text{amb}}} \tag{3.3}$$

$$\varepsilon_{\text{sur}}(\theta, \varphi, \lambda) = \frac{\varepsilon'_{\text{sur}}(\theta, \varphi, \lambda) T^4_{\text{sur}}(\theta, \varphi)}{T^4_{\text{amb}}} \tag{3.4}$$

where $\varepsilon'_{\text{gro}}(\theta, \varphi, \lambda)$ and $\varepsilon'_{\text{sur}}(\theta, \varphi, \lambda)$ are the real spectral emissivity of the ground and aboveground surroundings at the direction (θ, φ) relative to the RC emitter; and $T_{\text{gro}}(\theta, \varphi)$ and $T_{\text{sur}}(\theta, \varphi)$ denote the temperature of the ground and aboveground surroundings at the direction (θ, φ) relative to the RC emitter, K.

Further referring to the approach adopted in Eq.2.7, Eq.3.2 can be formulated as:

$$P_{\text{env}} = \alpha_{\text{emi}} \varepsilon_{\text{env}} \sigma T^4_{\text{amb}} \tag{3.5}$$

where ε_{env} is the total, hemispherical emissivity of the external environment. Recalling the concentric rings illustrated in Figure 3-4 and dividing the entire external environment into specific concentric ring zones (wherein each ring shares the same zenith angle θ), ε_{env} can then be expressed as:

$$\varepsilon_{\text{env}} = \int_0^{\pi/2} \left[\varepsilon_{\text{sky}}(\theta) \beta_{\text{sky}}(\theta) + \varepsilon_{\text{gro}}(\theta) \beta_{\text{gro}}(\theta) + \varepsilon_{\text{sur}}(\theta) \beta_{\text{sur}}(\theta) \right] d\theta \tag{3.6}$$

where $\varepsilon_{\text{sky}}(\theta)$, $\varepsilon_{\text{gro}}(\theta)$, and $\varepsilon_{\text{sur}}(\theta)$ are respectively the equivalent emissivity of the sky, ground, and aboveground surroundings in the concentric ring with a zenith angle of θ; and $\beta_{\text{sky}}(\theta)$, $\beta_{\text{gro}}(\theta)$ and $\beta_{\text{sur}}(\theta)$

denote the respective ratios of the radiation beam from the RC emitter reaching the sky, ground, and aboveground surroundings in the corresponding concentric ring to the total hemispherical radiation beam from the RC emitter. Obviously, $\beta_{gro}(\theta)$ and $\beta_{sur}(\theta)$ typically exhibit gradual decreases as the zenith angle decreases and are likely to approach zero at certain small zenith angles (as those blue concentric rings depicted in Figure 3-4 (c and d).

Determining the $\varepsilon_{gro}(\theta)$ and $\varepsilon_{sur}(\theta)$ is straightforward, as they are directly related to the specific surface spectral characteristics of the ground and aboveground surroundings. However, the determination of $\varepsilon_{sky}(\theta)$ is more intricate due to the complex atmospheric spectral properties against wavelengths and zenith angles. $\varepsilon_{sky}(\theta)$ can be expressed as:

$$\varepsilon_{sky}(\theta) = \frac{\int_0^\infty \varepsilon_{sky}(\theta,\lambda) E_{\lambda,b}(\lambda, T_{amb}) d\lambda}{\int_0^\infty E_{\lambda,b}(\lambda, T_{amb}) d\lambda} \tag{3.7}$$

where $E_{\lambda,b}(\lambda, T_{amb})$ is the spectral emissive power of a blackbody at the ambient temperature T_{amb}, $W \cdot m^{-2} \cdot \mu m^{-1}$. The spectral, directional sky emissivity $\varepsilon_{sky}(\theta, \lambda)$ can be calculated by [50]:

$$\varepsilon_{sky}(\theta,\lambda) = 1 - \left[1 - \varepsilon_{sky}(0,\lambda)\right]^{1/\cos\theta} \tag{3.8}$$

where $\varepsilon_{sky}(0, \lambda)$ is the spectral, directional sky emissivity of zenith direction and can be obtained from MODTRAN [52].

Figure 3-5 illustrates the variation of spectral, directional sky emissivity of five different zenith angles under the total water vapor column (TWC) of 1000 atm-cm. It is evident that when compared to that in other zenith angles, the spectral, directional sky emissivity in the zenith direction consistently demonstrates the lowest values, particularly within the "atmospheric window" region, estimated at approximately 0.1. Consequently, the zenith direction features the highest spectral, directional transmittance of the sky, $\tau_{sky}(0, \lambda)$, facilitating the penetration of the emitter's thermal radiation through the atmosphere to outer space. Conversely, as the zenith angle increases, the sky emissivity also increases, leading to a decrease in sky transmittance, thereby affecting the emitter's thermal radiation reaching outer space.

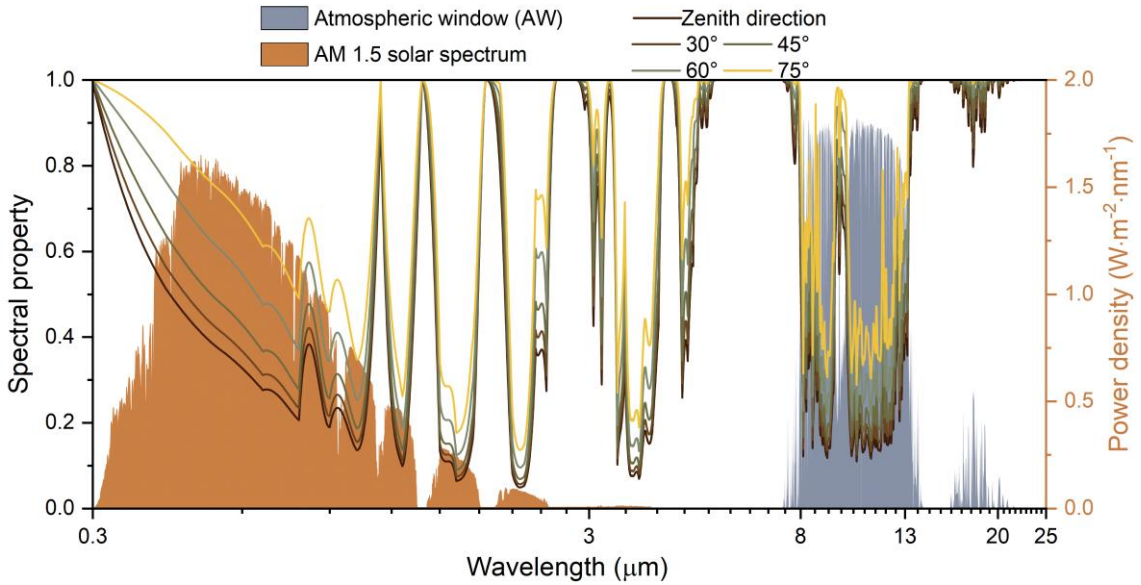

Figure 3-5: Spectral sky emissivity at different zenith angles. The zenith direction exhibits the lowest emissivity among different zenith angles, equivalent to the highest sky transmittance, which is more conducive to radiative cooling.

The primary objective of this work is to determine a modelling approach capable of accurately capturing the variations in cooling performance among different RC modules under various local surrounding conditions. Therefore, only the nocturnal cooling power densities have been calculated, i.e., solar radiation is absent (0 W/m^2). Future research will involve investigating the impact of the concentrator on the cooling performance of the concentrated-RC module, specifically examining its role in either shielding or concentrating sunlight on to the RC emitter during different daytime scenarios.

3.2.3 Model validation

To validate the accuracy and reasonableness of the proposed modelling approach, a comparison between the simulated results and experimental data reported by Zhao et al. [11] is conducted. This verification process involved calculating the equivalent sky emissivity and net RC power density under the experimental conditions and environmental factors detailed in Ref. [11]. To quantify the disparity between the simulated and experimental data, the root mean square deviation (*RMSD*) as a metric is employed [232]. The *RMSD* calculation formula is provided as:

$$RMSD = \sqrt{\frac{\sum\left[x_{\text{sim}} - x_{\text{exp}}) / x_{\text{exp}} \right]^2}{n}} \tag{3.9}$$

where x_{sim} represents the simulation result, x_{exp} represents the corresponding experimental value, and n is the total number of data groups under consideration.

The net RC power density, as both predicted and experimentally determined, is presented in Figure 3-6. The red points and yellow line depict the corresponding experimental and modelling results from Ref. [11], and the green points signify the data computed using the approach proposed in this chapter. It is evident that the values of the red points and green points are very close, with an *RMSD* of only 1.94%, which is smaller than the 2.96% *RMSD* for the coupling of red points and yellow lines. This shows good agreement between the results generated by the approach proposed in this chapter and the experimental outcomes of Ref. [11]. Consequently, the simulation method and mathematical model are demonstrated to be highly effective for calculating the ε_{sky} and for evaluating the net P_{cool} for various RC modules.

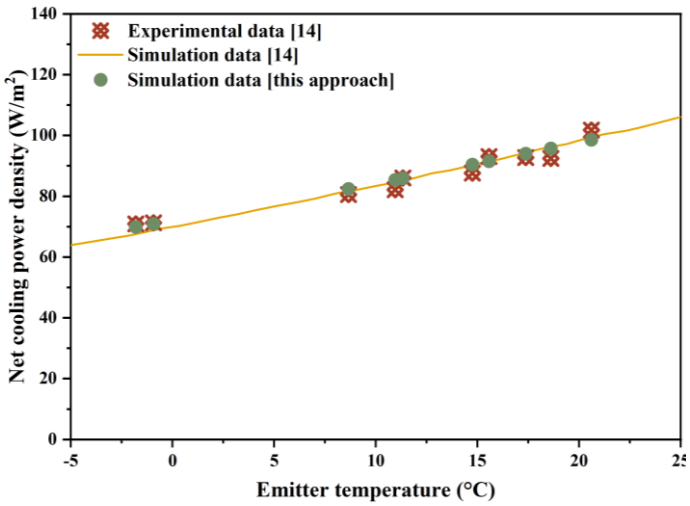

Figure 3-6: Simulated and experimental net cooling power densities of an RC module. The data computed using the proposed approach (green points) is very close to the experimental data (red points), with the *RMSD* being 34.45% lower than that in Ref. [11].

3.3 Nighttime maximum net cooling performance analysis of RC modules

3.3.1 Description of different configurations of RC modules

The universality and accuracy of this approach are attained by computing the net cooling power densities of RC modules placed on concrete ground under various module structures (with/without concentrators, different emitter deployment strategies), diverse external environments (including scenarios with and without obstacles). Key parameter settings for the case studies are detailed in Table 3-1.

Table 3-1: Key parameter settings for case study.

Parameters	Descriptions	Values
T_{amb}	Ambient temperature (°C)	30
T_{emi}	Emitter temperature (°C)	30
T_{gro}	Ground temperature (°C)	27
T_{sur}	Aboveground surrounding temperature (°C)	27
α_{emi} (ε_{emi})	Emitter's weighted averaged absorptivity (emissivity) in the infrared region	0.95
ρ_{con}	Concentrator's reflectivity	1
ε'_{gro}	Ground emissivity	0.85
ε_{gro}	Equivalent ground emissivity	0.82
ε'_{sur}	Aboveground surrounding emissivity	0.85
ε_{sur}	Equivalent Aboveground surrounding emissivity	0.82
TWC	Total water vapor column (atm-cm)	1000
W	Bottom width of the RC modules (mm)	20
H	Height of the concentrated-RC modules (mm)	40
L	Length of the flat and 2D trapezoidal-RC modules (mm)	200
α	Vertical tilt angle of the concentrator (°)	20

Firstly, the cooling performance of RC modules with various structures is evaluated in Section 3.3.2 to verify the universality of the modelling approach. The involved RC modules, including traditional flat-RC module, common 2D inverted trapezoidal-RC module, and two 3D structured RC modules (crossed inverted trapezoidal-RC and inverted cone-RC modules), are illustrated in Figure 3-7. To avoid interferences caused by local surroundings' different level of radiative heat exchange with different RC module structures, the modules are placed horizontally with a sky view factor of 1 in this case.

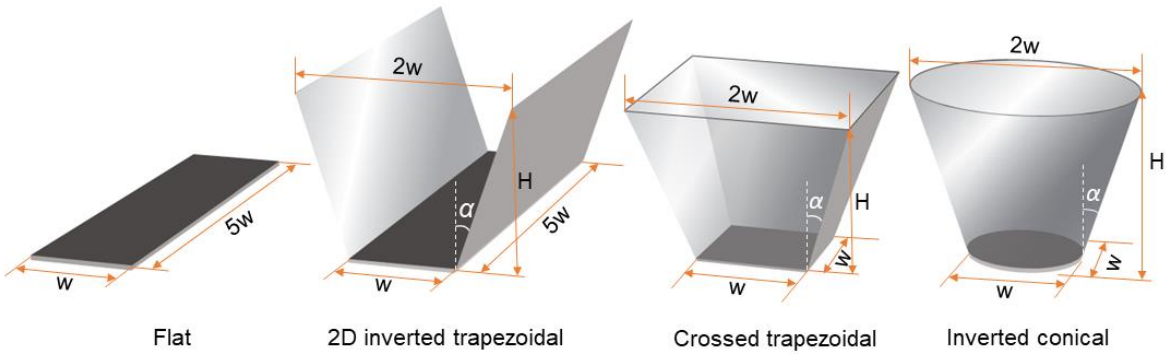

Figure 3-7: Schematic of a flat-RC module and three concentrated-RC modules with different concentrators.

Secondly, the effectiveness of this approach in capturing performance differences in more complex RC module configurations deserves further exploration. Section 3.3.3 is dedicated to evaluating the cooling capability of a 2D inverted trapezoidal-RC module with different emitter deployment strategies in an aboveground obstacle-free environment. Figure 3-8 shows a schematic diagram of the researched RC modules. The RC emitters selected for analysis include a horizontally placed flat emitter, a vertically placed flat emitter whose height is equal to the module's width and can emit radiation from both sides

(referred to as the emitter placed vertically) and three inverted V-shaped emitters inclined at varying angles of 30°, 45°, and 60° to the horizontal plane. Furthermore, the figure displays that the change in the shape of the emitter leads to a corresponding variation in the cooling area.

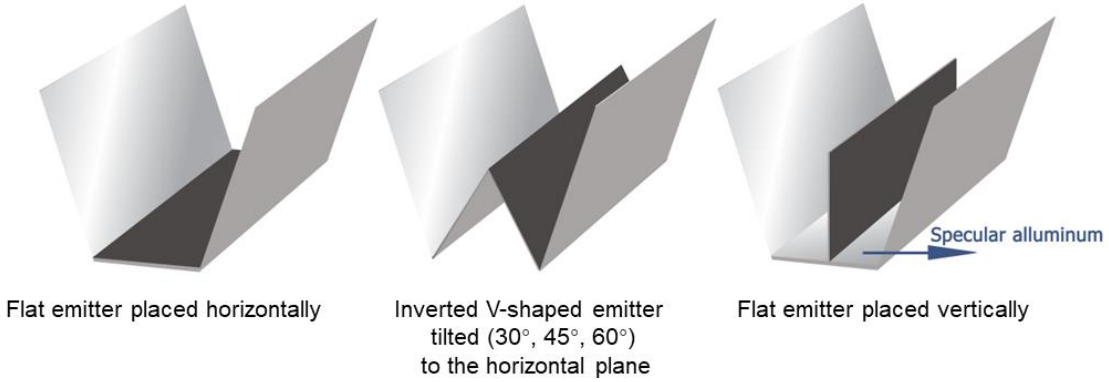

Figure 3-8:Schematic of 2D inverted trapezoidal-RC modules with different emitter deployment strategies.

Finally, the previous two case studies are based on a situation where the view factor between the RC module and the sky is 1. However, in practical applications, RC modules are often installed with an inclination angle or surrounded by aboveground objects, which results in a limited sky view factor below 1. Therefore, evaluating the cooling performance in more common real-world scenarios where surrounding obstacles are present is necessary. The primary aim of section 3.3.4 is to evaluate the effectiveness of the method in quantifying the thermal radiation power absorbed by the RC module from both the sky and near-ground environment.

3.3.2 Effect of modules structures

The curves depicting the directional radiation angular ratios of the four modules under different zenith angles are displayed in Figure 3-9. Notably, these curves exhibit skewed distributions across the four modules. Similarities exist in the variation trends between the flat-RC and 2D inverted trapezoidal-RC modules. Their trend demonstrates a gradual increase until a specific zenith angle (51° for the flat-RC module and 29° for the trapezoidal-RC module), followed by a gradual decrease, with peak directional radiation angular ratios of 1.78% and 2.32%, respectively. Conversely, the directional radiation angular ratio curves of the remaining two 3D structured RC modules exhibit a rapid ascent followed by a sharp decline, reaching zero around the zenith angle of 50°. This observation suggests that the 3D structured RC module can concentrate the radiation beam more effectively at smaller zenith

angles, thereby potentially receiving a lower incoming environmental radiation power and achieving a higher net RC power.

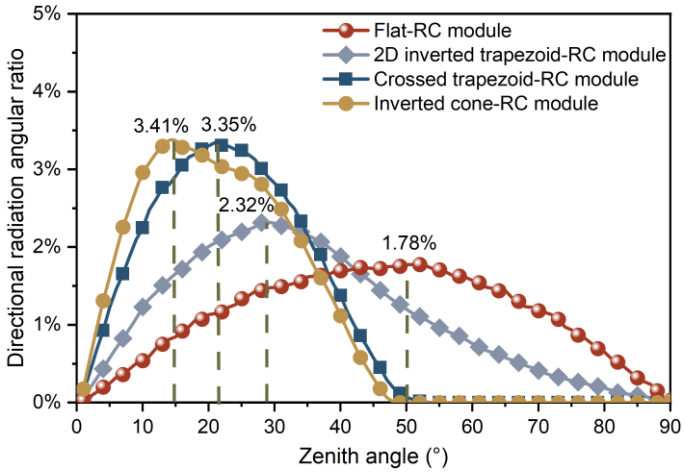

Figure 3-9:Directional radiation angular ratio curves of the flat-RC module and three concentrated-RC modules with different concentrating structures.

The ε_{env} for the four RC modules is listed in Table 3-2. The ε_{env} for the inverted cone-RC module is the lowest among the four modules, with a value being 0.661. This is attributed to the concentration of most of the thermal radiation near the zenith direction by the cone. Closely following the inverted cone-RC module is the crossed trapezoidal-RC module, with an ε_{env} of 0.662. In contrast, the 2D inverted trapezoidal-RC module and flat-RC module, one features a 2D concentrator allowing a part of thermal radiation from nearby warm obstacles to reach the emitter through its side openings, while the other lacks a concentrator and consequently radiatively exchanges heat with the external environment in all directions, show higher ε_{env} of 0.686 and 0.716, respectively.

Table 3-2: Total, hemispherical emissivity of the external environment for four RC modules.

Module structures	Flat-RC	2D inverted trapezoidal-RC	Crossed trapezoidal-RC	Inverted cone-RC
ε_{env}	0.716	0.686	0.662	0.661

The P_{env} for the four RC modules is calculated based on ε_{env}. As demonstrated in Figure 3-10, the 3D structured RC modules exhibit lower ε_{env} compared to the 2D concentrated-RC module, leading to a small P_{env}. Specifically, the crossed trapezoidal-RC module absorbs 300.69 W/m^2, and the inverted cone-RC module absorbs only 299.89 W/m^2. In contrast, the P_{env} for the 2D concentrated-RC module is 311.43 W/m^2, which is lower than the 325.21 W/m^2 observed for the flat-RC module.

Figure 3-10 also indicates the P_{cool} for the four RC modules. It can be observed that the highest P_{cool} is achieved by the inverted cone-RC module, reaching 154.13 W/m^2, followed by the crossed

trapezoidal-RC module at 153.33 W/m^2. The P_{cool} obtained by the 2D inverted trapezoidal-RC module is 11.54 W/m^2 lower than the 3D structured RC module, while the P_{cool} for the flat-RC module is 13.78 W/m^2 lower than that of the 2D inverted trapezoidal-RC module. These results demonstrate the superior cooling capacity exhibited by RC modules with concentrators compared to the flat-RC module. Additionally, the result differences prove the effectiveness of this modelling approach in terms of evaluating the cooling capacity of RC modules with different structures.

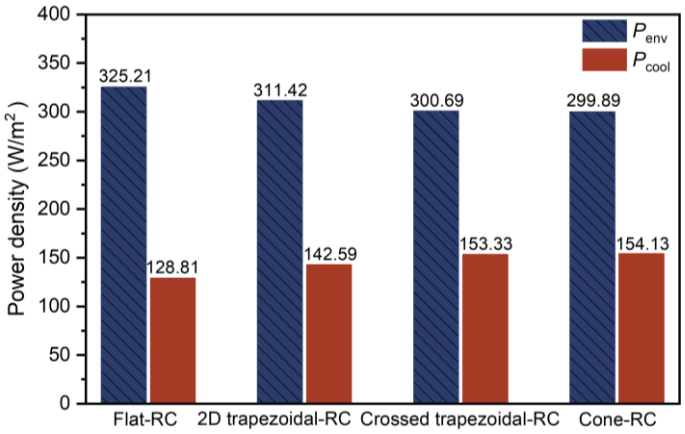

Figure 3-10: Absorbed external environmental thermal radiation and net cooling power density of four RC modules.

3.3.3 Effect of different emitter deployment strategies

Figure 3-11 exhibits the different RC modules' directional radiation ratio curves at different zenith angles. These curves reveal a decreased radiation angular ratio at the same zenith angle with the increasing inclination angles of the inverted V-shaped emitters. Additionally, the maximum radiation angular ratio of the RC module decreases from 2.15% of the horizontally placed emitter to 1.55% of the V-shaped emitter inclined 60° to the horizontal plane. This occurs because a portion of the thermal radiation from the inverted V-shaped emitter reaches the ground instead of the sky, and another part is trapped within the RC module due to the concentrator's optical and geometrical characteristics. However, it can be observed that the directional radiation angular ratio curve is slightly different when the emitter is placed vertically. This variation arises from the material at the base of this module being configured as specular aluminium allowing thermal radiation from the emitter to be reflected towards the sky when it reaches the bottom of the module.

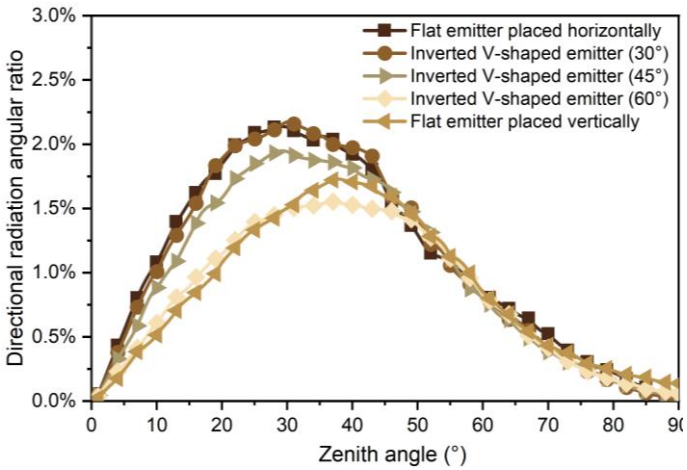

Figure 3-11: Ratio of directional radiation beam reaching different zenith angles to total hemispheric radiation beam from the RC emitter.

Figure 3-12 (a) and (b) illustrate the radiative heat exchange between a flat and an inverted V-shaped emitters with the external environment based on the same 2D inverted trapezoidal concentrator. In Figure 3-12 (a), it can be observed that when the flat emitter is placed horizontally, the shielding and concentrating functions of the concentrator limit the thermal radiation emitted and absorbed by the emitter to a small range. In contrast, with the RC module employing an inverted V-shaped emitter inclined at an angle θ from the horizontal plane, the emitter captures not only the sky thermal radiation but also ground thermal radiation entering through the side openings.

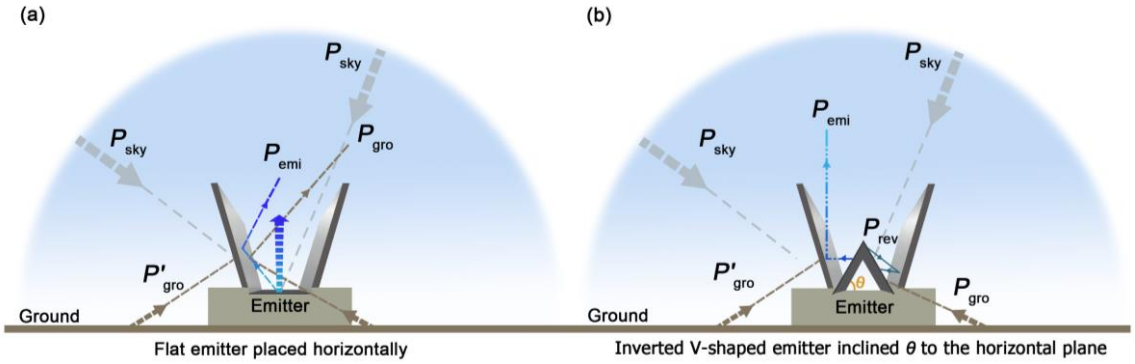

Figure 3-12: Radiative heat transfer of 2D inverted trapezoidal-RC modules with (a) flat emitter and (b) inverted V-shaped emitter.

Additionally, due to the reflective properties of the concentrator, a portion of the thermal radiation emitted by the emitter is reversed back to the emitter. These thermal radiations, which are unable to escape the module, can be characterized as P_{rev}:

$$P_{rev} = \varepsilon_{emi} \sigma T_{emi}^4 \beta_{rev} \tag{3.10}$$

where β_{rev} is the ratio of radiation beams emitted by the emitter and reversed to the emitter by the concentrator to the emitter's total hemispherical radiation beam.

In Table 3-3, the ε_{env} and β_{rev} for the five 2D inverted trapezoidal-RC modules and the effective emitting areas of the RC emitters are presented. In general, ε_{env} decreases as the tilt angle of the inverted V-shaped emitter increases (except for the flat emitter placed vertically). Specifically, ε_{env} drops from 0.686 for horizontally placed emitter to 0.536 for inverted V-shaped emitter (60°). Simultaneously, a gradual increase is observed in the β_{rev}, from 0 for the horizontally placed emitter to 22.62% for the inverted V-shaped emitter (60°), which means only 77.38% of the radiation beams are directed towards the external environment, further explaining the reason for the reduction in ε_{env}.

Table 3-3: Key parameters of the 2D inverted trapezoidal-RC modules with five different emitters.

	Emitter placed horizontally	Inverted V-shaped emitter (30°)	Inverted V-shaped emitter (45°)	Inverted V-shaped emitter (60°)	Emitter placed vertically
ε_{env}	0.686	0.674	0.624	0.536	0.568
β_{rev}	0	1.49%	9.11%	22.62%	18.63%
Emitting area (m^2)	0.30	0.35	0.42	0.60	0.60

Figure 3-13 (a) illustrates the P_{rev} for five RC modules with different emitter deployment strategies. The results reveal that the RC module with a horizontally placed flat emitter remains unaffected by the P_{rev} and only engages in radiative heat exchange with the sky. As the RC emitter's shape is altered, an increase in thermal radiation reversed back to the emitter by the concentrator is observed. For instance, P_{rev} reaches 41.36 W/m^2 with the inverted V-shaped emitter (45°) and escalates to 102.68 W/m^2 with the inverted V-shaped emitter (60°), indicating that over a quarter of the emitted thermal radiation becomes trapped within the module, significantly impacting cooling performance. In contrast, a vertically placed emitter with specular aluminium as the bottom material shows a reduction in P_{rev} by 18.09 W/m^2 compared to the inverted V-shaped emitter (60°). Despite this reduction, 18.63% of the thermal radiation still cannot escape from the RC module.

Figure 3-13 (b) displays the P_{env} and P_{cool} for the five RC modules. The results reveal that with the inverted V-shaped emitter inclined at angles below 30°, P_{cool} remains consistently above 140 W/m^2, while P_{env} shows a decrease of 5 W/m^2, with only minor fluctuations. However, once the inclination exceeds 30°, both P_{env} and P_{cool} exhibit a noticeable decline, attributed to the increasing P_{rev}. For instance,

P_{env} decreases from 311.43 W/m^2 for a horizontally placed emitter to 240.32 W/m^2 for the inverted V-shaped emitter (60°), P_{cool} also decreases from 142.59 W/m^2 to 108.08 W/m^2, showing a 24.20% reduction in cooling performance. Therefore, maintaining the inclination of the inverted V-shaped emitter within 30° is recommended for optimizing the net cooling power density of the RC module. However, as Table 3-3 suggests, an increased inclination angle of the emitter relative to the horizontal plane leads to an expansion of the module's emitter area. Consequently, focusing exclusively on net cooling power density provides a limited view, necessitating a more comprehensive assessment of the module's cooling capabilities.

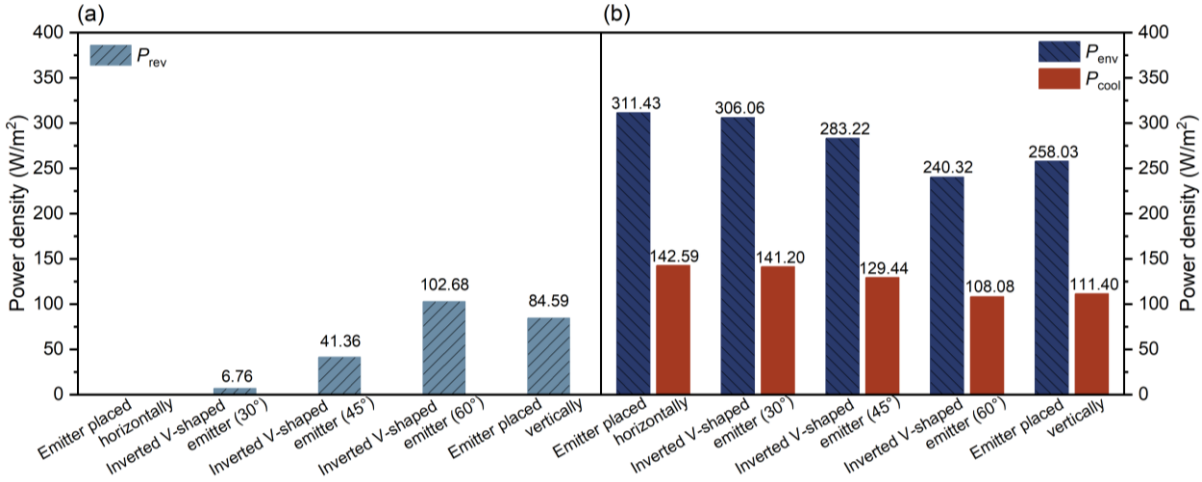

Figure 3-13: (a) Thermal radiation power that cannot escape from the 2D inverted trapezoidal-RC modules with different emitter deployment strategies. (b) External environmental thermal radiation and net cooling power density for five RC modules.

To this end, in addition to the cooling power density (P_{cool}) presented in Figure 3-13, Figure 3-14 displays the cooling power (P'_{cool}) for selected RC modules and a special RC module with an emitter of maximum permissible area. This special module features an inverted V-shaped emitter inclined at 70.35° to the horizontal plane, matching the height of the inverted trapezoidal concentrator. The results demonstrate an increase in P'_{cool} with the inclination angle of the inverted V-shaped emitter. Notably, at the maximum allowable tilt angle, P'_{cool} reaches 79.23 W, nearly double that achieved by the horizontally placed flat emitter (42.78 W). Furthermore, considering the footprint of the concentrated-RC module is determined by its aperture area, a comparative analysis is needed between the concentrated-RC modules with an inverted V-shaped emitter inclined maximum tilt angle and configurations where the entire aperture area acts as an emitter (flat-RC emitter). The result shows that when the aperture area is 0.60 m^2, P'_{cool} achieved at the module's maximum tilt angle still surpasses that

of the latter configuration by 5.71%. This highlights the efficiency of the V-shaped emitter in enhancing P'_{cool} when optimally tilted. Moreover, the results indicate that in practical scenarios where installation space for the RC module is constrained, such as when integrated with the building envelopes, using the V-shaped emitter can effectively enlarge the cooling area of the module, thereby achieving better cooling performance.

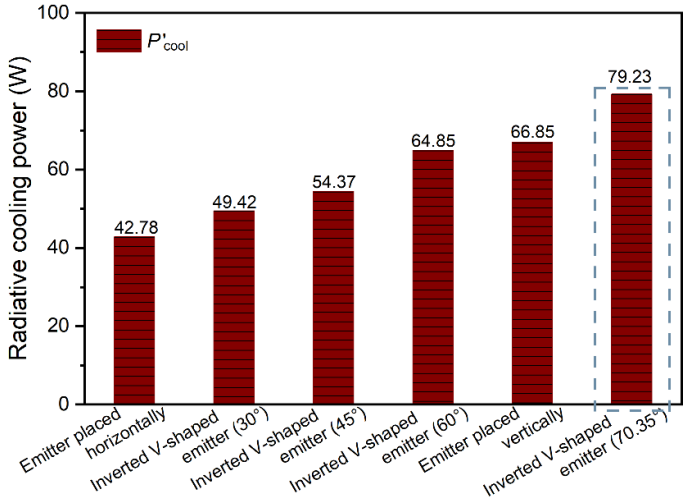

Figure 3-14: Cooling power of six 2D inverted trapezoidal-RC modules with different emitter deployment strategies. At the maximum allowable tilt angle, it is shown in the blue square that the cooling power of the module can reach 79.23 W.

The analysis in this case study reveals that the modelling approach can accurately capture the emitted thermal radiation power that cannot escape from the concentrated-RC modules with different emitter deployment strategies and characterizes their net cooling power density and cooling power in the effective cooling area.

3.3.4 Effect of diverse external environments

The radiative heat exchange between the flat-RC module and the external environment is depicted in Figure 3-15. In the case of the flat-RC module, the emitter's thermal radiation is uniformly emitted in all directions. Consequently, when nearby aboveground obstacles surround the module, a portion of the thermal radiation is blocked by these obstacles, impacting the emitter's RC performance. The yellow part in Figure 3-15 represents the area where radiation heat exchange occurs between the local surroundings and the RC module. Varying the proportion of these areas covering the entire sky dome directly affects the thermal radiation absorbed by the flat-RC module from the entire external environment. To quantitatively assess this interaction, this section introduces a new factor named the

sky dome coverage ratio (ξ). This factor is defined as the ratio of the emitter's directional radiation beams reaching the local surroundings to the total hemispherical radiation beam, recalled in Figure 3-4 (c), which is equivalent to the proportion of the yellow area to the entire area of the outermost circle. Therefore, ξ can represent different situations in the external environment. Furthermore, a larger ξ value signifies a smaller proportion of sky within the external environment. This decrease leads to enhanced heat exchange between the local surroundings and the RC module.

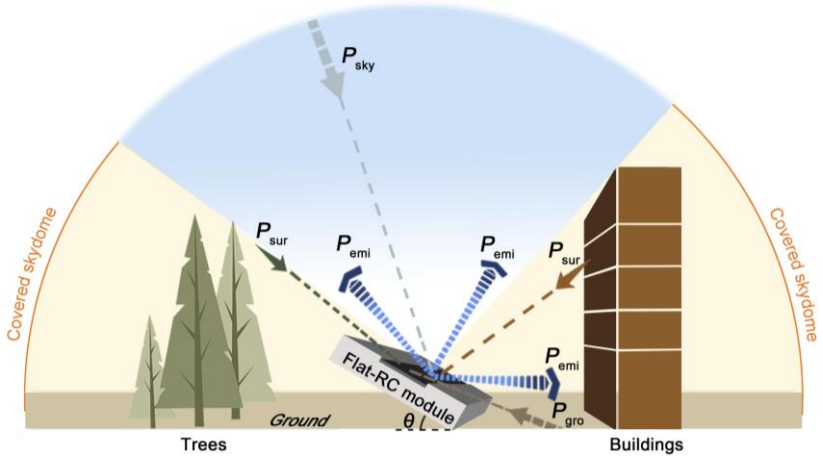

Figure 3-15:Radiative heat exchange between the flat-RC module and sky and local surroundings. To more clearly and simplified express the radiative heat exchange, the external environment is represented in the form of a cross-section diagram (actually the entire external environment is a hemisphere.)

Table 3-4 delineates the ε_{env} for the flat-RC module under various ξ scenarios. It is evident that ε_{env} escalates with an increasing ξ. Specifically, ε_{env} is 0.716 when the sky view factor is 1 (i.e., ξ equals 0); however, when ξ is augmented to 0.5, ε_{env} rises to 0.759, indicating an increase in the P_{env} absorbed by the RC module.

Table 3-4: Total, hemispherical emissivity of the external environment for the flat-RC module under different sky dome coverage ratios (ξ)

ξ	0	0.1	0.2	0.3	0.4	0.5
ε_{env}	0.716	0.718	0.728	0.739	0.752	0.759

Figure 3-16 (a) depicts the variations in P_{env} and P_{cool} under different ξ values. An increase in ξ leads to a rise in P_{env} and a decrease in P_{cool}. Specifically, with an increase in ξ from 0.1 to 0.5, P_{env} augments from 325.20 W/m^2 to 345.09 W/m^2, representing a 6.12% increase in adverse radiation absorbed by the RC module. Concurrently, a reduction in P_{cool} of 15.43%, an equivalent decrease of 19.88 W/m^2 is observed. This non-remarkable variation is attributed to the minor temperature differential between the ambient air and local obstacles at night. However, during the daytime, T_{sur} and T_{gro} in general significantly surpass T_{amb} due to the absorption of solar radiation. Figure 3-16 (b) presents the values of

P_{env} and P_{cool} when ξ is 0.5 and T_{sur} and T_{gro} are 50 °C (a typical daytime scenario in populated cities). The results indicate that the increase in T_{sur} and T_{gro} raises ε_{env} to 0.90, leading to an increase in P_{env} to 408.93 W/m^2 and a decrease in P_{cool} to 45.99 W/m^2. Consequently, under the same ξ value, the daytime cooling performance experiences a substantial reduction of 58.13% compared to nighttime, highlighting the significant impact of nearby obstacles on RC performance.

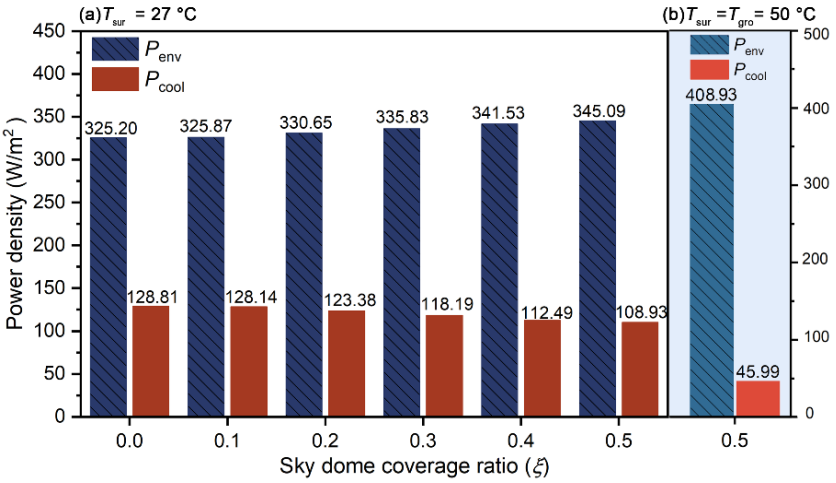

Figure 3-16: (a) Absorbed external environmental thermal radiation and net cooling power density of the flat-RC module at night under different sky dome coverage ratios. (b) A comparative case with the local surrounding temperature and sky dome coverage ratio set at 50 °C and 0.5, respectively.

This case study confirms that the proposed modelling approach can effectively display discrepancies of the external environmental thermal radiation and net cooling power density under various environmental settings.

3.4 Daytime solar radiation absorption analysis of RC modules

In addition to characterizing the P_{env} for the RC modules, the simulation software (Photopia) offers a wide range of commercially available lamps and includes sun and sky models based on the IESNA RP-21 standard, enabling the simulation of realistic outdoor daylighting conditions, so the solar radiation reaching the RC module's emitters can be calculated. In this section, the solar radiation absorbed by the RC modules under different configurations will be evaluated.

3.4.1 Solar radiation-related simulation model

The concentrator could be a double-edged sword for the cooling performance of the RC emitter during the daytime, depending on whether it blocks or concentrates more solar radiation for the emitter in a specific scenario. When the solar incident angle is greater than the concentrator's maximum half-

acceptance angle (θ_{max}), the concentrator acts as a solar shield which contributes to RC performance enhancement. Otherwise, the concentrator becomes a solar concentrator which deteriorates the RC performance. Therefore, this work employs the simulation software Photopia to quantitatively exam the effect of the concentrator on the solar irradiance absorbed by the RC emitter in various cases.

In the simulation, it is necessary to determine the position of the sun to simulate real illumination. The solar coordinates ($-\cos\theta_h\cos\varphi$, $\cos\theta_h\sin\varphi$, $\sin\theta_h$) at different times are determined according to the method proposed by Xu Yu et al. [233], where θ_h represents the solar altitude angle, and φ denotes the solar azimuth angle. These values are all calculated by the online calculator [234]. Besides, the reflectors of the concentrated RC modules are assigned by specular aluminium with a reflectance of 95%. Finally, the solar radiation absorbed by the ideal RC emitter and black-painted RC emitter are simulated respectively with different placement conditions. The spectral properties of the RC emitters as shown in Figure 3-17. The weighted average absorptivity of the ideal emitter is set to 0.1 [10], while the black-painted RC emitter has a weighted average solar absorptivity of 0.66, as measured using a Fourier Transform Infrared Spectrometer.

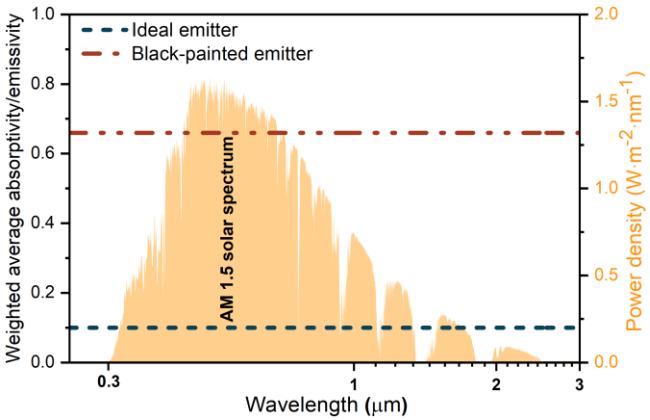

Figure 3-17: Different spectral properties of RC emitters under solar spectrum.

3.4.2 Performance indicator

Using Photopia software, it is possible to analyse the solar radiation absorbed (P_{sol}) by the RC emitter in both the inverted trapezoidal-RC and flat-RC modules under various conditions. By comparing the solar radiation absorption of the inverted trapezoidal-RC module emitter to that of the flat-RC module under the same conditions, scenarios can be identified where the inverted trapezoidal concentrator functions as either a solar shielding or a concentrator. To ensure accurate modelling in the software, the

dimensions of the inverted trapezoidal-RC and flat-RC modules used in the simulations are kept consistent with those in Section 3.3.

3.4.3 Effect of tilt angle on RC modules

Figure 3-18 presents the P_{sol} for the inverted trapezoidal-RC and flat-RC modules in Nottingham from June to September, across different placements between 4:00 and 20:00. In Figure 3-18 (a), both modules exhibit high P_{sol} when tilted 30° to the sunward side, with the inverted trapezoidal-RC module reaching over 800 W/m^2 at noon in June and July, which is 400 W/m^2 more than the flat-RC module. As the month progresses, P_{sol} for the inverted trapezoidal-RC module decreases due to increasing solar incident angles, which shift the trapezoidal concentrator's role from a solar concentrator to a solar shield. In contrast, the flat-RC module maintains steady P_{sol} of around 400 W/m^2. When the RC modules are placed horizontally, the inverted trapezoidal-RC module shows more P_{sol} than the flat-RC module in June and July but less in the later months. Specifically, when tilted 30° to the anti-sunward side, the inverted trapezoidal-RC module generally absorbs less than the flat-RC module, except during the early and late hours of the day in June and July, due to sunlight entering through the side openings of the trapezoidal concentrator.

Figure 3-18 (b) shows a similar trend for the RC modules with ideal emitters, which exhibit less P_{sol} due to their lower absorptivity in the solar spectrum. The results indicate that, except for the side openings of the trapezoidal concentrator, when the solar incident angle exceeds the concentrator's θ_{max}, the trapezoidal concentrator functions effectively as a solar shield. This is particularly relevant in scenarios such as when the inverted trapezoidal RC module is positioned horizontally during August and September or tilted at a 30° angle towards the anti-sunward side. In these cases, the concentrator's shielding effect results in lower P_{sol} compared to flat-RC module.

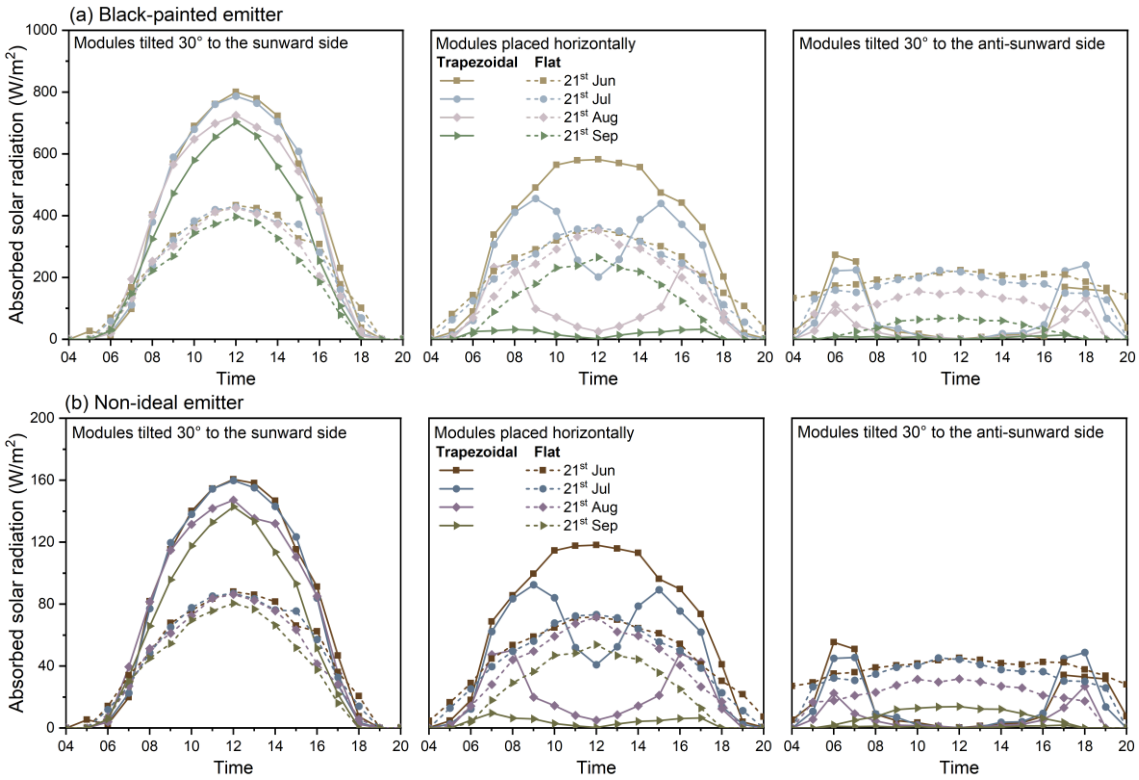

Figure 3-18: Solar radiation absorbed by (a) black-painted emitter and (b)ideal emitter different tilt angles on typical days.

3.4.4 All-day total absorbed solar radiation on RC modules

Figure 3-19 shows the total solar radiation absorbed by the modules throughout the day. Figure 3-19 (a) shows the total solar radiation absorbed by the modules using black-painted RC emitters. In the south-facing configuration, the inverted trapezoidal concentrator acts as a solar concentrator, resulting in significantly higher solar radiation absorption in the inverted trapezoidal-RC module compared to the flat-RC module on four typical days. Notably, on 21st June, the inverted trapezoidal-RC module absorbs 6169.78 Wh/m^2, which is 1.64 times that of the flat-RC module. However, the gap narrows by September. Additionally, in the horizontal placement group, the inverted trapezoidal-RC module continues to absorb more solar radiation, which is 1953.6 and 462.08 Wh/m^2 more than the flat-RC module on 21st June and 21st July, respectively. However, by September, its total solar radiation absorption significantly decreases, to only one-eighth that of the flat-RC module. Conversely, in the north-facing configuration, the flat-RC module consistently absorbs more solar radiation, indicating the inverted trapezoidal concentrator's effectiveness as a solar shield. Figure 3-19 (b) displays the total solar radiation absorbed by the ideal RC emitter in different placements on four typical days. The overall

trend mirrors that of Figure 3-19 (a), suggesting the potential of using ideal emitters to enhance cooling in the inverted trapezoidal-RC module for all-day cooling.

Additionally, when comparing Figure 3-19 (a) and (b) in certain cases, even when the inverted trapezoidal-RC module utilizes a black-painted emitter with a higher solar absorptivity, the total solar radiation absorbed throughout the day remains lower than that of the flat-RC module with an ideal emitter. Notably, on 21st September, in the north-facing group, the inverted trapezoidal-RC module with the black-painted RC emitter absorbed 48.18 Wh/m^2 of solar radiation, significantly less than the 110.88 Wh/m^2 absorbed by the flat-RC module with the ideal emitter. This further highlights the effectiveness of the concentrator in providing shading and achieving all-day radiative cooling.

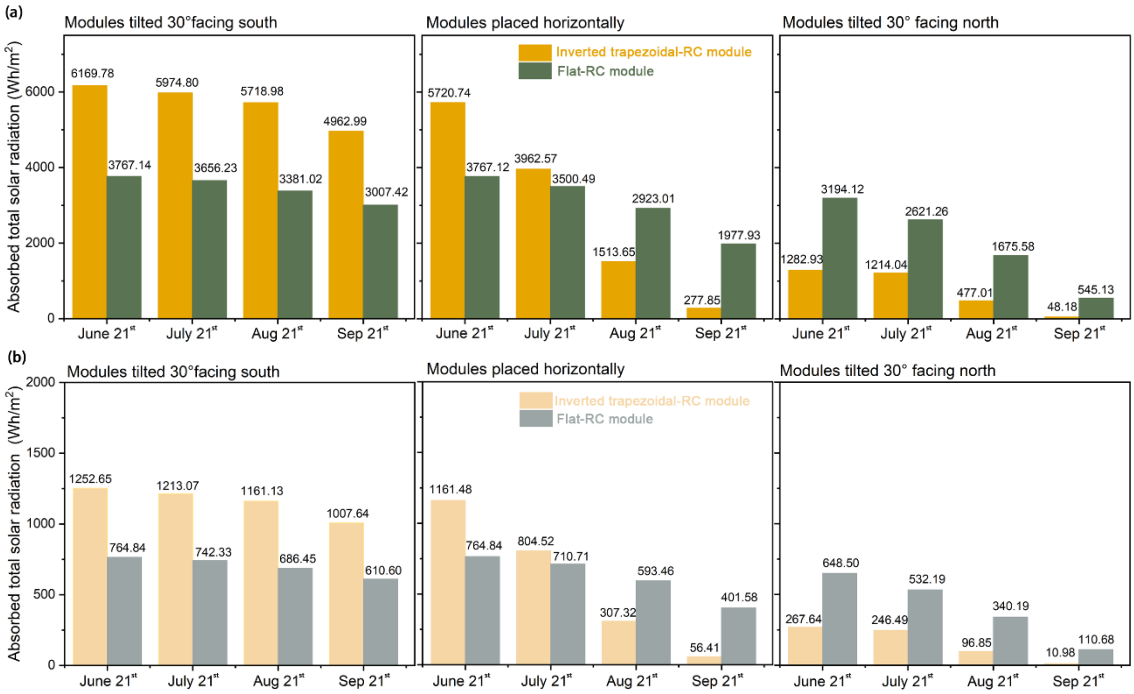

Figure 3-19: Total solar radiation absorbed by the inverted trapezoidal-RC and flat-RC modules at three placements on four typical days. (a) Black-painted RC emitter (b) Ideal RC emitter

3.5 Summary

In this chapter, a novel modelling approach developed to accurately characterize the cooling performance of RC modules is proposed. The approach captures thermal radiation from various directions precisely by segmenting the entire external environment into 90 concentric circles using optical software. Additionally, a new parameter is defined to thoroughly evaluate the radiative heat exchange (P_{env}) between the RC module and external environment. This approach can address the issue that existing methods often ignore the complex radiative heat exchange between the RC emitter and its

local environment and overestimate the cooling power (P_{cool}) for the RC modules. To validate the modelling approach, a series of application analyses are conducted, demonstrating its capability to capture performance differences among RC modules with varying structures in diverse scenarios (local environment and placement conditions), highlighting its effectiveness and universality. Additionally, the optical software can quantitatively assess the solar radiation absorbed by the module, allowing for a simplified comparison of the solar radiation absorbed by RC modules with different structures.

However, this approach can be further improved to make it more widely applicable. First, the approach proposed in this chapter only characterizes the cooling performance of RC modules at night. While the influence of solar radiation is discussed, it does not fully capture the cooling performance of RC modules during the daytime. The next chapter of the thesis should further refine the mathematical framework to better characterize the impact of direct and diffuse solar radiation on RC emitters during the daytime. Moreover, the reflectivity of the concentrator is assumed to be 1 in this chapter, but in practical applications, such reflectivity is unattainable. Therefore, the next chapter need to characterize the effective emissivity/absorptivity of RC emitters at varying concentrator reflectivity, to more accurately assess the cooling performance of concentrated RC modules.

4. Numerical study and experimental evaluation of two-dimensional (trough) compound parabolic concentrator (CPC) - based radiative cooling (CPC-RC) module

4.1 Introduction

In Chapter 3, the cooling performance of traditional RC and inverted trapezoidal-RC modules during the nighttime is accurately characterized through the proposed modelling approach, and the adverse impact of solar radiation on RC modules during the daytime is determined. While realizing daytime sub-ambient radiative sky cooling is no longer a hurdle, achieving a substantial cooling effect during the daytime continues to pose challenges. The primary obstacle is the RC emitter's direct exposure to intense solar radiation, approximately 1000 W/m^2 [41], which significantly impacts the cooling effect. Despite these challenges, reducing daytime building cooling consumption through RC technology, particularly concentrated RC module with high cooling power, remains appealing due to its environmentally friendly and cost-effective benefits.

After an extensive review of the literature on concentrated RC systems and concentrators, we found that the two-dimensional compound parabolic concentrator (CPC) is widely utilized in building-integrated PV/T systems, demonstrating excellent solar energy collection capabilities. Based on the design principles of the CPC, this concentrator can block a portion of solar radiation and unwanted thermal radiation during the daytime, demonstrating its potential to enhance daytime RC performance. Consequently, this chapter provides an in-depth discussion of the solar and adverse thermal radiation shielding capabilities of the CPC-integrated RC module (referred to as CPC-RC module [235]. This chapter first applies the optical modelling approach introduced in Chapter 3 to accurately evaluate the cooling performance of CPC-RC module and traditional RC modules under typical weather conditions, demonstrating the superior performance of CPC-RC modules. Additionally, to facilitate the integration of the CPC-RC module into buildings, this chapter analyses the optimal tilt angle of modules under different seasons in Guangzhou, China to provide installation guidance for cities with similar latitudes.

Furthermore, by adjusting the spectral characteristics of the RC emitter, the study shows that the CPC structure can effectively reduce the spectral requirements for the RC emitter. Finally, a series of outdoor experiments conducted during the daytime and nighttime verify the cooling effect of the CPC-RC module and evaluate its advantages over a flat-RC and a common concentrated RC module.

4.2 Function of the CPC structure in CPC-RC module

4.2.1 Solar shield mode

CPCs are widely utilized in solar energy applications due to their ability to concentrate sunlight without requiring additional solar tracking systems [21,159,236,237]. When combined with RC technology, its thermal radiation concentrating property allows it to direct the hemispherical thermal radiation emitted by the RC emitter predominantly towards directions near the zenith angle. As a result, the RC emitter's thermal radiation is able to reach outer space through the most transparent atmospheric region. Additionally, CPC can act as a shielding device by blocking adverse radiation (such as thermal radiation from the sky, sun, and obstacles) whose incident angle exceeds the maximum half-acceptance angle (θ_{max}) of the CPC structure, as shown in Figure 4-1.

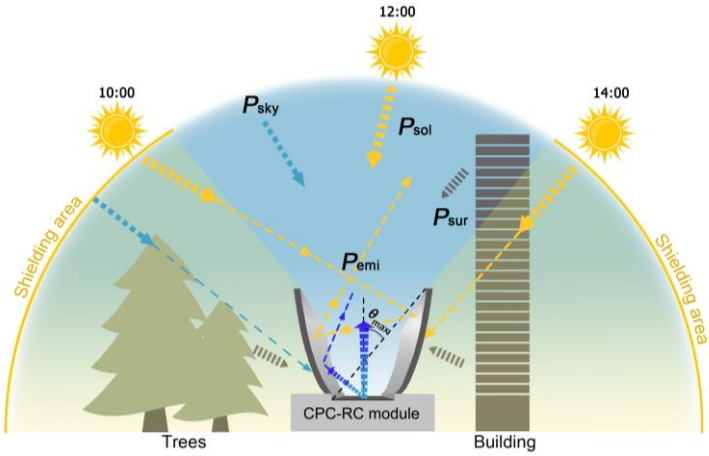

Figure 4-1: Schematic of the radiative heat exchange for the CPC-RC module.

Figure 4-2 illustrates the transformation of the CPC function in CPC-RC modules during the daytime. It is observed that when the CPC-RC module is placed horizontally, its cooling performance at each moment changes with the trajectory of the sun. This is because changes in the solar incident angle and azimuth angle will change the solar radiation absorbed by the module. As depicted in the Figure 4-2, when the side openings of the CPC-RC module are oriented east-west, the morning sunlight from the southeast allows to reach the RC emitter through the module's side openings, rendering the CPC

ineffective as a solar shield at this time. As time progresses to noon and the sun is positioned in the south, if the solar incidence angle exceeds the θ_{max} of the CPC, then the CPC can successfully block direct sunlight from reaching the RC emitter, contributing to daytime sub-ambient RC. However, this scenario is highly idealized. The relationship between the θ_{max} and the concentration ratio (C) of CPC can be found in Section 2.3.1. It can be shown that a larger θ_{max} leads to a smaller C. Consequently, the θ_{max} of most low-concentration CPCs is usually kept around 30°. However, in lower latitude regions, the sun's incident angle around noon is often less than 30° and will even come from the zenith direction. This results in most sunlight being concentrated onto the receiver by the CPC during this period, paradoxically hindering the realization of daytime RC. Therefore, if the use of CPC as a solar shield to mitigate the adverse effects of solar radiation on RC modules in low latitudes is desired, consideration must be given to how the position of the module can be changed so that the incident sunlight exceeds the θ_{max}.

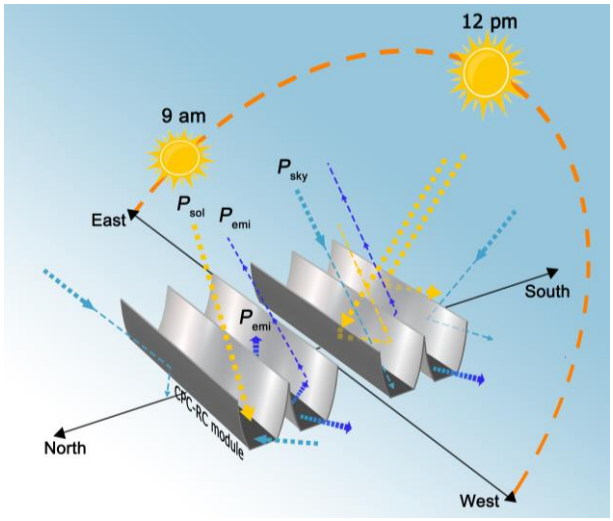

Figure 4-2: Schematic of the CPC-RC module shield against part of unfavourable radiation during the daytime.

4.2.2 Thermal radiation concentration and shield mode

At night, the absence of solar radiation allows sub-ambient temperatures to be easily achieved by the RC module. To enhance the RC module's cooling power, further improvement of the spectral selectivity of the RC emitter to approach ideal properties is essential. However, such improvements require the use of precision instruments and complex manufacturing processes, resulting in increased material costs and a lengthened period for investment recovery post-implementation. Fortunately, the developed CPC-RC module can effectively enhance cooling performance without further improving

the spectral selectivity of the RC emitter. In the CPC-RC module, one of the primary functions of the CPC is to concentrate the hemispherical thermal radiation emitted by the RC emitter towards directions near the zenith to improve cooling performance.

Figure 4-3 (a) shows the spectral atmospheric emissivity at four different zenith angles (0°, 30°, 45° and 60°) within the 0-25 μm wavelength range, while Figure 4-3 (b) illustrates the weighted average atmospheric emissivity within the "atmospheric window". The weighted average emissivity remains around 0.37 from the zenith direction up to a zenith angle of 40°. However, beyond 50°, the weighted average emissivity increases rapidly, reaching 0.76 at 80°. As the zenith angle increases, the path length of thermal radiation passing through the atmosphere also increases, leading to higher atmospheric emissivity in that direction. As a result, more thermal radiation emitted by the flat RC emitter absorbed by the atmosphere instead of being radiated into deep space. This increases the radiative thermal resistance between the emitter and outer space, reducing the net radiative cooling power in that direction. In contrast, the CPC-RC module effectively minimizes the radiative thermal resistance by concentrating hemispherical thermal radiation within a small zenith angle range (the CPC's θ_{max}), where the sky is most transparent.

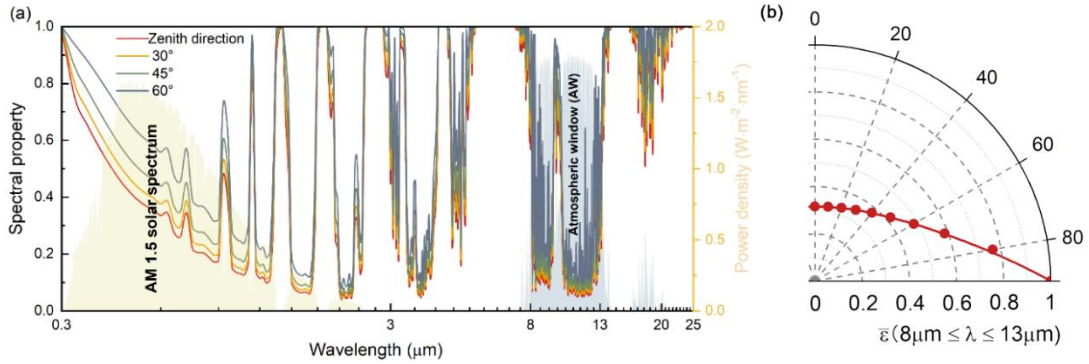

Figure 4-3: (a) Spectral atmospheric emissivity of four different zenith angles in the 0.3-25 μm wavelength range; (b) the weighted average atmospheric emissivity between the 8 and 13 μm.

As shown in Figure 4-4 (a), the radiation direction of the flat RC emitter is hemispherical when it radiates outwards. The longest path, L_1, is parallel to the earth's sea level. On the contrary, when the RC emitter emits thermal radiation in the concentrated RC module, the radiation direction is limited within the θ_{max} range of the concentrator, and the longest path, L_2 which is showed in Figure 4-4 (b). Although the relationship between atmospheric thickness and atmospheric transmittance is nonlinear due to

variations in air density and water vapor content at different altitudes, i.e., L_2 being one-third of L_1 does not necessarily result in a threefold increase in atmospheric transmittance, it is certain that longer thermal radiation paths are associated with lower spectral, directional atmospheric transmittance.

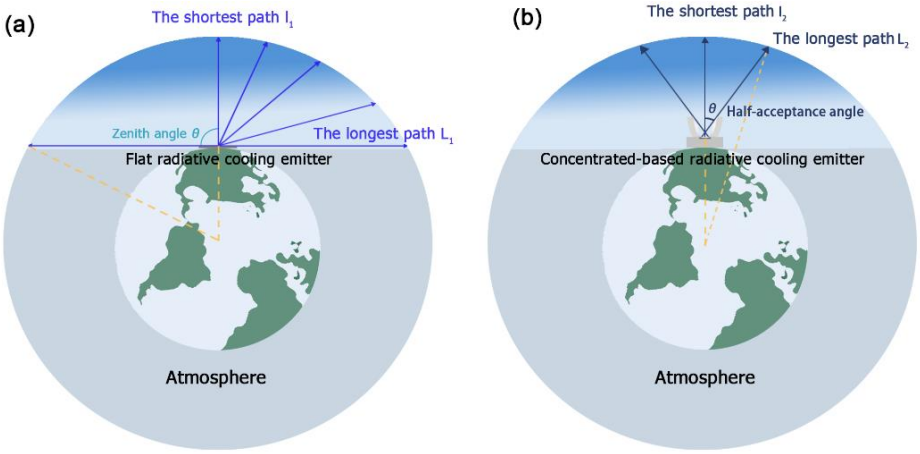

Figure 4-4: Schematic diagram of (a) the radiation path through the atmosphere; and (b) the radius of the earth, thickness of the atmospheric layer, and size of the CPC are indicative.

In addition to the concentrating function, CPC also acts as a shielding structure to block undesirable thermal radiation, as shown in Figure 4-5. It can block external ambient thermal radiation at incident angles greater than θ_{max}. This blocking is significant because larger incident angles are associated with higher sky emissivity, leading to increased downward sky thermal radiation which the CPC effectively reduces the absorption of this radiation by the RC emitter.

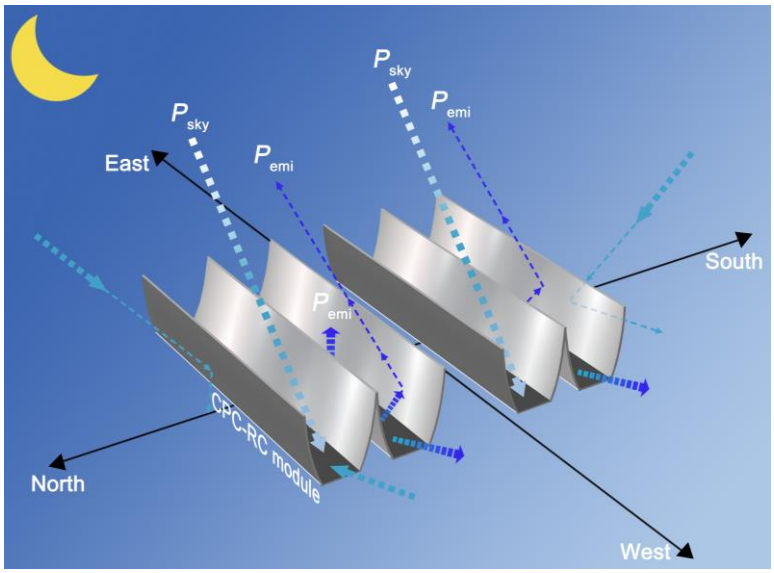

Figure 4-5: Schematic of the CPC-RC module shield angular thermal radiation at night.

4.3 Comparative numerical study of CPC-RC module on four typical days

4.3.1 Novel modelling approach

Chapter 3 proposed a novel modelling approach based on the principle of reciprocity, tailored for accurately characterizing the cooling performance of complex RC structures. However, the chapter is predominantly on the nocturnal cooling effects of RC modules. When evaluating the cooling power density (P_{cool}) for the RC module throughout the day, it is necessary to account for the impact of solar radiation. The P_{cool} can be further expressed as:

$$P_{cool} = P_{emi} - \underbrace{(P_{sky} + P_{gro} + P_{sur})}_{P_{env}} - \underbrace{(P_{sol_dir} + P_{sol_dif})}_{P_{sol}} - P_{non\text{-}rad} \tag{4.1}$$

Among them, the derivation process of P_{emi} has been detailed in the literature review and will not be repeated here. Furthermore, as this chapter assumes that the temperatures of the RC emitter and the thermal radiation concentrator are equal to the ambient temperature, non-radiative heat transfer ($P_{non\text{-}rad}$) will not be further discussed. P_{env} represents the thermal radiation absorbed by the RC module from the entire external environment. A detailed explanation of its derivation and components is provided in the Subsection 3.2.2. Furthermore, taking into account the Stefan-Boltzmann law, P_{env} can be simplified to:

$$P_{env} = \alpha_{emi}\varepsilon_{env}\sigma T_{amb}^4 \tag{4.2}$$

where ε_{env} is the total, hemispheric emissivity of the external environment. However, in Section 3.2, the reflectivity of the concentrator is assumed to be 1 to simplify the calculation process. When the reflectivity of the concentrator is not 1, ε_{env} can be expressed as:

$$\varepsilon_{env} = \int_0^{\pi/2} \left[\varepsilon_{sky}(\theta)\beta_{sky} \underbrace{\left(\sum_{i=0}^{+\infty} \rho_{con}^i \omega_i(\theta) \right)}_{\rho_{con_eff_sky}} + \varepsilon_{gro}(\theta)\beta_{gro} \underbrace{\left(\sum_{i=0}^{+\infty} \rho_{con}^i \omega_i(\theta) \right)}_{\rho_{con_eff_gro}} + \varepsilon_{sur}(\theta)\beta_{sur} \underbrace{\left(\sum_{i=0}^{+\infty} \rho_{con}^i \omega_i(\theta) \right)}_{\rho_{con_eff_sur}} \right] d\theta \tag{4.3}$$

where $\varepsilon_{sky}(\theta)$, $\varepsilon_{gro}(\theta)$, and $\varepsilon_{sur}(\theta)$ are respectively the equivalent emissivity of the sky, ground, and aboveground surroundings zenith angle of θ; the definitions of $\beta_{sky}(\theta)$, $\beta_{gro}(\theta)$ and $\beta_{sur}(\theta)$ are detailed in Subsection 3.2.2; $\rho_{con_eff_sky}$, $\rho_{con_eff_gro}$, and $\rho_{con_eff_sur}$ are the effective concentrator reflectivity for thermal radiation concentrator to the thermal radiation from the sky, ground, and aboveground surroundings; i represents the number of reflections by the thermal radiation concentrator required for

thermal radiation to reach the RC emitter; ρ_{con} is the real material reflectivity of the thermal radiation concentrator; $\omega_i(\theta)$ represents the ratio of the number of incoming radiation beams from the same zenith angle θ that reach the RC module after i-time reflections to the total radiation beams.

Figure 4-6 shows different paths of incoming thermal radiation beams that reach the concentrated RC module's emitter. In concentrated RC modules, incoming thermal radiation must traverse the thermal radiation concentrator structure to reach the RC emitter. However, not all incoming thermal radiation is reflected by the concentrator, some reaches the RC emitter directly. Consequently, it becomes essential to characterize the effective reflectivity of the concentrator (ρ_{con_eff}). This figure indicates three distinct types of radiation paths reaching the RC emitter: The red lines are the direct radiation beams that are not reflected by the CPC; The blue lines are the radiation beams reflected once by the CPC; The yellow lines are the radiation beams that undergo multiple reflections before reaching the emitter.

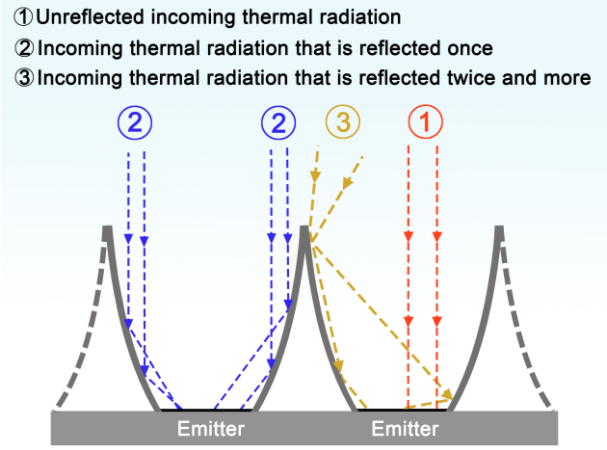

Figure 4-6: Different incoming thermal radiation beam paths reach the CPC-RC module's emitter.

When the thermal radiation beams from the zenith angle θ are reflected by the concentrator and reach the RC emitter, ω_i is different. Furthermore, $\omega_i(\theta)$ differs among various types of thermal radiation concentrators. Figure 4-7 (a) and (b) show the $\omega_i(\theta)$ for the CPC-RC and inverted trapezoidal-RC modules at various zenith angles. When the zenith angle ranges from 0° to 10°, the ratio of the thermal radiation beams reaches the two RC modules' emitter after one reflection by the thermal radiation concentrator (ω_1) is the largest. However, differences emerge as the zenith angle exceeds 10°. For the CPC-RC module, ω_1 remains above 0.5 between 10° and 30° zenith angles, exceeding the directional radiation angular ratio that reach the emitter directly without reflection (ω_0). However, after the zenith

angle exceeds 30°, the share of ω_0 surges, ultimately reaching 1 at 90°. Conversely, for the inverted trapezoidal-RC module, ω_0 is dominant between the 10° to 35° zenith angle, with ω_1 briefly overtaking after 35° zenith angle, before ω_0 regains and extends its lead past 40°. Additionally, ω_2 is consistently observed to be higher in the inverted trapezoidal concentrator than in the CPC-RC module.

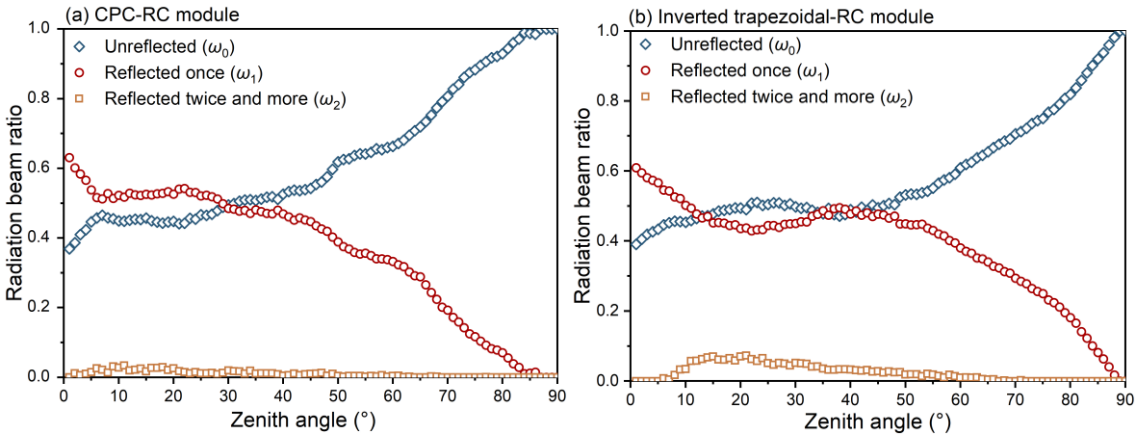

Figure 4-7: Ratio of the radiation beam from zenith angles (θ) that reaches the RC emitter after i-reflections to the total radiation beam at that zenith angle. (a) CPC-RC module. (b) Inverted trapezoidal-RC module.

In addition to external environmental radiation power, solar radiation is another important factor affecting the daytime P_{cool}. The solar radiation absorbed by the flat RC emitter can be given by:

$$P_{\text{sol}} = \alpha_{\text{emi}} G \tag{4.4}$$

where α_{emi} is the weighted average absorptivity of the RC emitter in the solar spectrum; G is the total incident solar radiation, W/m^2.

However, for the concentrated RC module, the thermal radiation concentrator focuses part of the incident solar radiation while also blocking some that exceed its θ_{max}. Since solar radiation comprises both diffuse and direct irradiance, each with different incident directions, the quantity of radiation reaching the emitter varies accordingly. Therefore, it is essential to distinguish between the absorbed direct solar radiation ($P_{\text{sol_dir}}$) and diffuse solar radiation ($P_{\text{sol_dif}}$) for the concentrated RC module at a specific daytime hour (t), which can be expressed as follows:

$$P_{\text{sol_dir}}(t) = C\eta_{\text{sol_dir}}(t)\alpha_{\text{emi}} G_{\text{sol_dir}}(t)\rho_{\text{sol_dir}}(t) \tag{4.5}$$

$$P_{\text{sol_dif}}(t) = C\eta_{\text{sol_dif}}(t)\alpha_{\text{emi}} G_{\text{sol_dif}}(t)\rho_{\text{sol_dif}}(t) \tag{4.6}$$

where $\eta_{sol_dir}(t)$ and $\eta_{sol_dif}(t)$ are respectively defined as the ratios of the direct and diffuse solar radiation received by the RC emitter to the direct and diffuse solar radiation received by the thermal radiation concentrator's aperture at a specific daytime hour (t); $G_{sol_dir}(t)$ and $G_{sol_dif}(t)$ are the direct and diffuse solar irradiance at a specific daytime hour (t), W/m^2; $\rho_{sol_dir}(t)$ and $\rho_{sol_dif}(t)$ is the effective reflectivity for thermal radiation concentrator to direct and diffuse solar radiation at a specific daytime hour (t), which can be obtained using the Eq.4.9 and 4.10.

$$\rho_{sol_dir}(t) = \sum_{i=0}^{+\infty} \rho_{con}^{i} \omega_{sol_dir_i}(t) \tag{4.7}$$

$$\rho_{sol_dif}(t) = \sum_{i=0}^{+\infty} \rho_{con}^{i} \omega_{sol_dif_i}(t) \tag{4.8}$$

where $\omega_{sol_dir_i}$ and $\omega_{sol_dif_i}$ are the ratios of direct and diffuse solar radiation beams reaching the RC emitter after different reflection times (i) at a specific daytime hour (t) to the total solar radiation beams at the same time.

4.3.1.1 Performance indicators

To comprehensively characterize the all-day cooling effect of the RC modules, take the net radiative cooling power density per hour (hourly P_{cool}) on four typical days as the primary indicator. EnergyPlus software is employed to determine hourly direct and diffuse solar radiation and ambient temperatures for four typical days [238]. Additionally, the sun's position and the incident angle of solar radiation on each typical day are determined using the method proposed by Yu and Su [233]. Furthermore, the equivalent external environment emissivity and effective reflectivity for different RC modules obtained through the proposed modelling method will also be compared as performance indicators. Finally, to better reflect the comprehensive cooling performance of the RC modules throughout the daytime and night, the average value of P_{cool} during daytime and nighttime is introduced, which is denoted as $\overline{P}_{cool}$.

4.3.1.2 Key parameter settings

Figure 4-8 shows the ambient temperature and direct and diffuse solar irradiance on four typical days in Guangzhou, China. According to the solar irradiance, the daytime in March, September and

December is set from 7:00 to 18:00, while the daytime in June is from 7:00 to 19:00. Key parameter settings for the case studies are detailed in Table 4-1.

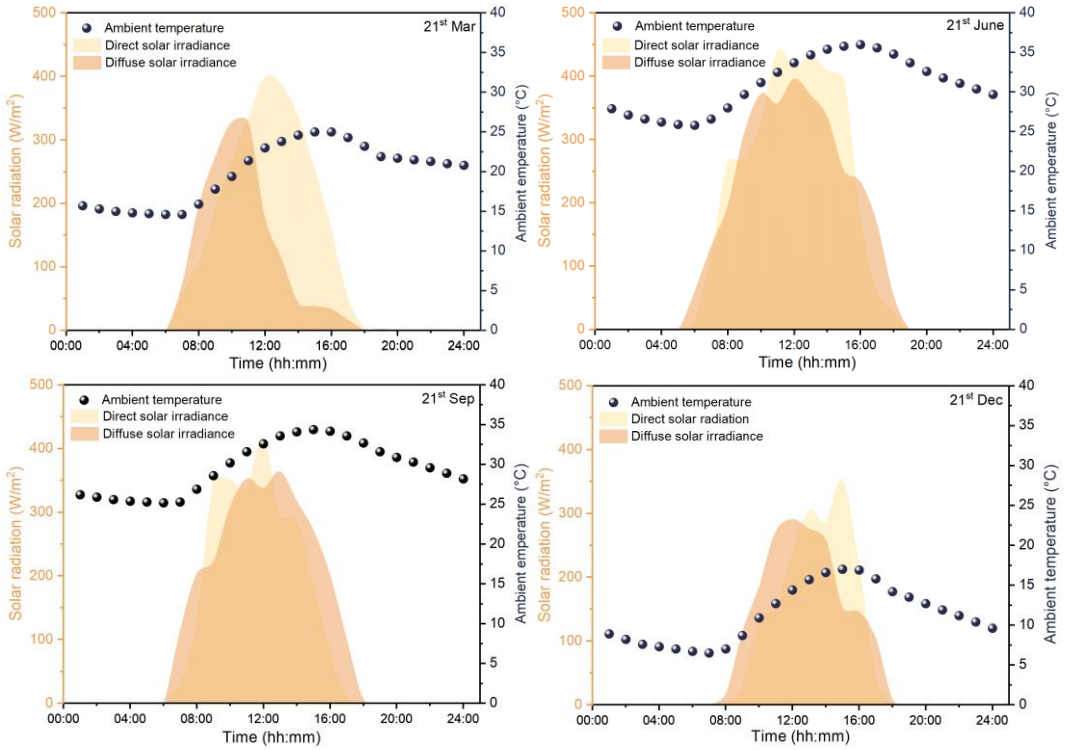

Figure 4-8: Ambient temperature and solar irradiance for four typical days in Guangzhou, China from the EnergyPlus database.

Table 4-1: Key parameter settings for case study.

Parameters	Descriptions	Values
T_{gro_day}	Daytime ground temperature (°C)	T_{amb}+20 °C [239, 240]
T_{gro_night}	Nighttime ground temperature (°C)	T_{amb}-5 °C [241]
ρ_{con}	Concentrator material's reflectivity	0.95
ε_{gro}	Ground emissivity	0.85
W	Bottom width of the RC modules (mm)	300
L	Length of the flat and concentrated RC modules (mm)	1000
H	Height of the concentrated RC modules (mm)	420

4.3.2 Comparative analysis of CPC-RC module and other RC modules

This section compares the cooling performance of the 2D CPC-RC module against other RC modules (including the common 2D inverted trapezoidal-RC module, and the traditional flat-RC module) on four typical days. The schematic diagram of the RC modules is shown in Figure 4-9. In this section, the RC modules are placed horizontally with no environmental obstacles around them. Additionally, the weighted average emissivity (ε_{emi}) for the RC emitter is set to 0.95, and its weighted average solar absorptivity (α_{emi}) is set to 0.1.

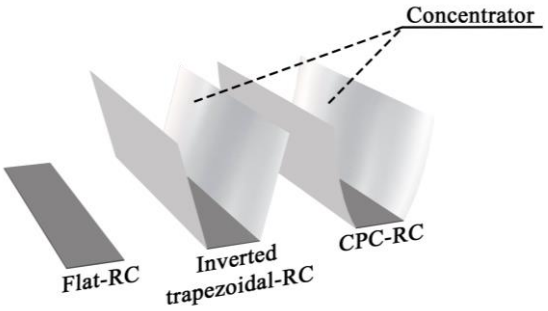

Figure 4-9: Schematic diagram of the three RC modules.

Since this chapter focuses on studying the daytime cooling effect of the RC modules, accurately determining the solar receiving ratio ($\eta_{_sol}$) for the thermal radiation concentrators in the concentrated RC modules is crucial for characterizing the P_{sol_dir} and P_{sol_dif} by the modules, as shown in Eqs. 4.7 and 4.8. The $\eta_{_sol}$ for the thermal radiation concentrators proposed in this chapter is essentially consistent with the optical efficiency of the solar concentrators, and this parameter has great significance for the cooling performance of the RC module.

Figure 4-10 displays the direct solar receiving ratio (η_{sol_dir}) for two concentrated RC modules on four typical days. Except for 21st December, the η_{sol_dir} for the inverted trapezoidal concentrator is lower than that of the CPC, although their η_{sol_dir} changing trends are similar. For instance, on the 21st of March and September, an increase in the η_{sol_dir} for both thermal radiation concentrators are seen in the morning, followed by a gradual decrease after noon. However, the η_{sol_dir} change curve of the inverted trapezoidal concentrator is found to be relatively stable, peaking at 0.68 in March and 0.75 in September at noon. In contrast, the η_{sol_dir} change curve of CPC is more pronounced, with peaks of 0.93 and 0.95 at noon, and the number of hours per day when η_{sol_dir} exceeds 0.80 surpassing 6 hours. While a higher η_{sol_dir} is advantageous for solar energy utilization, it also indicates that the CPC-RC module may exhibit a higher P_{sol} by the RC emitter, negatively impacting the cooling effect. On 21st June, both thermal radiation concentrators are shown to have higher η_{sol_dir}, with peak η_{sol_dir} at noon reaching 0.96 and 0.97, respectively. Conversely, the η_{sol_dir} for both thermal radiation concentrators on 21st December is less than 0.10, indicating that sunlight can hardly reach the RC emitter, with both thermal radiation concentrators acting as solar shields at this daytime. However, Figure 4-10 shows that except in winter,

the thermal radiation concentrators of the CPC-RC and inverted trapezoidal-RC modules cannot effectively block sunlight when the modules are placed horizontally.

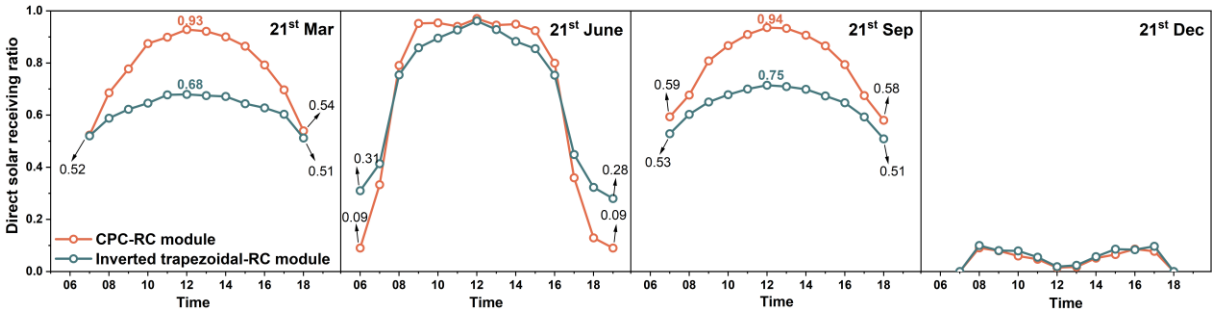

Figure 4-10: Direct solar receiving ratio for two RC modules on four typical days.

In addition to simulating the η_{sol_dir} for the thermal radiation concentrators under direct sunlight, simulating the diffuse solar receiving ratio (η_{sol_dif}) for the thermal radiation concentrators under diffuse sunlight is also needed. In the simulating model, a cloudy weather solar model is selected to represent diffuse sunlight from all directions. The simulation results show that, regardless of season or time, the ratio of diffuse sunlight received at the RC emitter to the diffuse sunlight received at the aperture of the concentrated RC modules remain constant, meaning the η_{sol_dif} for the same thermal radiation concentrator does not change. In this section, the η_{sol_dif} for the CPC structure is 0.485, while that of the inverted trapezoidal concentrator is 0.455.

The equivalent external environmental emissivity (ε_{env}) for the three RC modules is obtained by the modelling approach proposed in Section 3.2. The thermal radiation concentrators in both the CPC-RC and inverted trapezoidal-RC modules effectively block unfavourable external environmental thermal radiation from large zenith angles. As a result, these modules exhibit lower ε_{env} compared to the 0.713 for the flat-RC module, which lacks a thermal radiation concentrator. Specifically, the ε_{env} for the CPC-RC and inverted trapezoidal-RC modules are 0.665 and 0.683, respectively.

Table 4-2 shows the effective direct sunlight reflectivity (ρ_{sol_dir}) for the two thermal radiation concentrators during four typical days. The ρ_{sol_dir} for both thermal radiation concentrators are higher than the real reflectivity of the material, which is 0.95. This is because part of the direct sunlight can directly reach the RC emitter without being reflected by the thermal radiation concentrator. The variation for the ρ_{sol_dir} for the two thermal radiation concentrators on the 21st of March and September are similar, with the lowest ρ_{sol_dir} of about 0.967 at noon. This is because most of the incident sunlight

at this time cannot reach the RC emitter directly but needs to be reflected through the thermal radiation concentrator to reach the RC emitter. In contrast, ρ_{sol_dir} shows higher in the morning and evening. The reason for this phenomenon is that most of the incident sunlight enters directly from the side openings and reaches the RC emitter without being reflected by the thermal radiation concentrator. Moreover, the minimum ρ_{sol_dir} for CPC on 21st June is 0.971, which is lower than the ρ_{sol_dir} for the inverted trapezoidal concentrator (minimum ρ_{sol_dir} is 0.975). This occurs because, with the CPC, more sunlight is observed to reach the RC emitter after being reflected twice or more, compared to the case with the inverted trapezoidal concentrator. On 21st December, sunlight entering the CPC-RC module through side openings is not reflected by the CPC, resulting in the ρ_{sol_dir} of 1 for the CPC. Conversely, in the inverted trapezoidal-RC module, some sunlight reaching the RC emitter after reflection results in the ρ_{sol_dir} that is lower than that of the CPC.

Table 4-2: Effective direct sunlight reflectivity for the RC modules. (CPC in the table refers to CPC-RC module, and trapezoidal refers to inverted trapezoidal-RC module)

	Time	7:00	8:00	9:00	10:00	11:00	12:00	13:00	14:00	15:00	16:00	17:00	18:00
21st Mar	CPC	0.992	0.980	0.974	0.971	0.969	0.967	0.967	0.969	0.971	0.975	0.985	1
	Trapezoidal	0.992	0.982	0.974	0.971	0.968	0.966	0.967	0.969	0.972	0.977	0.985	1
21st June	CPC	1	0.977	0.976	0.973	0.972	0.971	0.972	0.973	0.975	0.978	1	1
	Trapezoidal	0.979	0.976	0.976	0.975	0.975	0.975	0.975	0.975	0.976	0.976	0.979	1
21st Sep	CPC	0.992	0.981	0.974	0.971	0.969	0.968	0.968	0.969	0.972	0.975	0.985	1
	Trapezoidal	0.992	0.982	0.974	0.971	0.969	0.967	0.967	0.969	0.972	0.976	0.985	1
21st Dec	CPC		1	1	1	1	1	1	1	1	1	1	
	Trapezoidal		1	0.991	0.981	0.979	0.975	0.976	0.977	0.982	0.994	1	

Figure 4-11 (a) presents the hourly P_{cool} variation curves for three RC modules on four typical days, and Figure 4-11 (b) and (c) shows the $\overline{P}_{cool}$ for the RC modules during the day and night, and the $\overline{P}_{cool}$ for the entire day, respectively. The results show that on four typical days, the RC modules can obtain cooling power both during the daytime and at night. However, due to the influence of solar radiation during the daytime, the hourly P_{cool} for all modules during the daytime is lower than at night. On 21st March night, the CPC-RC module shows excellent cooling performance attributed to its thermal radiation concentrating characteristics. Its nighttime $\overline{P}_{cool}$ shows 130.10 W/m^2, which is 5.7% and 18.1% higher than the inverted trapezoidal-RC and flat-RC modules, respectively. However, also due to the solar concentration property, the hourly P_{cool} obtained from 10:00 to 15:00 is lower than the other two modules, with only 48.41 W/m^2 at noon. Nonetheless, when considering the overall performance, the CPC-RC module's daytime $\overline{P}_{cool}$ reaches 86.04 W/m^2, slightly surpassing the 80.58 W/m^2 of the flat-RC

module. Furthermore, the inverted trapezoidal-RC module exhibits less P_{sol} due to lower η_{sol_dir} compared to CPC, obtaining the $\overline{P}_{cool}$ of 89.81 W/m^2.

The night situation of the remaining three typical days is similar to those of 21st March, where the CPC-RC module is shown to have the best cooling performance, followed by the inverted trapezoidal-RC module, and lastly the flat-RC module. Conversely, the hourly P_{cool} for these modules varied significantly during the daytime. For instance, from 9:00 to 16:00 on 21st June, the hourly P_{cool} for both concentrated RC modules is negatively impacted by the solar concentration effect, resulting in performance inferior to that of the flat-RC module. Fortunately, when evaluating the cooling performance throughout the day, the $\overline{P}_{cool}$ for the CPC-RC and inverted trapezoidal-RC modules are 88.32 and 86.06 W/m^2, respectively, slightly higher than the 83.57 W/m^2 shown for the flat-RC module. The trends on 21st September mirrored those of 21st March, with an increase in P_{cool} across all three modules due to elevated ambient temperatures. However, on 21st December, the cooling performance of the three RC modules diverged notably. The large solar zenith angle in winter, often exceeding the θ_{max} of the thermal radiation concentrators, resulted in relatively stable P_{cool} curves for the concentrated RC modules. In contrast, the absence of a solar shield caused significant fluctuations in the P_{cool} curve of the flat-RC module. Consequently, the daytime $\overline{P}_{cool}$ for the CPC-RC module reached 100.89 W/m^2, 49.2% higher than that of the flat-RC module. These results underscore the critical role of P_{sol} in determining cooling capacity, particularly for concentrated RC modules. To optimize cooling efficiency throughout the day, it is essential to lessen P_{sol} in concentrated RC modules.

When comparing the cooling performance of different RC modules throughout the day, it is found that, regardless of the season, the CPC-RC module consistently achieved the highest all-day $\overline{P}_{cool}$, followed by the inverted trapezoidal-RC module, with the flat-RC module performing the least efficiently. For example, on 21st June, the CPC-RC module's all-day $\overline{P}_{cool}$ is 119.04 W/m^2, which is 4.55% and 13.2% higher than that of the inverted trapezoidal-RC and flat-RC modules, respectively.

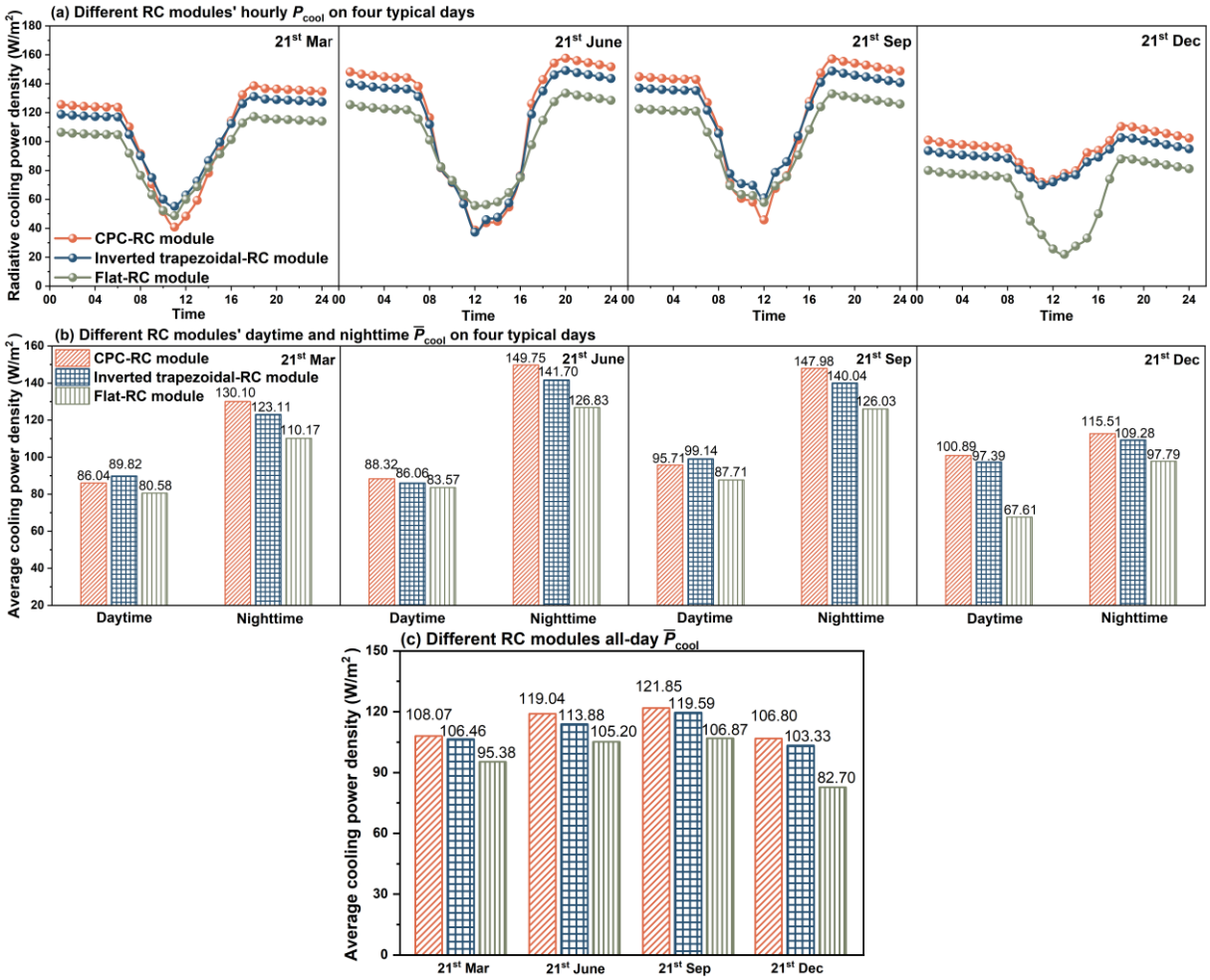

Figure 4-11: (a) Difference in hourly cooling power density for different RC modules on four typical days. (b) Average cooling power density for different RC modules during daytime and nighttime. (c) All-day average cooling power density for different RC modules.

4.3.3 Performance analysis of CPC-RC module with different inclined placements

The previous section revealed the superior cooling performance of the horizontally placed CPC-RC module at night, which can achieve higher cooling power than common inverted trapezoidal-RC and flat-RC modules. However, during the daytime on three typical days in March, June, and September, it is noted that the CPC-RC module absorbs more solar radiation due to the concentrator's solar concentrating properties, resulting in the lowest cooling power at noon. To enhance the daytime cooling capacity of the CPC-RC module, further studies are needed to determine how to reduce the solar radiation absorbed by CPC-RC modules. This section investigates the variations in P_{cool} for the CPC-RC module tilted at different angles to the anti-sunward side. The aim is to identify the optimal tilt angle to obtain the highest daytime and nighttime $\overline{P}_{cool}$ on four typical days. Considering that a larger tilt angle will increase the heat exchange between the module and the ground, CPC-RC modules tilted at angles

ranging from 0° to 45° are chosen for investigation. Furthermore, spectral characteristics of the RC emitter in this section are consistent with those set in Section 4.3.2.

In Figure 4-12, the η_{sol_dir} for four tilted CPC-RC modules on four typical days is depicted. On the 21st of March and September, the same trend is observed: the highest η_{sol_dir} is obtained by the horizontally placed CPC-RC module, as the solar incident angle falls within its θ_{max}, which is not conducive to the cooling effect. Conversely, when the module is tilted to the anti-sunward side, whether at 15°, 30°, or 45°, the sunlight reaching the RC emitter is reduced, as the CPC functions as a solar shield at certain hours. However, during morning and evening periods, due to the sun's azimuth angle to the east and west, sunlight can reach the emitter through the module's side openings, causing η_{sol_dir} to be higher than at noon. On 21st March, η_{sol_dir} for 15°, 30°, and 45° tilted modules is 0.47,0.36 and 0.30 at 6:00, respectively. Fortunately, the impact of higher η_{sol_dir} on cooling power during these times is minimal due to its weaker solar intensity. Furthermore, On 21st December, thanks to the low solar altitude angle, the solar radiation reaching the RC emitters of all four modules is almost negligible.

In contrast, on 21st June, when the solar altitude angle approaches 90°, the horizontally placed CPC-RC module effectively concentrates sunlight for most of the daytime. For modules tilted 15° and 30° to the anti-sunward side, the duration during which the η_{sol_dir} exceeds 0.8 decreases from nine to six hours. Although this is suboptimal for daytime RC, η_{sol_dir} drops below 0.8 around noon. Specifically, when the module is tilted 30°, most sunlight is blocked by the CPC, and the η_{sol_dir} at noon is 0.36, which aids in reducing the P_{sol_dir} for the RC module.

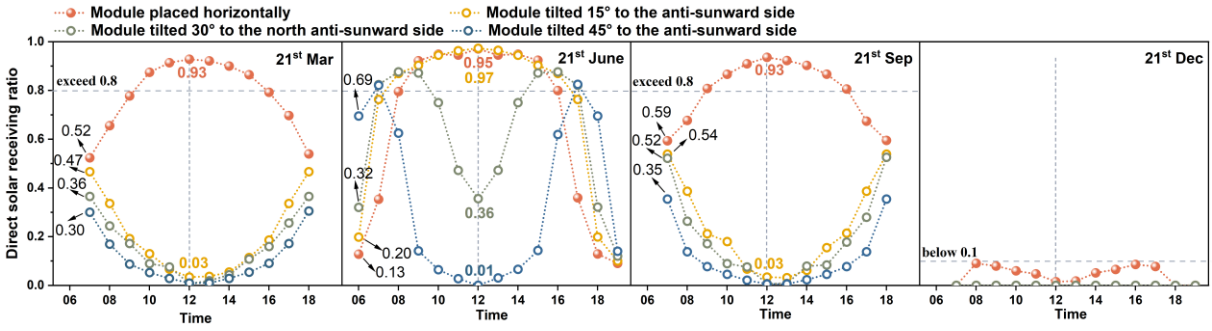

Figure 4-12: Direct solar receiving ratio for CPC-RC modules on four typical days.

When determining the η_{sol_dif} for the CPC-RC module with different tilt angles, it is found that if the CPC structure is not changed, the η_{sol_dif} for the RC module remains constant, regardless of the direction

or tilt angle, consistently staying around 0.485. Therefore, the same η_{sol_dif} will be used when characterizing the P_{sol_dif} for the module in this section.

Table 4-3 presents the ε_{env} for these CPC-RC modules. The T_{gro_day} increase results in higher ε_{env} compared to nighttime. It is observed that the horizontally placed CPC-RC module possesses the smallest ε_{env}, at 0.665. With an increase in the tilt angle to the anti-sunward side, ε_{env} correspondingly rises. Notably, when the module is tilted 45° to the anti-sunward side, ε_{env} reaches 0.702 at night and 0.706 during the daytime, indicating the thermal radiation absorbed by the module from the external environment increases under this configuration.

Table 4-3: Equivalent external environmental emissivity for the CPC-RC modules tilted at different angles to the anti-sunward side.

	Tilted 0°	Tilted 15°	Tilted 30°	Tilted 45°
ε_{env}(night)	0.665	0.670	0.678	0.702
ε_{env}(day)	0.665	0.670	0.680	0.706

Table 4-4 displays the ρ_{sol_dir} for CPC in different tilted CPC-RC modules under direct sunlight. On the 21st of March and September, it shows that except for changes in ρ_{sol_dir} when the module is tilted 0°, the ρ_{sol_dir} for the other three modules titled to the anti-sunward side remains at 1, indicating that the sunlight reaches the emitter directly through the side openings. On 21st June, except for the ρ_{sol_dir} for the module tilted 45° to the anti-sunward side, which remains at 1, variations over time are seen in the other three.

Table 4-4: Effective direct sunlight reflectivity for the CPC-RC modules tilted to the anti-sunward side (module tilted 0° represents the module is placed horizontally).

		7:00	8:00	9:00	10:00	11:00	12:00	13:00	14:00	15:00	16:00	17:00	18:00
21st Mar	Tilted 0°	0.992	0.981	0.974	0.971	0.969	0.968	0.968	0.970	0.972	0.975	0.985	1
	Tilted 15-45°	1	1	1	1	1	1	1	1	1	1	1	1
21st June	Tilted 0°	1	0.977	0.976	0.973	0.972	0.971	0.972	0.973	0.975	0.978	1	1
	Tilted 15°	0.979	0.976	0.976	0.975	0.975	0.974	0.975	0.975	0.976	0.976	0.979	1
	Tilted 30°	0.978	0.977	0.972	0.970	0.975	0.977	0.975	0.970	0.972	0.977	0.978	1
	Tilted 45°	0.979	0.977	1	1	1	1	1	1	1	0.978	0.978	0.982
21st Sep	Tilted 0	0.992	0.981	0.974	0.971	0.969	0.968	0.968	0.970	0.972	0.975	0.985	0.997
	Tilted 15-45°	1	1	1	1	1	1	1	1	1	1	1	1
21st Dec	Tilted 0°		1	1	1	1	1	1	1	1	1	1	
	Tilted 15-45°		1	1	1	1	1	1	1	1	1	1	

Figure 4-13 depicts the P_{sol} (including P_{sol_dir} and P_{sol_dif}) absorbed by CPC-RC modules tilted at different angles to the anti-sunward side during the daytime on four typical days. On the 21st of March and September, the horizontally placed CPC-RC module exhibits significantly higher P_{sol} than the other three configurations, particularly at noon, with P_{sol} for 89.24 and 99.88 W/m^2, respectively, affecting the RC performance. In contrast, when the modules are tilted at 15°, 30°, and 45° to the anti-sunward

side, their P_{sol} is considerably. For instance, at noon on 21st March, the modules tilted at 15°, 30°, and 45° exhibit P_{sol} for 20.16, 17.15, and 16.22 W/m^2, respectively, with little difference among the three, indicating that the CPC begins to play a solar-shield function when the modules are tilted to the anti-sunward side. On 21st June, the P_{sol} for the module tilted at 15° to the anti-sunward side is similar to that of the horizontally placed module, exceeding 118.60 W/m^2 at noon, demonstrating that the CPC concentrates sunlight at this time. However, when the tilt angle reaches 30°, the P_{sol} for the module at noon drops by 90.2%, reflecting the lowest η_{sol_dir} at this time. In the morning and evening, higher P_{sol} is observed because solar radiation directly enters the module from the side openings. When the module tilts 45° to the anti-sunward side, the P_{sol} is significantly reduced, remaining below 40 W/m^2 most of the time, indicating effective solar radiation blocking by the CPC. On 21st December, aside from the horizontally placed CPC-RC module, the η_{sol_dir} for the other three modules is zero, indicating that no direct sunlight can reach the RC emitter. However, since the η_{sol_dir} of the horizontally placed CPC-RC module is less than 0.1, the direct solar radiation absorbed is also negligible. Consequently, the P_{sol} for the four modules throughout the day is almost equal, peaking at no more than 30 W/m^2.

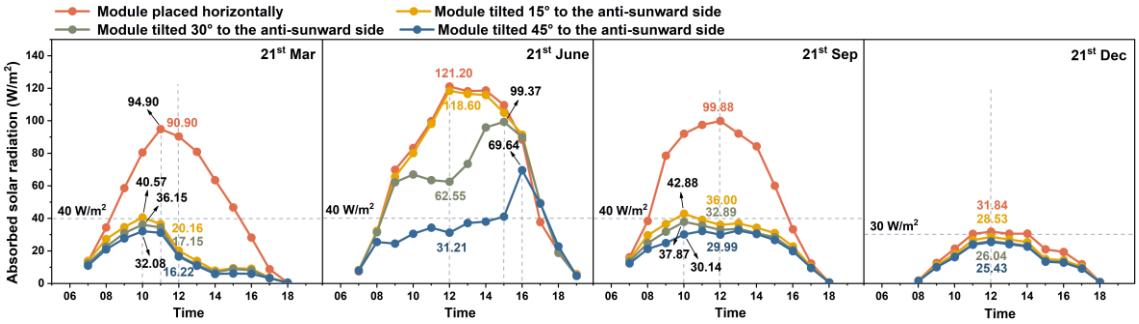

Figure 4-13: Absorbed solar radiation for CPC-RC modules on four typical days.

Figure 4-14 depicts the variations in hourly P_{cool} for the CPC-RC module at different tilt angles to the anti-sunward side on four typical days. On 21st March night, modules with larger tilt angles show less hourly P_{cool}. For instance, at 20:00, the P_{cool} of the horizontally placed CPC-RC module is 136.38 W/m^2, while it is 134.10 W/m^2 for the module tilted 15° to the anti-sunward side, 130.89 and 116.77 W/m^2 for the module tilted 30° and 45° to the anti-sunward side, respectively. In contrast, from 7:00 to 18:00 during the daytime, a significant difference is noted in the hourly P_{cool} for the horizontally placed module compared to other tilted modules. Specifically, due to absorbing more solar radiation, the P_{cool} for the horizontally placed module at noon is just 48.41 W/m^2, which is 57.9% lower than that of the

module tilted 15° to the anti-sunward side. However, it has been observed that an increase in the tilt angle does not necessarily lead to a higher P_{cool}. During the daytime, modules tilted 15° and 30° to the anti-sunward side are found to have almost identical P_{cool} at the same time, but modules tilted 45° to the anti-sunward side exhibited a lower P_{cool} than those at the smaller angles, which is 15.2% lower than the module tilted at 15° to the anti-sunward side. The reduction in P_{cool} for the modules with greater tilt angles is due to the enhanced impact of external environmental radiation on the modules. The change trend in P_{cool} of 21st September is observed to be similar to that on 21st March. However, due to the increased ambient temperature, the P_{cool} at the same hour on 21st September is higher than that on 21st March.

On 21st June night, the horizontally placed module is shown the highest hourly P_{cool}, while the same hour P_{cool} for other modules show a gradual decrease with an increase in the tilt angle of modules. For instance, at 20:00, the cooling performance of the module tilted 45° to the anti-sunward side exhibited a 14.4% reduction compared to the horizontally placed module. Conversely, during the daytime, a shift in the cooling effect of four modules is observed. For the module placed horizontally and tilted 15° to the anti-sunward side, the CPC does not function as a solar shield, resulting in the P_{cool} curves of the two being almost identical and reaching a minimum around noon. In contrast, in the case of modules tilted more than 30° to the anti-sunward side, most of the sunlight is blocked by the CPC, leading to enhanced P_{cool}. For instance, the P_{cool} for modules placed horizontally and tilted 15° to the anti-sunward side are 38.65 and 38.85 W/m^2 at noon, which are considerably lower than the 87.94 and 101.83 W/m^2 obtained in modules tilted 30° and 45° to the anti-sunward side.

The performance trends of the four modules on 21st December are remarkably consistent. This consistency arises because the CPC effectively blocks sunlight, limiting the emitters to heat exchange only with the local surroundings and the sky. However, an increase in the tilt angle of the CPC-RC module will enhance the heat transfer with the warm ground and consequently reduce in P_{cool}. Specifically, the cooling performance of the module tilted 45° to the anti-sunward side is 15.8% lower compared to that of the horizontally placed module at noon.

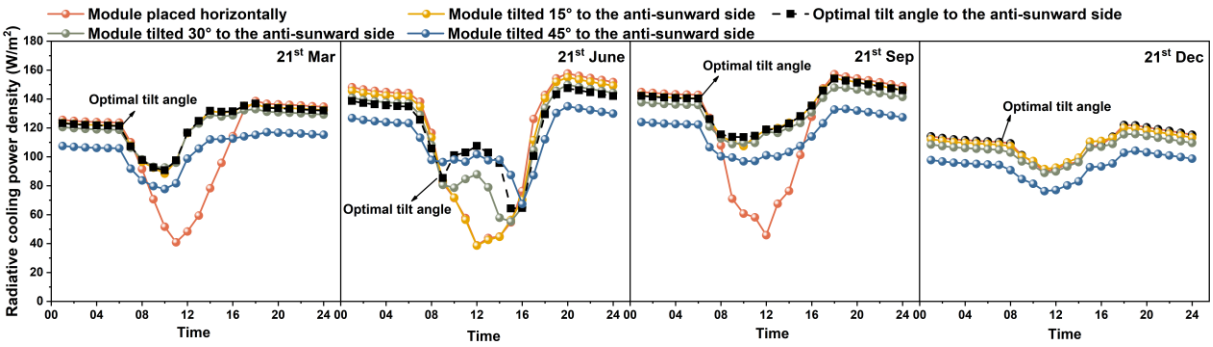

Figure 4-14: Difference in hourly cooling power density for CPC-RC modules on four typical days.

Figure 4-15 (a) illustrates the daytime and nighttime $\overline{P}_{cool}$ for the CPC-RC module under various tilt angles to the anti-sunward side. The optimal tilt angle of the module on four typical days is determined by characterizing the $\overline{P}_{cool}$ for the module from placed horizontally to a 45° tilt, in 1° increments. Furthermore, the hourly P_{cool} curve of the module tilted at the optimal angle is also shown in Figure 4-14 (the black line). On 21st March, tilting the module 16° to the anti-sunward side can obtain the highest daytime $\overline{P}_{cool}$ at 115.98 W/m^2, 34.8% higher than the horizontally placed module. At night, its $\overline{P}_{cool}$ reaches 127.55 W/m^2, only 2.55 W/m^2 lower than the horizontal configuration. The daytime optimal tilt angle on 21st September mirrored that of 21st March, achieving the $\overline{P}_{cool}$ of 125.67 W/m^2 at 16° tilt. Furthermore, the best nighttime performance is also observed at module tilted at 0°, with the $\overline{P}_{cool}$ of 147.98 W/m^2. However, conditions on 21st June differed significantly. When tilting at 15° to the anti-sunward side, the module's daytime $\overline{P}_{cool}$ is low, at 85.89 W/m^2. This low performance is due to the η_{sol_dir} curve at this angle being similar to that of the horizontally placed module, indicating that the CPC does not effectively shield solar radiation. As the tilt angle exceeds 25°, the CPC begins to serve its solar shielding function, increasing $\overline{P}_{cool}$. Furthermore, when increasing the tilt angle to 35°, the module achieves the highest $\overline{P}_{cool}$ of 102.21 W/m^2, 15.7% higher than the horizontally placed module. However, at the same tilt angle, nighttime $\overline{P}_{cool}$ decreased to 140.12 W/m^2, which is 6.8% lower than the 149.75 W/m^2 observed with the module placed horizontally. Finally, on 21st December, the highest daytime and nighttime $\overline{P}_{cool}$ can be obtained when the module is placed horizontally, at 102.00 and 115.51 W/m^2, respectively.

These findings indicate that while a 16° tilt to the anti-sunward side enhances daytime performance in March and September, it slightly underperforms at night compared to horizontal placement. However,

due to the differences being minor, maintaining a consistent tilt angle could simplify operations. Yet, for June, considering the significant decrease in nighttime cooling power at a 35° tilt, adjusting the tilt angle promptly may be necessary. When timely adjustment of the tilt angle is challenging, a fixed angle should be selected to achieve optimal all-day cooling performance, as shown in Figure 4-15 (b). Although tilting the RC module 25° toward the back in the summer may result in less competitive daytime RC, it achieves the best $\overline{P}_{cool}$ throughout the day, reaching 121.29 W/m^2.

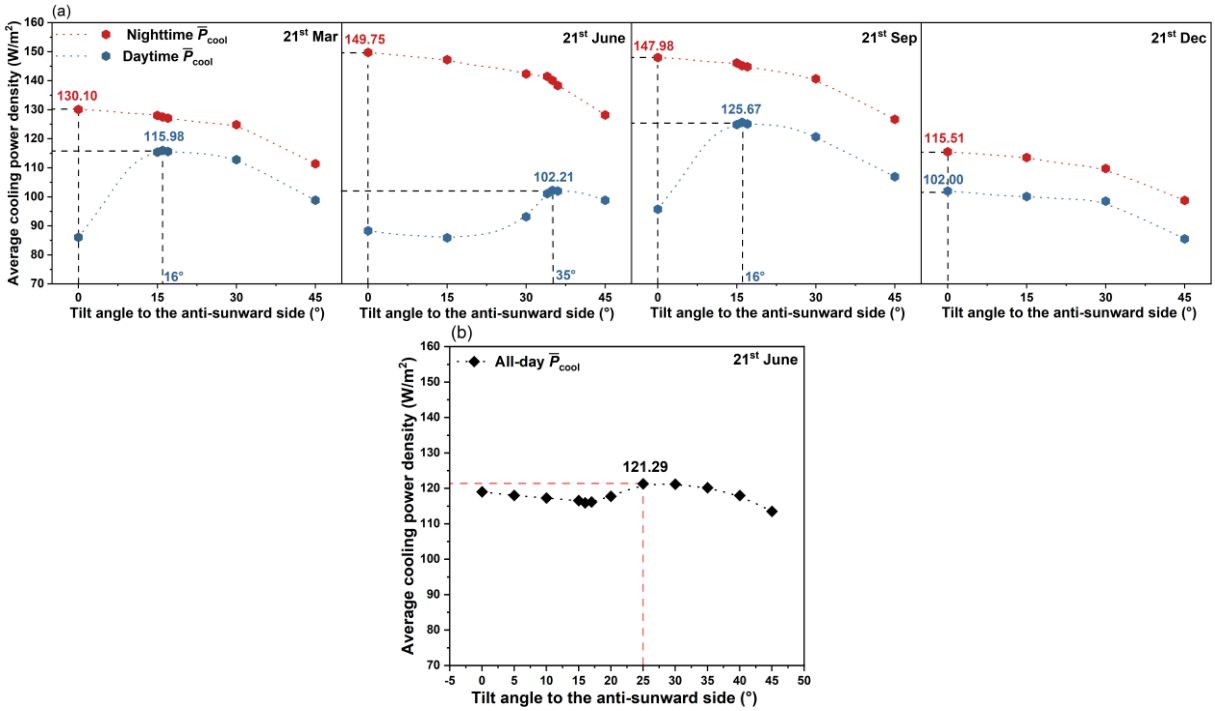

Figure 4-15: (a) Average cooling power density of CPC-RC modules with different tilt angles during the daytime and nighttime in Guangzhou, China. (b) Optimal tilt angle to obtain best all-day cooling performance on 21st June in Guangzhou, China.

4.3.4 Performance analysis of CPC-RC module with different RC emitters

The previous section established that optimal cooling performance is achieved by tilting the CPC-RC module at a specific angle to the anti-sunward side. However, the RC emitter assumed in the analyses possess favourable spectral characteristics, with a solar absorptivity and weighted average emissivity of 0.1 and 0.95. As mentioned previously, achieving near-ideal spectral characteristics typically involves high production costs and complex manufacturing processes, which could impede the broader adoption of RC technology. The analysis of this section aims to determine whether the CPC-RC module tilted at optimal angle to the anti-sunward side can mitigate the strict spectral requirements of the RC. In this section, the flat-RC module is placed horizontally on four typical days, but the CPC-

RC module is tilted at different angles. Specifically, it is tilted 16° to the anti-sunward side on the 21st of March and September, tilted 35° to the anti-sunward side on 21st June, and placed horizontally on 21st December.

The weighted average absorptivity/emissivity of the flat-RC emitter and three CPC-RC emitters are shown in Figure 4-16. Among them, the spectral characteristics of the flat-RC emitter are close to those of an ideal RC emitter, with its solar absorptivity set to 0.05 and its broadband infrared emissivity set to 0.95. Case 1 emitter features the same solar absorptivity of the flat-RC emitter at 0.05 but with a slightly lower broadband emissivity of 0.9. Cases 2 and 3 maintain a high broadband infrared emissivity of 0.95, but increase the solar absorptivity to 0.1 and 0.15, respectively.

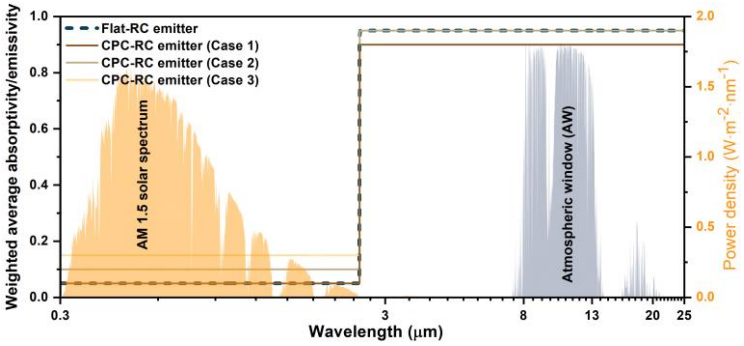

Figure 4-16: Spectral properties of the different RC emitters.

Figure 4-17 (a), (b) and (c) display the hourly P_{cool}, daytime and nighttime $\overline{P}_{cool}$ alongside the all-day $\overline{P}_{cool}$ for different RC modules using different RC emitters on four typical days. On 21st March, the CPC-RC module with Case 1 or 2 emitter shows higher hourly P_{cool} than the flat-RC module throughout the day. However, when the CPC-RC module uses Case 3 emitter (with a solar absorptivity of 0.15), its hourly P_{cool} falls below that of the flat-RC module from 8:00 to 12:00 due to higher P_{sol}. Observations of the daytime and nighttime $\overline{P}_{cool}$ across the four RC modules reveal that the flat-RC module, even with a near-ideal emitter, consistently exhibits lower $\overline{P}_{cool}$ than the three CPC-RC modules. For instance, when the CPC-RC module utilizes the Case 3 emitter, its daytime $\overline{P}_{cool}$ remains 8.46 W/m^2 higher than that of the flat-RC module (97.93 W/m^2). Additionally, at night, despite the poorer emissivity of the Case 1 emitter, the CPC-RC module's cooling performance is still 9.6% superior to that of the flat-RC module. The cooling trend of the four RC modules on 21st September is similar to that in March. The

higher ambient temperature brings the hourly P_{cool} curves of the CPC-RC module using Case 3 emitter closer to those of the flat-RC module.

However, on 21st June, even with the CPC-RC module tilted 35° to the anti-sunward side, it did not consistently outperform the flat-RC module in terms of P_{cool} throughout the day. There are several hours when P_{cool} is lower than the flat-RC module, regardless of the emitter used. Notably, the hourly P_{cool} curve of the CPC-RC module fluctuates more as the solar absorptivity of the RC emitter increases. Especially at 9:00 and 15:00, higher P_{sol} substantially reduces the module's P_{cool}. For instance, when using the Case 3 emitter, the CPC-RC module achieves the P_{cool} of only 41.04 W/m^2 at 15:00, which is 59.7% lower than that of the flat-RC module. Additionally, its overall daytime $\overline{P}_{cool}$ is 84.63 W/m^2, still 22.3% lower than the $\overline{P}_{cool}$ obtained in the flat-RC module. This occurs because even when the CPC-RC module is tilted at the optimal angle to avoid direct solar radiation, the intense diffuse solar radiation significantly impacts its P_{cool}. Therefore, to enhance daytime cooling effect, the solar absorptivity of the RC emitter should not exceed 0.1 during summer, or further strategies should be explored to minimize the absorption of diffuse solar radiation by the CPC-RC module. Conversely, on 21st December, the horizontally placed CPC-RC modules effectively shaded most solar radiation. When CPC-RC modules use Case 1 or 2 emitters, their cooling performance consistently surpasses the flat-RC modules throughout the day. However, the hourly P_{cool} for the CPC-RC module with Case 3 emitter is slightly lower than that of the flat-RC module for four morning hours due to the higher solar absorptivity. Nevertheless, when comparing the $\overline{P}_{cool}$ for the four RC modules, the flat-RC module consistently shows the lowest performance during the daytime and nighttime, 5.3% and 15.3% lower than the CPC-RC module with Case 3 emitter, respectively.

When discussing the all-day $\overline{P}_{cool}$ for CPC-RC and flat-RC modules, it is evident that, even when the solar absorptivity of the CPC-RC module's emitter increases to 0.15, the all-day cooling performance of the CPC-RC module is higher than that of the flat-RC module, except in summer. For example, on 21st March, the $\overline{P}_{cool}$ for the CPC-RC module with the Case 3 emitter is 117.84 W/m^2, which is 13.3% higher than that of the flat-RC module.

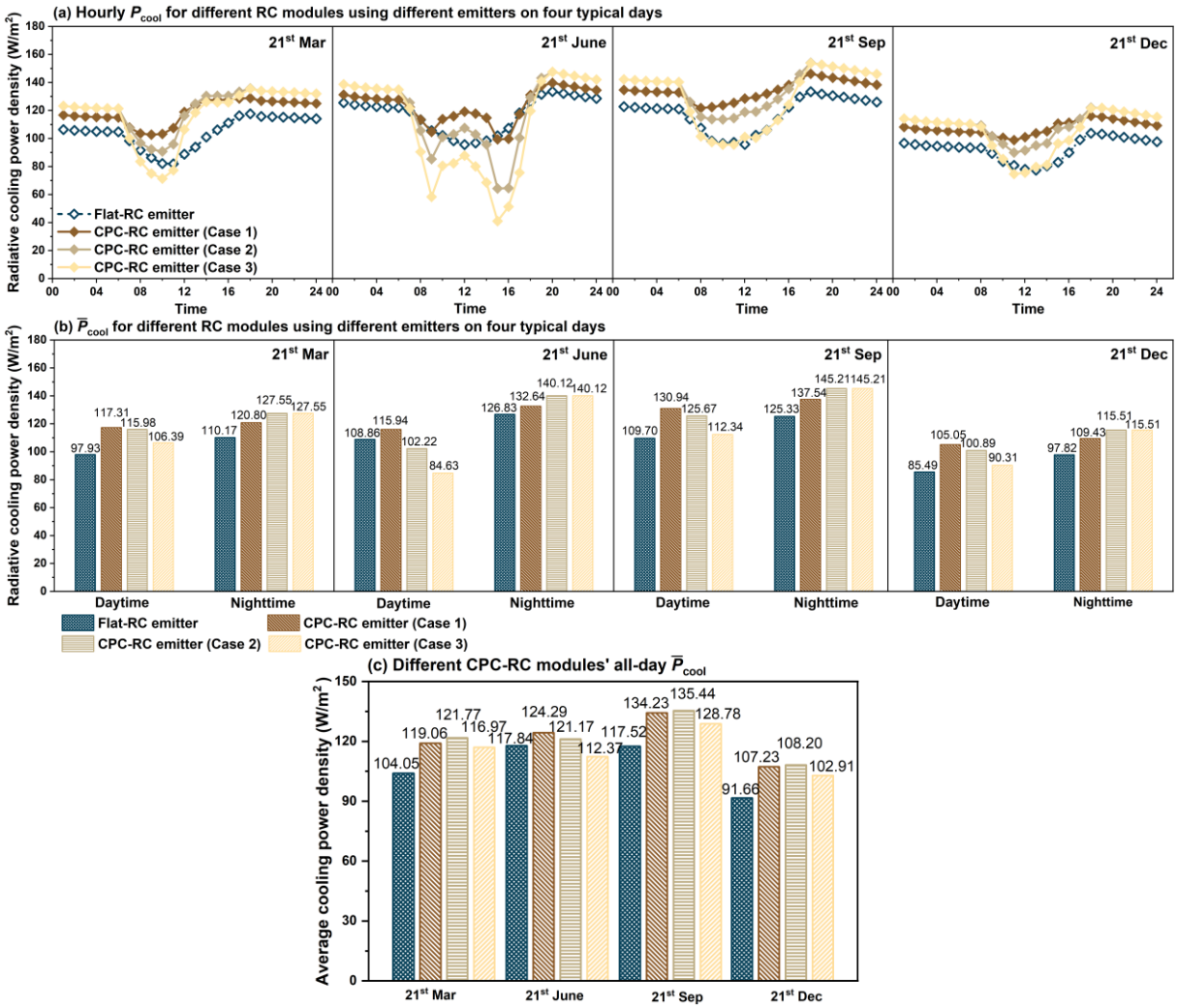

Figure 4-17: (a) Difference in hourly cooling power density and (b) daytime and nighttime average cooling power density for the CPC-RC modules tilted at the optimal tilt angle with different RC emitter on four typical days. (c) All-day average cooling power density for different RC modules on four typical days.

The performance comparison between CPC-RC and flat-RC modules with different RC emitters shows that when the emitter's solar absorptivity is 0.15, the all-day $\overline{P}_{cool}$ for the CPC-RC module is generally higher than that of the flat-RC module, except in summer. For instance, on 21st March, the all-day $\overline{P}_{cool}$ for the CPC-RC module is 116.97 W/m^2, 12.4% higher than that of the flat-RC module.

4.4 Comparative experiment of CPC-RC module against other RC modules

In the previous section, we employed modelling approach to analyse the cooling performance of CPC-RC modules on various typical days. In this section, we will further verify the cooling advantages of CPC-RC modules through field experiments.

4.4.1 Design and preparation of experimental RC modules

The schematic cross-section view of the experimental CPC-RC module is depicted in Figure 4-18. The CPC-RC module consists of two CPC-shaped reflectors, a transparent polyethene (PE) film, an RC emitter, and a thermal insulation layer. The reflectors are two symmetrical paraboloids, each 15 mm thick, covered with 0.3 mm aluminium mirrors with extremely high reflectivity in the range of 0.3-25 μm (see Figure 4-19). The total length of the reflectors is 200 mm. The front aperture of CPC (A) has a width of 60 mm, while the exit aperture (W) has a width of 30 mm. Based on the theoretical concentration ratio of the CPC [21], the CPC has a concentration ratio (C) of 2×, and the θ_{max} is 30°. Once the θ_{max} of the CPC is determined, the focal length and the parabolic equation for the compound parabola can be calculated, as expressed by the following formula:

$$f = W / 2(\sin\theta_{max} + 1) \tag{4.9}$$

$$y = \frac{1}{4f} x^2 \tag{4.10}$$

where f is the focal length of the CPC; θ_{max} can be determined based on the C.

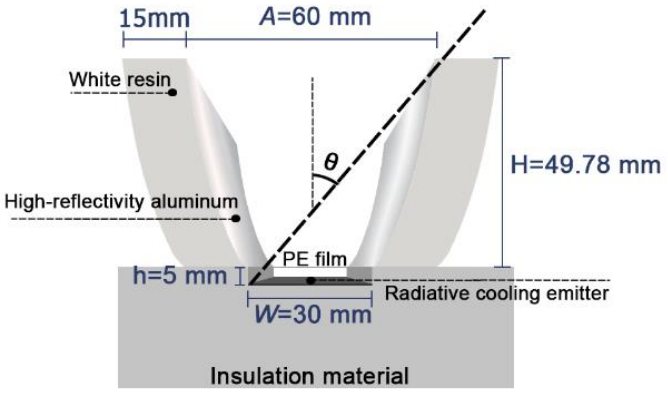

Figure 4-18: Schematic cross-section view of the experimental CPC-RC module.

To minimize convective heat transfer between the radiative emitter and ambient air, a 15 μm thick PE film is placed 5 mm above the emitter, creating an air gap. The PE film exhibits high transmittance (around 0.9) in the range of 0.2-25 μm. For the experiment, a hybrid metamaterial-covered RC emitter formed by a 0.4 mm thick aluminium plate and metamaterial is selected [242]. Figure 4-19 illustrates the spectral properties of this RC emitter and another black-painted RC emitter as a comparison group. The black-painted RC emitter exhibits a weighted average solar absorptivity of 0.66, while the metamaterial-covered RC emitter has a significantly lower weighted average solar absorptivity of 0.13.

However, both materials exhibit a high weighted average emissivity of 0.94 in the AW, indicating their strong thermal radiation capacity. To minimize cooling losses on the backside of the emitter, a 45 mm thick foam insulation layer is placed at the bottom.

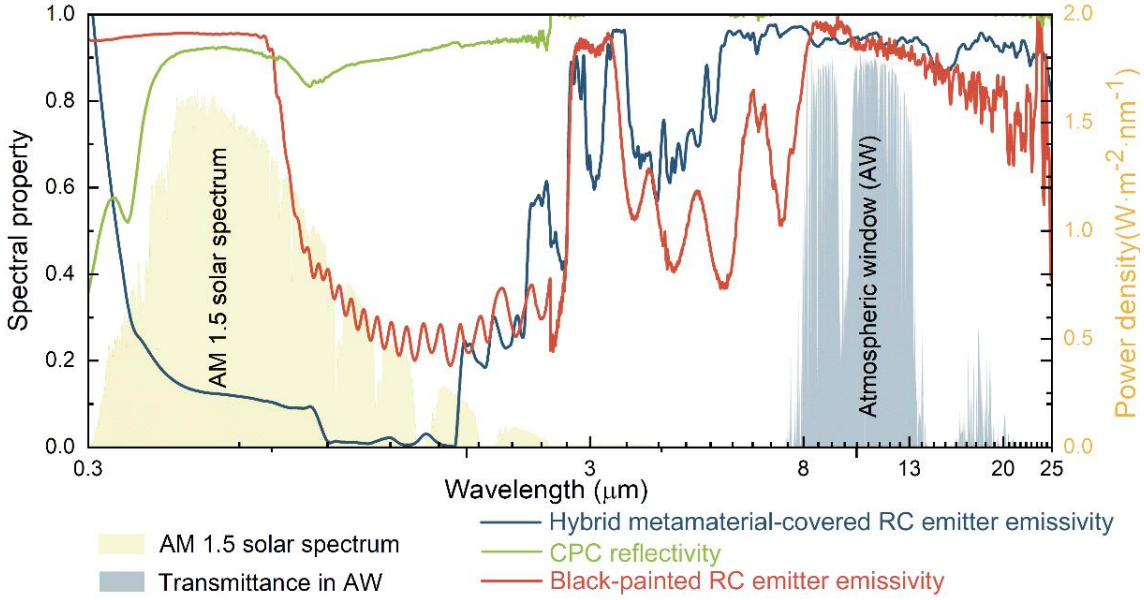

Figure 4-19: Spectral characteristics of the metamaterial-covered emitter, black-painted emitter, and CPC surface. The reason for the CPC reflectivity exceeding 1 after 3 μm in the graph is that the measured reflectivity of the CPC surface by the Fourier Transform Infrared Spectrometer surpassed that of the reference material.

Figure 4-20 depicts the experimental setup of the whole system. The experimental system comprises several key components, including different RC modules, K-type thermocouples, a thermocouple shelter, a weather station, a pyranometer, a data logger, and a computer. The K-type thermocouples, calibrated by a high-precision mercury thermometer with an uncertainty of only ±0.05 °C, are positioned at the centre of the backside of the RC emitters to record the emitter temperature. Additionally, another thermocouple, protected by the thermocouple shelter, is placed separately to measure the ambient temperature. The weather station records weather parameters such as wind speed and relative humidity. The pyranometer is utilized to measure the solar radiation on the plane where the module is situated. The test and monitoring devices, along with their uncertainties, are listed in Table 4-5.

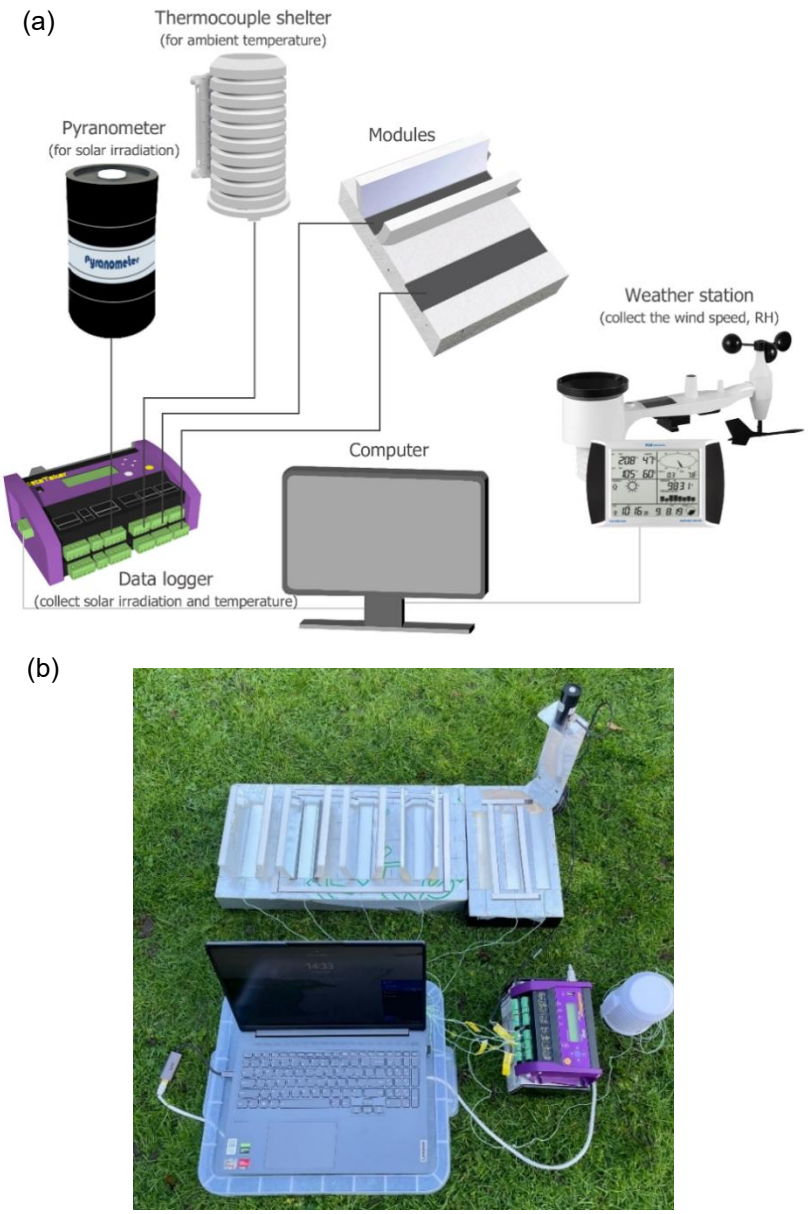

Figure 4-20: (a) Schematic of the RC experimental system. (b) In-situ experimental setup of the RC system. The experimental system is located in the open field at the University of Nottingham (52.94°N, 1.09°W), UK with the site altitude being 60 m.

Table 4-5: List of testing and monitoring devices in the experimental system.

Device	Specification	Uncertainty
Data logger	Data Taker DT80	/
Pyranometer 1	SKL 2650	±2%
Pyranometer 2 and 3	SMP 3	±3%
Thermocouple (calibrated)	Type K	±0.05 °C
Weather station for wind speed	CE-FWS 20N-2	±1 m/s
Weather station for relative humidity	CE-FWS 20N-2	±4% within 20-80%

To evaluate the effect of CPC in the RC module and explore its potential as an alternative to the fragile PE film for wind shading, the first set of experiments compares the emitter temperature

difference between the main modules (CPC-RC and flat-RC modules) with and without PE film. Figure 4-21 illustrates the schematic of the experiment.

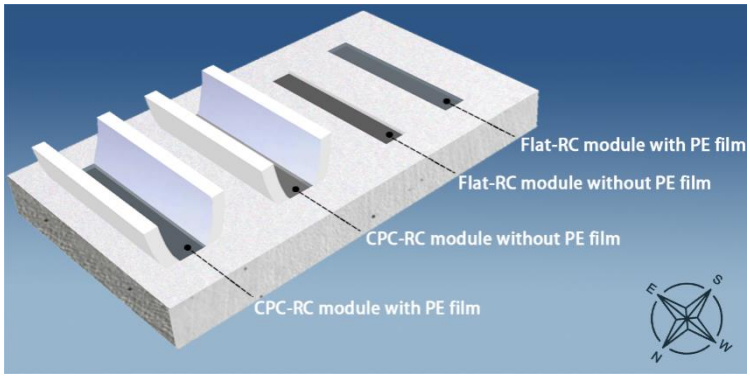

Figure 4-21: Experimental setup schematic of the CPC-RC and flat-RC modules with and without PE film.

Another comparative experiment is conducted to investigate whether a CPC offers potential advantages for cooling compared to other commonly used concentrators. This experiment involved three modules: a trapezoidal-RC module, a CPC-RC module, and a flat-RC module without any concentrator. Figure 4-22 illustrates the experimental setup for this group, in which the trapezoidal concentrator is designed with identical dimensions in terms of height, length, and width as the CPC. The concept of the geometric concentration ratio of the trapezoidal concentrator is also the same as that of the CPC [243]. The base angle of the trapezoidal concentrator is determined based on the geometric characteristics of the CPC, resulting in an equivalent geometrical concentration ratio of 2×.

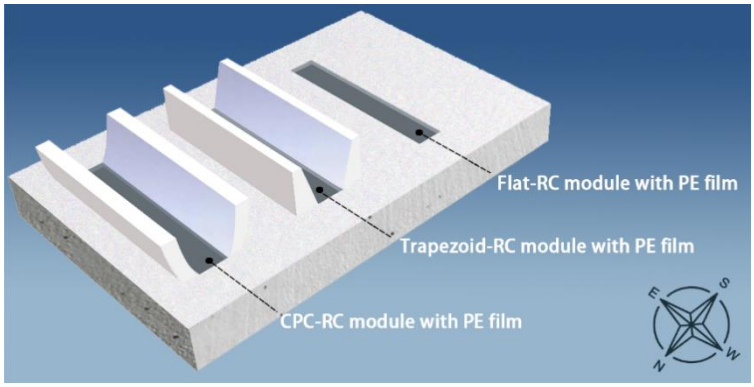

Figure 4-22: Experimental setup schematic of three different RC modules.

Given that building-integrated RC systems often feature RC modules installed on inclined roofs, a third set of experiments is carried out to assess and compare the cooling performance of the CPC-RC and flat-RC modules at various installation angles. Figure 4-23 illustrates the arrangement of the RC modules. The sunward group comprises one CPC-RC module and one flat-RC module positioned at a 30° inclination angle facing due south. The anti-sunward group consists of one CPC-RC module and

one flat-RC module positioned at a 30° inclination angle towards due north. Additionally, the comparative experimental group includes one CPC-RC module, and one flat-RC module placed horizontally.

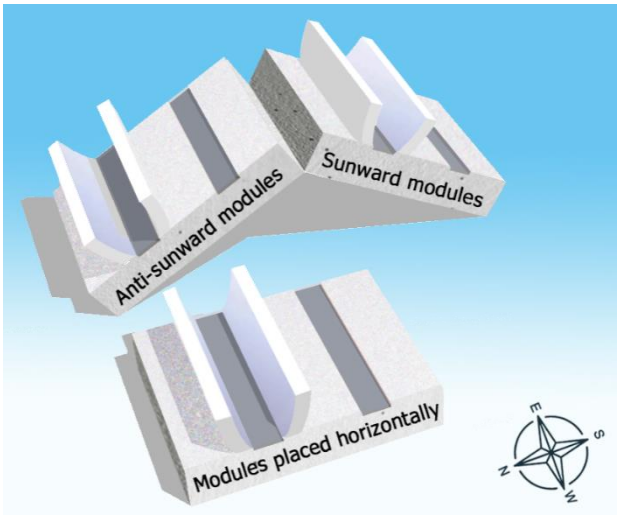

Figure 4-23: Experimental setup schematic of three different RC groups under different placements.

4.4.2 Performance of CPC-RC and flat-RC modules with and without PE film

In this experiment, the cooling performance of CPC-RC and flat-RC modules with and without PE film was compared to verify the advantage of CPC in RC modules. Figure 4-24 (a) displays the nocturnal meteorological parameters in Nottingham on 16th May. The ambient temperature exhibited a gradual decrease from 12.29 °C to 7.29 °C during the time span from 21:00 to 23:00. The sky was predominantly clear with minimal cloud cover, and the wind speeds remained relatively low, originating from the east-northeast direction. Significantly, the wind direction aligned almost parallel to the CPC's reflectors, resulting in the wind could through the entire module via the CPC side openings. When employing a PE film to reduce thermal losses arising from convection and conduction, the CPC-RC module theoretically enhances its cooling capacity by constraining the emitted and absorbed thermal radiation within the half-acceptance angle. As expected, the experimental results depicted in Figure 4-24 (b) corroborated the significant cooling effect obtained by the CPC-RC module with the PE film. This module consistently maintained the maximum temperature difference compared to the ambient temperature during the entire experimental period. The flat-RC module with PE film ranked second in terms of temperature reduction, demonstrating the effectiveness of RC-coated material in achieving RC at night.

Another objective of this experiment is to investigate the feasibility of utilizing a CPC as a substitute for a PE film to suppress convective heat exchange. The experimental results revealed that the CPC-RC module without the PE film did not achieve the same level of cooling performance as the flat-RC module with a PE film, indicating the CPC's failure in the wind-blocking during this specific test. The effectiveness of the wind-blocking function of the CPC mainly attributes to the wind direction. In cases where the wind velocity component in the length direction of the CPC is dominating, the side openings of the CPC allow wind to enter the module, thereby diminishing the wind-shielding effect, as observed in this experiment. However, it is worth noting that, when the wind velocity component in the length direction of the CPC is minimal or if a CPC without side openings is employed, the CPC may demonstrate potential in replacing the fragile PE film to mitigate convective heat exchange between the RC emitter and ambient air, which requires further experimental demonstration in future studies.

Although this experiment cannot definitively establish the potential of CPC to replace PE film, it highlights CPC's contribution to improving the RC effect. As shown in Figure 4-24 (b), around 22:20, all modules experienced a certain degree of temperature increase attributable to the presence of thin cloud cover in the sky. This phenomenon is raised from the heightened moisture content introduced by the clouds into the atmosphere, resulting in diminished atmospheric transparency and consequent attenuation of the RC effect. However, the clouds dissipated shortly thereafter, and the temperature of the emitters gradually decreased, albeit at a reduced rate, reaching its lowest point at 23:00. Towards the end of the experiment, the CPC-RC module with PE film achieved the lowest emitter temperature, measured at 1.68 °C. This temperature was 1.55 °C lower than the flat-RC module with PE film and 2.18 °C lower than the CPC-RC module without PE film. The temperature difference (ΔT) between the average emitter temperature and ambient temperature during the experiment is plotted in Figure 4-24 (c). The CPC-RC module with PE film exhibited the most substantial temperature difference, reaching 5.83 °C, 30% higher than the emitter temperature reduction observed in the flat-RC module with PE film. These results underscore the considerable potential of combining the CPC and PE film with RC modules to enhance its cooling performance. It has to be acknowledged that, the emitter temperature drop observed in all modules during this experiment is relatively modest compared to the temperature

drops reported in other works [18]. This discrepancy can be attributed primarily to the exceptionally humid climate of the test site in the Nottingham area. However, it does not undermine the evidence supporting the positive impact of CPC on enhancing RC performance.

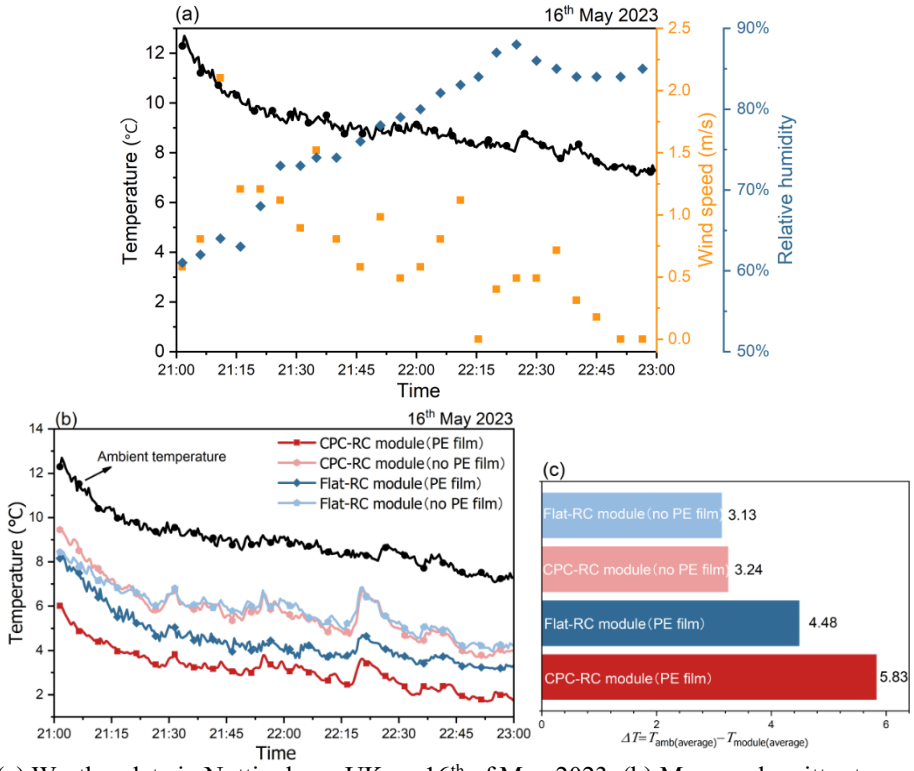

Figure 4-24: (a) Weather data in Nottingham, UK on 16th of May 2023. (b) Measured emitter temperatures of the CPC-RC and flat-RC modules with or without PE film. (c) Average temperature differences (ΔT) between the ambient air and emitters.

4.4.3 Performance of CPC-RC, trapezoidal-RC and flat-RC modules

The second set of experiment compared the cooling performance of three different RC modules, including a CPC-RC module, a trapezoidal-RC module, and a flat-RC module. This experiment was conducted simultaneously with the first set of experiment in Section 4.4.2. A PE film was installed on the top surface of each emitter to minimize the effect of heat convection. Figure 4-25 (a) illustrated the nocturnal emitter temperature of the three modules. Consistent with the findings of the first experiment, the CPC-RC module exhibited the most significant temperature reduction among the three modules, indicating the high potential of CPC in enhancing RC capabilities. The trapezoidal-RC module, also benefiting from its concentrators, achieved a greater temperature drop compared to the flat-RC module. Nevertheless, despite having the same geometric concentration ratio as the CPC, the trapezoidal-based module exhibited inferior focusing ability due to its lack of a specially designed curved surface that

optimizes light concentration. Consequently, its RC performance was lower than that of the CPC-RC module. Figure 4-25 (b) presented the average temperature difference between the emitter and ambient air. The CPC-RC module demonstrated the most substantial average temperature reduction, reaching 5.83 °C. The trapezoidal-RC module followed closely with an average temperature reduction of 5.13 °C, showcasing an enhancement of 14.5% compared to the temperature drop observed in the flat-RC module. However, this improvement fell significantly lower than the 30% enhanced RC effect achieved by the CPC-RC module.

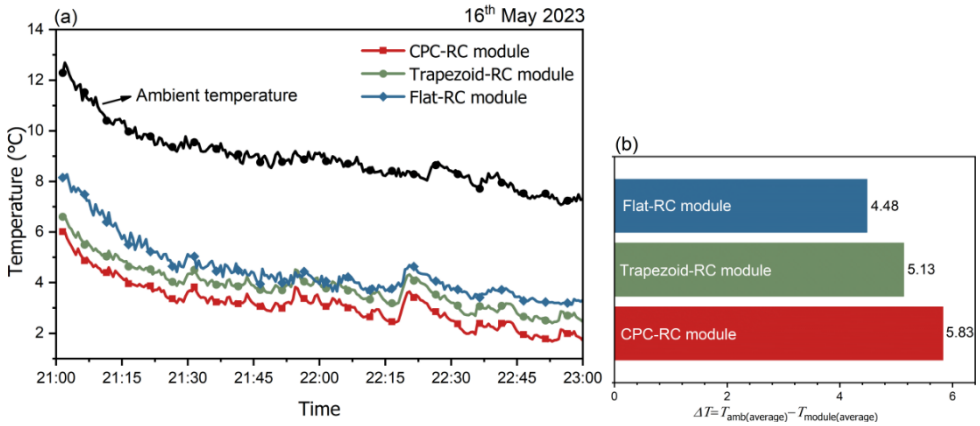

Figure 4-25: (a) Measured emitter temperatures of the CPC-RC, trapezoidal-RC and flat-RC modules. (b) Average temperature difference (ΔT) between the ambient air and emitters.

4.4.4 Performance of CPC-RC and flat-RC modules with different inclined placements

The shielding function of the CPC-RC module also offers a promising solution to overcome challenges faced in utilizing RC technology as a passive cooling strategy for buildings. Typically, RC modules are installed on the roofs or vertical surfaces of buildings. Installing an RC module on a flat roof can achieve efficient cooling capacity. Conversely, when installed on vertical surfaces or steep roofs, the amount of P_{atm} and P_{sur} reaching the RC emitter surface increases, resulting in reduced cooling capability. However, CPC-RC modules can block unfavourable radiation from large incident angles. This characteristic presents a potential solution to mitigate the negative impact resulting from tilted installations. Therefore, the objective of the third experiment is to assess whether the cooling advantages offered by the CPC-RC module can compensate for the inhibitory effects associated with tilted placements. This will be accomplished by analysing the temperature variations of both the CPC-RC module and the flat-RC module under various placement conditions. Additionally, the experiment aims

to investigate the potential of a north-facing, tilted CPC-RC module in achieving effective RC throughout the day.

This experiment was conducted during two distinct periods: a clear night on the 2nd and a nearly cloudless day on the 24th of May. Figure 4-26 (a) illustrates the weather conditions during the nocturnal experiment. From 21:30 to 23:00, the ambient temperature gradually declined from 9.50 °C to 6.97 °C. During the first hour, a gentle breeze was present, but it had mostly subsided by 22:30, and the relative humidity remained constant at 84% to 89%. Due to the geographical conditions, there are a few trees and buildings surrounding the north-facing tilted group, while the south-facing tilted, and horizontally placed module enjoy a more open view of the sky. These variables may contribute to minor variations in the results.

Figure 4-26 (b) shows the emitter temperature of six RC modules with three different placements. It is evident that the temperature variations among the emitters in all six modules followed similar trends. Among these modules, the CPC-RC module placed horizontally exhibited the lowest emitter temperature, whereas the flat-RC module facing north recorded the highest emitter temperature. Figure 4-26 (c) showed the average temperature difference between the emitters and ambient air. In the horizontal placement group, the CPC-RC module achieved optimal cooling performance, with a temperature drop surpassing that of the flat-RC module by 0.62 °C.

The cooling performance of the south-facing group modules was comparatively lower than that of the CPC-RC module in the horizontal placement group. In particular, the flat-RC module exhibited worse cooling performance than the same module in the horizontal placement group. This is attributed to the increased zenith angle, which causes thermal radiation to pass through a portion of the atmosphere with lower transmittance before reaching space. Additionally, an emitter placed at an angle experiences a reduced sky view factor, leading to heat exchange with warmer surroundings (e.g., the ground, trees, and buildings) rather than with the cooler sky. However, the adverse effects of oblique placement can be mitigated by the CPC design, as demonstrated by the fact that the emitter temperature of the CPC-RC module in the south-facing group was 0.21 °C lower than that of the flat-RC module in the horizontal placement group.

Both modules in the north-facing group exhibited lower cooling performance during the experiment. This phenomenon was due to the obstruction caused by trees and buildings, blocking the thermal radiation emitted by the emitters from reaching outer space, while also causing the emitters to absorb thermal radiation from the trees and buildings. Nevertheless, the emitter temperature of the CPC-RC module was still 0.24 °C lower than that of the flat-RC module.

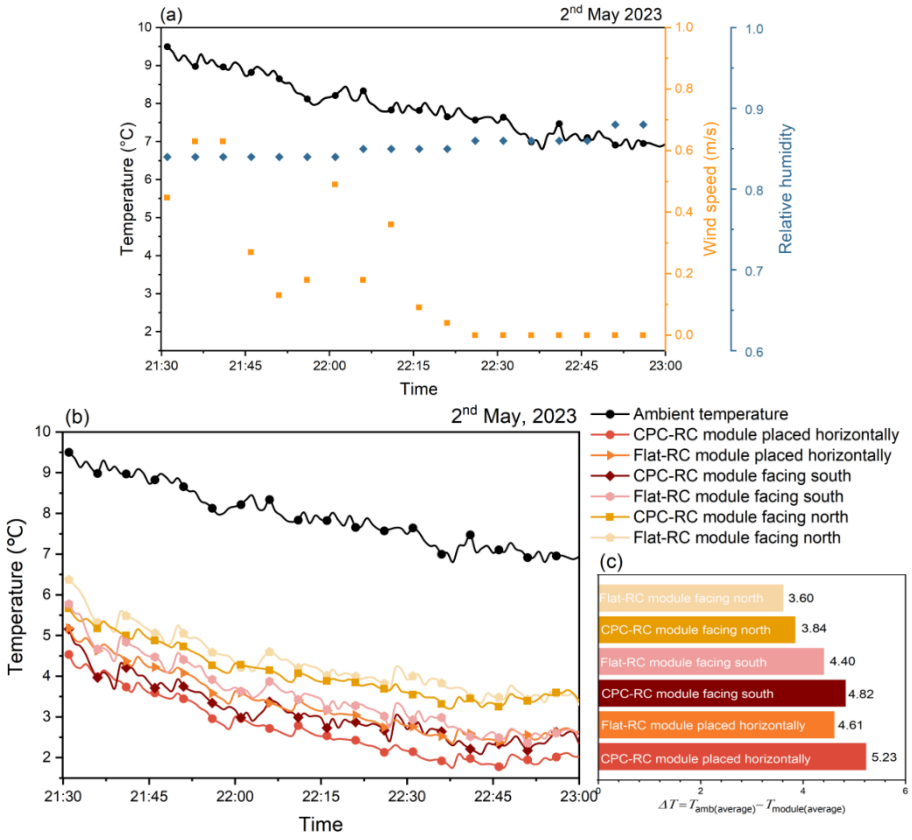

Figure 4-26: (a) Weather data in Nottingham, UK on 2nd of May 2023. (b) Measured emitter temperatures of the three placements. (c) Average temperature differences (ΔT) between the ambient air and emitters.

Figure 4-27 (a) depicted the weather conditions during the diurnal experiment. There were light and consistent wind speeds ranging from 0.25 to 1.5 m/s, while the relative humidity remained relatively stable within the range of 40% to 60%. The sunward group recorded the highest solar radiation, surpassing 1000 W/m^2 around 13:00. The horizontal placement group observed lower solar radiation than the sunward group, peaking at approximately 900 W/m^2. In contrast, the anti-sunward group recorded the lowest solar irradiance (the highest value was less than 545 W/m^2).

The emitter temperature of the six modules across the three RC modules were depicted in Figure 4-27 (b), alongside the ambient temperature. The figure clearly illustrated that the majority of modules failed to reach sub-ambient temperature, except for the CPC-RC module in the anti-sunward group.

Figure 4-27 (c) showed that the average emitter temperature of the CPC-RC module in the anti-sunward group was 1.59 °C lower than the average ambient temperature throughout the experimental period. Although the temperature difference narrowed at noon, it gradually increased over time. This behaviour could be thanked to the function of the CPC as a solar shield, effectively impeding a substantial portion of solar radiation from reaching the emitter. In contrast, the flat-RC module in the anti-sunward group exhibits considerably 3.90 °C higher than the ambient temperature. This discrepancy can be attributed to the absence of a CPC as a shading device, resulting in direct exposure to solar radiation.

With horizontal placement, neither of the modules achieved sub-ambient temperature. Unlike the anti-sunward group, the average temperature of the CPC-RC module in this group was 4.73 °C higher than that of the flat-RC modules, indicating that the CPC acted as a solar concentrator rather than a solar shield in this case.

In the sunward group, the solar incident angle was significantly smaller than the half-acceptance angle of the CPC, so the CPC effectively concentrated the sunlight onto the emitter. In addition, the flat-RC module was directly exposed to sunlight, resulting in much higher temperatures for the two modules throughout the experiment compared to the other two groups. As shown in Figure 4-27 (b) and (c), due to the concentrating effect of the CPC, the emitter temperature of the CPC-RC module exceeded 43.21 °C at noon, with an average temperature of 38.78 °C during the entire experiment, surpassing the flat-RC module in the same group by 3.26 °C and the same module in the horizontal group by 1.07 °C. While this temperature is beneficial for solar energy utilization, it can adversely impact RC performance.

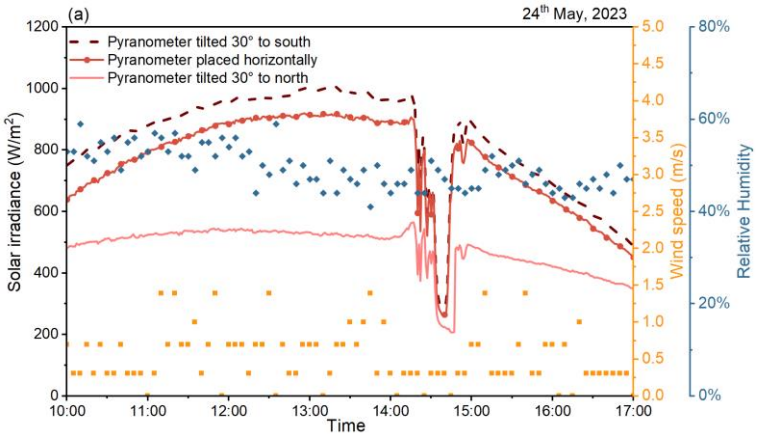

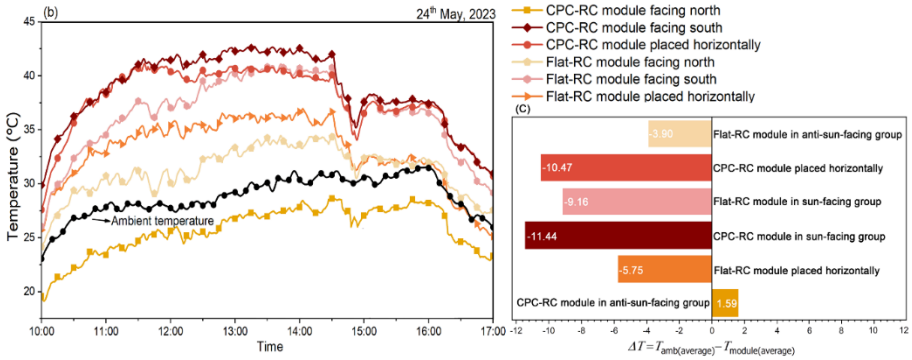

Figure 4-27: (a) Weather data in Nottingham, UK on 24th of May 2023, and solar irradiance received by pyranometers in different orientations. (b) The temperature of the 3 groups of modules during the day. (c) Average temperature differences ((Δ*T*) between the ambient air and emitters

4.5 Summary

This chapter employs proposed modelling approach to comprehensively evaluate the cooling performance of the RC module integrated with a compound parabolic concentrator (termed CPC-RC module) and demonstrates its solar radiation shielding advantages. Additionally, a series of outdoor experiments were conducted to compare the temperature reduction effects of CPC-RC modules with other RC modules, demonstrating that north-facing CPC-RC module can achieve all-day RC effects in Nottingham.

In summary, the CPC-RC module can achieve excellent nighttime cooling performance while alleviating the strict spectral selectivity requirements of the RC emitter. When tilted at an optimal angle to the anti-sunward side, it can also achieve high cooling power during the daytime, making it highly promising for reducing building cooling demands. These findings provide valuable insights for the development of efficient concentrated RC systems for building cooling applications.

However, while CPC-RC module tilting to the anti-sunward side can increase cooling power during the daytime, they compromise some cooling performance at night. Additionally, since CPC-RC module occupies more space than flat-RC modules, the effective cooling area is relatively reduced, which limits their advantage in building applications. Therefore, the next chapter will explore how to optimize CPC-RC modules to achieve improved cooling performance throughout the day.

5. Comprehensive analysis of RC module integrated with dissimilar material-based CPC (DCPC-RC module)

5.1 Introduction

Chapter 4 provides a detailed introduction to the novel CPC-RC module, employing a modelling approach to evaluate its cooling performance on different typical days. However, the results still reveal the negative impact of daytime solar radiation on the CPC-RC module, making it difficult to provide high-quality cooling during summer daytime. Although tilting the RC module to the anti-sunward side can mitigate this issue, the increased tilt angle also enhances heat exchange between the RC module and the external environment. Additionally, the configuration of the CPC-RC module lacks extra space for solar radiation utilization, preventing it from generating other forms of energy and causing a loss of solar resources. This limitation reduces its functional flexibility and year-round adaptability for various applications. Therefore, further discussion is warranted on solutions that can simultaneously address both challenges.

In this chapter, a novel RC module based on CPC with dissimilar materials (termed DCPC-RC module) is further proposed to address the challenges of solar radiation harassment on RC and the waste of solar radiation resources. Firstly, a preliminary numerical study is employed to accurately evaluate the absorbed solar radiation and obtained net cooling power density by the DCPC-RC module, comparing it with the mirrored CPC-RC module to demonstrate its ability to mitigate the impact of solar radiation. Additionally, this chapter examines the influence of various parameters, such as the DCPC wing frameworks with different spectral splitting films and the module's tilt angle, on the cooling performance of the module. Finally, this chapter analyses the hour's percentage occupied by different solar profile angles throughout the year in cities at varying latitudes to determine the optimal tilt angle for the DCPC-RC module that maximizes cooling performance.

5.2 Description of DCPC-RC module and solar profile angle

5.2.1 Introduction of DCPC-RC module

As illustrated in Figure 5-1, the DCPC-RC multi-module system comprises multiple identical DCPC-RC modules, with each module's side openings facing east-west. Within each DCPC-RC module, the DCPC wing frameworks are made of two different materials: the north-facing side features a transparent wing framework covered with a transparent infrared-reflective film (TIRF), which allows sunlight to pass through while reflecting infrared thermal radiation, while the south-facing side is a standard specular metal wing framework. The RC emitters are located at the bottom of the DCPC structures. Two adjacent modules are interconnected by their wing frameworks. Each module in the system features an aperture width of 40 mm and an emitter width of 20 mm. And the module's height and length are 40 and 200 mm, respectively. Additionally, to minimize non-radiative heat transfer, such as convection and conduction, a PE film is applied to the top of the RC emitter, with the DCPC structure mounted above the PE film.

In a typical mirror CPC-RC multi-module system, the space formed by the wing frameworks of adjacent modules remains unutilized, and only the bottom of the CPC serves as the effective cooling area, resulting in low utilization rates. However, in the DCPC-RC multi-module system, the yellow middle area created by the wing frameworks of adjacent modules can function as a solar collector, absorbing sunlight passing through the transparent side of the module. This configuration demonstrates the potential of this system to obtain cooling power and solar energy collection simultaneously. Nevertheless, the primary focus of this chapter is not on the utilization of solar energy by the system but rather on its impact on RC performance. Therefore, the utilization of the solar collector will not be involved in this chapter.

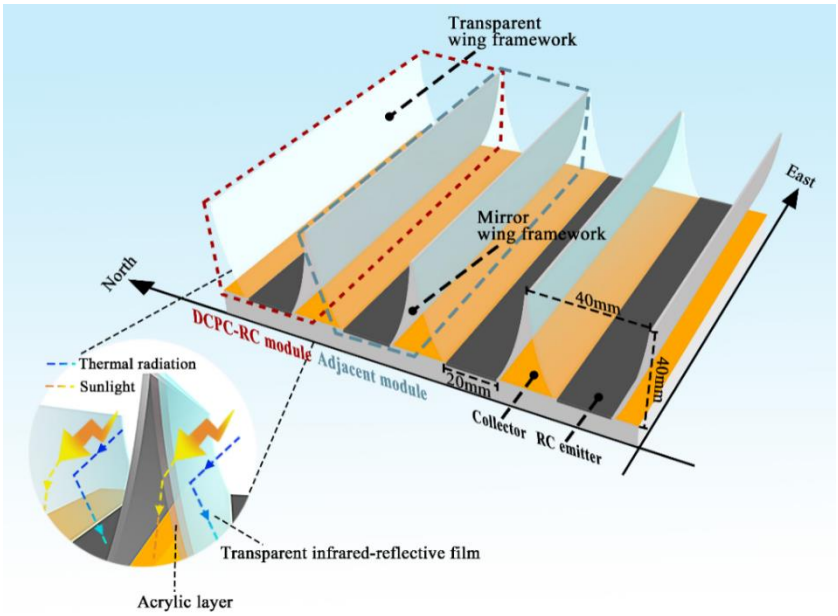

Figure 5-1: Schematic diagram of DCPC-RC multi-module system.

Figure 5-2 shows the radiative heat exchange between (a) the mirror CPC-RC module and (b) the DCPC-RC system and the surroundings. The traditional CPC with opaque mirror wing frameworks on both sides concentrates solar radiation, whose incident angle falls within the CPC's acceptance angle range, onto the RC emitter. This concentration typically weakens the cooling performance of the module during the daytime. In contrast, the transparent side of the DCPC structure allows solar radiation to pass through it to the collectors on the sides, thereby reducing its impact on the RC emitter. Moreover, since the transparent wing framework covered with TIRF exhibits high reflectivity under the "atmospheric window", the DCPC can concentrate the thermal radiation emitted by the RC emitter to a smaller range of zenith angles, similar to the mirror CPC. Finally, both structures can shield the unfavourable radiation from the sky and the sun whose incident angle exceeds the θ_{max} of CPC and DCPC, preventing it from reaching the RC emitter. Therefore, theoretically, DCPC-RC system's configuration enhances the cooling efficiency by reducing unwanted thermal gain during the day while maximizing cooling power under favourable conditions.

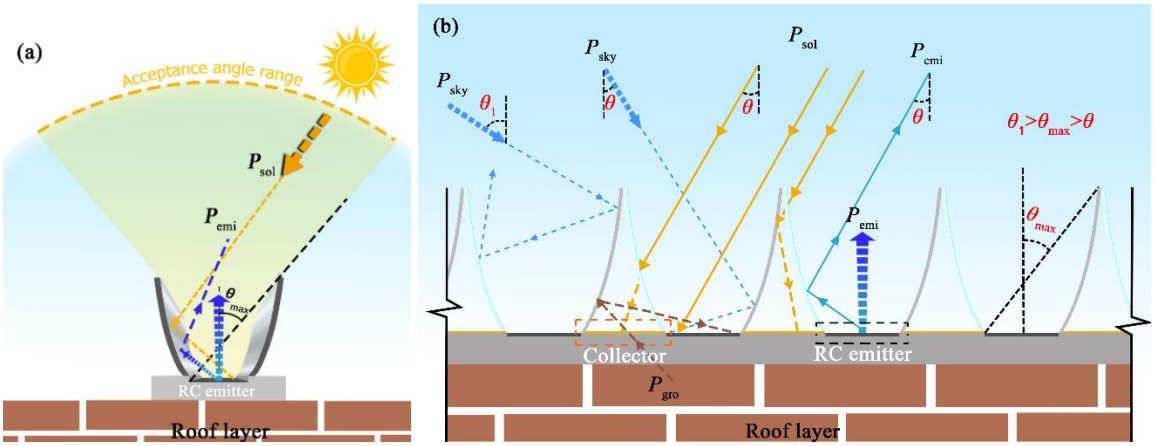

Figure 5-2: Radiative heat exchange between (a) mirror CPC-RC and (b) DCPC-RC system and external environment.

5.2.2 Solar profile angle

Previously, CPC application areas are generally focused on solar collections. To maximize the collection of solar radiation, the tilt angle of the solar energy collection system is adjusted according to the local solar path. However, in the DCPC-RC module, conducting a study on the solar path is also imperative, but the purpose changes to prevent incident sunlight from reaching the RC emitter. This will help mitigate the impact of solar radiation on cooling performance. As the solar azimuth angle (φ) and altitude angle (θ_h) change every moment, the solar position vector is divided into two projection components, i.e., east-west and north-south directions, as shown in Figure 5-3. Since the side openings of the DCPC-RC multi-module system are oriented east-west, whereby the projection components in the east-west direction are parallel to the module surface and do not contribute to the solar radiation absorbed by the module. However, the projection component in the north-south direction determines the amount of solar radiation absorbed [233]. In this chapter, the solar profile angle [244] is used to characterize the projection angle of the southern horizon and the solar position on the north and south meridian planes (ϕ in Figure 5-3), ranging from 0° (south horizon) to 180° (northern horizon).

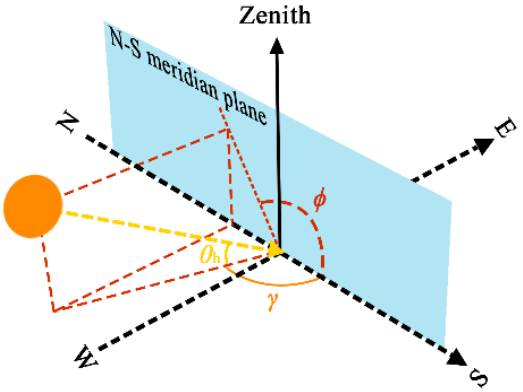

Figure 5-3: Definition of solar profile angle (ϕ).

5.3 Experiment study of DCPC-RC module

5.3.1 Experimental RC module

This section introduces the different RC modules and measuring equipment in the field experiment from the night of 25th June and the day of 26th in Nottingham (52.94 °N, 1.09 °W), UK, as shown in Figure 5-4. The whole experimental system is composed of several key components, including three RC modules, which are DCPC-RC, mirror CPC-RC, and flat-RC modules, K-type thermocouples, a data logger, a pyranometer, a weather station, a thermocouple shelter and a laptop. The pyranometer is used to measure the total solar irradiance of the plane where the modules are located. Meanwhile, the weather station obtains real-time weather parameters such as wind speed and relative humidity. Several K-type thermocouples are attached to the bottom of the RC emitters of different modules to measure the temperature of the emitter. The ambient temperature is measured by a thermocouple in the shelter at the same height as the module. All the measured data is collected by the data logger and collected in the laptop. Furthermore, to minimize convective and conductive heat transfer between the RC emitter and ambient air, a 15 μm thick PE film is positioned 5 mm above the emitter. Some test and monitoring equipment and their uncertainties are listed in Table 5-1. The uncertainties of other instruments are described in Table 4-5.

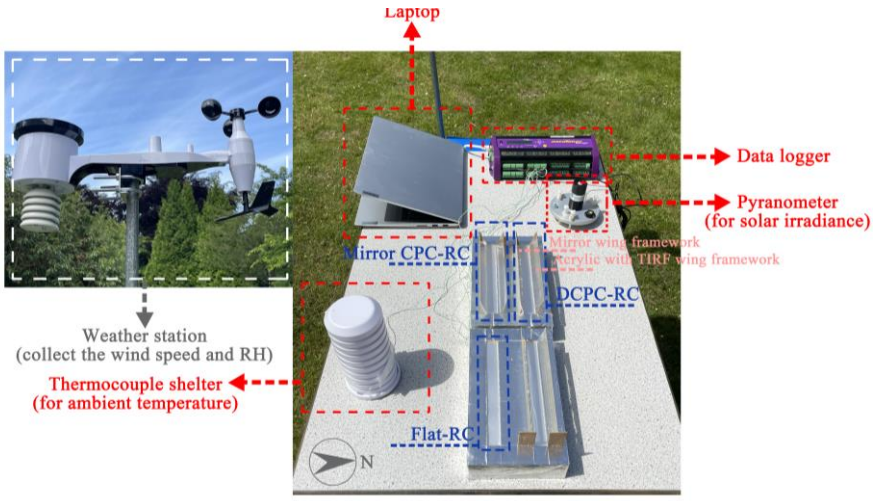

Figure 5-4: In-situ experimental setup of the RC systems.

Table 5-1: List of testing and monitoring devices in the experimental system.

Device	Specification	Uncertainty
Data logger	Data Taker DT85	/
Thermocouples	K-type	±0.05 °C

5.3.2 Experimental results

Figure 5-5 (a) illustrates the temperatures of three RC modules alongside ambient temperatures and solar irradiance, while Figure 5-5 (b) shows the weather data, including relative humidity and wind speed. Furthermore, Figure 5-5 (c) depicts the differences between ambient and RC emitter temperatures. Notably, relative humidity during this period was stable, ranging from 50%-56%, and wind speeds remained below 2.5 m/s. These conditions facilitated the RC modules in achieving sub-temperature easily. However, when solar irradiance was present, the flat-RC module, lacking concentrator shading, showed the highest emitter temperatures among the three. For instance, at 19:00, with solar radiation at 318.09 W/m^2, the emitter temperature of the flat-RC module reached 26.73 °C, in contrast to 25.47 °C for the mirror CPC-RC and 24.86 °C for the DCPC-RC modules. As solar radiation diminished to 50 W/m^2, the temperatures of the flat-RC module and the DCPC-RC module, both dropping to approximately 16.65 °C by 21:00. In contrast, the mirror CPC-RC module demonstrates a better cooling performance, achieving a lower temperature of 15.87 °C.

When analysing temperature differences between the three RC modules and ambient temperature, it is shown that under solar irradiance, the flat-RC module exhibits the smallest temperature difference, indicating minimal cooling performance. The mirror CPC-RC module, which reflects some solar radiation to the emitter by mirror CPC, shows a slightly larger temperature difference. The DCPC-RC

module, due to its distinctive structure, demonstrates the largest temperature differential under these conditions. As solar radiation diminishes, the mirror CPC-RC module achieves the most significant temperature reduction, followed by the flat-RC module, with the DCPC-RC module slightly lagging behind the flat-RC module. Throughout the experiment, the mirror CPC-RC module maintained an average temperature reduction of 3.97 °C from ambient, surpassing the DCPC-RC module, which averaged a 3.37 °C reduction. Finally, the flat-RC module showed the least cooling effect, with a temperature drop of 3.09 °C.

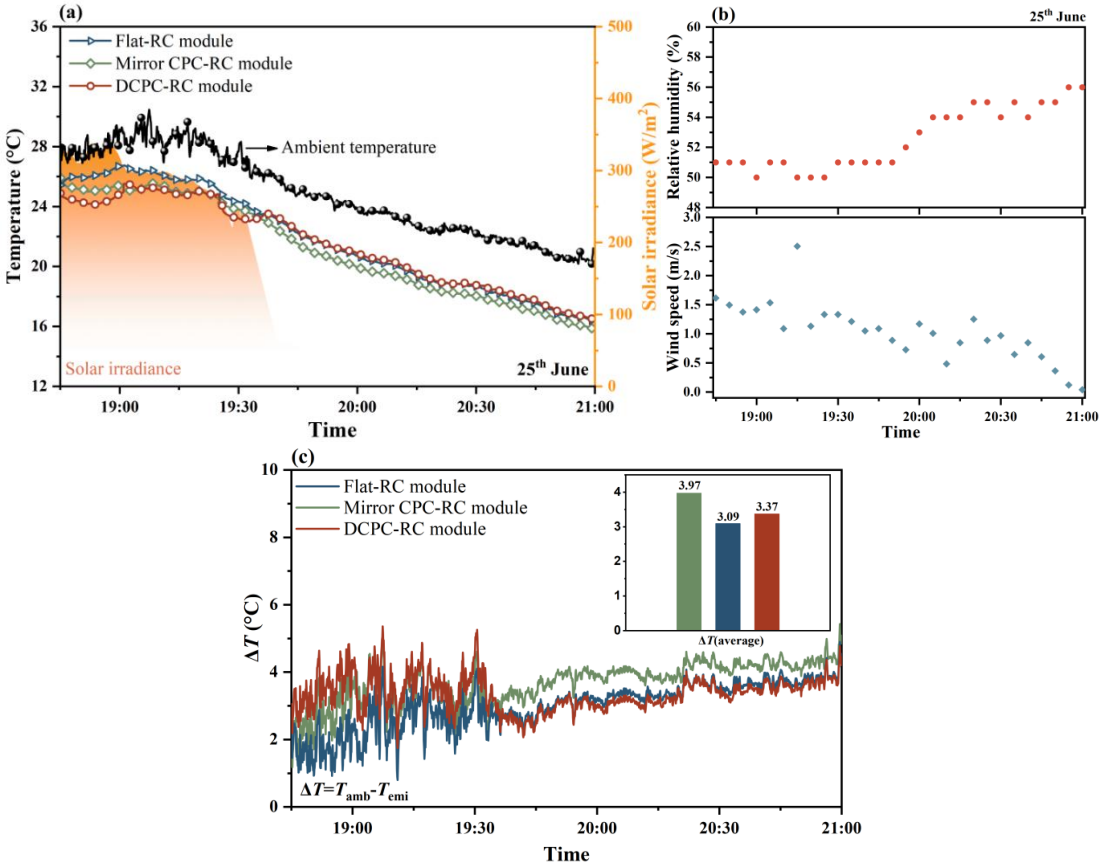

Figure 5-5:(a) Measured emitter temperatures of three RC modules alongside ambient temperature and solar irradiance. (b) Weather data in Nottingham, UK on 25th June 2024. (c) Temperature differences (ΔT) between the ambient air and RC emitters.

The experimental results from 26th June are shown in Figure 5-6. On this condition, relative humidity was higher than the previous night, ranging from 56% to 66%, while wind speeds remained similar. Additionally, solar radiation increased from 715.65 W/m^2 at 10:15 to 933.40 W/m^2 at 13:15, significantly impacting the cooling performance of the RC modules. Among the three, the flat-RC module was most affected by adverse thermal radiation and could not achieve a sub-ambient temperature. While the mirror CPC-RC module utilizes the CPC as a shield against adverse radiation.

However, as the solar altitude angle increased, the solar incident angle fell within the CPC's θ_{max} range, concentrating part of solar radiation on the emitter and causing its temperature to rise above ambient. The DCPC-RC module performed the best cooling effect due to its unique structure, which minimized solar radiation reaching the emitter, consistently maintaining sub-ambient temperatures. Around 12:35, cloud cover temporarily blocked the solar, leading to a sharp drop in temperatures for three RC modules, most notably for the flat-RC module, which fell from 30.39 to 27.29 °C, while the others experienced smaller declines. These results illustrate the significant impact of solar radiation on RC performance. Furthermore, despite the CPC's shielding capability, in the absence of solar radiation, the CPC-RC module cools slightly slower than the flat-RC module. Figure 5-6 (c) displays the temperature difference between the ambient temperature and three RC modules. Notably, apart from the DCPC-RC module, the temperature differences for the other two modules are consistently negative, indicating that their temperatures remain above ambient. At 12:35, cloud cover briefly blocked the sun, causing the temperature differences for all three modules to surge, each exceeding 2 °C. However, once the clouds dispersed, the temperature differences reverted to their previous states. Throughout the experiment, the DCPC-RC module maintained an average emitter temperature of 0.95 °C below the ambient, with a maximum difference of 2.23 °C. In contrast, the mirror CPC-RC and flat RC modules recorded average temperatures of 0.33 °C and 0.85 °C above the ambient level, respectively.

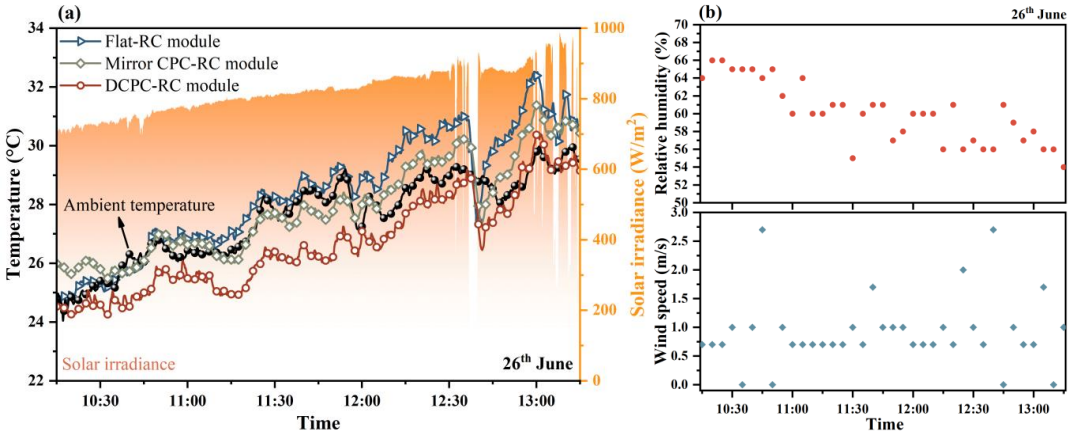

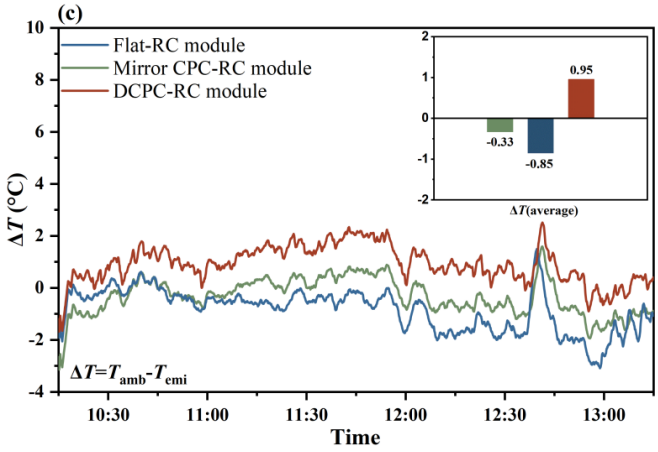

Figure 5-6: (a) Measured emitter temperatures of three RC modules alongside ambient temperature and solar irradiance. (b) Weather data in Nottingham, UK on 26th June 2024. (c) Temperature differences (ΔT) between the ambient air and RC emitters.

The results from daytime and nighttime experiments highlight the DCPC-RC module's potential for achieving effective all-day RC. However, there is still space for improvement, such as enhancing daytime cooling capacity and nighttime performance. The following sections will explore the cooling power of the DCPC-RC module under various configurations and discuss strategies for further optimizing the module.

5.4 Effect of different structural and external environment configurations on DCPC-RC module cooling performance

5.4.1 Effect of different CPC wing frameworks

This section firstly evaluates the solar receiving ratio ($\eta_{_sol}$) for RC modules at various solar profile angle (ϕ). Since this section studies the different structural CPC-RC modules, the $\eta_{_sol}$ for RC module is defined as the ratio of solar radiation reaching the RC emitter to the solar radiation reaching the CPC aperture surface. The higher the $\eta_{_sol}$, the greater the P_{sol}, which in turn negatively impacts the RC power. Therefore, this chapter proposes a solar shielding ratio (η) to explain the shielding effect of the CPC structure. η can be expressed as:

$$\eta = 1 - \eta_{_sol} \tag{5.1}$$

For the flat-RC module, which lacks CPC structure, η remains consistently at 1. In contrast, the η for the two CPC-RC modules: the mirror CPC-RC and DCPC-RC modules, are determined through simulation. Subsequently, P_{sol} and P_{cool} for Guangzhou, a typical subtropical city, are analysed throughout the day on 21st June to compare their different cooling performance. All RC modules are

placed horizontally without surrounding obstacles. Weather data for 21st June in Guangzhou, obtained from EnergyPlus, is presented in Figure 5-7, and key parameter settings for this study are provided in Table 5-2.

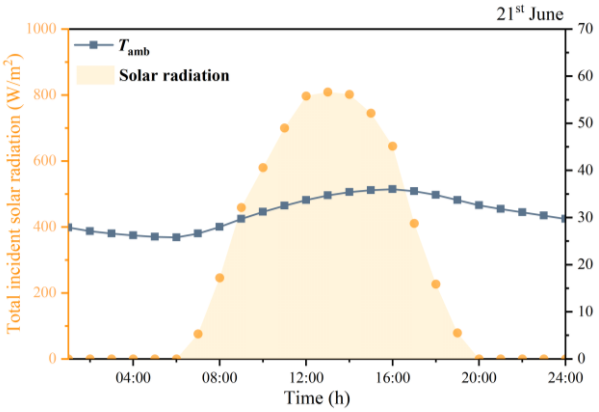

Figure 5-7: Hourly total incident solar radiation, ambient and surrounding temperatures on 21st June.

Table 5-2: Key parameters setting for case studies

Parameter	Value	Unit
T_{gro_day}	T_{amb}+20 [239, 240]	°C
T_{gro_night}	T_{amb} -5 [241]	°C
ε_{gro}	0.85	
ε_{emi}	0.95	
α_{emi}	0.1	
θ_{max} of CPC (DCPC)	30	°
ρ_{cpc}	1	
ρ_{TIRF} (Infrared region)	1	

Figure 5-8 illustrates the η for two CPC-RC modules at different ϕ. Because the θ_{max} of the mirror CPC is 30°, almost all incoming solar radiation within ± 30° of the zenith direction (i.e., ϕ is 60-120°) will be reflected by the mirror CPC to the RC emitter, resulting in η near zero in this range. In this ϕ range, the CPC concentrates solar radiation, adversely affecting RC performance. However, outside the half-acceptance range, the module's η remains at 1, indicating no solar radiation reaches the RC emitter. In contrast, the η curves for the DCPC-RC modules at different ϕ exhibit significant fluctuations, notably when ϕ is 20° or 150°, its η vastly differs from the mirror CPC-RC module. For instance, when ϕ is 20° or 150°, η for the mirror CPC-RC module is 1, while for the DCPC-RC, η is 0.52 or 0.26, respectively. This discrepancy is attributed to the dissimilarity in the material of DCPC wing frameworks.

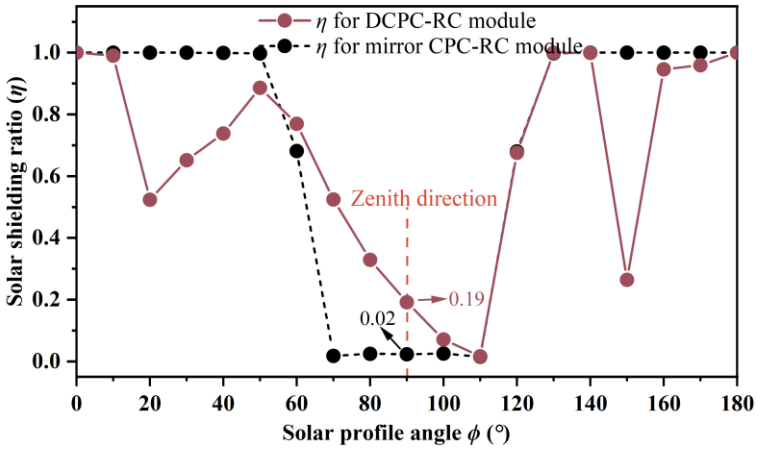

Figure 5-8: Solar shielding ratio of different CPC-RC modules under different solar profile angles (ϕ).

Figure 5-9 clarifies the incident paths of solar radiation entering the DCPC-RC module at various ϕ. Figure 5-9 (a) and (c) illustrate that when ϕ is 20° and 150°, most of the incoming solar radiation, after passing through the transparent wing framework, will be reflected by the adjacent mirror wing framework back to the RC module, eventually reaching the RC emitter, resulting in a lower η at this ϕ. Furthermore, Figure 5-9 (b) shows that when ϕ is 100°, the angle falls within the half-acceptance angle range of the DCPC. Consequently, a portion of the solar radiation reaches the RC emitter directly, while the mirror wing framework of the DCPC reflects another portion. This results in η being less than 0.1 at this ϕ. The results show that as ϕ increases, the η for the DCPC-RC module has no obvious regularity in variation, but in the ϕ range of 70-110°, the η for the DCPC is still higher than that of the mirror CPC, indicating its potential to reduce the absorbed P_{sol} by the DCPC-RC module.

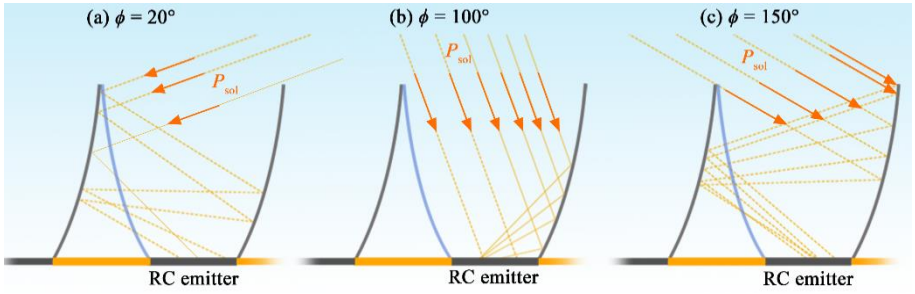

Figure 5-9: Traced incoming solar radiation on DCPC-RC multi-module system under different solar profile angles (ϕ).

Figure 5-10 shows the P_{sol} and P_{cool} for three RC modules over a 24-hour period on 21st June. It can be seen that during the nighttime, both mirror CPC-RC and DCPC-RC modules exhibit higher P_{cool}, as the infrared reflectivity of the TIRF is assumed to be the same as that of mirror CPC structure, resulting in similar cooling performance. At 1:00, their P_{cool} reaches 148.35 W/m^2, showing an excellent cooling effect. In contrast, the flat-RC module, lacking a concentrator, shows lower cooling performance, with

a P_{cool} 15.5% lower than the previous two at the same time. However, the situation changes with the presence of solar radiation. The mirror CPC-RC module, due to its concentrating properties, absorbs more solar radiation during the daytime. At noon, its P_{sol} exhibits 120.10 W/m^2, resulting in a P_{cool} of only 40.03 W/m^2. In comparison, the optimized DCPC-RC module, which absorbs only 59.1 W/m^2 of solar radiation at the same time, shows a P_{cool} that is double that of the mirror CPC-RC module, demonstrating superior cooling capability. Meanwhile, the flat-RC module's P_{cool} currently is slightly higher than that of the mirror CPC-RC module, at 54.01 W/m^2, but still lower than the DCPC-RC module. Notably, as previously mentioned, when the solar profile angle is around 100°, the DCPC-RC module's η is minimized, meaning it absorbs more solar radiation. As a result, from 13:00 to 14:00 on 21st June, its P_{cool} is at its lowest for the day, approximately 87.89 W/m^2.

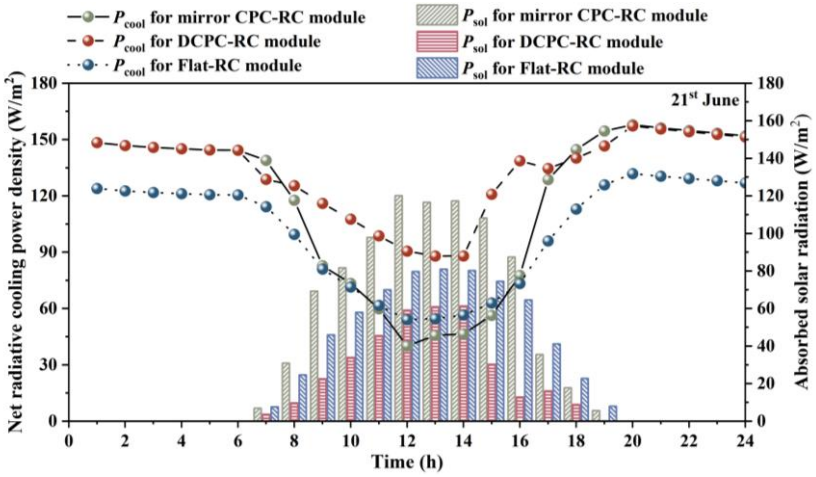

Figure 5-10: Absorbed solar radiation and net cooling power density for three RC modules under different solar profile angles.

5.4.2 Effect of DCPC wing frameworks with different spectral characteristics

This section discusses the impact on the RC effect when TIRFs cover the acrylic wing framework of the DCPC-RC module with different spectral selectivity.

Figure 5-11 presents the weighted average transmittance (τ) under the solar spectrum and infrared broadband for two types of TIRFs and the acrylic wing framework without TIRF. The TIRF with near-ideal spectral selectivity (called near-ideal TIRF) is shown to have a τ of 0.99 under the solar spectrum, while its τ at the infrared broadband is extremely low, only 0.01, which is equivalent to an infrared broadband reflectivity of 0.99. The second type is a relatively poor TIRF from ref. [245] (called relatively poor TIRF), displays a τ of 0.92 under the solar spectrum and 0.1 at the infrared broadband.

For comparison, the acrylic wing framework without TIRF (called without TIRF), selected as the control group, exhibits a τ of 0.90 under the solar spectrum and 0.80 at the infrared broadband.

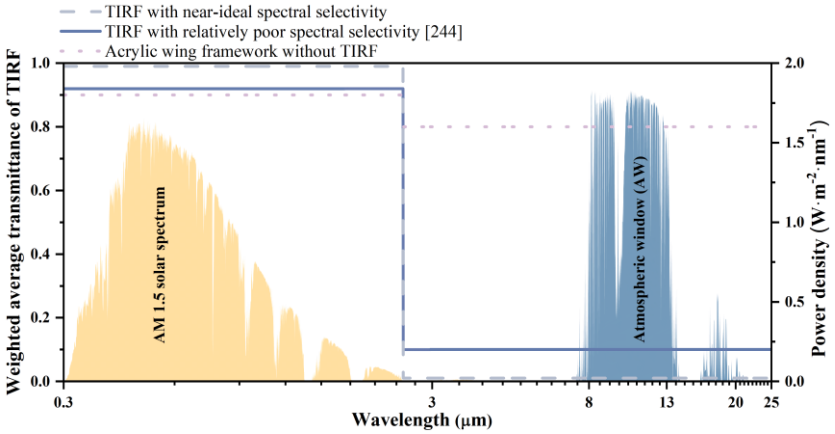

Figure 5-11: Weighted average transmittance of DCPC acrylic wing framework with and without TIRF.

Figure 5-12 shows the η for the three DCPC-RC modules at different ϕ. The η for all three modules follows similar trends as ϕ changes. At ϕ smaller than 10°, the three modules show the η of 1. But when the ϕ at 20°, a rapid decline in η is observed, with the module with near-ideal TIRF showing the lowest η of 0.43, while the other two modules display slightly higher η of 0.52 and 0.65, respectively. From 20° to 50°, η for all three modules increases as ϕ increases, almost all of them reaching 0.88 at 50°. This indicates that at 50°, only 12% of the sunlight on the CPC's aperture can reach the RC emitter. However, beyond ϕ of 50°, η for the three modules decreases rapidly and approaches 0 at 110°, suggesting that most of the incident sunlight still reaches the RC emitter when the solar is close to the zenith direction. Fortunately, when ϕ exceeds 110°, a sharp increase in the η for the three modules is seen, particularly for the module with near-ideal TIRF, where η reaches 1 at 130°, which means almost no sunlight reaches the emitter. Nonetheless, at ϕ of 150°, η rebounds as some sunlight is reflected by the mirror wing framework of the adjacent module back to the emitter.

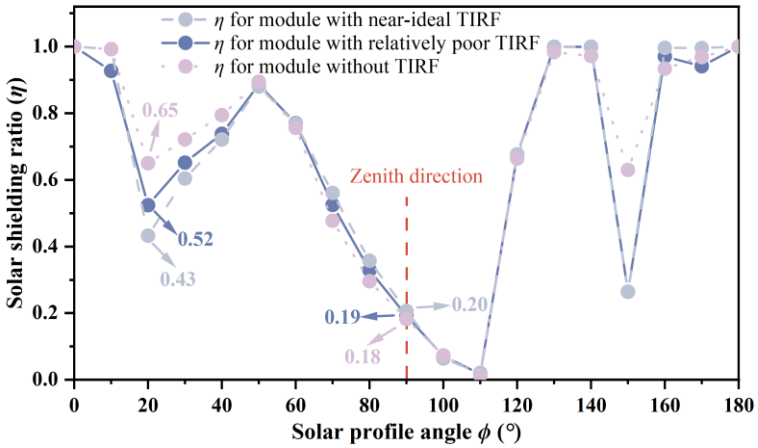

Figure 5-12: Solar shielding ratio for the DCPC-RC modules with and without TIRFs under different solar profile angles.

In addition to determining the η for the three DCPC-RC modules at different ϕ, the determination of the ε_{sky} for the three modules is also necessary for characterizing their P_{sky}. The ε_{sky} for the three modules is listed in Table 5-3. The ε_{sky} for the module with near-ideal TIRF is 0.669, slightly exceeding 0.664 for the module with relatively poor TIRF. This difference is due to the lower τ for the former under the infrared broadband region, which results in almost all the sky thermal radiation being concentrated on the RC emitter by the DCPC. Furthermore, the ε_{sky} for the module without TIRF is 0.627, which is significantly lower than the first two modules. This is also due to its τ under the infrared broadband region being only 0.8, allowing a portion of the sky thermal radiation to pass through the acrylic wing framework.

Table 5-3: Equivalent sky emissivity for three DCPC-RC modules.

Name	Near-ideal TIRF	Relatively poor TIRF	Without TIRF
ε_{sky}	0.669	0.664	0.627

However, it is noted that a lower ε_{sky} does not necessarily imply a higher P_{cool} for the module. This is because if the infrared broadband reflectivity of the DCPC's acrylic wing framework is not 1, it permits thermal radiation from the solar collector to pass through and reach the RC emitter, as illustrated by the brown line in Figure 5-13. Simultaneously, thermal radiation emitted by the emitter can also pass through the acrylic wing framework, either being captured by the collector or returning to the RC emitter, thereby not escaping the system, as depicted by the blue line in Figure 5-13.

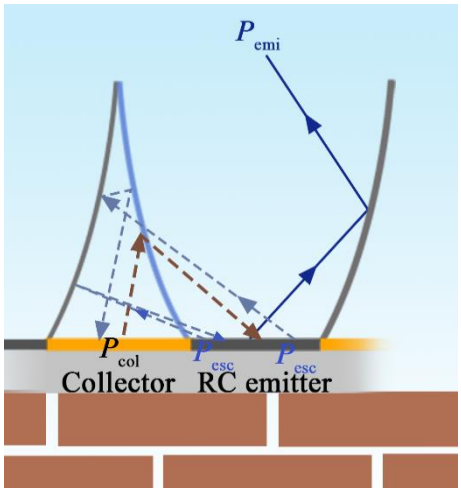

Figure 5-13: Schematic diagram of thermal radiation from the solar collector and thermal radiation that cannot escape from the DCPC-RC multi-module system.

In this case, the thermal radiation from the emitter finally being trapped in the system (P_{esc}), and the thermal radiation from the solar collector (P_{col}) can be expressed as follows:

$$P_{esc} = \varepsilon_{emi}\sigma T_{emi}^4 \beta_{esc} \tag{5.2}$$

where β_{esc} is the ratio of the emitted thermal radiation beam that cannot escape from the system to the total hemispheric emitted radiation beam.

$$P_{col} = \alpha_{emi}\varepsilon_{col}\sigma T_{emi}^4 \beta_{col} \tag{5.3}$$

where ε_{col} is the real material emissivity of the solar collector; β_{col} is the ratio of the radiation beam from the system reaching the solar collector to the total hemispheric emitted radiation beam.

Figure 5-14 shows the P_{sol} and P_{cool} for the DCPC-RC modules using different TIRFs on 21st June. During the nighttime, the DCPC-RC module with near-ideal TIRF exhibits the highest P_{cool} for the three, close to 150 W/m^2 due to its high infrared reflectivity. In contrast, the DCPC-RC module with relatively poor TIRF, with an infrared emissivity of 0.9, reflects less infrared radiation emitted by the emitter, resulting in a lower P_{cool} . For instance, at 1:00, its P_{cool} is 130.27 W/m^2, which is 12.1% lower than the DCPC-RC module with near-ideal TIRF. However, the DCPC-RC module without TIRF has a much lower infrared reflectivity of 0.2. Although the infrared thermal radiation passing through the transparent wing framework is partially reflected by the mirror wing framework of the adjacent module, the P_{cool} remains the lowest of the three, 17.2% lower than the DCPC-RC module with near-ideal TIRF.

During the daytime, the influence of solar radiation causes the P_{cool} for all three DCPC-RC modules to reach its lowest value around noon. This is because the solar transmittance of both TIRF materials and acrylic is above 0.9, with little difference, allowing most solar radiation to pass through the transparent wing framework. However, due to variations in infrared reflectivity, the P_{esc} and P_{col} for the modules differ. It can be seen that the DCPC-RC module without TIRF absorbs the most solar radiation, resulting in the lowest P_{cool}. For example, at noon, the P_{cool} for the DCPC-RC module without TIRF is 99.45 W/m^2, while the modules with near-ideal and relatively poor TIRF show P_{cool} of 119.06 and 105.24 W/m^2, respectively.

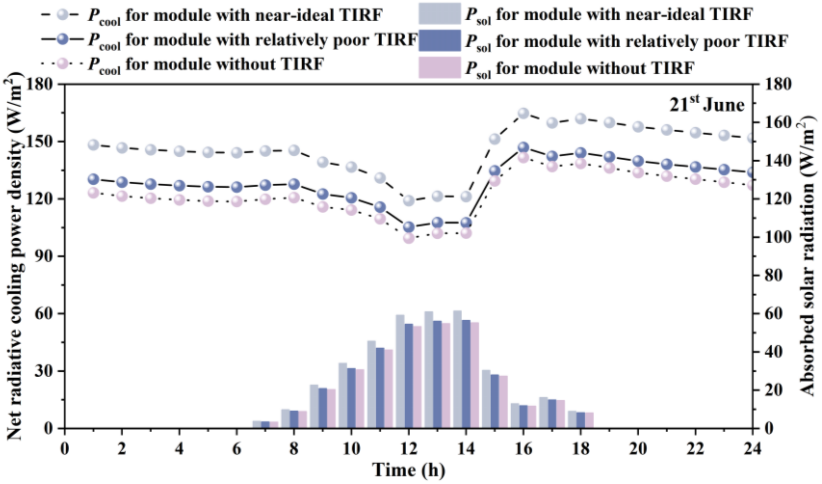

Figure 5-14: Absorbed solar radiation and radiative cooling power density for DCPC-RC modules with and without TIRF.

By characterizing the maximum net cooling power density of the DCPC-RC modules with TIRFs of varying spectral selectivity or without TIRF, it is observed that the solar radiation absorbed by the three module emitters shows minimal variation, primarily due to the slight differences in solar transmittance among them. The critical factor influencing performance is the reflectivity of the TIRFs in the infrared broadband. Consequently, DCPC-RC modules with near-ideal TIRF demonstrate superior cooling performance.

5.4.3 Effect of the geographical location of DCPC-RC modules

This section examines the cooling performance of horizontally placed DCPC-RC modules in three typical cities at different latitudes including Guangzhou (23°N), Rome (42°N), and Nottingham (53°N) to determine the hours percentage of different ϕ intervals throughout the year. Additionally, the chapter explored the cooling performance of the modules at various ϕ across different cities when the modules

are tilted at a specific angle to the anti-sunward side. The transparent wing framework of the DCPC-RC module in this section is covered with near-ideal TIRF.

Figure 5-15 shows the number of hours of incident sunlight from different ϕ intervals (in 10° intervals) as a percentage of the total daylight duration throughout the year (γ) for the three cities. Statistical data reveal that Guangzhou experiences 4404 hours of total daylight duration throughout the year, while Rome and Nottingham register 4310 and 3850 hours respectively. Distinct variations in γ across each ϕ interval are evident among the three cities. For instance, at ϕ ranging from 0~10°, Guangzhou records γ of 1.4%, whereas Rome and Nottingham exhibit 3.4% and 6.6%, respectively. This indicates that higher latitudes experience a greater γ of sunlight coming from the 0°-10° interval annually. Moreover, the ϕ interval corresponding to the maximum γ differs among the cities: Guangzhou's maximum γ exhibits 14.7% corresponds to ϕ interval of 40~50°, Rome's 14.4% to ϕ interval of 20°-30°, and Nottingham's highest γ is 17.1% occurs at 10~20°. Given that solar radiation is highest when ϕ is at the zenith, it is less favourable for RC. By comparing the total γ within the ϕ range of 70° to 110°, the challenge of achieving effective RC during the day in each city can be preliminarily assessed. For example, Nottingham's total γ between 70° and 110° is 11.4%, while Rome and Guangzhou show total γ of 23.3% and 39.0%, respectively. This indicates that mitigating the effects of solar radiation on RC modules in Guangzhou is essential for achieving cooling effects.

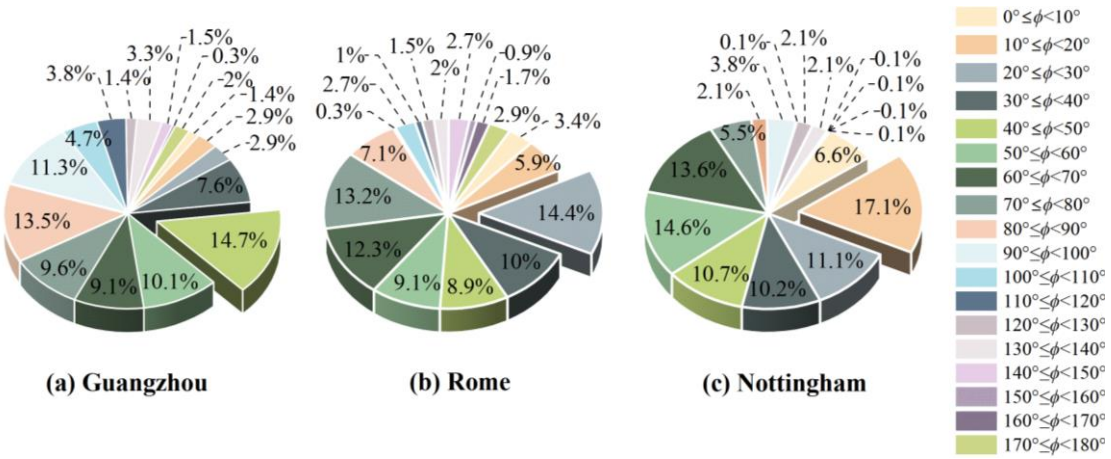

Figure 5-15: Hours percentage of different solar profile angle intervals in different cities.

Figure 5-16 shows the solar irradiance distribution in different ϕ intervals, calculated by the total solar irradiance in ϕ intervals relative to the horizontal solar irradiance throughout the year. In Guangzhou, 36.2% of the solar irradiance distribution originates from the ϕ interval of 40°-60°, while

the interval of 80°-100° contributes 28.5%. This indicates that the highest amount of solar radiation reaching the ground surface in Guangzhou occurs within these two intervals. Therefore, for RC systems, it is crucial to block as much solar radiation from these angles as possible. In Rome, solar irradiance within the 30°-100° range accounts for 75.8% of the total horizontal irradiance. In contrast, due to its higher latitude, Nottingham experiences a solar irradiance distribution in the 20°-80° of ϕ range, which accounts for 78.2% of the total horizontal irradiance. The results indicate that, to achieve optimal RC performance throughout the year in different geographic locations, it is essential to further reduce the P_{sol} by tilting the RC module in the ϕ ranges where solar irradiance distribution is most concentrated. Therefore, characterizing the P_{cool} for the DCPC-RC modules tilted at various angles to the anti-sunward side across different ϕ ranges holds significant research value.

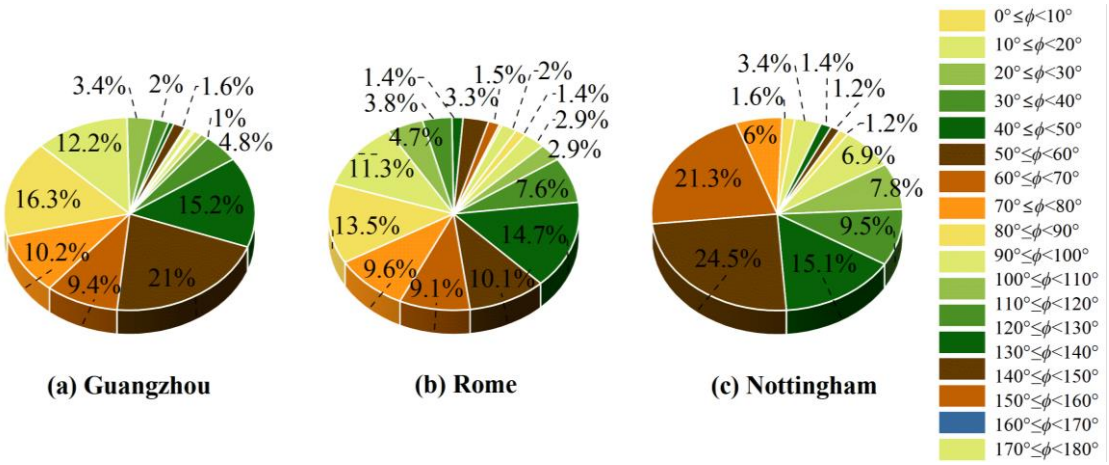

Figure 5-16: Percentage of total solar irradiance in different ϕ intervals to the total solar irradiance throughout the year.

To explore the appropriate tilt angle to the anti-sunward side for the RC module in each city, determining the η and ε_{sky} for the tilted modules is first needed. As depicted in Figure 5-17, the η for three DCPC-RC modules with different tilt angles at various ϕ shows apparent differences. At ϕ is 0°, the η for three modules is observed to be 1. When ϕ reaches 10°, η of 0.45 is recorded for the module tilted at 0°, while the other two maintain the η of 1. As ϕ further increases, a sharp rise in η to 0.88 (at 50°) followed by a sharp drop to 0 (at 110°) is observed for the module tilted at 0°. The other two modules show a similar general trend, albeit with a delay. Specifically, for the module tilted at 15°, η rises to 0.88 at 70° and drops to 0 at 120°; for the module tilted at 30°, η rises to 0.88 at 80° and falls to 0 at 140°. Furthermore, in the zenith direction, the η for the module tilted at 0° is 0.21, which is 54.6%

and 73.7% lower than that of the modules tilted at 15° and 30° respectively, indicating that an inclined placement allows the RC module to block more solar radiation at noon. Finally, as η drops to 0 and ϕ further increases, a rapid rise in η to about 1 is observed. However, like the previous subsection, fluctuations in the η for the three modules are experienced after ϕ reaches 150° due to reflections from the metal wing framework of the adjacent module. These fluctuations result in η falling to about 0.2 before rising back to 1.

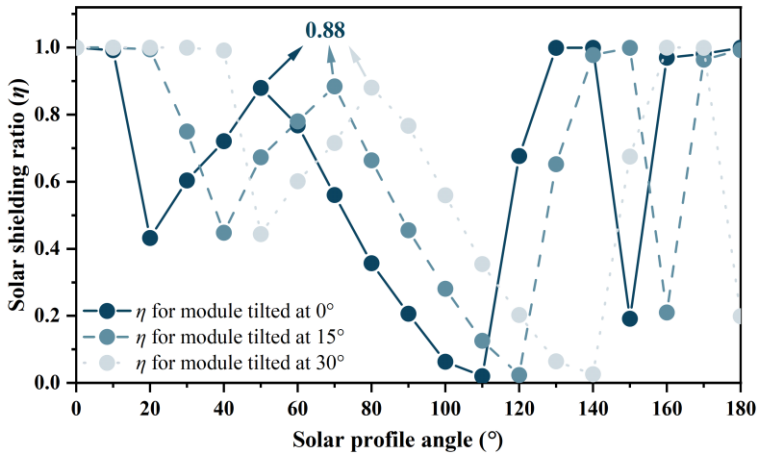

Figure 5-17: Solar shielding ratio for the DCPC-RC modules tilted at different angles to the anti-sunward side under different solar profile angles.

Table 5-4 presents the ε_{sky} for the DCPC-RC modules at three different tilt angles. It can be observed that an increase in ε_{sky} with the increase of the tilt angle, rising from 0.669 when the module tilted at 0° to 0.675 when the module tilted at 30°. This is due to the larger sky emissivity at larger zenith angles, and the tilted placement of the module causes the module to receive more sky thermal radiation from the larger zenith angle.

Table 5-4: Equivalent sky emissivity for DCPC-RC modules tilted at three different angles.

Name	Tilted at 0°	Tilted at 15°	Tilted at 30°
ε_{sky}	0.669	0.671	0.675

When the module is tilted at different angles, the total global solar radiation in the normal direction of the tilted surface will be different from that when the module is placed horizontally. In this case, the direct solar radiation in the normal direction of the surface tilted at different solar profile angles(ϕ) can be calculated as:

$$G(\theta,\phi) = G(\phi)\sin(90-\phi)\cos(-\theta) + G(\phi)\cos(90-\phi)\cos\varphi\sin(-\theta) \tag{5.4}$$

where $G(\phi)$ is direct solar radiation at different ϕ, W/m^2; θ is the tilt angle of the module to the anti-sunward side; φ is solar azimuth angle. Since the solar azimuth angle in this chapter is due south, φ is 0°. In this study, the average solar radiation for each angular interval is calculated by statistically analysing the solar radiation from different ϕ intervals over a typical year. This data is then used to characterize the P_{cool} for RC modules under various configurations

Figure 5-18 displays the P_{cool} for DCPC-RC modules tilted at different angles to the anti-sunward side in three cities when the ambient temperature is 30 °C alongside the solar irradiance distribution in different ϕ intervals. It can be observed that in Guangzhou, within the ϕ interval (50-60°), which has the highest solar energy contribution, the P_{cool} is the lowest, regardless of whether the DCPC-RC module is tilted. When the RC module is tilted at 30° to the anti-sunward side, the P_{cool} increases to 127.35 W/m^2, which is 15.2% higher than the horizontally placed DCPC-RC module. However, in other ϕ intervals, the larger tilt angle leads to higher P_{gro}, in regions with relatively low solar energy distribution, the P_{cool} for the tilted 30° module to the anti-sunward side is lower compared to the one tilted at 15°. In Rome, where the high solar energy distribution is more concentrated within certain ϕ intervals, RC module is tilted at 30° to the anti-sunward side shows good cooling performance. For example, when ϕ is between 40-50°, the P_{cool} reaches 135.24 W/m^2, which is 22.7% higher than that of the horizontally placed DCPC-RC module. In contrast, in the Nottingham, the horizontally placed DCPC-RC module consistently achieves higher cooling performance throughout the year.

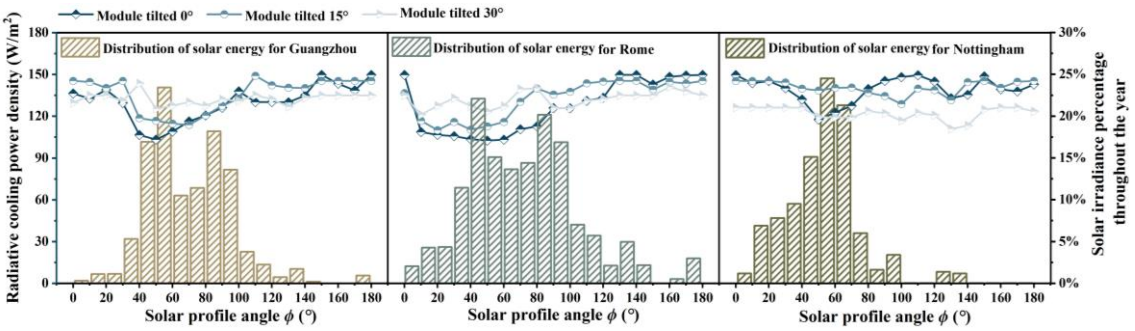

Figure 5-18: Cooling performance for DCPC-RC modules tilted at different angles to the anti-sunward side in different cities and the corresponding solar energy distribution throughout the year.

5.5 Summary

In this chapter, a novel RC system based on a dissimilar material CPC (termed as DCPC-RC system) is proposed, and its ability to reduce the absorption of solar radiation by RC emitters is explored. The modelling approach developed in Section 3.2 is applied and validated through experiments conducted in Nottingham, UK. The comparisons show that the simulation results yield good consistency with the experimental data. During the daytime experiments, the DCPC-RC module demonstrates superior performance, with the average emitter temperature being 0.95 °C lower than the ambient temperature and the minimum temperature exceeding 2 °C below the ambient. Additionally, this chapter studies the impact of changing the configuration and locations of the DCPC-RC module on cooling power density (P_{cool}) under varying solar profile angles (ϕ).

While this chapter does not propose a method for utilizing solar radiation that passes through the CPC's transparent wing frame to reach the solar collector, subsequent chapters will explore strategies to effectively harness this solar energy. The goal is to minimize solar energy waste and enhance the overall energy efficiency of the system. Additionally, the current dissimilar CPC configuration still reflects some solar radiation onto the RC emitter, so further adjustments to its design are needed. In the following chapter, we will explore potential improvements to the DCPC-RC module and integrate the RC with PVT modules to better meet the dynamic energy needs of buildings throughout the year. However, a key challenge in multifunctional solar energy-RC harnessing systems is addressing the mutual attenuation effect between the two different forms of energy (heat and cold).

6. Incorporation of transparent infrared-reflective film (TIRF) with CPC-RC for novel simultaneous solar collection and radiative cooling

6.1 Introduction

Chapter 5 introduces a novel CPC-RC system based on arrays of dissimilar material CPC structures (named as DCPC-RC system) and explores its structural design and potential to enhance the cooling power of RC modules. In this system, transparent wing frameworks allow sunlight to pass through to the solar collector module. Unlike the traditional mirror CPC structures, which direct sunlight onto the RC emitter, this new DCPC-RC system effectively reduces the absorption of solar radiation by the RC emitter. However, the previous chapter primarily focused on improving the system's cooling performance, without delving deeply into solar energy utilization. Additionally, while analysing the solar shielding ratio of the RC modules, it was found that when one side of the CPC reflectors using the mirror material, reflects part of the solar radiation back to the RC emitter or causes solar radiation to escape from the system at larger solar incident angles.

To further minimize the impact of solar radiation on the RC module and prevent the collected solar energy from going to waste, this chapter proposes a novel energy system with an innovative configuration. This system replaces the dissimilar CPC structure in the DCPC-RC module with a transparent CPC configuration covered with transparent infrared reflective film (TIRF), forming a TIRF-TCPC-RC module. Furthermore, a PVT module is placed in the gap between two adjacent TCPC-TIRF-RC modules, forming a hybrid system called TIRF-TCPC-PVTRC system. This system aims to efficiently and simultaneously utilize solar radiation and radiative sky cooling for the goal of versatile energy generation.

6.2 Description and optimization of TIRF-TCPC-PVTRC system

6.2.1 Introduction of the TIRF-TCPC-PVTRC system

This section presents the structural schematic of the novel TIRF-TCPC-PVTRC system and introduces the required spectral characteristics of the materials. The proposed system mainly comprises arrays of TCPC modules covered with TIRF alongside PVT and RC modules, as shown in Figure 6-1. Unlike traditional CPVT systems that place the PVT module in the mirror CPC bottom slot, the novel

system situates the RC emitter at the bottom of the TCPC structure and the PVT modules places between adjacent TCPC modules. This configuration addresses the issue of CPC-RC module concentrating unwanted solar radiation onto the RC emitter while also collecting solar radiation for PVT modules. Additionally, it resolves the issue of poor thermal regulation flexibility in standalone RC and PVT modules, enabling the collection of both heat and cooling fluxes.

In this chapter, the material used in the TCPC is a high light-transmitting resin acrylic which shows high solar transmittance. When covered with TIRF, which also boasts high solar spectrum transmittance, the TIRF-TCPC structure exhibits unique spectral selectivity: high transmittance within the solar spectrum and high reflectivity within the infrared region. This design enables solar radiation to pass directly through the TIRF-TCPC structure to the underlying PVT module during the daytime, minimizing the solar radiation that reaches the RC emitter. Additionally, this structure also can block adverse thermal radiation from large zenith angles, such as from the sky and surrounding obstacles, thereby enhancing the cooling performance of the RC module.

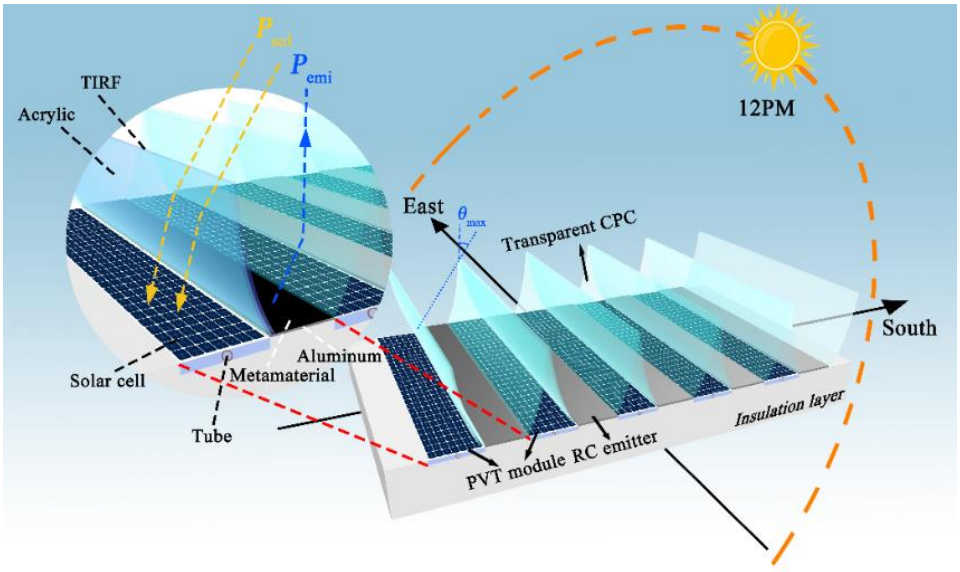

Figure 6-1: The schematic diagram of the TIRF-TCPC-PVTRC system.

In the following subsections, the optical modelling approach will be used to initially evaluate the cooling performance of the TIRF-TCPC-PVTRC module within the system.

6.2.2 Cooling performance evaluation of TIRF-TCPC-PVTRC module

6.2.2.1 Model validation

The modelling approach used in this chapter is described in detail in Section 3.2. To verify the accuracy of this approach in characterizing the cooling performance of the TIRF-TCPC-PVTRC module, a series of outdoor experiments were conducted on the morning of 26th June 2024 in the University of Nottingham to measure the RC emitter temperature of the RC module. The specific data and analysis of the experiment are provided in the Appendix. Additionally, the mathematical model is employed to calculate the RC emitter temperature under the same environmental conditions, and the results are compared with the experimental data. To quantify the discrepancy between simulated and experimental results, *RMSD* is employed as a metric.

Figure 6-2 presents the Nottingham experiment data and simulated emitter temperatures, demonstrating a good agreement between the modelling approach used in this chapter and the actual experimental data. At the onset of the experiment, the measured emitter temperature (T_{emi_exp}) of the TIRF-TCPC-PVTRC module is recorded at 23.05 °C, while the simulated temperature (T_{emi_sim}) is slightly higher at 23.39 °C. By the end of the experiment, T_{emi_exp} increases to 28.38 °C, closely followed by T_{emi_sim} at 28.65 °C. According to Equation 7, the *RMSD* for the TIRF-TCPC-PVTRC module is 1.32%, underscoring the precision of the modelling approach used in this chapter.

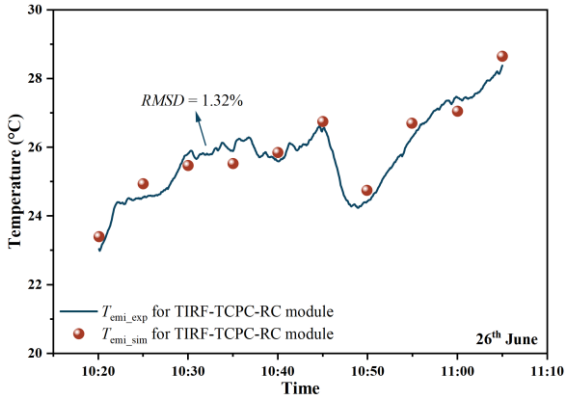

Figure 6-2: Simulated and experimental temperatures of the TIRF-TCPC-PVTRC module in the Nottingham, UK.

6.2.2.2 Absorbed solar radiation and cooling performance of TIRF-TCPC-PVTRC module

This subsection uses the modelling approach to characterize the $\eta_{_sol}$ for the PVT collector and flat RC emitter within the TIRF-TCPC-PVTRC module across various zenith angle. For the PVT collector, a higher $\eta_{_sol}$ is advantageous, whereas for the RC emitter, a higher $\eta_{_sol}$ indicates increased P_{sol}, which is detrimental to the cooling effect. Subsequently, the P_{cool} for the TIRF-TCPC-PVTRC module is

compared with that of the flat-RC module under various zenith angles and ambient temperatures. Some key parameters setting for discussion are shown in Table 6-1.

Table 6-1: Key parameters setting for case studies.

Parameter	Value	Unit
ε_{emi}	0.95	
α_{emi} in solar region	0.13	
α_{PVT}	0.90	
τ_{TIRF} in solar region	0.90	
ρ_{TIRF} in infrared region	0.95	
$G(0°)$	1000	W/m^2

To obtain the solar radiation absorbed by the PVT collector and RC emitter in the system, first their solar receiving ratio needs to be determined.

$$\eta_{PVT} = \Phi_{PVT} / \Phi_{aper} \tag{6.1}$$

$$\eta_{RC} = \Phi_{RC} / \Phi_{aper} \tag{6.2}$$

where Φ_{PVT} and Φ_{RC} *i*s the solar flux reaching the PVT collector and RC emitter in the optical software, W/m^2; Φ_{aper} is the solar flux reaching the TIRF-TCPC aperture in the optical software, W/m^2.

Since the wing frameworks of the TIRF-TCPC structure in this chapter is made of materials with high solar transmittance, sunlight from various zenith angles can directly reach, pass through, or be reflected onto different modules. The solar radiation reaching the PVT collector and RC emitter can be expressed as:

$$P_{sol_PVT} = \alpha_{PVT} \tau_{TIRF} \eta_{_sol} G(\theta) \tag{6.3}$$

where α_{PVT} is the solar absorptivity of the PVT collector; τ_{TIRF} is the solar transmittance of the TIRF; $\eta_{_sol}$ is the solar receiving ratio for the PVT collector; $G(\theta)$ is the solar radiation under different zenith angles, W/m^2. In the chapter, solar radiation at zenith direction is 1000 W/m^2, and $G(\theta)$ is equal to $G(0°)$ $\cos(\theta)$.

$$P_{sol_RC} = \alpha_{emi} \eta_{RC} G(\theta) \tag{6.4}$$

where η_{RC} is the solar receiving ratio for the RC emitter.

Figure 6-3 displays the $\eta_{_sol}$, η_{RC} and P_{sol} for the PVT collector and flat RC emitter within the system. It can be seen that when zenith angle is 0°, most sunlight enters the system vertically, causing the $\eta_{_sol}$

for the PVT collector to decrease to 0.34, while the η_{RC} for the RC emitter increases to 0.65. At this zenith angle, the P_{sol} is 293.46 W/m^2 for the PVT collector and 87.41 W/m^2 for the RC emitter, which is not conducive to daytime RC performance. As the zenith angle increases, the η_{RC} for the RC emitter reaches its lowest value of approximately 0.37 at 30 °C, while the $\eta_{_sol}$ for the PVT collector is highest at 0.61. Additionally, when the zenith angle exceeds 30°, the P_{sol} for both the RC emitter and PVT collector decreases, which benefits RC performance but impacts the solar collection.

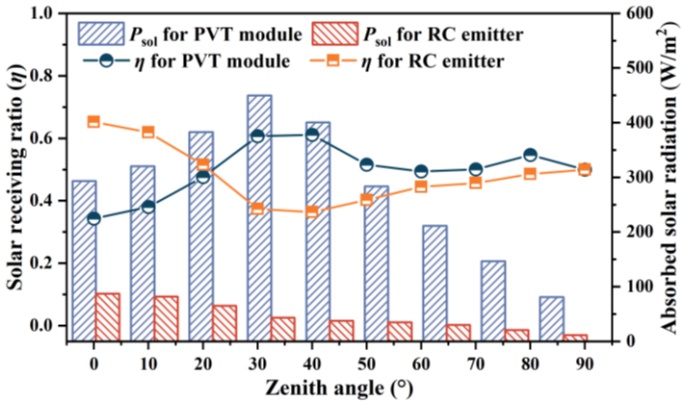

Figure 6-3: Solar receiving ratio and absorbed solar radiation for the PVT collector and flat RC emitter of the TIRF-TCPC-PVTRC module.

Figure 6-4 illustrates the P_{cool} for two different RC modules under varying ambient temperatures and zenith angles. In Figure 6-4 (a), the TIRF-TCPC-PVTRC module demonstrates superior cooling performance thanks to it experiencing less interference from solar radiation. Notably, even the solar radiation from zenith direction (0°) and an ambient temperature above 20 °C, its P_{cool} remains at 59.09 W/m^2. Furthermore, as the ambient temperature increases to 35 °C, the P_{cool} at this angle rises by 54.8% compared to when the temperature is at 20 °C. Additionally, at zenith angles of 90°, i.e., during nighttime conditions, P_{cool} can surpass 140 W/m^2 at an ambient temperature of 20 °C, and escalate to 170.81 W/m^2 when the temperature reaches 35 °C, highlighting its exceptional cooling capabilities.

Conversely, as depicted in Figure 6-4 (b), the flat-RC module without TCPC exhibits absorbing more solar and unfavorable thermal radiation, resulting in poor cooling performance. For instance, at 0° and 20 °C ambient temperature, it fails to achieve effective cooling effect. When the ambient temperature increases to 35 °C, its P_{cool} is only 24.93 W/m^2, which is 72.7% lower than that of the TIRF-TCPC-PVTRC module under identical conditions. However, during nighttime, its P_{cool} at 35 °C can reach 158.93 W/m^2, although 11.88 W/m^2 less than the TIRF-TCPC-RC module, still underscores its cooling

capacity. This comparison vividly demonstrates the severe effect of solar radiation on the cooling performance of RC modules.

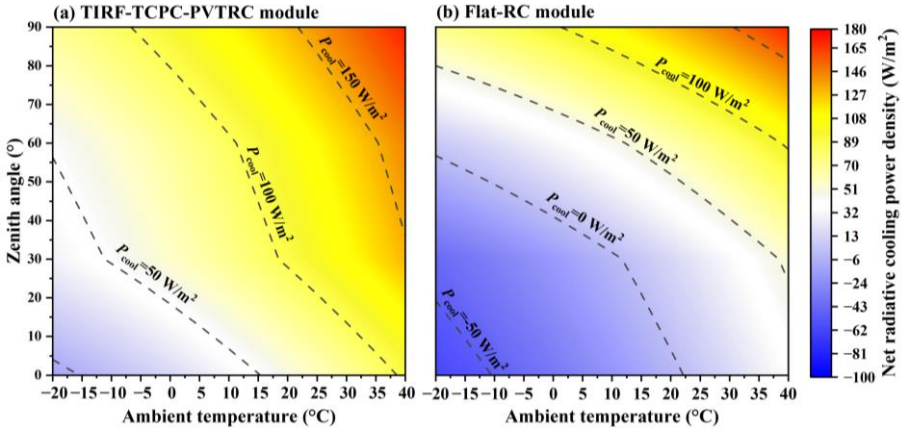

Figure 6-4: Net cooling power density for (a) TIRF-TCPC-PVTRC module and (b) flat-RC module under different ambient temperatures and zenith angles.

However, the structure of various components within the system can be further optimized to enhance solar energy collection and improve cooling power. The optimization of these component structures will be explored in the following subsections.

6.2.2 Optimization of the TIRF-TCPC-PVTRC module

A TIRF-TCPC-RC module consists of two TIRF-TCPC structures, two RC emitters and a PVT module. The two TIRF-TCPC structures are positioned side by side, A PVT module is installed between two adjacent TIRF-TCPCs. To enhance the overall performance of the module, two key aspects must be considered. The first is optimizing the TIRF-TCPC structure to allow more solar radiation toward the PVT module. The second aspect is to optimize the shape of the RC emitters to maximize the reflection of solar radiation and ensure that as much emitted thermal radiation as possible is directed out of the system.

6.2.2.1 Evaluation indicators

Based on the discussion above, we will determine the solar receiving ratio ($\eta_{_sol}$) for the PVT module under different TIRF-TCPC structures to preliminarily assess the performance of the module. This factor represents the ratio of solar radiation reaching the system aperture to the solar radiation concentrated on the PVT module. A higher $\eta_{_sol}$ indicates that more solar energy reaches the PVT module, reducing the solar radiation absorbed by the RC emitter. Additionally, after identifying the

optimal TIRF-TCPC structure, we will further examine the $\eta_{_sol}$ for PVT module when RC emitters change to different shapes, considering ease of fabrication, to ultimately determine an optimized TIRF-TCPC-PVTRC system.

6.2.2.2 Structure optimization of TIRF-TCPC structures

This section compares TIRF-TCPC structures with different configurations to identify the optimal design that maximizes solar radiation received by the PVT module. The TIRF-TCPC structure is made of high-transmittance acrylic, with an assumed solar transmittance of 0.9. Additionally, the solar reflectivity of the RC emitter is set at 0.9. Figure 6-5 presents schematic diagrams of various TIRF-TCPC-PVTRC modules. Figure 6-5 (a) depicts a standard TIRF-TCPC structure. Figure 6-5 (b) shows a lens-walled TIRF-TCPC structure, and Figure 6-5 (c) illustrates a solid TIRF-TCPC structure. Furthermore, the cross-sections of three different structures are shown in Figure 6-5 (d). The standard TIRF-TCPC structure consists of a transparent CPC with θ_{max} of 30° and a thickness of 2 mm, attached to the TIRF. In contrast, the lens-walled CPC structure uses the parabola of the standard CPC, rotating it outward by an angle around its top point to form a new parabola, which is then filled to create a solid transparent structure. This rotation angle is referred to as the lens forming angle [246]. In this chapter, lens-walled CPCs with lens forming angles of 3°, 4°, and 5° were selected for discussed. The solid TIRF-TCPC structure is created by filling the space between two adjacent TIRF-TCPC parabolas with transparent materials.

Additionally, when comparing different TIRF-TCPC structures, three different RC emitters are selected: a traditional flat plate, an inverted V-type, and a specialized CPC-typed. For developed the CPC-typed emitter, first set the width of the PVT module as the exit aperture width of the CPC-typed RC emitter. The appropriate θ_{max} is decided. With a maximum of 30° to ensure the CPC structure does not extend beyond the external TCPC structure. Finally, the focal length of the parabola is calculated. The height of the inverted V-type RC emitter matches that of the CPC emitter, approximately 3/4 of the external TCPC structure. The purpose of proposing the CPC-type and inverted V-type emitters is to create a double-layer CPC structure with the external TCPC, allowing the PVT module to function as a CPV module, which can collect more solar energy and improve its $\eta_{_sol}$.

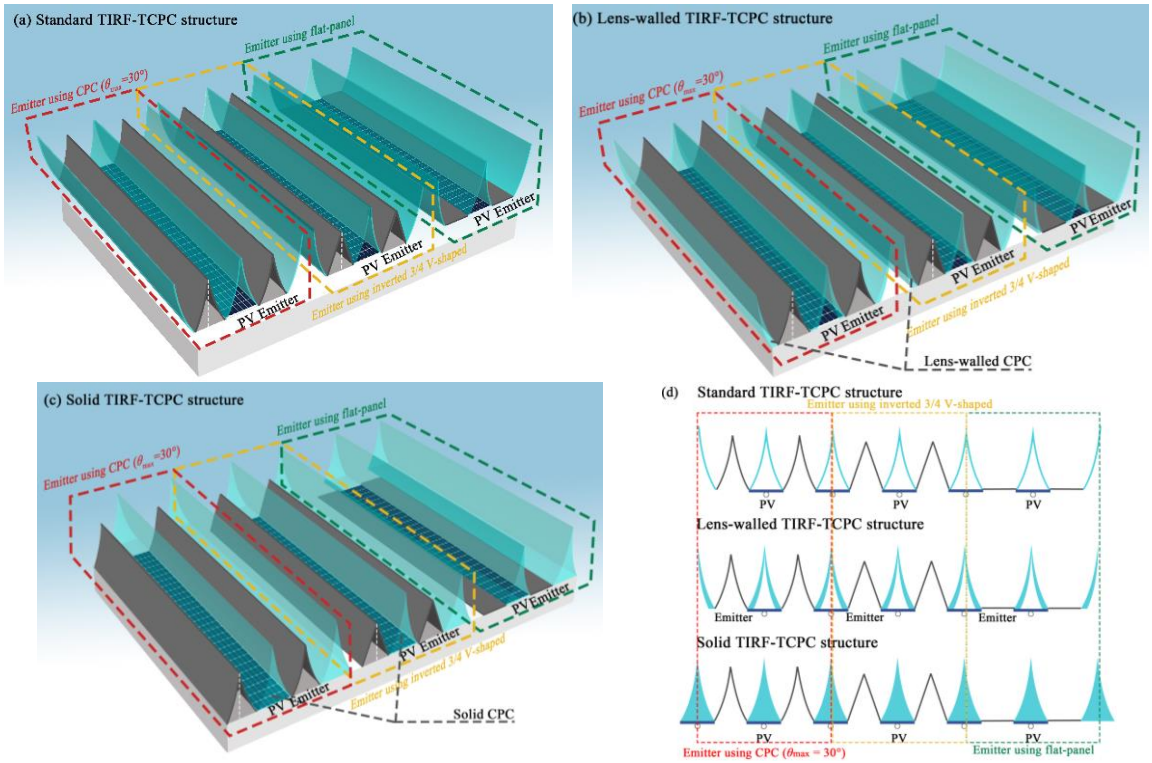

Figure 6-5: Different TIRF-TCPC structures in TIRF-TCPC-PVTRC modules. (a) Standard structure. (b) Lens-walled structure. (c) Solid structure. (d) Cross-sections of three TIRF-TCPC structures.

Figure 6-6 illustrates the $\eta_{_sol}$ for PVT modules under three different TIRF-TCPC structures. Figure 6-6 (a) shows the $\eta_{_sol}$ under standard TIRF-TCPC structure. When the CPC-type emitter is used, $\eta_{_sol}$ exceeds 0.8 for zenith angles between 0° and 20°, indicating that most of the solar radiation within this angle range can reach the PVT module, with only up to 20% of the solar radiation being absorbed by the RC emitter or escaping the module. In the zenith direction, $\eta_{_sol}$ is 0.85, showing a good advantage to the solar collection. When using the inverted V-shaped emitter, $\eta_{_sol}$ in the zenith direction increases slightly to 0.89 compared to the CPC-type emitter. However, the angle range where $\eta_{_sol}$ exceeds 0.8 narrows to 0°-15°. With the flat emitter, $\eta_{_sol}$ decreases near the zenith direction because most of the solar radiation reaches the RC emitter directly and cannot be reflected to the PVT module. In the zenith direction, $\eta_{_sol}$ is 0.34, indicating poor solar energy collection performance. Figure 6-6 (b) presents the $\eta_{_sol}$ curve of the lens-walled CPC structures with three different lens forming angles. As the rotation angle of the lens-walled CPC increases, the $\eta_{_sol}$ curve shifts upward. Specifically, when using the inverted V-shaped emitter, η in the zenith direction is 0.89 for the 3° lens-walled structure and 0.91 for the 5° lens-walled structure. However, the impact of changing the angle is minimal, and the differences between the $\eta_{_sol}$ curves for the CPC-type emitter and the inverted V-shaped emitter are negligible.

Figure 6-6 (c) displays the $\eta_{_sol}$ for the PVT module under the solid TIRF-TCPC structure. In contrast to previous structures, the solid structure allows $\eta_{_sol}$ to maintain high values across most zenith angles. For example, the 5° lens-walled CPC maintains $\eta_{_sol}$ above 0.8 within the 0°-25° range, while the solid structure sustains $\eta_{_sol}$ above 0.8 over a broader range of 0°-45°, indicating excellent solar energy collection potential. Similar to the initial structures, the $\eta_{_sol}$ curves for the CPC-type emitter and the inverted V-shaped emitter are quite similar, and the performance with the flat emitter does not significantly improve.

Therefore, standard TIRF-TCPC and lens-walled TIRF-TCPC structures with 3° and 4° lens forming angles are excluded from further consideration, as is the use of the flat emitter. In the subsequent optimization of RC emitter shapes, the $\eta_{_sol}$ for the CPC-type and inverted V-shaped emitters of varying heights under 5° lens-walled TIRF-TCPC and solid TIRF-TCPC structures will be further investigated to determine the optimal TIRF-TCPC-PVTRC module design.

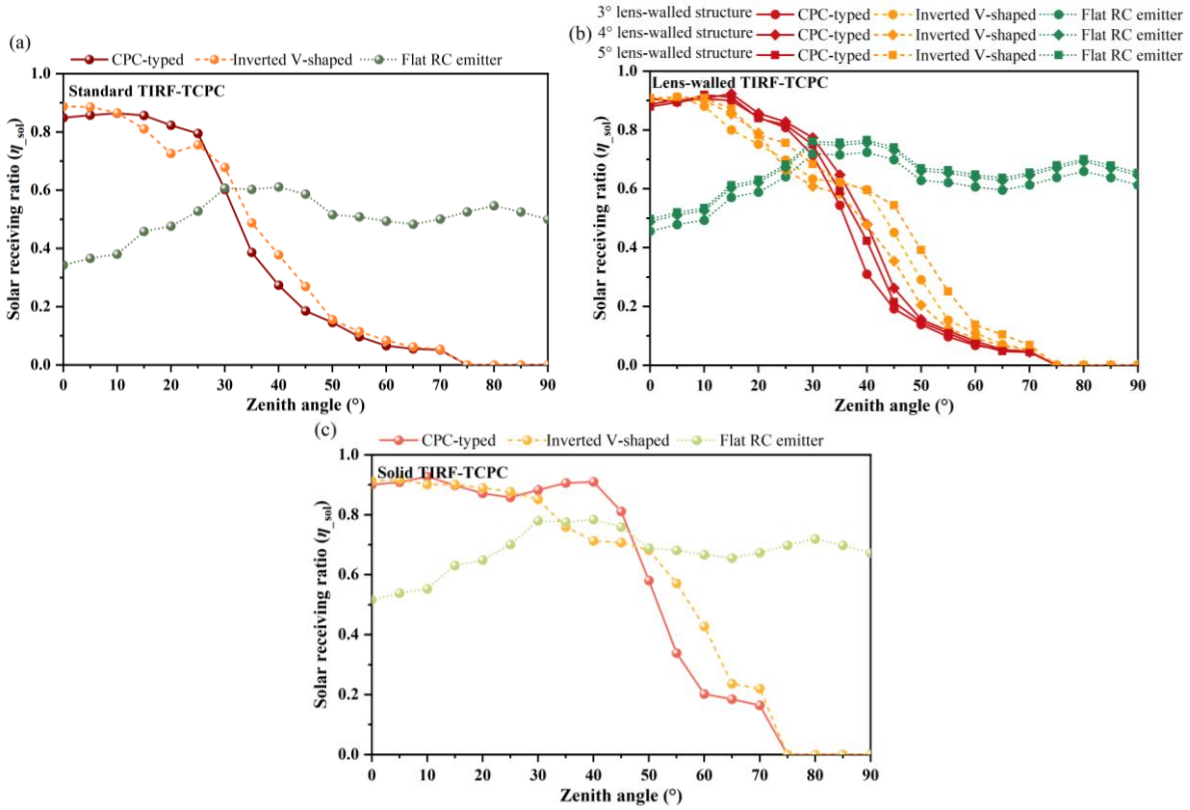

Figure 6-6: Solar receiving ratio for PVT module under (a) standard TIRF-TCPC. (b) Lens-walled TIRF-TCPC. (c)Solid TIRF-TCPC structures.

6.2.2.3 Shape optimization of RC emitter on TIRF-TCPC-PVTRC module

This subsection investigates the impact of different heights of CPC-type and inverted V-shaped emitters on the $\eta_{_sol}$ for the PVT in the TIRF-TCPC-PVTRC module. Six RC emitters are selected for comparison: CPC-type emitters with θ_{max} of 30°, 28°, and 25°, and inverted V-shaped RC emitters with heights of 75%, 50%, and 25% of the TIRF-TCPC structure. The cross-section view of the TIRF-TCPC-PVTRC module and RC emitters is shown in Figure 6-7.

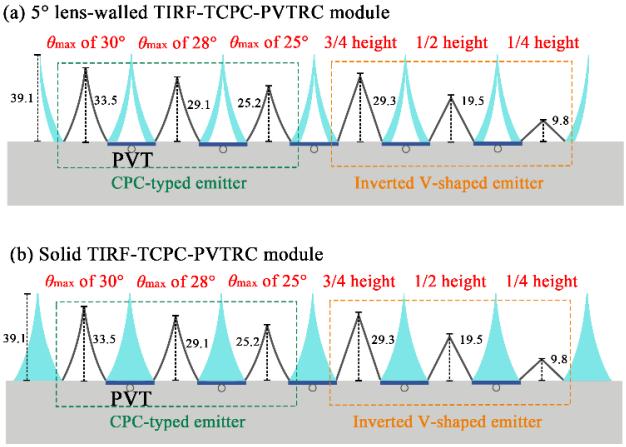

Figure 6-7: (a) 5° lens-walled TIRF-TCPC-PVTRC and (b) Solid TIRF-TCPC-PVTRC modules with different RC emitters.

Figure 6-8 shows the $\eta_{_sol}$ for the PVT module in lens-walled and solid TIRF-TCPC-PVTRC modules when coupled with various RC emitters. Since the $\eta_{_sol}$ curve is symmetric along the zenith direction, Figure 6-8 only presents data from 0° (zenith direction) to 90° (horizon). Figure 6-8 (a) demonstrates that in the 5° lens-walled TIRF-TCPC-PVTRC module, except for the 1/4-height inverted V-shaped emitter, the $\eta_{_sol}$ for the other five emitters in the zenith direction are all around 0.9, with minimal variation. Additionally, their trends with changing zenith angles are generally similar, slightly increasing near the zenith direction and then decreasing in smaller zenith angles, except for the 50%-height inverted RC module. Its $\eta_{_sol}$ is 0.69 at 25°, but it rises to 0.73 at 30° before rapidly declining at 40°. This allows it to collect more solar energy in regions where the solar profile angle is between 50° and 90° throughout the year. For instance, in the three cities at different latitudes analyzed in Section 5.4.3, the γ in the 50°-90°range exceeds 50%, indicating that solar radiation from this angle range accounts for more than half of the total daylight duration.

In the solid TIRF-TCPC-PVTRC module, as shown in Figure 6-8 (b), the three CPC-type emitters maintain $\eta_{_sol}$ above 0.8 across most angle ranges (0°-40°). Among the inverted V-shaped emitters, the

3/4-height emitter performs as well as or better than the CPC-type emitters in the 0°-30° range, though its $\eta_{_sol}$ decreases sharply beyond 30°. While the $\eta_{_sol}$ for the PVT module using the 50%-height emitter does not surpass the others near the zenith, it remains close, and at zenith angle is 40°, its $\eta_{_sol}$ exceeds that of the other RC emitters.

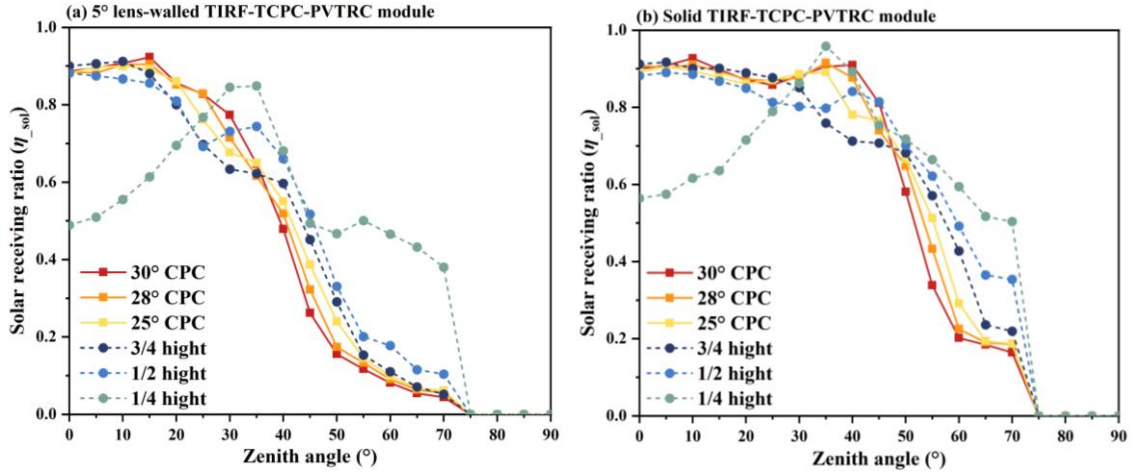

Figure 6-8: Solar receiving ratio for the PVT module in different TIIRF-TCPC-PVTRC module with different RC emitters.

From the figure, it can be observed that the $\eta_{_sol}$ for the PVT module is higher when using the solid TIRF-TCPC structure compared to the lens-walled TIRF-TCPC structure. However, the production cost and weight of the solid TIRF-TCPC structure are significantly greater than those of the lens-walled structure, making it less suitable for building integration. Additionally, while $\eta_{_sol}$ is slightly higher, the difference is not substantial enough to provide a clear advantage. Therefore, considering both cost-effectiveness and practicality, the 5° lens-walled TCPC structure is selected as the primary structure for the optimized system.

Regarding the selection of RC emitters, it is challenging to shape aluminum of a certain thickness into a CPC form while maintaining it focusing characteristics. Furthermore, there is minimal difference in the $\eta_{_sol}$ for the PVT module when using this RC emitter versus an inverted V-shaped emitter. In contrast, the inverted V-shaped emitter demonstrates higher $\eta_{_sol}$ at lower zenith angles. Thus, after comprehensive consideration, the optimized system used for subsequent modellings and experimental analysis is a 5° lens-walled TIRF-TCPC-PVTRC system with a 50%-height RC emitter. This configuration will be referred to as the "optimized system" in the following text.

6.3 Experimental study of optimized TIRF-TCPC-PVTRC system

6.3.1 Experimental preparation

The optimized TIRF-TCPC-PVTRC system has three main components: several transparent CPC structures, inverted V-shaped RC emitters, and PVT panels. The transparent CPC structure is selected as a lens-walled CPC with a 5° lens forming angle made from high-transparency acrylic utilizing 3D-printing technology. Additionally, the inner layer of the lens-walled CPC is coated with a TIRF, which has a weighted average solar transmittance of 0.69 and demonstrates excellent infrared reflection properties, as shown in Figure 6-9. The spectral characteristics of TIRF in the solar spectrum were measured using a UV-Vis-NIR spectrometer (SolidSpec-3700 DUV, Shimadzu), while its infrared spectral properties were analysed with a Fourier transform infrared spectrometer (INVENIO S, Bruker). The inverted V-shaped RC emitter is composed of two aluminium microchannels coated with a commercial metamaterial (the same material used in the experiment shows in Section 4.4). The height of the emitter is half that of the lens-walled CPC and it is attached to insulation foam with tape. The PVT module consists of a copper tube welded to the back panel of the dripping solar cell. Additionally, aside from the main components, the bottom of the system is lined with 40 mm thick insulation foam to minimize reverse heat loss.

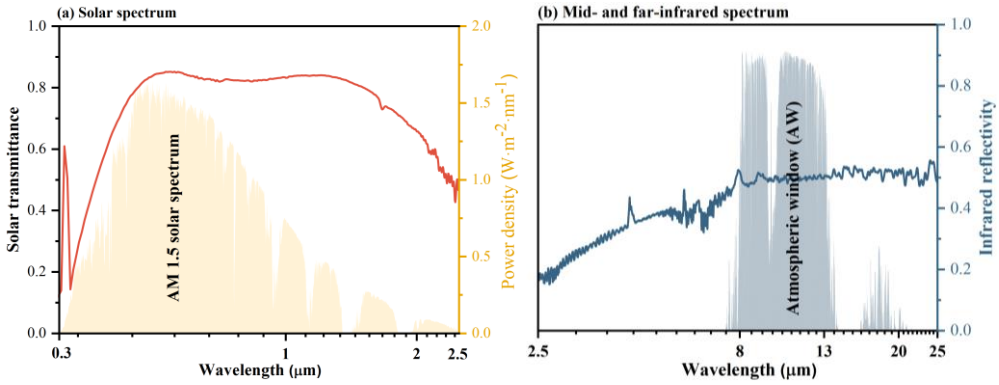

Figure 6-9: Spectral properties of the TIRF. (a) Transmittance in solar spectrum. (b) Reflectivity under mid- and far-infrared spectrum.

Figure 6-10 (a) shows the in-site experimental devices conducted on the roof of the University of Science and Technology of China in Hefei, China. The experimental devices include a weather station to measure solar irradiance and environmental parameters on the day of the experiment, a data logger to record the temperature of different system modules, and two PVTRC systems: one is the optimized system, and another is the PVTRC system used as a comparison group. Several T-type thermocouples are placed at various locations to measure the components' temperature, and a PV Analyzer is used to

measure the power of the solar cells. The front of the setup faces south and the test and monitoring devices along with their uncertainties, are listed in Table 6-2. Figure 6-10 (b) provides a cross-sectional view of the two systems. In the PVT-RC system, the PVT and RC emitters are alternately placed, with the PVT module embedded in the insulation layer and the RC emitter attached to the insulation layer. T_1 to T_6 represent the positions and numbers of the thermocouples in the system. T_1 and T_6 are placed inside the PVT copper tubes and fixed to the tube wall, while T_2 and T_4 are located on the anti-sunward side of the RC emitter: T_2 is positioned in the middle of the microchannel, and T_4 is at the bottom. T_3 measures the temperature of the sunward side of the RC emitter, and T_5 is placed on the back of the solar cell panel to allow comparison with T_1 and T_6. In the optimized system, the structure is mostly the same as in the PVTRC module, with the addition of lens-walled CPCs placed on either side of the RC emitter to form a TCPC-RC module. The lens-walled CPCs sandwich the PVT module, allowing only visible light to pass through while reflecting near- and far-infrared radiation to reduce the temperature of the PVT module. The positions of T_7 to T_{12} correspond to those in the PVTRC system for more accurate comparison.

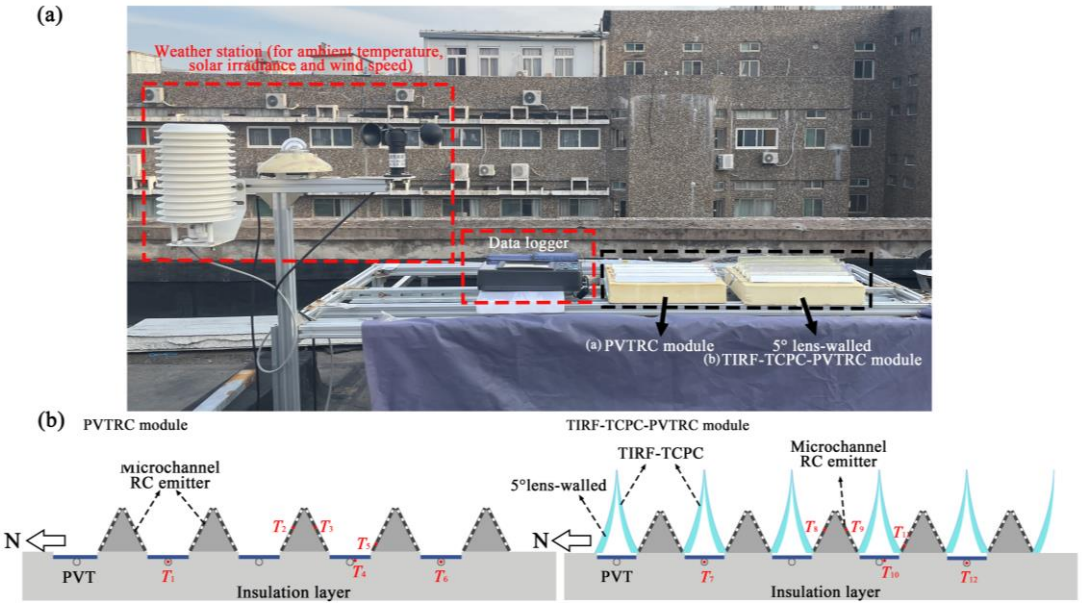

Figure 6-10: (a) Photograph of in-site experimental devices in Hefei, China. (b) Cross-section view of the two PVTRC systems.

Table 6-2: List of testing and monitoring devices in the experimental system.

Device	Specification	Uncertainty
Data logger	HIOKI LR8402-21	/
Thermocouple (calibrated)	Type T	±0.05 °C
PV Analyzer	PROVS-200A	±1%

Weather station for pyranometer	PC-08	< 5%
Weather station for relative humidity	PC-08	±2% (< 80%RH)
Weather station for wind speed	PC-08	±4 (0.3+0.03V) m/s

6.3.2 Experimental results analysis

6.3.2.1 Solar energy conversion performance

This section analyses the solar energy conversion efficiency of the two PVTRC systems by measuring the maximum power output (P_{max}) of the solar cells at 5-minute intervals between 11:00 and 12:00 on 7th August 2024. As shown in Figure 6-11 (a) and (b), the PVTRC system and the optimized system are equipped with five 260 mm × 20 mm epoxy solar cells. The solar cell's conversion efficiency (η_{eff}) was calculated prior to installation and found to be 11.1%. When measuring P_{max}, five solar cells are connected in series to form a photovoltaic panel using soldering technology. The effective area coefficient of the photovoltaic panel is 0.8. During the experiment, the PV Analyzer was used to obtain the hourly P_{max}, as shown Figure 6-11 (c). Table 6-3 shows the P_{max} of the two PVTRC systems during 11:00-12:00. Then, using the solar irradiance data from the weather station recorded at the same time to calculate the different η_{eff} for the two systems based on the solar energy conversion efficiency equation, which can be expressed as:

$$\eta_{eff} = \frac{P_{max}}{A \times G \times f} \times 100\% \tag{6.5}$$

where P_{max} is the maximum output power, W; A is the total area of the photovoltaic panel, m^2; G is the solar radiation intensity, W/m^2; f is the effective area coefficient.

Table 6-3:Maximum power output of the two systems on 7th August,2024 (1 is PVTRC system and 2 is optimized system)

	11:00	11:05	11:10	11:15	11:20	11:25	11:30	11:35	11:40	11:45	11:50	11:55	12:00
1	1.61	1.70	1.73	1.70	1.73	1.71	1.75	1.81	1.64	1.69	1.38	1.81	1.76
2	1.29	1.31	1.32	1.08	1.36	1.33	1.37	1.31	1.37	1.38	1.22	1.56	1.53

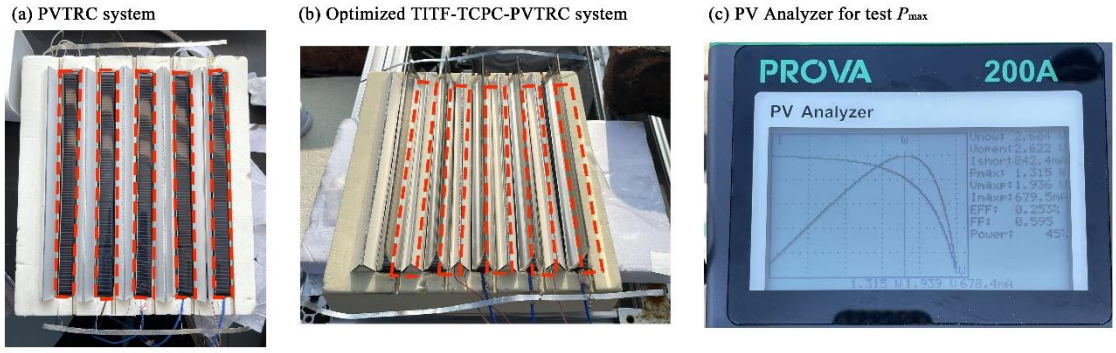

Figure 6-11: Schematic diagram of solar cells in (a) PVTRC system and (b) optimized TIRF-TCPC-RC system. (c) Photo of PV Analyzer field test.

Table 6-4 presents the calculated η_{eff} for the two systems. The results show that the η_{eff} for the PVTRC system is higher than that of the optimized system, as the solar cells in the PVTRC system are directly exposed to solar radiation without any shielding. During the experiment, the maximum η_{eff} for the PVTRC system reached 13.3%. In contrast, in the optimized system, the solar cells are positioned between two TIRF-TCPC structures, which restricts part of solar radiation reaching the solar cells due to the solar transmittance of the TIRF-TCPC being approximately 0.6. As a result, the η_{eff} for the optimized system was reduced to a maximum of 8.4%, which is 36.8% lower than the PVTRC system.

To improve the η_{eff} for the system, selecting TIRF materials with higher solar transmittance should be considered. However, increasing the solar transmittance of TIRF materials often results in reduced thermal radiation reflectivity, affecting the RC modules' cooling performance. Therefore, when selecting materials for the hybrid system, a balance between solar energy conversion efficiency and RC performance must be carefully considered to achieve optimal overall performance. The following subsections will discuss the temperature variations of different components in the two systems during the day to evaluate their cooling performance.

Table 6-4: Solar energy conversion efficiency of the two systems on 7th August,2024 (1 is PVTRC system and 2 is optimized system)

	11:00	11:05	11:10	11:15	11:20	11:25	11:30	11:35	11:40	11:45	11:50	11:55	12:00
η_{eff-1}	0.117	0.122	0.125	0.125	0.127	0.124	0.126	0.133	0.120	0.123	0.118	0.122	0.121
η_{eff-2}	0.075	0.075	0.076	0.079	0.080	0.077	0.079	0.077	0.080	0.080	0.084	0.084	0.084

6.3.2.2 Radiative cooling performance

This subsection discusses the temperature variation of the two PVTRC systems over a 24-hour period, from 9:00 am on 8th August to 9:00 am on 9th August, to explore the cooling performance of the

RC modules in the systems. During experimental time, the weather alternated between sunny and cloudy during the day, while the sky remained clear at night. Figure 6-12 presents the meteorological data recorded during the experiment. It can be seen that solar irradiance was unstable, particularly after 12:00, where it often dropped sharply and then rose again due to cloud cover. At noon, solar irradiance peaked at 964 W/m^2, which benefited the PVT modules to collect solar energy but negatively impacted the cooling performance of the RC modules. The presence of clouds also caused slight fluctuations in longwave thermal radiation during the day, which stabilized after 18:00. During the day, longwave thermal radiation averaged around 500 W/m^2, while at night it was slightly lower, at approximately 450 W/m^2. Additionally, relative humidity was low during the day, averaging around 52.3%, but it suddenly increased to over 80% between 17:00 and 18:00 due to showers. The sky then cleared, and the humidity remained around 85% until it gradually decreased after 7:00 on the 9th of August. Furthermore, wind speed was relatively stable throughout the experiment, averaging 0-3 m/s, except for a peak of 5.7 m/s at 17:00.

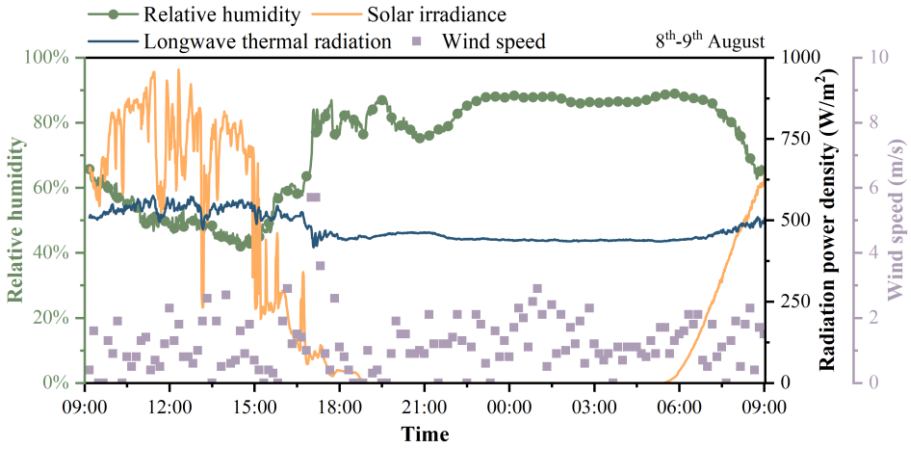

Figure 6-12: Meteorological data during the experiment

Figure 6-13 illustrates the temperature variations of different thermocouples (T_1-T_{12}) in the two PVTRC systems. Specifically, Figure 6-13 (a) shows the temperatures of the PVTRC system (T_1-T_6) alongside the ambient temperature (T_{amb}), while Figure 6-13 (b) presents the T_{amb} and thermocouple reading (T_7-T_{12}) for the optimized system. It can be observed that all thermocouples recorded temperatures higher than the T_{amb} during the daytime (9:00-17:00) on the 8th, indicating that neither the RC nor the PVT modules in either system achieved a cooling effect during the daytime. Additionally, the temperature curves for all thermocouples exhibited significant fluctuations, mirroring the trend of

the solar irradiance curve. This is because higher solar radiation leads to increased absorption by the PVT and RC modules, causing their temperatures to rise. In both the PVTRC and optimized systems, the PVT module temperature was higher than that of the RC module during the daytime, with the PVTRC system temperatures being slightly higher. In the PVTRC system, T_1 and T_6, located in the PVT copper tubes, reached peak temperatures of 87 and 84.2 °C at 11:43. At the same time, T_7 and T_{12}, located at corresponding positions in the optimized system, recorded lower temperatures of 80.85 and 75.4 °C, representing reductions of 7.1% and 10.4%, respectively. The temperature curves for T_7 and T_{12} remained lower than those for T_1 and T_6 during the daytime because the TIRF layer blocked some solar radiation from reaching the PVT module.

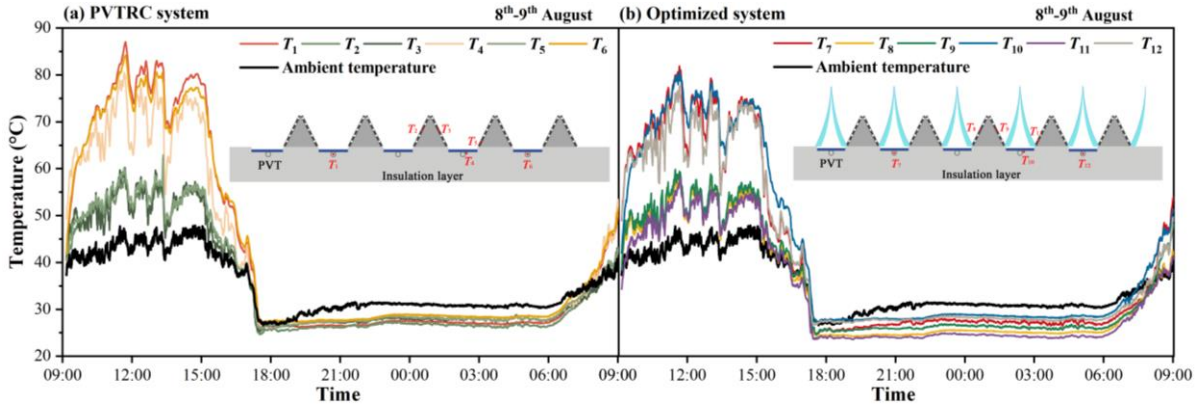

Figure 6-13:Ambient temperature and the temperature of different modules in the (a) PVTRC system and (b) optimized system.

When comparing the RC module temperatures of the two systems, it is evident that the temperature curves of the RC emitters within the same system largely overlap. However, the RC module temperature in the PVTRC system remained slightly higher than that of the optimized system. Specifically, at noon, T_8 and T_{11} in the optimized system measured 49.25 and 50.3 °C, approximately 7 °C above ambient temperature. In contrast, without the lens-walled TCPC, T_2 and T_5 in the PVTRC system recorded higher temperatures of 50.65 and 52.65°C. Additionally, the RC emitter on the sunward side showed higher temperatures than on the anti-sunward side; specifically, temperature sensor T_3 recorded a maximum of 51.2 °C, marginally higher than the 50.43 °C measured at sensor T_9 in the optimized system. These results indicate that while neither system achieved daytime radiative cooling effect, the temperatures in the optimized system are consistently lower for both the PVT and RC modules.

At 17:00, the temperatures of the RC modules in the optimized system began to drop below the ambient temperature, while the RC modules in the PVTRC system remained slightly above ambient. Specifically, at 17:00, the temperatures of T_8, T_9, and T_{11} were 37.75 °C, 38.25 °C, and 36.02 °C, respectively, all still lower than the T_{amb} of 38.75 °C. Meanwhile, the temperatures of T_2, T_3, and T_6 were 38.85 °C, 39.25 °C, and 39.12 °C. As solar irradiance decreased, the temperatures of the RC modules in both systems gradually dropped. The figure shows that during the nighttime (from 17:00 on 8th to 7:00 on 9th), all measured modules reached sub-ambient temperatures. Among them, T_{11} in the optimized system recorded the lowest temperature, reaching 23.6 °C, which was 5.35 °C lower than the ambient temperature at that time. The temperatures of T_8 and T_9 followed closely. At 0:00, the temperatures of T_{11}, T_8, and T_9 were 24.65 °C, 25.55 °C, and 26.55 °C, respectively, representing reductions of 21.1%, 18.1%, and 14.9% compared to the T_{amb}. In contrast, the temperature drop in the PVTRC system was smaller than the optimized system. At 0:00, T_2 and T_3 recorded temperatures of 26.95 °C and 28.1 °C, while T_5 was at 28.85 °C. These results demonstrate that the optimized system has better cooling capacity at night compared to the PVTRC system, achieving a greater temperature drop. However, the top of the PVT in the optimized system is blocked by the lens-walled CPC, preventing effective heat radiation to the sky, thus limiting the cooling effect. In contrast, the PVTRC system, which lacks lens-walled shielding, allows the PVT module to emit most of thermal radiation to the sky, resulting in better cooling performance.

Table 6-5 presents the average temperatures of T_1 to T_{12} during the daytime (9:00-17:00) and at night (from 17:00 on 8th to 7:00 on 9th) in the two systems, along with the average T_{amb}. During the daytime, the average T_{amb} shows 41.46 °C, while the average temperatures of T_1 to T_{12} are all higher than T_{amb}. Among them, the temperature of PVT components is much higher than that of RC components. Specifically, in the PVTRC system, the temperatures of the PVT modules (T_1, T_4, T_6) are 65.33 °C, 62.5 °C, and 64.58 °C, which are 45.6% to 57.6% higher than the average T_{amb}. In contrast, the average temperatures of the PVT modules in the optimized system are slightly lower, ranging from 42.4% to 45.7% higher than T_{amb}. Additionally, although the RC modules' average temperatures in both systems do not achieve sub-ambient temperatures, they are maintained around 45 °C, near the T_{amb}.

Table 6-5: Average daytime and nighttime temperatures of various components of the two systems.

	T_1	T_2	T_3	T_4	T_5	T_6	T_{amb}	T_7	T_8	T_9	T_{10}	T_{11}	T_{12}
Daytime	65.33	47.31	47.80	62.50	48.84	64.58	41.46	60.42	46.69	47.59	60.37	45.53	59.03
nighttime	27.12	26.59	27.23	27.98	27.89	27.99	30.48	27.76	25.12	26.19	28.49	24.36	28.58

During the nighttime, the average T_{amb} is 30.48 °C. It can be observed that the temperatures of all measured thermocouples are lower than that, demonstrating that both systems can achieve the RC effect. In the PVTRC system, the RC and PVT modules exhibit high thermal radiation emissivity, resulting in similar average temperatures for T_1 to T_6, around 27.5 °C, except for T_2. Since T_2 had the lowest average temperature during the daytime, its nighttime temperature remains slightly lower than that of the other components, at 26.59 °C. In the optimized system, due to the shielding effect of the lens-walled CPC structures, the average temperatures of the PVT modules are slightly higher than that in the PVTRC system, as seen with T_{10} and T_{11}, which have average temperatures of 28.49 °C and 28.58 °C, respectively However, the lens-walled CPC structure also results in a significant reduction in the average temperature of the RC modules, particularly at T_{11}, which is 6.12 °C lower than the average T_{amb}. This represents an average temperature drop of the RC module that is 88.31% greater than that of the PVTRC system. Additionally, T_8 and T_9 are 5.36 °C and 4.29 °C lower than the T_{amb}, respectively, indicating excellent cooling performance.

6.4 Summary

This chapter proposes a hybrid system that integrates PVT and RC modules. In the RC module of this system, a transparent CPC covering with transparent infrared reflective film (TIRF) is utilized to replace the traditional mirror CPC structure, forming a novel TIRF-TCPC-RC module. Additionally, the RC modules and PVT modules are arranged alternately, with the PVT modules positioned in the gap between two adjacent TIRF-TCPC structures, which enables this system to collect both solar and cold energy, named TIRF-TCPC-PVTRC module. In this chapter, firstly the solar energy receiving ratio for the PVT module under different TIRF-TCPC configurations is evaluated using simulation software, leading to the selection of an appropriate TIRF-TCPC structure. The performance of the TIRF-TCPC-PVTRC module with various RC emitters is then analyzed, ultimately resulting in an optimized system. Outdoor experiments measure the solar energy conversion efficiency and the temperature of different components in both the optimized system and the conventional PVTRC system. The experimental results indicate that its nighttime cooling capacity improves by 88%, demonstrating excellent cooling

performance, while the solar energy conversion efficiency of the optimized system is 36% lower than that of the PVTRC system due to limitations with TIRF materials.

This novel system effectively collects both solar and cold energy, addressing the limitation of conventional RC or PVT systems that only provide a single energy utilization in building applications. It offers flexibility and versatility for building energy supply and introduces attractive research directions for achieving net-zero energy buildings in the future. However, further research should focus on identifying suitable TIRF materials to simultaneously enhance the efficiency of both PVT and RC modules within the system.

7. Conclusion

7.1 Summary of findings and contributions

The literature review indicates that among the various strategies for zero-energy buildings, photovoltaic thermal (PVT) systems, which harness solar energy (~5800K) to provide heat and electricity, and passive radiative sky cooling (RC) technologies, which utilize the cold universe (~3K) to cool buildings, are considered promising approaches. While research on PVT systems is relatively mature, systematic investigations into RC technology have only begun after the 1960s. To enhance the cooling performance of RC technology, researchers have proposed a new concentrating RC system. Traditionally, concentrators have been used in solar energy collection, but recent findings suggest that they can also serve as thermal radiation concentrators, increasing the cooling power density of RC technologies. Nevertheless, there remains a gap in research on the application of concentrating RC systems. Moreover, theoretical models characterizing RC cooling performance, particularly for concentrating RC systems, are still incomplete.

The purpose of this thesis is to optimize a novel concentrated RC system with superior cooling performance and to couple it with a solar energy collection system. This integration aims to combine solar energy and radiative cooling technologies to meet the flexibility and versatility required for energy provision in building applications. First, the thesis introduces an optical modelling approach that accurately characterizes the cooling performance of RC systems under complex configurations. This addresses the limitations of existing theoretical models, which often overlook the impact of the

surrounding environment on cooling power and thus overestimate cooling capacity. The proposed modelling approach can accurately assess the heat exchange between the RC modules and the external environment, providing a precise characterization of the module's cooling capacity throughout a day. Additionally, this thesis conducts an in-depth study of the mirrored compound parabolic concentrator (CPC)-based RC module, referred to as the CPC-RC module. The function of CPC in shielding solar and adverse thermal radiation to enhance cooling performance is further explored. Outdoor experiments have demonstrated that its average nighttime temperature reduction capacity is 30% higher than that of a flat-RC module, highlighting its excellent nighttime cooling performance. Utilizing the proposed approach to investigate the cooling performance of the CPC-RC module on four typical days, it is found that the CPC-RC module consistently exhibits the highest all-day average cooling power density compared to traditional flat-RC module and concentrated RC modules with inverted trapezoidal concentrators. Even in summer, its cooling power density is 4.5% and 13.2% higher than the inverted trapezoidal-RC and flat RC modules, respectively.

However, it is found that the impact of solar radiation on the CPC-RC module is significantly greater than on flat-RC modules due to the concentrating properties of the CPC. Therefore, it is necessary to further mitigate the adverse effects of solar radiation on the CPC-RC module. To address this issue, a novel RC module based on CPC with dissimilar materials (termed DCPC-RC module) is proposed. In this module, dissimilar CPC structures covered with transparent infrared reflective film (TIRF) allow solar radiation to pass through the transparent wing framework rather than being reflected onto the emitter, reducing the solar radiation absorbed by the emitter. The results of the outdoor experiment in Nottingham demonstrated that the DCPC-RC module effectively achieves a cooling effect during the daytime. Specifically, the module's average temperature was 0.95 °C lower than the average ambient temperature. The cooling performance of the DCPC-RC, mirror CPC-RC, and flat-RC modules is verified through a modelling approach. It is shown that when solar radiation from the zenith direction, the mirror CPC-RC module cannot achieve the cooling effect, while the cooling power of the flat-RC module is only 49.18 W/m^2, which is 30.9% lower than that of the DCPC-RC module. Additionally, the hours percentage of different solar profile angles interval throughout the year in different regions is

analysed. The results show that in Guangzhou, the solar profile angle peaks at 40° - 50° and 80° - 90°, accounting for 14.7% and 13.5% of the total daylight duration, respectively. When the module is tilted 30° to the anti-sunward side, the average cooling power density can reach 138.08 and 130.78 W/m^2. This indicates that in low-latitude regions, tilting the RC module to the anti-sunward side is essential for achieving optimal heat dissipation.

The study of DCPC-RC modules revealed that the use of transparent CPCs can redirect solar radiation to another area, reducing its impact on the RC module. The solar radiation separated by the TIRF can still be utilized for building heating. Therefore, it is highly significant to further explore the collection and utilization of this solar radiation. Related studies have also shown that previous standalone solar energy utilization or RC technology faces challenges like seasonal adaptability and single functionality. To address these issues, an innovative integrated system of a photovoltaic thermal (i.e., PVT) and RC modules, based on a transparent CPC covered with TIRF (referred to as the TIRF-TCPC-PVTRC system) is proposed, which simultaneously enables heating and cooling, thereby improving the overall energy efficiency of buildings. After analysing the solar receiving ratio for the PVT module in the system, the optimized configuration is determined to be the 5° lens-walled TIRF-TCPC-PVTRC system with a 50%-height inverted V-shaped emitter (referred to as the optimized system). The experimental results show that the temperature reduction of the optimized system is 88% greater than that of the PVTRC system without the TIRF-TCPC structure, demonstrating excellent cooling performance. However, since the experiment used TIRF with a weighted average emissivity of only 0.69, the conversion efficiency of the PVT component is 36% lower than that of the PVTRC system. Despite this, a significant temperature reduction effect was still achieved.

7.2 Limitation and recommendation

Although RC technology is considered as an attractive strategy for saving building energy consumption, its large-scale application in buildings remains limited due to the mismatch between its cooling time and the peak demand for building cooling, as well as its relatively low cooling power density. This thesis investigates a concentrated RC module (CPC-RC module) with the potential to achieve all-day RC, integrated with a solar energy collection system to better meet building energy

needs by continuously adjusting its structural configuration. However, several aspects can still be improved to enhance system efficiency while maintaining versatility and flexibility for building applications.

First, although the optimized TIRF-TCPC-PVTRC system demonstrated excellent nighttime cooling performance in outdoor experiments, its daytime cooling performance failed to achieve sub-ambient temperature. This shortfall is primarily due to three factors: (1) the RC emitter material used has a relatively high solar absorptivity (weighted average of 0.13), causing excessive absorption of solar radiation. (2) During the experiment, solar radiation remained at a high level, and since the system is positioned horizontally, it is unable to effectively shield additional solar radiation, which negatively impacted the RC effect during the daytime. And (3) the TIRF material has low infrared reflectivity, preventing thermal radiation emitted by the emitter from being concentrated into a smaller zenith range. Therefore, future research should focus on updating the materials used for the RC emitter and TIRF. Additionally, the cooling performance of the system should be evaluated under different climatic conditions.

Second, the temperatures of the PVT modules and the conversion efficiency of the solar cells in the optimized system were measured, revealing that solar radiation reaching the PVT module was limited due to the imperfect TIRF material, resulting in a low conversion efficiency. Future research should investigate the solar energy conversion efficiency of the PVT module using updated materials. Moreover, the thermal efficiency of the PVT module could be further tested when using air-based or water-based modules, enabling the simultaneous collection of cold, heat, and electricity in a single system.

Finally, since the modelling approach proposed in this thesis focuses solely on the cooling performance of RC module, it does not evaluate the performance of the PVT module. Therefore, future research should develop a comprehensive model that characterizes the dynamic performance of the integrated system to better assess its potential for reducing building energy consumption.

References

[1] International Energy Agency, IEA (n.d.). https://www.iea.org (accessed September 16, 2024).

[2] Heat and health, (n.d.). https://www.who.int/news-room/fact-sheets/detail/climate-change-heat-and-health (accessed September 16, 2024).

[3] International Energy Agency, IEA (n.d.). The Future of Cooling – Analysis. https://www.iea.org/reports/the-future-of-cooling (accessed September 27, 2024).

[4] UN, (2022). CO2 emissions from buildings and construction hit new high, leaving sector off track to decarbonize by 2050. https://www.unep.org/news-and-stories/press-release/co2-emissions-buildings-and-construction-hit-new-high-leaving-sector (accessed September 16, 2024).

[5] J.L. Hernández, I. de Miguel, F. Vélez, A. Vasallo, Challenges and opportunities in European smart buildings energy management: A critical review, Renewable and Sustainable Energy Reviews 199 (2024) 114472. https://doi.org/10.1016/j.rser.2024.114472.

[6] Status, (n.d.). Power to heat and cooling. https://www.irena.org/Innovation-landscape-for-smart-electrification/Power-to-heat-and-cooling/Status (accessed September 16, 2024).

[7] International Energy Agency, IEA (n.d.). Greenhouse Gas Emissions from Energy Data Explorer – Data Tools. https://www.iea.org/data-and-statistics/data-tools/greenhouse-gas-emissions-from-energy-data-explorer (accessed September 16, 2024).

[8] International Energy Agency, IEA (2023). Final energy consumption and carbon emissions for space cooling by region in the Net Zero Scenario. https://www.iea.org/data-and-statistics/charts/final-energy-consumption-and-carbon-emissions-for-space-cooling-by-region-in-the-net-zero-scenario-2000-2030, Licence: CC BY 4.0, IEA (n.d.). https://www.iea.org (accessed September 16, 2024).

[9] International Energy Agency, IEA (2023). Global Energy and Climate Model Documentation. https://www.iea.org/reports/global-energy-and-climate-model (accessed October, 2024).

[10] S. Suhendri, M. Hu, Y. Su, J. Darkwa, S. Riffat, Performance evaluation of combined solar chimney and radiative cooling ventilation, Building and Environment 209 (2022) 108686. https://doi.org/10.1016/j.buildenv.2021.108686.

[11] D. Zhao, A. Aili, Y. Zhai, J. Lu, D. Kidd, G. Tan, X. Yin, R. Yang, Subambient Cooling of Water: Toward Real-World Applications of Daytime Radiative Cooling, Joule 3 (2019) 111–123. https://doi.org/10.1016/j.joule.2018.10.006.

[12] D. Zhao, A. Aili, Y. Zhai, S. Xu, G. Tan, X. Yin, R. Yang, Radiative sky cooling: Fundamental principles, materials, and applications, Applied Physics Reviews 6 (2019) 021306. https://doi.org/10.1063/1.5087281.

[13] T. Wang, Y. Wu, L. Shi, X. Hu, M. Chen, L. Wu, A structural polymer for highly efficient all-day passive radiative cooling, Nat Commun 12 (2021) 365. https://doi.org/10.1038/s41467-020-20646-7.

[14] M. Ono, K. Chen, W. Li, S. Fan, Self-adaptive radiative cooling based on phase change materials, Opt. Express, OE 26 (2018) A777–A787. https://doi.org/10.1364/OE.26.00A777.

[15] Q. Wang, Y. Dan, S. Riffat, H. Yang, Y. Su, M. Hu, Harvesting energy from the sun and space: A versatile collector for simultaneous production of electricity, heat, and cold energy, The Innovation Energy 1 (2024) 100013. https://doi.org/10.59717/j.xinn-energy.2024.100013.

[16] T. Zuo, J. Zhang, L. Xu, T. Xu, W. Ren, W. Liu, T. Wang, S. Wang, Y. Cai, L. Yi, Superhydrophobic cotton fabric based on aqueous paint for passive daytime radiative cooling, Progress in Organic Coatings 190 (2024) 108395. https://doi.org/10.1016/j.porgcoat.2024.108395.

[17] E. Aramendia, P.E. Brockway, P.G. Taylor, J.B. Norman, Exploring the effects of mineral depletion on renewable energy technologies net energy returns, Energy 290 (2024) 130112. https://doi.org/10.1016/j.energy.2023.130112.

[18] M. Hu, B. Zhao, Suhendri, X. Ao, J. Cao, Q. Wang, S. Riffat, Y. Su, G. Pei, Applications of radiative sky cooling in solar energy systems: Progress, challenges, and prospects, Renewable and Sustainable Energy Reviews 160 (2022) 112304. https://doi.org/10.1016/j.rser.2022.112304.

[19] A. Herez, H. El Hage, T. Lemenand, M. Ramadan, M. Khaled, Review on photovoltaic/thermal hybrid solar collectors: Classifications, applications and new systems, Solar Energy 207 (2020) 1321–1347. https://doi.org/10.1016/j.solener.2020.07.062.

[20] R.V. Parupudi, H. Singh, M. Kolokotroni, Low Concentrating Photovoltaics (LCPV) for buildings and their performance analyses, Applied Energy 279 (2020) 115839. https://doi.org/10.1016/j.apenergy.2020.115839.

[21] M. Tian, Y. Su, H. Zheng, G. Pei, G. Li, S. Riffat, A review on the recent research progress in the compound parabolic concentrator (CPC) for solar energy applications, Renewable and Sustainable Energy Reviews 82 (2018) 1272–1296. https://doi.org/10.1016/j.rser.2017.09.050.

[22] X. Lu, P. Xu, H. Wang, T. Yang, J. Hou, Cooling potential and applications prospects of passive radiative cooling in buildings: The current state-of-the-art, Renewable and Sustainable Energy Reviews 65 (2016) 1079–1097. https://doi.org/10.1016/j.rser.2016.07.058.

[23] H. Ju, S. Lei, F. Wang, D. Yang, J. Ou, A. Amirfazli, Daytime radiative cooling performance and building energy consumption simulation of superhydrophobic calcined kaolin/poly(vinylidene fluoride-co-hexafluoropropylene) coatings, Energy and Buildings 292 (2023) 113184. https://doi.org/10.1016/j.enbuild.2023.113184.

[24] D. Zhao, A. Aili, X. Yin, G. Tan, R. Yang, Roof-integrated radiative air-cooling system to achieve cooler attic for building energy saving, Energy and Buildings 203 (2019) 109453. https://doi.org/10.1016/j.enbuild.2019.109453.

[25] H. Tang, J. Wu, C. Li, Experimental and numerical study of a reversible radiative sky cooling PV window, Solar Energy 247 (2022) 441–452. https://doi.org/10.1016/j.solener.2022.10.057.

[26] T. Hu, T.H. Kwan, G. Pei, An all-day cooling system that combines solar absorption chiller and radiative cooling, Renewable Energy 186 (2022) 831–844. https://doi.org/10.1016/j.renene.2022.01.058.

[27] T. Liao, Q. Xu, Y. Dai, C. Cheng, Q. He, M. Ni, Radiative cooling-assisted thermoelectric refrigeration and power systems: Coupling properties and parametric optimization, Energy 242 (2022) 122546. https://doi.org/10.1016/j.energy.2021.122546.

[28] A. Ben-Shalom, B. Barzilai, D. Cabib, A.D. Devir, S.G. Lipson, U.P. Oppenheim, Sky radiance at wavelengths between 7 and 14 μm: measurement, calculation, and comparison with lowtran-4 predictions, Appl. Opt., AO 19 (1980) 838–839. https://doi.org/10.1364/AO.19.000838.

[29] C.G. Granqvist, A. Hjortsberg, Surfaces for radiative cooling: Silicon monoxide films on aluminum, Appl. Phys. Lett. 36 (1980) 139–141. https://doi.org/10.1063/1.91406.

[30] K. Lin, Y. Du, S. Chen, L. Chao, H. Him Lee, T. Chung Ho, Y. Zhu, Y. Zeng, A. Pan, C. Yan Tso, Nanoparticle-polymer hybrid dual-layer coating with broadband solar reflection for high-performance daytime passive radiative cooling, Energy and Buildings 276 (2022) 112507. https://doi.org/10.1016/j.enbuild.2022.112507.

[31] A.P. Raman, M.A. Anoma, L. Zhu, E. Rephaeli, S. Fan, Passive radiative cooling below ambient air temperature under direct sunlight, Nature 515 (2014) 540–544. https://doi.org/10.1038/nature13883.

[32] J. Huang, C. Lin, Y. Li, B. Huang, Effects of humidity, aerosol, and cloud on subambient radiative cooling, International Journal of Heat and Mass Transfer 186 (2022) 122438. https://doi.org/10.1016/j.ijheatmasstransfer.2021.122438.

[33] L. Zhou, H. Song, J. Liang, M. Singer, M. Zhou, E. Stegenburgs, N. Zhang, C. Xu, T. Ng, Z. Yu, B. Ooi, Q. Gan, A polydimethylsiloxane-coated metal structure for all-day radiative cooling, Nat Sustain 2 (2019) 718–724. https://doi.org/10.1038/s41893-019-0348-5.

[34] J. Peoples, Y.-W. Hung, X. Li, D. Gallagher, N. Fruehe, M. Pottschmidt, C. Breseman, C. Adams, A. Yuksel, J. Braun, W.T. Horton, X. Ruan, Concentrated radiative cooling, Applied Energy 310 (2022) 118368. https://doi.org/10.1016/j.apenergy.2021.118368.

[35] T.L. Bergman, F.P. Incropera, eds., Fundamentals of heat and mass transfer, 7th ed, Wiley, Hoboken, NJ, 2011.

[36] T. Yan, D. Xu, J. Meng, X. Xu, Z. Yu, H. Wu, A review of radiative sky cooling technology and its application in building systems, Renewable Energy 220 (2024) 119599. https://doi.org/10.1016/j.renene.2023.119599.

[37] J. Zhang, Z. Zhou, J. Quan, D. Zhang, J. Sui, J. Yu, J. Liu, A flexible film to block solar radiation for daytime radiative cooling, Solar Energy Materials and Solar Cells 225 (2021) 111029. https://doi.org/10.1016/j.solmat.2021.111029.

[38] L. Evangelisti, C. Guattari, F. Asdrubali, On the sky temperature models and their influence on buildings energy performance: A critical review, Energy and Buildings 183 (2019) 607–625. https://doi.org/10.1016/j.enbuild.2018.11.037.

[39] A. Pirvaram, N. Talebzadeh, S.N. Leung, P.G. O'Brien, Radiative cooling for buildings: A review of techno-enviro-economics and life-cycle assessment methods, Renewable and Sustainable Energy Reviews 162 (2022) 112415. https://doi.org/10.1016/j.rser.2022.112415.

[40] S. Lv, X. Sun, B. Zhang, Y. Lai, J. Yang, Research on the influence and optimization of sunshade effect on radiative cooling performance, Energy (2024) 131172. https://doi.org/10.1016/j.energy.2024.131172.

[41] L. Yu, Z. Xi, S. Li, D. Pang, H. Yan, M. Chen, All-day continuous electrical power generator by solar heating and radiative cooling from the sky, Applied Energy 322 (2022) 119403. https://doi.org/10.1016/j.apenergy.2022.119403.

[42] Y. Zhai, Y. Ma, S.N. David, D. Zhao, R. Lou, G. Tan, R. Yang, X. Yin, Scalable-manufactured randomized glass-polymer hybrid metamaterial for daytime radiative cooling, Science 355 (2017) 1062–1066. https://doi.org/10.1126/science.aai7899.

[43] B. Zhao, K. Lu, M. Hu, K. Wang, D. Gao, K. Chen, Q. Xuan, G. Pei, Sub-ambient daytime radiative cooling based on continuous sunlight blocking, Solar Energy Materials and Solar Cells 245 (2022) 111854. https://doi.org/10.1016/j.solmat.2022.111854.

[44] Z. Chen, L. Zhu, A. Raman, S. Fan, Radiative cooling to deep sub-freezing temperatures through a 24-h day–night cycle, Nat Commun 7 (2016) 13729. https://doi.org/10.1038/ncomms13729.

[45] A. Skartveit, J.A. Olseth, G. Czeplak, M. Rommel, On the estimation of atmospheric radiation from surface meteorological data, Solar Energy 56 (1996) 349–359. https://doi.org/10.1016/0038-092X(95)00117-A.

[46] T.M. Crawford, C.E. Duchon, An Improved Parameterization for Estimating Effective Atmospheric Emissivity for Use in Calculating Daytime Downwelling Longwave Radiation, Journal of Applied Meteorology and Climatology 38 (1999) 4. https://doi.org/10.1175/1520-0450(1999)038<0474:AIPFEE>2.0.CO;2.

[47] N.G. Loeb, J.M. Lyman, G.C. Johnson, R.P. Allan, D.R. Doelling, T. Wong, B.J. Soden, G.L. Stephens, Observed changes in top-of-the-atmosphere radiation and upper-ocean heating consistent within uncertainty, Nature Geosci 5 (2012) 110–113. https://doi.org/10.1038/ngeo1375.

[48] Y. Jiang, B.-H. Tang, H. Zhang, Estimation of downwelling surface longwave radiation for cloudy skies by considering the radiation effect from the entire cloud layers, Remote Sensing of Environment 298 (2023) 113829. https://doi.org/10.1016/j.rse.2023.113829.

[49] X. Berger, J. Bathiebo, F. Kieno, C.N. Awanou, Clear sky radiation as a function of altitude, Renewable Energy 2 (1992) 139–157. https://doi.org/10.1016/0960-1481(92)90100-H.

[50] C.G. Granqvist, A. Hjortsberg, Radiative cooling to low temperatures: General considerations and application to selectively emitting SiO films, Journal of Applied Physics 52 (1981) 4205–4220. https://doi.org/10.1063/1.329270.

[51] F. Kneizys, E. Shettle, W. Gallery, Atmospheric transmittance and radiance - The LOWTRAN 5 code, 277 (1981). https://doi.org/10.1117/12.931910.

[52] MODTRAN®, (n.d.). http://modtran.spectral.com/ (accessed June 23, 2023).

[53] L.S. Rothman, D. Jacquemart, A. Barbe, D. Chris Benner, M. Birk, L.R. Brown, M.R. Carleer, C. Chackerian, K. Chance, L.H. Coudert, V. Dana, V.M. Devi, J.-M. Flaud, R.R. Gamache, A. Goldman, J.-M. Hartmann, K.W. Jucks, A.G. Maki, J.-Y. Mandin, S.T. Massie, J. Orphal, A. Perrin, C.P. Rinsland, M.A.H. Smith, J. Tennyson, R.N. Tolchenov, R.A. Toth, J. Vander Auwera, P. Varanasi,

G. Wagner, The HITRAN 2004 molecular spectroscopic database, Journal of Quantitative Spectroscopy and Radiative Transfer 96 (2005) 139–204. https://doi.org/10.1016/j.jqsrt.2004.10.008.

[54] D.O. Staley, G.M. Jurica, Effective Atmospheric Emissivity under Clear Skies, Journal of Applied Meteorology and Climatology 11 (1972). https://doi.org/10.1175/1520-0450(1972)011<0349:EAEUCS>2.0.CO;2.

[55] S.B. Idso, A set of equations for full spectrum and 8- to 14-μm and 10.5- to 12.5-μm thermal radiation from cloudless skies, Water Resources Research 17 (1981) 295–304. https://doi.org/10.1029/WR017i002p00295.

[56] E.L. Andreas, S.F. Ackley, On the Differences in Ablation Seasons of Arctic and Antarctic Sea Ice, Journal of the Atmospheric Sciences 39 (1982) 188–201. https://doi.org/10.1175/JPO-2675.1.

[57] A.C. Dilley, D.M. O'brien, Estimating downward clear sky long-wave irradiance at the surface from screen temperature and precipitable water, Quarterly Journal of the Royal Meteorological Society 124 (1998) 1391–1401. https://doi.org/10.1002/qj.49712454903.

[58] R. Tang, Y. Etzion, I.A. Meir, Estimates of clear night sky emissivity in the Negev Highlands, Israel, Energy Conversion and Management 45 (2004) 1831–1843. https://doi.org/10.1016/j.enconman.2003.09.033.

[59] J.E. Sicart, R. Hock, P. Ribstein, J.P. Chazarin, Sky longwave radiation on tropical Andean glaciers: parameterization and sensitivity to atmospheric variables, Journal of Glaciology 56 (2010) 854–860. https://doi.org/10.3189/002214310794457182.

[60] E Clark, P Berdahl, Radiative cooling: Resource and Applications, Journal of the Royal Statistical Society. Series A (General) 143 (1980) 177–194. https://doi.org/10.2307/2981989.

[61] T.M.J. Nilsson, G.A. Niklasson, Radiative cooling during the day: simulations and experiments on pigmented polyethylene cover foils, Solar Energy Materials and Solar Cells 37 (1995) 93–118. https://doi.org/10.1016/0927-0248(94)00200-2.

[62] E. Erell, Y. Etzion, Radiative cooling of buildings with flat-plate solar collectors, Building and Environment 35 (2000) 297–305. https://doi.org/10.1016/S0360-1323(99)00019-0.

[63] M. Hanif, T.M.I. Mahlia, A. Zare, T.J. Saksahdan, H.S.C. Metselaar, Potential energy savings by radiative cooling system for a building in tropical climate, Renewable and Sustainable Energy Reviews 32 (2014) 642–650. https://doi.org/10.1016/j.rser.2014.01.053.

[64] Z. Liu, H. Tan, G. Ma, Experimental investigation on night sky radiant cooling performance of duct-type heat exchanger, International Journal of Ventilation 16 (2017) 255–267. https://doi.org/10.1080/14733315.2017.1299520.

[65] A.A. Alshammari, E.M. Salilih, E. Almatrafi, M. Rady, Polymeric coatings for passive radiative cooling of PV modules in hot and humid weather: Design, optimization, and performance evaluation, Case Studies in Thermal Engineering 57 (2024) 104341. https://doi.org/10.1016/j.csite.2024.104341.

[66] S. Zhao, B. Da, F. Peng, B. Hu, C. Gao, K. Dai, G. Zheng, C. Liu, C. Shen, Facilely fabricated polyethylene film composed of directional microfibrils for passive radiative cooling, Polymer 299 (2024) 126979. https://doi.org/10.1016/j.polymer.2024.126979.

[67] Y. Wu, B. Liu, R. Zhang, T. Yu, M. Pu, X. Li, X. Ma, Y. Guo, X. Luo, Temperature-adaptive porous polymer radiative cooling coatings for all-season thermal management and annual energy-saving, Energy and Buildings 296 (2023) 113423. https://doi.org/10.1016/j.enbuild.2023.113423.

[68] X. Wu, J. Li, F. Xie, X.-E. Wu, S. Zhao, Q. Jiang, S. Zhang, B. Wang, Y. Li, D. Gao, R. Li, F. Wang, Y. Huang, Y. Zhao, Y. Zhang, W. Li, J. Zhu, R. Zhang, A dual-selective thermal emitter with enhanced subambient radiative cooling performance, Nat Commun 15 (2024) 815. https://doi.org/10.1038/s41467-024-45095-4.

[69] Y. Zhang, C.Y. Tso, C.F.N. Tse, A.M.-L. Fong, K. Lin, Y. Sun, A novel radiative sky cooler system with enhanced daytime cooling performance to reduce building roof heat gains in subtropical climate, Renewable Energy 220 (2024) 119686. https://doi.org/10.1016/j.renene.2023.119686.

[70] J. Chen, L. Lu, Q. Gong, B. Wang, S. Jin, M. Wang, Development of a new spectral selectivity-based passive radiative roof cooling model and its application in hot and humid region, Journal of Cleaner Production 307 (2021) 127170. https://doi.org/10.1016/j.jclepro.2021.127170.

[71] T.S. Eriksson, S.-J. Jiang, C.G. Granqvist, Surface coatings for radiative cooling applications: Silicon dioxide and silicon nitride made by reactive rf-sputtering, Solar Energy Materials 12 (1985) 319–325. https://doi.org/10.1016/0165-1633(85)90001-2.

[72] N.M. Nahar, P. Sharma, M.M. Purohit, Performance of different passive techniques for cooling of buildings in arid regions, Building and Environment 38 (2003) 109–116. https://doi.org/10.1016/S0360-1323(02)00029-X.

[73] H. Bao, C. Yan, B. Wang, X. Fang, C.Y. Zhao, X. Ruan, Double-layer nanoparticle-based coatings for efficient terrestrial radiative cooling, Solar Energy Materials and Solar Cells 168 (2017) 78–84. https://doi.org/10.1016/j.solmat.2017.04.020.

[74] Z. Huang, X. Ruan, Nanoparticle embedded double-layer coating for daytime radiative cooling, International Journal of Heat and Mass Transfer 104 (2017) 890–896. https://doi.org/10.1016/j.ijheatmasstransfer.2016.08.009.

[75] J. Peoples, X. Li, Y. Lv, J. Qiu, Z. Huang, X. Ruan, A strategy of hierarchical particle sizes in nanoparticle composite for enhancing solar reflection, International Journal of Heat and Mass Transfer 131 (2019) 487–494. https://doi.org/10.1016/j.ijheatmasstransfer.2018.11.059.

[76] X. Li, J. Peoples, Z. Huang, Z. Zhao, J. Qiu, X. Ruan, Full Daytime Sub-ambient Radiative Cooling in Commercial-like Paints with High Figure of Merit, Cell Reports Physical Science 1 (2020) 100221. https://doi.org/10.1016/j.xcrp.2020.100221.

[77] X. Li, J. Peoples, P. Yao, X. Ruan, Ultrawhite BaSO4 Paints and Films for Remarkable Daytime Subambient Radiative Cooling, ACS Appl. Mater. Interfaces 13 (2021) 21733–21739. https://doi.org/10.1021/acsami.1c02368.

[78] Subambient passive radiative cooling effects of barium sulfate and calcium carbonate paints under Malaysia's tropical climate, Environmental Science Advances 2 (2023) 1662–1679. https://doi.org/10.1039/d3va00161j.

[79] H. Tang, S. Li, Y. Zhang, Y. Na, C. Sun, D. Zhao, J. Liu, Z. Zhou, Radiative cooling performance and life-cycle assessment of a scalable MgO paint for building applications, Journal of Cleaner Production 380 (2022) 135035. https://doi.org/10.1016/j.jclepro.2022.135035.

[80] A. Felicelli, I. Katsamba, F. Barrios, Y. Zhang, Z. Guo, J. Peoples, G. Chiu, X. Ruan, Thin layer lightweight and ultrawhite hexagonal boron nitride nanoporous paints for daytime radiative cooling, Cell Reports Physical Science 3 (2022) 101058. https://doi.org/10.1016/j.xcrp.2022.101058.

[81] S. Atiganyanun, J.B. Plumley, S.J. Han, K. Hsu, J. Cytrynbaum, T.L. Peng, S.M. Han, S.E. Han, Effective Radiative Cooling by Paint-Format Microsphere-Based Photonic Random Media, ACS Photonics 5 (2018) 1181–1187. https://doi.org/10.1021/acsphotonics.7b01492.

[82] J. Syurik, G. Jacucci, O.D. Onelli, H. Hölscher, S. Vignolini, Bio-inspired Highly Scattering Networks via Polymer Phase Separation, Advanced Functional Materials 28 (2018) 1706901. https://doi.org/10.1002/adfm.201706901.

[83] W. Zou, L. Pattelli, J. Guo, S. Yang, M. Yang, N. Zhao, J. Xu, D.S. Wiersma, Biomimetic Polymer Film with Brilliant Brightness Using a One-Step Water Vapor–Induced Phase Separation Method, Advanced Functional Materials 29 (2019) 1808885. https://doi.org/10.1002/adfm.201808885.

[84] J. Kou, Z. Jurado, Z. Chen, S. Fan, A.J. Minnich, Daytime Radiative Cooling Using Near-Black Infrared Emitters, ACS Photonics 4 (2017) 626–630. https://doi.org/10.1021/acsphotonics.6b00991.

[85] J. Mandal, Y. Yang, N. Yu, A.P. Raman, Paints as a Scalable and Effective Radiative Cooling Technology for Buildings, Joule 4 (2020) 1350–1356. https://doi.org/10.1016/j.joule.2020.04.010.

[86] A.R. Gentle, G.B. Smith, A Subambient Open Roof Surface under the Mid-Summer Sun, Adv Sci (Weinh) 2 (2015) 1500119. https://doi.org/10.1002/advs.201500119.

[87] J. Mandal, Y. Fu, A.C. Overvig, M. Jia, K. Sun, N.N. Shi, H. Zhou, X. Xiao, N. Yu, Y. Yang, Hierarchically porous polymer coatings for highly efficient passive daytime radiative cooling, Science 362 (2018) 315–319. https://doi.org/10.1126/science.aat9513.

[88] W. Huang, Y. Chen, Y. Luo, J. Mandal, W. Li, M. Chen, C.-C. Tsai, Z. Shan, N. Yu, Y. Yang, Scalable Aqueous Processing-Based Passive Daytime Radiative Cooling Coatings, Advanced Functional Materials 31 (2021) 2010334. https://doi.org/10.1002/adfm.202010334.

[89] Q. Gong, L. Lu, J. Chen, W. Yin Lau, K. Ho Cheung, A novel aqueous scalable eco-friendly paint for passive daytime radiative cooling in sub-tropical climates, Solar Energy 255 (2023) 236–242. https://doi.org/10.1016/j.solener.2023.03.033.

[90] X. Xue, M. Qiu, Y. Li, Q.M. Zhang, S. Li, Z. Yang, C. Feng, W. Zhang, J.-G. Dai, D. Lei, W. Jin, L. Xu, T. Zhang, J. Qin, H. Wang, S. Fan, Creating an Eco-Friendly Building Coating with Smart Subambient Radiative Cooling, Advanced Materials 32 (2020) 1906751. https://doi.org/10.1002/adma.201906751.

[91] T. Li, Y. Zhai, S. He, W. Gan, Z. Wei, M. Heidarinejad, D. Dalgo, R. Mi, X. Zhao, J. Song, J. Dai, C. Chen, A. Aili, A. Vellore, A. Martini, R. Yang, J. Srebric, X. Yin, L. Hu, A radiative cooling structural material, Science 364 (2019) 760–763. https://doi.org/10.1126/science.aau9101.

[92] Hierarchically structured passive radiative cooling ceramic with high solar reflectivity | Science, (n.d.). https://www.science.org/doi/full/10.1126/science.adi4725 (accessed September 24, 2024).

[93] X. Zhao, T. Li, H. Xie, H. Liu, L. Wang, Y. Qu, S.C. Li, S. Liu, A.H. Brozena, Z. Yu, J. Srebric, L. Hu, A solution-processed radiative cooling glass, Science 382 (2023) 684–691. https://doi.org/10.1126/science.adi2224.

[94] A.L. Pisello, State of the art on the development of cool coatings for buildings and cities, Solar Energy 144 (2017) 660–680. https://doi.org/10.1016/j.solener.2017.01.068.

[95] A. Baniassadi, D.J. Sailor, P.J. Crank, G.A. Ban-Weiss, Direct and indirect effects of high-albedo roofs on energy consumption and thermal comfort of residential buildings, Energy and Buildings 178 (2018) 71–83. https://doi.org/10.1016/j.enbuild.2018.08.048.

[96] A. Baniassadi, D.J. Sailor, G.A. Ban-Weiss, Potential energy and climate benefits of super-cool materials as a rooftop strategy, Urban Climate 29 (2019) 100495. https://doi.org/10.1016/j.uclim.2019.100495.

[97] H. Fang, D. Zhao, J. Yuan, A. Aili, X. Yin, R. Yang, G. Tan, Performance evaluation of a metamaterial-based new cool roof using improved Roof Thermal Transfer Value model, Applied Energy 248 (2019) 589–599. https://doi.org/10.1016/j.apenergy.2019.04.116.

[98] M. Ma, K. Zhang, L. Chen, S. Tang, Analysis of the impact of a novel cool roof on cooling performance for a low-rise prefabricated building in China, Building Services Engineering Research and Technology 42 (2021) 26–44. https://doi.org/10.1177/0143624420960276.

[99] J. Chen, L. Lu, Q. Gong, W.Y. Lau, K.H. Cheung, Techno-economic and environmental performance assessment of radiative sky cooling-based super-cool roof applications in China, Energy Conversion and Management 245 (2021) 114621. https://doi.org/10.1016/j.enconman.2021.114621.

[100] N. Wang, Y. Lv, D. Zhao, W. Zhao, J. Xu, R. Yang, Performance evaluation of radiative cooling for commercial-scale warehouse, Materials Today Energy 24 (2022) 100927. https://doi.org/10.1016/j.mtener.2021.100927.

[101] J. Yang, D. llamathy Mohan Kumar, A. Pyrgou, A. Chong, M. Santamouris, D. Kolokotsa, S.E. Lee, Green and cool roofs' urban heat island mitigation potential in tropical climate, Solar Energy 173 (2018) 597–609. https://doi.org/10.1016/j.solener.2018.08.006.

[102] Y. He, H. Yu, A. Ozaki, N. Dong, Thermal and energy performance of green roof and cool roof: A comparison study in Shanghai area, Journal of Cleaner Production 267 (2020) 122205. https://doi.org/10.1016/j.jclepro.2020.122205.

[103] H. Yazdani, M. Baneshi, Building energy comparison for dynamic cool roofs and green roofs under various climates, Solar Energy 230 (2021) 764–778. https://doi.org/10.1016/j.solener.2021.10.076.

[104] J. Testa, M. Krarti, A review of benefits and limitations of static and switchable cool roof systems, Renewable and Sustainable Energy Reviews 77 (2017) 451–460. https://doi.org/10.1016/j.rser.2017.04.030.

[105] Z. Yuxuan, Z. Yunyun, Y. Jianrong, Z. Xiaoqiang, Energy saving performance of thermochromic coatings with different colors for buildings, Energy and Buildings 215 (2020) 109920. https://doi.org/10.1016/j.enbuild.2020.109920.

[106] M. Zinzi, S. Agnoli, G. Ulpiani, B. Mattoni, On the potential of switching cool roofs to optimize the thermal response of residential buildings in the Mediterranean region, Energy and Buildings 233 (2021) 110698. https://doi.org/10.1016/j.enbuild.2020.110698.

[107] X. Yue, H. Wu, T. Zhang, D. Yang, F. Qiu, Superhydrophobic waste paper-based aerogel as a thermal insulating cooler for building, Energy 245 (2022) 123287. https://doi.org/10.1016/j.energy.2022.123287.

[108] R.F. De Masi, V. Festa, S. Ruggiero, G.P. Vanoli, Thermal behaviour of a cool roof Aerogel-based: summer and autumn in-field campaign in a full-scale test-room, Solar Energy 259 (2023) 298–319. https://doi.org/10.1016/j.solener.2023.05.033.

[109] J. Chen, L. Lu, Comprehensive evaluation of thermal and energy performance of radiative roof cooling in buildings, Journal of Building Engineering 33 (2021) 101631. https://doi.org/10.1016/j.jobe.2020.101631.

[110] W. Zhang, D. Jiao, B. Zhao, G. Pei, Experimental and numerical investigation of the effects of passive radiative cooling-based cool roof on building energy consumption, Applied Energy 376 (2024) 124161. https://doi.org/10.1016/j.apenergy.2024.124161.

[111] J. Liu, L. Xie, H. Wu, G. Zhang, C. Fang, J. Gu, Exploring energy-saving performance of radiative cooling roofs with a transient heat transfer model, Journal of Building Engineering 88 (2024) 109174. https://doi.org/10.1016/j.jobe.2024.109174.

[112] A. Zuazua-Ros, C. Martín Gómez, J.C. Ramos, J. Bermejo-Busto, Towards cooling systems integration in buildings: Experimental analysis of a heat dissipation panel, Renewable and Sustainable Energy Reviews 72 (2017) 73–82. https://doi.org/10.1016/j.rser.2017.01.065.

[113] X. Liu, Z. Fan, X. Cao, Y. Wang, K. Luo, L. Wang, Comprehensive performance of a novel radiative cooling phase change roof: An experimental study, Applied Thermal Engineering 243 (2024) 122568. https://doi.org/10.1016/j.applthermaleng.2024.122568.

[114] C. Zhang, L. Chen, Z. Zhou, Z. Wang, L. Wang, Y. Zhang, Cooling performance of all-orientated building facades integrated with photovoltaic-sky radiative cooling system in summer, Renewable Energy 217 (2023) 119193. https://doi.org/10.1016/j.renene.2023.119193.

[115] E. Erell, Y. Etzion, A Radiative Cooling System Using Water as a Heat Exchange Medium, Architectural Science Review 35 (1992) 39–49. https://doi.org/10.1080/00038628.1992.9696712.

[116] M.C. Yew, M.K. Yew, L.H. Saw, T.C. Ng, K.P. Chen, D. Rajkumar, J.H. Beh, Experimental analysis on the active and passive cool roof systems for industrial buildings in Malaysia, Journal of Building Engineering 19 (2018) 134–141. https://doi.org/10.1016/j.jobe.2018.05.001.

[117] M.G. Meir, J.B. Rekstad, O.M. LØvvik, A study of a polymer-based radiative cooling system, Solar Energy 73 (2002) 403–417. https://doi.org/10.1016/S0038-092X(03)00019-7.

[118] J. Yuan, H. Yin, P. Cao, D. Yuan, S. Xu, Daytime radiative cooling of enclosed water using spectral selective metamaterial based cooling surfaces, Energy for Sustainable Development 57 (2020) 22–31. https://doi.org/10.1016/j.esd.2020.04.008.

[119] X. Yang, S. Wang, D. Zhang, J. Yu, Theoretical investigation of two ideal radiative cooling materials and radiative sky water-cooling module with ideal selective radiative materials, Energy and Buildings 323 (2024) 114768. https://doi.org/10.1016/j.enbuild.2024.114768.

[120] K. Zhou, N. Miljkovic, L. Cai, Performance analysis on system-level integration and operation of daytime radiative cooling technology for air-conditioning in buildings, Energy and Buildings 235 (2021) 110749. https://doi.org/10.1016/j.enbuild.2021.110749.

[121] S. Fakouriyan, R. Mokhtari, R. Ghasempour, Investigating the effect of employing a 24-hour radiative cooling system on the photovoltaic/thermal systems performance: A case-based research, Energy Reports 11 (2024) 3624–3640. https://doi.org/10.1016/j.egyr.2024.02.030.

[122] T. Yan, J. Li, J. Gao, X. Xu, J. Yu, Model validation and application of the coupled system of pipe-encapsulated PCM wall and nocturnal sky radiator, Applied Thermal Engineering 194 (2021) 117057. https://doi.org/10.1016/j.applthermaleng.2021.117057.

[123] D. Shen, C. Yu, W. Wang, Investigation on the thermal performance of the novel phase change materials wall with radiative cooling, Applied Thermal Engineering 176 (2020) 115479. https://doi.org/10.1016/j.applthermaleng.2020.115479.

[124] C. Yu, D. Shen, W. He, Z. Hu, S. Zhang, W. Chu, Parametric analysis of the phase change material wall combining with micro-channel heat pipe and sky radiative cooling technology, Renewable Energy 178 (2021) 1057–1069. https://doi.org/10.1016/j.renene.2021.07.001.

[125] T. Yan, X. Xu, J. Gao, Y. Luo, J. Yu, Performance evaluation of a PCM-embedded wall integrated with a nocturnal sky radiator, Energy 210 (2020) 118412. https://doi.org/10.1016/j.energy.2020.118412.

[126] T. Yan, Y. Luo, T. Xu, H. Wu, X. Xu, J. Li, Experimental study of the coupled wall system of pipe-encapsulated PCM wall and nocturnal sky radiator for self-activated heat removal, Energy and Buildings 241 (2021) 110964. https://doi.org/10.1016/j.enbuild.2021.110964.

[127] W. He, C. Yu, J. Yang, B. Yu, Z. Hu, D. Shen, X. Liu, M. Qin, H. Chen, Experimental study on the performance of a novel RC-PCM-wall, Energy and Buildings 199 (2019) 297–310. https://doi.org/10.1016/j.enbuild.2019.07.001.

[128] Y. Zhou, S. Wang, J. Peng, Y. Tan, C. Li, F.Y.C. Boey, Y. Long, Liquid Thermo-Responsive Smart Window Derived from Hydrogel, Joule 4 (2020) 2458–2474. https://doi.org/10.1016/j.joule.2020.09.001.

[129] T. Jiang, X. Zhao, X. Yin, R. Yang, G. Tan, Dynamically adaptive window design with thermo-responsive hydrogel for energy efficiency, Applied Energy 287 (2021) 116573. https://doi.org/10.1016/j.apenergy.2021.116573.

[130] Z. Yi, Y. lv, D. Xu, J. Xu, H. Qian, D. Zhao, R. Yang, Energy saving analysis of a transparent radiative cooling film for buildings with roof glazing, Energy and Built Environment 2 (2021) 214–222. https://doi.org/10.1016/j.enbenv.2020.07.003.

[131] B. Zhao, C. Wang, M. Hu, X. Ao, J. Liu, Q. Xuan, G. Pei, Light and thermal management of the semi-transparent radiative cooling glass for buildings, Energy 238 (2022) 121761. https://doi.org/10.1016/j.energy.2021.121761.

[132] X. Zhao, A. Aili, D. Zhao, D. Xu, X. Yin, R. Yang, Dynamic glazing with switchable solar reflectance for radiative cooling and solar heating, CR-PHYS-SC 3 (2022). https://doi.org/10.1016/j.xcrp.2022.100853.

[133] S. Wang, Y. Zhou, T. Jiang, R. Yang, G. Tan, Y. Long, Thermochromic smart windows with highly regulated radiative cooling and solar transmission, Nano Energy 89 (2021) 106440. https://doi.org/10.1016/j.nanoen.2021.106440.

[134] S. Wang, T. Jiang, Y. Meng, R. Yang, G. Tan, Y. Long, Scalable thermochromic smart windows with passive radiative cooling regulation, Science 374 (2021) 1501–1504. https://doi.org/10.1126/science.abg0291.

[135] S. Zhang, J. Niu, Cooling performance of nocturnal radiative cooling combined with microencapsulated phase change material (MPCM) slurry storage, Energy and Buildings 54 (2012) 122–130. https://doi.org/10.1016/j.enbuild.2012.07.041.

[136] A. Leroy, B. Bhatia, C.C. Kelsall, A. Castillejo-Cuberos, M. Di Capua H., L. Zhao, L. Zhang, A.M. Guzman, E.N. Wang, High-performance subambient radiative cooling enabled by optically selective and thermally insulating polyethylene aerogel, Sci. Adv. 5 (2019) eaat9480. https://doi.org/10.1126/sciadv.aat9480.

[137] E. Mu, Z. Wu, Z. Wu, X. Chen, Y. Liu, X. Fu, Z. Hu, A novel self-powering ultrathin TEG device based on micro/nano emitter for radiative cooling, Nano Energy 55 (2019) 494–500. https://doi.org/10.1016/j.nanoen.2018.10.057.

[138] J. Song, J. Seo, J. Han, J. Lee, B.J. Lee, Ultrahigh emissivity of grating-patterned PDMS film from 8 to 13 μ m wavelength regime, Applied Physics Letters 117 (2020) 094101. https://doi.org/10.1063/5.0017838.

[139] J.J. García-Esteban, J. Bravo-Abad, J.C. Cuevas, Deep Learning for the Modeling and Inverse Design of Radiative Heat Transfer, Phys. Rev. Applied 16 (2021) 064006. https://doi.org/10.1103/PhysRevApplied.16.064006.

[140] I. Haechler, H. Park, G. Schnoering, T. Gulich, M. Rohner, A. Tripathy, A. Milionis, T.M. Schutzius, D. Poulikakos, Exploiting radiative cooling for uninterrupted 24-hour water harvesting from the atmosphere, Sci. Adv. 7 (2021) eabf3978. https://doi.org/10.1126/sciadv.abf3978.

[141] A. Pirvaram, T. Cooper, S.N. Leung, P.G. O'Brien, A comprehensive study on using underside infrared reflectors to enhance the performance of radiative cooling structures, Energy Conversion and Management 304 (2024) 118180. https://doi.org/10.1016/j.enconman.2024.118180.

[142] L. Zhou, H. Song, N. Zhang, J. Rada, M. Singer, H. Zhang, B.S. Ooi, Z. Yu, Q. Gan, Hybrid concentrated radiative cooling and solar heating in a single system, Cell Reports Physical Science 2 (2021) 100338. https://doi.org/10.1016/j.xcrp.2021.100338.

[143] M. Dong, L. Zhu, B. Jiang, S. Fan, Z. Chen, Concentrated radiative cooling and its constraint from reciprocity, Opt. Express 30 (2022) 275. https://doi.org/10.1364/OE.445544.

[144] E. du M. van Voorthuysen, R. Roes, Blue Sky Cooling for Parabolic Trough Plants, Energy Procedia 49 (2014) 71–79. https://doi.org/10.1016/j.egypro.2014.03.008.

[145] A.F.G. Jacobs, B.G. Heusinkveld, S.M. Berkowicz, Passive dew collection in a grassland area, The Netherlands, Atmospheric Research 87 (2008) 377–385. https://doi.org/10.1016/j.atmosres.2007.06.007.

[146] A. Gentle, A. Nuhoglu, M. Arnold, G. Smith, 3D printable optical structures for sub-ambient sky cooling, 2017. https://doi.org/10.1117/12.2274568.

[147] R. Winston, Principles of solar concentrators of a novel design, Solar Energy 16 (1974) 89–95. https://doi.org/10.1016/0038-092X(74)90004-8.

[148] W.N.A. Wan Roshdan, H. Jarimi, A.H.A. Al-Waeli, O. Ramadan, K. Sopian, Performance enhancement of double pass photovoltaic/thermal solar collector using asymmetric compound parabolic concentrator (PV/T-ACPC) for façade application in different climates, Case Studies in Thermal Engineering 34 (2022) 101998. https://doi.org/10.1016/j.csite.2022.101998.

[149] G. Li, Design and Development of a Lens-walled Compound Parabolic Concentrator-A Review, J. Therm. Sci. 28 (2019) 17–29. https://doi.org/10.1007/s11630-019-1083-3.

[150] M.S. Marreiros, R. Rosa, Enhancement of radiation cooling by means of reflectors, Solar Energy 30 (1983) 463–471. https://doi.org/10.1016/0038-092X(83)90117-2.

[151] W.N.A. Wan Roshdan, H. Jarimi, A.H.A. Al-Waeli, O. Ramadan, K. Sopian, Performance enhancement of double pass photovoltaic/thermal solar collector using asymmetric compound parabolic concentrator (PV/T-ACPC) for façade application in different climates, Case Studies in Thermal Engineering 34 (2022) 101998. https://doi.org/10.1016/j.csite.2022.101998.

[152] F. Karimi, H. Xu, Z. Wang, J. Chen, M. Yang, Experimental study of a concentrated PV/T system using linear Fresnel lens, Energy 123 (2017) 402–412. https://doi.org/10.1016/j.energy.2017.02.028.

[153] O. Bel Hadj Brahim Kechiche, M. Hamza, Enhancement of a commercial PV module performance under Low Concentrated Photovoltaic (LCPV) conditions: A numerical study, Renewable Energy Focus 41 (2022) 258–267. https://doi.org/10.1016/j.ref.2022.04.002.

[154] G. Li, Q. Xuan, M.W. Akram, Y. Golizadeh Akhlaghi, H. Liu, S. Shittu, Building integrated solar concentrating systems: A review, Applied Energy 260 (2020) 114288. https://doi.org/10.1016/j.apenergy.2019.114288.

[155] G. Pei, G. Li, Y. Su, J. Ji, S. Riffat, H. Zheng, Preliminary Ray Tracing and Experimental Study on the Effect of Mirror Coating on the Optical Efficiency of a Solid Dielectric Compound Parabolic Concentrator, (2012) 13.

[156] Q. Xuan, G. Li, Y. Lu, B. Zhao, F. Wang, G. Pei, Daylighting utilization and uniformity comparison for a concentrator-photovoltaic window in energy saving application on the building, Energy 214 (2021) 118932. https://doi.org/10.1016/j.energy.2020.118932.

[157] A. Parthiban, T.K. Mallick, K.S. Reddy, Integrated optical-thermal-electrical modeling of compound parabolic concentrator based photovoltaic-thermal system, Energy Conversion and Management 251 (2022) 115009. https://doi.org/10.1016/j.enconman.2021.115009.

[158] R.J. Xu, Y.Q. Zhao, H. Chen, Q.P. Wu, L.W. Yang, H.S. Wang, Numerical and experimental investigation of a compound parabolic concentrator-capillary tube solar collector, Energy Conversion and Management 204 (2020) 112218. https://doi.org/10.1016/j.enconman.2019.112218.

[159] F. Masood, P. Nallagownden, I. Elamvazuthi, J. Akhter, M.A. Alam, A New Approach for Design Optimization and Parametric Analysis of Symmetric Compound Parabolic Concentrator for Photovoltaic Applications, Sustainability 13 (2021) 4606. https://doi.org/10.3390/su13094606.

[160] F. Masood, N.B.M. Nor, P. Nallagownden, I. Elamvazuthi, M.A. Alam, M. Yusuf, M. Ali, J. Akhter, M. Mehmood, Dataset on the effect of receiver size and acceptance half-angle on the aperture width and height of compound parabolic concentrator for low-concentrating photovoltaic applications using RSM, Data in Brief 39 (2021) 107630. https://doi.org/10.1016/j.dib.2021.107630.

[161] Optical and electrical performance investigation of truncated 3X non-imaging low concentrating photovoltaic-thermal systems, Energy Conversion and Management (2020) 18.

[162] Chandan, H. Baig, A. ali Tahir, K.S. Reddy, T.K. Mallick, B. Pesala, Performance improvement of a desiccant based cooling system by mitigation of non-uniform illumination on the coupled low concentrating photovoltaic thermal units, Energy Conversion and Management 257 (2022) 115438. https://doi.org/10.1016/j.enconman.2022.115438.

[163] G. Li, Q. Xuan, G. Pei, Y. Su, Y. Lu, J. Ji, Life-cycle assessment of a low-concentration PV module for building south wall integration in China, Applied Energy 215 (2018) 174–185. https://doi.org/10.1016/j.apenergy.2018.02.005.

[164] C. Deng, F. Chen, Model verification and photo-thermal conversion assessment of a novel facade embedded compound parabolic concentrator, Energy 220 (2021) 119739. https://doi.org/10.1016/j.energy.2020.119739.

[165] Q. Xuan, G. Li, Y. Lu, B. Zhao, X. Zhao, Y. Su, J. Ji, G. Pei, Design, optimization and performance analysis of an asymmetric concentrator-PV type window for the building south wall application, Solar Energy 193 (2019) 422–433. https://doi.org/10.1016/j.solener.2019.09.084.

[166] Q. Xuan, G. Li, H. Yang, C. Gao, B. Jiang, X. Liu, J. Ji, X. Zhao, G. Pei, Performance evaluation for the dielectric asymmetric compound parabolic concentrator with almost unity angular acceptance efficiency, Energy 233 (2021) 121065. https://doi.org/10.1016/j.energy.2021.121065.

[167] W. Lu, Y. Wu, P. Eames, Design and development of a Building Façade Integrated Asymmetric Compound Parabolic Photovoltaic concentrator (BFI-ACP-PV), Applied Energy 220 (2018) 325–336. https://doi.org/10.1016/j.apenergy.2018.03.071.

[168] S.H. Abu-Bakar, F. Muhammad-Sukki, R. Ramirez-Iniguez, T.K. Mallick, A.B. Munir, S.H. Mohd Yasin, R. Abdul Rahim, Rotationally asymmetrical compound parabolic concentrator for concentrating photovoltaic applications, Applied Energy 136 (2014) 363–372. https://doi.org/10.1016/j.apenergy.2014.09.053.

[169] S.H. Abu-Bakar, F. Muhammad-Sukki, D. Freier, R. Ramirez-Iniguez, T.K. Mallick, A.B. Munir, S.H. Mohd Yasin, A. Abubakar Mas'ud, N. Md Yunus, Performance analysis of a novel rotationally asymmetrical compound parabolic concentrator, Applied Energy 154 (2015) 221–231. https://doi.org/10.1016/j.apenergy.2015.04.122.

[170] S. Foster, F. Muhammad-Sukki, R. Ramirez-Iniguez, D.F. Raine, J. Deciga-Gusi, S.H. Abu-Bakar, N.A. Bani, A.B. Munir, A.A. Mas'ud, J.A. Ardila-Rey, Assessment of the RACPC Performance

under Diffuse Radiation for Use in BIPV System, Applied Sciences 10 (2020) 3552. https://doi.org/10.3390/app10103552.

[171] P. Zawadzki, F. Muhammad-Sukki, S.H. Abu-Bakar, N.A. Bani, A. Abubakar Mas'ud, J.A. Ardila-Rey, A.B. Munir, Life Cycle Assessment of a Rotationally Asymmetrical Compound Parabolic Concentrator (RACPC), Sustainability 12 (2020) 4750. https://doi.org/10.3390/su12114750.

[172] X. Meng, N. Sellami, A.R. Knox, A. Montecucco, J. Siviter, P. Mullen, A. Ashraf, A. Samarelli, L.F. Llin, D.J. Paul, W. Li, M.C. Paul, D.H. Gregory, G. Han, M. Gao, T. Sweet, R. Freer, F. Azough, R. Lowndes, X. Xia, T.K. Mallick, A novel absorptive/reflective solar concentrator for heat and electricity generation: An optical and thermal analysis, Energy Conversion and Management 114 (2016) 142–153. https://doi.org/10.1016/j.enconman.2016.02.011.

[173] M. Aykapadathu, M. Nazarinia, N. Sellami, Design and Fabrication of Absorptive/Reflective Crossed CPC PV/T System, Designs 2 (2018) 29. https://doi.org/10.3390/designs2030029.

[174] H. Baig, N. Sellami, T.K. Mallick, Trapping light escaping from the edges of the optical element in a Concentrating Photovoltaic system, Energy Conversion and Management 90 (2015) 238–246. https://doi.org/10.1016/j.enconman.2014.11.026.

[175] Y. Sun, D. Liu, J.-F. Flor, K. Shank, H. Baig, R. Wilson, H. Liu, S. Sundaram, T.K. Mallick, Y. Wu, Analysis of the daylight performance of window integrated photovoltaics systems, Renewable Energy 145 (2020) 153–163. https://doi.org/10.1016/j.renene.2019.05.061.

[176] K. Shanks, A. Knowles, A. Brierley, H. Baig, H. Orr, Y. Sun, Y. Wu, S. Sundaram, T. Mallick, An experimental analysis of the optical, thermal and power to weight performance of plastic and glass optics with AR coatings for embedded CPV windows, Solar Energy Materials and Solar Cells 200 (2019) 110027. https://doi.org/10.1016/j.solmat.2019.110027.

[177] Y. Tripanagnostopoulos, Ch. Siabekou, J.K. Tonui, The Fresnel lens concept for solar control of buildings, Solar Energy 81 (2007) 661–675. https://doi.org/10.1016/j.solener.2006.08.013.

[178] N. Sellami, Design and characterisation of a novel translucent solar concentrator, Thesis, Heriot-Watt University, 2013. https://www.ros.hw.ac.uk/handle/10399/2678 (accessed September 17, 2024).

[179] M. Khalid, K. Shanks, A. Ghosh, A. Tahir, S. Sundaram, T.K. Mallick, Temperature regulation of concentrating photovoltaic window using argon gas and polymer dispersed liquid crystal films, Renewable Energy 164 (2021) 96–108. https://doi.org/10.1016/j.renene.2020.09.069.

[180] S. Sharma, N. Sellami, A. Tahir, T. Mallick, R. Bhakar, Performance Improvement of a CPV System: Experimental Investigation into Passive Cooling with Phase Change Materials, Energies 14 (2021) 3550. https://doi.org/10.3390/en14123550.

[181] F. Chen, C. Gao, C. Yang, C. Li, Y. Bie, Surface-Shape Construction and Optical Analysis of Novel Solar Compound Parabolic Concentrator with Circular Absorber, Guangxue Xuebao/Acta Optica Sinica 39 (2019). https://doi.org/10.3788/AOS201939.0608001.

[182] C. Gao, F. Chen, Model building and optical performance analysis on a novel designed compound parabolic concentrator, Energy Conversion and Management 209 (2020) 112619. https://doi.org/10.1016/j.enconman.2020.112619.

[183] D.I. Paul, Optical performance analysis and design optimisation of multisectioned compound parabolic concentrators for photovoltaics application, International Journal of Energy Research 43 (2019) 358–378. https://doi.org/10.1002/er.4271.

[184] J. Xu, F. Chen, E. Xia, C. Gao, C. Deng, An optimization design method and optical performance analysis on multi-sectioned compound parabolic concentrator with cylindrical absorber, Energy 197 (2020) 117212. https://doi.org/10.1016/j.energy.2020.117212.

[185] X. Hu, F. Chen, Z. Zhang, Model construction and optical properties investigation for multi-sectioned compound parabolic concentrator with particle swarm optimization, Renewable Energy 179 (2021) 379–394. https://doi.org/10.1016/j.renene.2021.07.037.

[186] S. Sripadmanabhan Indira, C.A. Vaithilingam, R. Sivasubramanian, K.-K. Chong, R. Saidur, K. Narasingamurthi, Optical performance of a hybrid compound parabolic concentrator and parabolic

trough concentrator system for dual concentration, Sustainable Energy Technologies and Assessments 47 (2021) 101538. https://doi.org/10.1016/j.seta.2021.101538.

[187] A.B. Ortega, J.C. Castro, J.A. del R. Portilla, Experimental Study of a natural lighting system constructed with a Toroidal Parabolic Concentrator, in: OSA Advanced Photonics Congress (AP) 2020 (IPR, NP, NOMA, Networks, PVLED, PSC, SPPCom, SOF) (2020), Paper PvTu1G.5, Optica Publishing Group, 2020: p. PvTu1G.5. https://doi.org/10.1364/PVLED.2020.PvTu1G.5.

[188] A.B. Ortega, A. Terán-Franco, J.C. Castro, J.A. del Río, Optical and thermal performance of a toroidal compound parabolic concentrator, Appl. Opt., AO 60 (2021) 2213–2221. https://doi.org/10.1364/AO.413681.

[189] H.A. Hajjar, B. Fracasso, F. Lamarque, Mini optical concentrator design for indoor high bit rate optical wireless communications, in: 2013 2nd International Workshop on Optical Wireless Communications (IWOW), 2013: pp. 147–151. https://doi.org/10.1109/IWOW.2013.6777796.

[190] H.-J. Choi, C. Cho, S. Woo, J.-Y. Lee, Y.-E. Yoo, M. Jeon, G.-H. Kim, T.-J. Je, E. Jeon, Manufacturing of Compound Parabolic Concentrator Devices Using an Ultra-fine Planing Method for Enhancing Efficiency of a Solar Cell, Int. J. of Precis. Eng. and Manuf.-Green Tech. 8 (2021) 1405–1414. https://doi.org/10.1007/s40684-020-00287-3.

[191] E.-L. Hsiang, Z. He, Z. Yang, Y.-F. Lan, S.-T. Wu, Tailoring the light distribution of micro-LED displays with a compact compound parabolic concentrator and an engineered diffusor, Opt. Express, OE 29 (2021) 39859–39873. https://doi.org/10.1364/OE.445479.

[192] D. Chemisana, Building Integrated Concentrating Photovoltaics: A review, Renewable and Sustainable Energy Reviews 15 (2011) 603–611. https://doi.org/10.1016/j.rser.2010.07.017.

[193] Y. Lu, G. Li, Y.G. Akhlaghi, Q. Xuan, G. Pei, J. Ji, X. Zhao, Effect of grid and optimization on improving the electrical performance of compound parabolic concentrator photovoltaic cells, Solar Energy 196 (2020) 607–615. https://doi.org/10.1016/j.solener.2019.12.065.

[194] Q. Xuan, G. Li, G. Pei, Y. Lu, Y. Su, J. Ji, Optical design and experiment evaluation of a novel asymmetric compound parabolic concentrator (ACPC) integration with PV for building south wall

application, IOP Conf. Ser.: Mater. Sci. Eng. 556 (2019) 012019. https://doi.org/10.1088/1757-899X/556/1/012019.

[195] R.V. Parupudi, H. Singh, M. Kolokotroni, J. Tavares, Long term performance analysis of low concentrating photovoltaic (LCPV) systems for building retrofit, Applied Energy 300 (2021) 117412. https://doi.org/10.1016/j.apenergy.2021.117412.

[196] E. Radziemska, The effect of temperature on the power drop in crystalline silicon solar cells, Renewable Energy 28 (2003) 1–12. https://doi.org/10.1016/S0960-1481(02)00015-0.

[197] M. Tian, X. Yu, Y. Su, H. Zheng, S. Riffat, A study on incorporation of transpired solar collector in a novel multifunctional PV/Thermal/Daylighting (PV/T/D) panel, Solar Energy 165 (2018) 90–99. https://doi.org/10.1016/j.solener.2018.03.009.

[198] A.K. Athienitis, G. Barone, A. Buonomano, A. Palombo, Assessing active and passive effects of façade building integrated photovoltaics/thermal systems: Dynamic modelling and simulation, Applied Energy 209 (2018) 355–382. https://doi.org/10.1016/j.apenergy.2017.09.039.

[199] S. Nižetić, E. Giama, A.M. Papadopoulos, Comprehensive analysis and general economic-environmental evaluation of cooling techniques for photovoltaic panels, Part II: Active cooling techniques, Energy Conversion and Management 155 (2018) 301–323. https://doi.org/10.1016/j.enconman.2017.10.071.

[200] S. Sharma, A. Tahir, S. Reddy, T. Mallick, Performance enhancement of a Building-Integrated Concentrating Photovoltaic system using phase change material, Solar Energy Materials and Solar Cells 149 (2016). https://doi.org/10.1016/j.solmat.2015.12.035.

[201] G. Asefi, A. Habibollahzade, T. Ma, E. Houshfar, R. Wang, Thermal management of building-integrated photovoltaic/thermal systems: A comprehensive review, Solar Energy 216 (2021) 188–210. https://doi.org/10.1016/j.solener.2021.01.005.

[202] A. Karthick, K.K. Murugavel, P. Ramanan, Performance enhancement of a building-integrated photovoltaic module using phase change material, Energy 142 (2018) 803–812. https://doi.org/10.1016/j.energy.2017.10.090.

[203] Y. Chen, H. Hua, J. Wang, P.D. Lund, Integrated performance analysis of a space heating system assisted by photovoltaic/thermal collectors and ground source heat pump for hotel and office building types, Renewable Energy 169 (2021) 925–934. https://doi.org/10.1016/j.renene.2020.12.117.

[204] D.-C. Chou, T.-Y. Chou, C.-W. Li, ENHANCING BUILDING ENERGY CONSERVATION THROUGH THE INTEGRATION OF PHOTOVOLTAIC-THERMAL HYBRID SOLAR COLLECTORS, 技術學刊 33 (2018) 191–200.

[205] M. Tian, L. Zhang, Y. Su, Q. Xuan, G. Li, H. Lv, An evaluation study of miniature dielectric crossed compound parabolic concentrator (dCCPC) panel as skylights in building energy simulation, Solar Energy 179 (2019) 264–278. https://doi.org/10.1016/j.solener.2018.12.058.

[206] Y.S. Kim, K. Balkoski, L. Jiang, R. Winston, Efficient stationary solar thermal collector systems operating at a medium-temperature range, Applied Energy 111 (2013) 1071–1079. https://doi.org/10.1016/j.apenergy.2013.06.051.

[207] C. Deng, F. Chen, Preliminary investigation on photo-thermal performance of a novel embedded building integrated solar evacuated tube collector with compound parabolic concentrator, Energy 202 (2020) 117706. https://doi.org/10.1016/j.energy.2020.117706.

[208] E.-T. Xia, F. Chen, Analyzing thermal properties of solar evacuated tube arrays coupled with mini-compound parabolic concentrator, Renewable Energy 153 (2020) 155–167. https://doi.org/10.1016/j.renene.2020.02.011.

[209] X. Chen, X. Yang, Solar collector with asymmetric compound parabolic concentrator for winter energy harvesting and summer overheating reduction: Concept and prototype device, Renewable Energy 173 (2021) 92–104. https://doi.org/10.1016/j.renene.2021.03.119.

[210] G. Ma, Z. Yin, X. Liu, J. Qi, Y. Dai, Developments of CPC solar evacuated glass tube collector with a novel selective coating, Solar Energy 220 (2021) 1120–1129. https://doi.org/10.1016/j.solener.2020.08.052.

[211] P. Vijayakumar, G. Kumaresan, S. Gokul Kumar, M. Eswaran, A review on applications of nanofluid in evacuated tube heat pipe integrated with compound parabolic concentrator, Materials Today: Proceedings 45 (2021) 1227–1232. https://doi.org/10.1016/j.matpr.2020.04.250.

[212] V. Bhalla, V. Khullar, R.V. Parupudi, Design and thermal analysis of nanofluid-based compound parabolic concentrator, Renewable Energy 185 (2022) 348–362. https://doi.org/10.1016/j.renene.2021.12.064.

[213] G. Zhu, New adaptive method to optimize the secondary reflector of linear Fresnel collectors, Solar Energy 144 (2017) 117–126. https://doi.org/10.1016/j.solener.2017.01.005.

[214] Z.-D. Cheng, X.-R. Zhao, Y.-L. He, Y. Qiu, A novel optical optimization model for linear Fresnel reflector concentrators, Renewable Energy 129 (2018) 486–499. https://doi.org/10.1016/j.renene.2018.06.019.

[215] J.-J. Men, X.-R. Zhao, Z.-D. Cheng, Y.-K. Leng, Y.-L. He, Study on the annual optical comprehensive performance of linear Fresnel reflector concentrators with an effective multi-objective optimization model, Solar Energy 225 (2021) 591–607. https://doi.org/10.1016/j.solener.2021.07.051.

[216] J. Ma, C.-L. Wang, Y. Zhou, R.-D. Wang, Optimized design of a linear Fresnel collector with a compound parabolic secondary reflector, Renewable Energy 171 (2021) 141–148. https://doi.org/10.1016/j.renene.2021.02.100.

[217] S. Lokeswaran, T.K. Mallick, K.S. Reddy, Design and analysis of dense array CPV receiver for square parabolic dish system with CPC array as secondary concentrator, Solar Energy 199 (2020) 782–795. https://doi.org/10.1016/j.solener.2020.02.075.

[218] K.-K. Chong, T.-K. Yew, C.-W. Wong, M.-H. Tan, W.-C. Tan, B.-H. Lim, A.-C. Lai, Prototype of Dense-array Concentrator Photovoltaic System Using Non-imaging Dish Concentrators and Cross Compound Parabolic Concentrator, Energy Procedia 105 (2017) 131–136. https://doi.org/10.1016/j.egypro.2017.03.291.

[219] Y. Wu, K. Connelly, Y. Liu, X. Gu, Y. Gao, G.Z. Chen, Smart solar concentrators for building integrated photovoltaic façades, Solar Energy 133 (2016) 111–118. https://doi.org/10.1016/j.solener.2016.03.046.

[220] S. Liang, H. Zheng, S. Liu, X. Ma, Optical design and validation of a solar concentrating photovoltaic-thermal (CPV-T) module for building louvers, Energy 239 (2022) 122256. https://doi.org/10.1016/j.energy.2021.122256.

[221] G. Li, Q. Xuan, X. Zhao, G. Pei, J. Ji, Y. Su, A novel concentrating photovoltaic/daylighting control system: Optical simulation and preliminary experimental analysis, Applied Energy 228 (2018) 1362–1372. https://doi.org/10.1016/j.apenergy.2018.07.024.

[222] C. Feng, H. Zheng, R. Wang, Development of transparent greenhouse cover with function of generating electricity by surplus light and photovoltaic, Nongye Gongcheng Xuebao/Transactions of the Chinese Society of Agricultural Engineering 30 (2014) 135–141. https://doi.org/10.3969/j.issn.1002-6819.2014.08.016.

[223] T. Ulavi, T. Hebrink, J.H. Davidson, Analysis of a Hybrid Solar Window for Building Integration, Energy Procedia 57 (2014) 1941–1950. https://doi.org/10.1016/j.egypro.2014.10.058.

[224] Q. Ma, Y. Zhang, G. Wu, Q. Yang, Y. Yuan, R. Cheng, Y. Tong, H. Fang, Photovoltaic/spectrum performance analysis of a multifunctional solid spectral splitting covering for passive solar greenhouse roof, Energy Conversion and Management 251 (2022) 114955. https://doi.org/10.1016/j.enconman.2021.114955.

[225] E. Zhang, Q. Duan, J. Wang, Y. Zhao, Y. Feng, Experimental and numerical analysis of the energy performance of building windows with solar NIR-driven plasmonic photothermal effects, Energy Conversion and Management 245 (2021) 114594. https://doi.org/10.1016/j.enconman.2021.114594.

[226] H. Zhao, Q. Yan, J. Wang, D.-X. Hua, A Compound Parabolic Concentrator Coupled to an Optical Microlenslet Array for Projection Display, 2017. https://doi.org/10.2991/mme-16.2017.77.

[227] C.Y. Tso, K.C. Chan, C.Y.H. Chao, A field investigation of passive radiative cooling under Hong Kong's climate, Renewable Energy 106 (2017) 52–61. https://doi.org/10.1016/j.renene.2017.01.018.

[228] M.M. Hossain, B. Jia, M. Gu, A Metamaterial Emitter for Highly Efficient Radiative Cooling, Advanced Optical Materials 3 (2015) 1047–1051. https://doi.org/10.1002/adom.201500119.

[229] Optical Design Software | Photopia | Photopia Optical Design Software, (n.d.). https://www.ltioptics.com/en/optical-design-software-photopia.html (accessed January 31, 2023).

[230] S. Wittkopf, L. Oliver Grobe, D. Geisler-Moroder, R. Compagnon, J. Kämpf, F. Linhart, J.-L. Scartezzini, Ray tracing study for non-imaging daylight collectors, Solar Energy 84 (2010) 986–996. https://doi.org/10.1016/j.solener.2010.03.008.

[231] M. Tian, Y. Su, Multiple nonlinear regression model for predicting the optical performances of dielectric crossed compound parabolic concentrator (dCCPC), Solar Energy 159 (2018) 212–225. https://doi.org/10.1016/j.solener.2017.10.090.

[232] Y. Zhang, M. Hu, Z. Chen, Y. Su, S. Riffat, Modelling analysis of a solar-driven thermochemical energy storage unit combined with heat recovery, Renewable Energy 206 (2023) 722–737. https://doi.org/10.1016/j.renene.2023.02.076.

[233] X. Yu, Y. Su, A discussion of inner south projection angle for performance analysis of dielectric compound parabolic concentrator, Solar Energy 113 (2015) 101–113. https://doi.org/10.1016/j.solener.2014.12.024.

[234] Solar elevation angle (for a day) Calculator, High Accuracy Calculation for Life or Science. (n.d.). https://keisan.casio.com/exec/system/1224682277 (accessed January 31, 2023).

[235] Y. Dan, M. Hu, S. Suhendri, Y. Su, S. Riffat, Harnessing the characteristic of compound parabolic concentrators for directional concentration of emitted thermal radiation and solar shielding in building-integrated radiative cooling, Energy and Buildings 307 (2024) 113922. https://doi.org/10.1016/j.enbuild.2024.113922.

[236] G. Wang, Z. Zhang, Z. Chen, Design and performance evaluation of a novel CPV-T system using nano-fluid spectrum filter and with high solar concentrating uniformity, Energy 267 (2023) 126616. https://doi.org/10.1016/j.energy.2023.126616.

[237] H. Liu, J. Zhang, M. Pei, X. Ju, X. Ju, C. Xu, Optical, electrical, and thermal performance enhancement for a concentrating photovoltaic/thermal system using optimized polynomial compound parabolic concentrators, Applied Energy 358 (2024) 122596. https://doi.org/10.1016/j.apenergy.2023.122596.

[238] EnergyPlus, (n.d.). https://energyplus.net/weather (accessed February 15, 2024).

[239] K. Niachou, I. Livada, M. Santamouris, Experimental study of temperature and airflow distribution inside an urban street canyon during hot summer weather conditions. Part II: Airflow analysis, Building and Environment 43 (2008) 1393–1403. https://doi.org/10.1016/j.buildenv.2007.01.040.

[240] K. Guan, Surface and ambient air temperatures associated with different ground material: a case study at the University of California, Berkeley, in: 2011. https://www.semanticscholar.org/paper/Surface-and-ambient-air-temperatures-associated-a-Guan/b641d950ed67ab3e06748d328d29814e7c54c2fd (accessed October 16, 2024).

[241] A. Synnefa, M. Santamouris, I. Livada, A study of the thermal performance of reflective coatings for the urban environment, Solar Energy 80 (2006) 968–981. https://doi.org/10.1016/j.solener.2005.08.005.

[242] M. Hu, B. Zhao, S. Suhendri, J. Cao, Q. Wang, S. Riffat, R. Yang, Y. Su, G. Pei, Experimental study on a hybrid solar photothermic and radiative cooling collector equipped with a rotatable absorber/emitter plate, Applied Energy 306 (2022) 118096. https://doi.org/10.1016/j.apenergy.2021.118096.

[243] M. Alnajideen, M. Gao, A new configuration of V-trough concentrator for achieving improved concentration ratio of >3.0x, Solar Energy Materials and Solar Cells 245 (2022) 111877. https://doi.org/10.1016/j.solmat.2022.111877.

[244] B. Müller, T. Reis, A. Driesse, C. Reise, MAXIMIZING THE YIELD OF LARGE PV POWER PLANTS: WHAT CAN WE LEARN FROM MONITORING AND SIMULATION?, (2012).

[245] K.P. Sibin, N. Selvakumar, A. Kumar, A. Dey, N. Sridhara, H.D. Shashikala, A.K. Sharma, H.C. Barshilia, Design and development of ITO/Ag/ITO spectral beam splitter coating for photovoltaic-thermoelectric hybrid systems, Solar Energy 141 (2017) 118–126. https://doi.org/10.1016/j.solener.2016.11.027.

[246] Y. Su, S.B. Riffat, G. Pei, Comparative study on annual solar energy collection of a novel lens-walled compound parabolic concentrator (lens-walled CPC), Sustainable Cities and Society 4 (2012) 35–40. https://doi.org/10.1016/j.scs.2012.05.001.

Appendix

TIRF-TCPC-RC module experiment on 25th and 26th of June 2024

This part examines the differences in RC emitter temperature between the TIRF-TCPC-RC and flat-RC modules, as well as the ambient temperature measured during the night of 25th June and the day of 26th June in Nottingham, UK.

Figure 1 (a) illustrates the temperatures of two RC modules alongside ambient temperatures and solar irradiance, while Figure 1 (b) shows the weather data, including relative humidity and wind speed. Notably, relative humidity during this period was stable, ranging from 50-56%, and wind speeds remained below 2.5 m/s. These conditions facilitated the RC modules in achieving sub-temperature easily. However, when solar irradiance was present, the flat-RC module, lacking concentrator shading, showed the highest emitter temperatures. For instance, at 19:00, with solar radiation at 318.09 W/m^2, the emitter temperature of the flat-RC module reached 26.73 °C, while the TIRF-TCPC-RC module showed a temperature of 23.98 °C, which is 10.3% lower than the former. When solar radiation decreased to 50 W/m^2, the temperature of the flat-RC module was 0.52 °C higher than that of the TIRF-TCPC-RC module, highlighting the superior cooling performance of the latter.

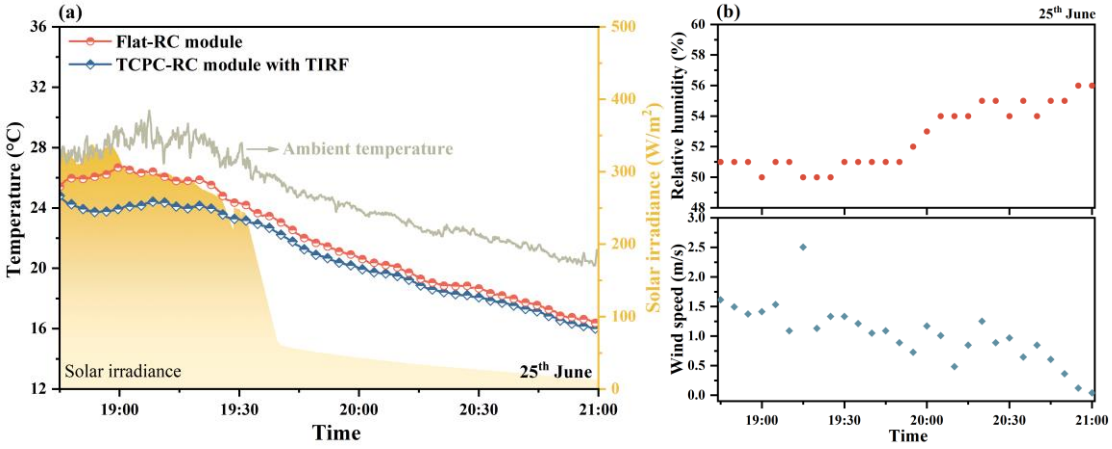

Figure 1: (a) Measured emitter temperatures of two RC emitters alongside ambient temperature and solar irradiance. (b) Weather data in Nottingham, UK, during the nighttime on 25th June of 2024.

The experimental results on 26th June are shown in Figure 2. On this day, relative humidity was higher than the previous night, ranging from 56 to 66%, while wind speeds remained similar. Additionally, solar radiation increased from 715.65 W/m^2 at 10:15 to 933.40 W/m^2 at 13:15, significantly impacting the cooling performance of the RC modules. It can be seen that the flat-RC

module was most affected by adverse thermal radiation and could not achieve a sub-ambient temperature. Additionally, while the transparent CPC in the TIRF-TCPC-RC module does not serve as a shield from adverse radiation like mirror CPC, it allows part of the incident light to pass through from the opposite side, thereby reducing the solar radiation impacting the RC emitter. However, as the solar altitude angle increases, the solar incident angle falls to the θ_{max} of the CPC. This period allows some solar radiation to directly reach the emitter, resulting in temperatures that exceed the ambient temperature. Around 12:35, cloud cover temporarily blocked the solar, leading to a sharp drop in temperatures for two RC modules, most notably for the flat-RC module, which fell from 30.39 to 27.29 °C, while the others experienced smaller declines. These results illustrate the significant impact of solar radiation on RC performance. Furthermore, despite the CPC's shielding capability, in the absence of solar radiation, the CPC-RC module cools slightly slower than the flat-RC module.

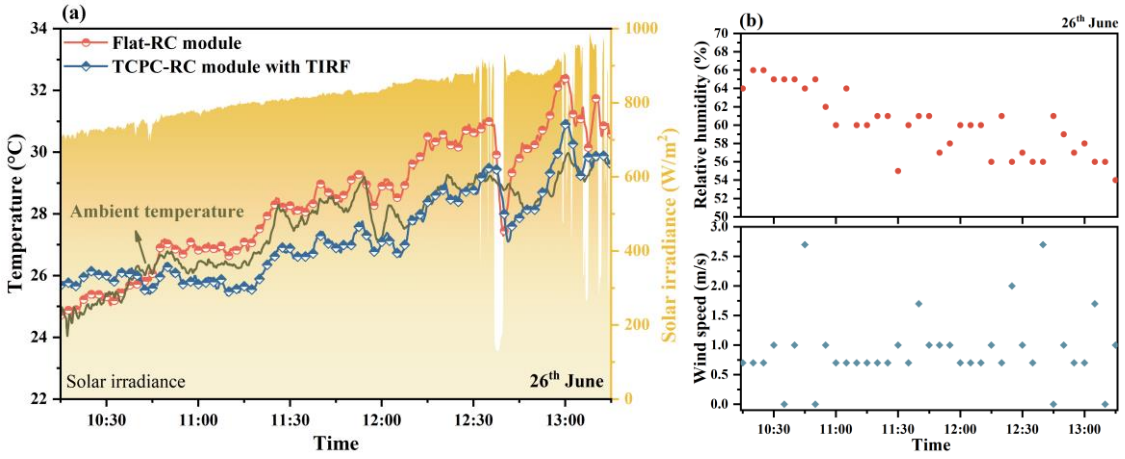

Figure 2: (a) Measured emitter temperatures of two RC emitters alongside ambient temperature and solar irradiance. (b) Weather data in Nottingham, UK, during the daytime on 26th June of 2024.

Error analysis.

The temperature of the RC emitter in this study is primarily measured using a thermocouple placed at the center of the emitter. The RC module in this experimental setup is small in size and features effective circumferential and bottom insulation. Additionally, the photovoltaic module is placed in a closed environment with a CPC structure above. As a result, the temperature on the surface of the RC emitter is less influenced by external factors and is more uniformly distributed. Therefore, the temperature at the center of the emitter can effectively represent the average temperature of the entire module. Using temperature data from Dr. Hu's previous experiment, the root means square difference (*RMSD*) is calculated between the temperature recorded by the center thermocouple (point 2) and the average temperature of 10

thermocouples. Figure 3 shows the experimental data and position of 10 thermocouples. After calculating, *RMSD* is 0.2027 °C. Given the small magnitude of this error relative to the temperature values, it indicates that the center temperature can reliably substitute for the average temperature of the entire RC emitter.

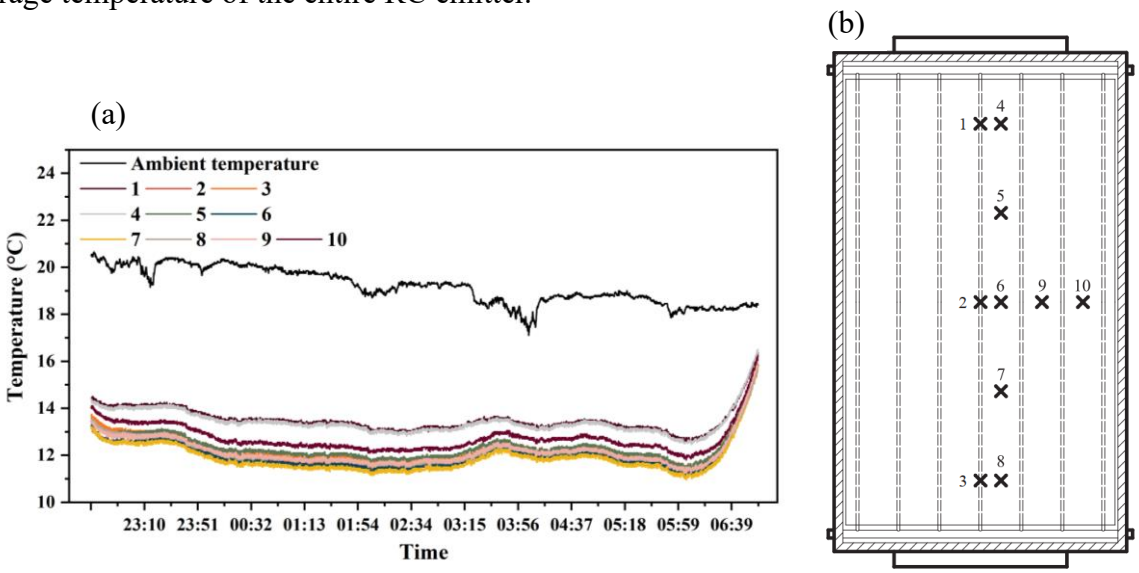

Figure 3: (a) Measured emitter temperatures and ambient temperatures. (b) Schematic diagram of the position of 10 thermocouples.

Additionally, the temperature measurement errors in chapter 5 during experiment primarily consist of two components: the test equipment error (thermocouple accuracy (ΔT_{sensor}) is ±0.5 °C and the installation/contact error ($\Delta T_{\text{contact}}$) is 0.2–0.3 °C). The total temperature error can thus be expressed as follows:

$$\Delta T_{\text{mean}} = \sqrt{\Delta T_{\text{sensor}}^2 + \Delta T_{\text{contact}}^2}$$

The calculated ΔT_{mean} is approximately 0.583 °C, which represents the temperature measurement error during the experiment.

The error in ΔP_{cool} is calculated using the following error propagation formula, which accounts for the radiative heat exchange between the RC emitter and the sky.

$$\Delta P_{\text{cool}} = \sqrt{\begin{aligned}&(\sigma T_{\text{emi}}^4 \Delta\varepsilon_{\text{emi}})^2 + (4\varepsilon_{\text{emi}}\varepsilon_{\text{sky}}\sigma T_{\text{amb}}^3 \Delta T_{\text{emi}}^4)^2 + (-\alpha_{\text{emi}}\sigma T_{\text{amb}}^4 \Delta\varepsilon_{\text{sky}})^2 + (-\varepsilon_{\text{sky}}\sigma T_{\text{amb}}^4 \Delta\alpha_{\text{emi}})^2 \\ &+(-4\alpha_{\text{emi}}\varepsilon_{\text{sky}}\sigma T_{\text{amb}}^3 \Delta T_{\text{amb}})^2\end{aligned}}$$

Among these, $\Delta T_{\text{emi}} = \Delta T_{\text{mean}} = 0.583$ °C; $\Delta\varepsilon_{\text{emi}} = \Delta\varepsilon_{\text{sky}} = \Delta\alpha_{\text{emi}} = 0.02$. Since P_{cool} represents the net radiative cooling power density in this study, and $T_{\text{amb}} = T_{\text{emi}}$. The result shows that $\Delta P_{\text{cool}} = 12.99$ W/m^2.